



**HAL**  
open science

# Characterization of nano-mechanical properties of biological lipid membranes with circular mode atomic force microscopy

Risa Nurin Baiti

► **To cite this version:**

Risa Nurin Baiti. Characterization of nano-mechanical properties of biological lipid membranes with circular mode atomic force microscopy. Biomechanics [physics.med-ph]. Université de Technologie de Compiègne, 2017. English. NNT : 2017COMP2403 . tel-01977441

**HAL Id: tel-01977441**

**<https://theses.hal.science/tel-01977441>**

Submitted on 10 Jan 2019

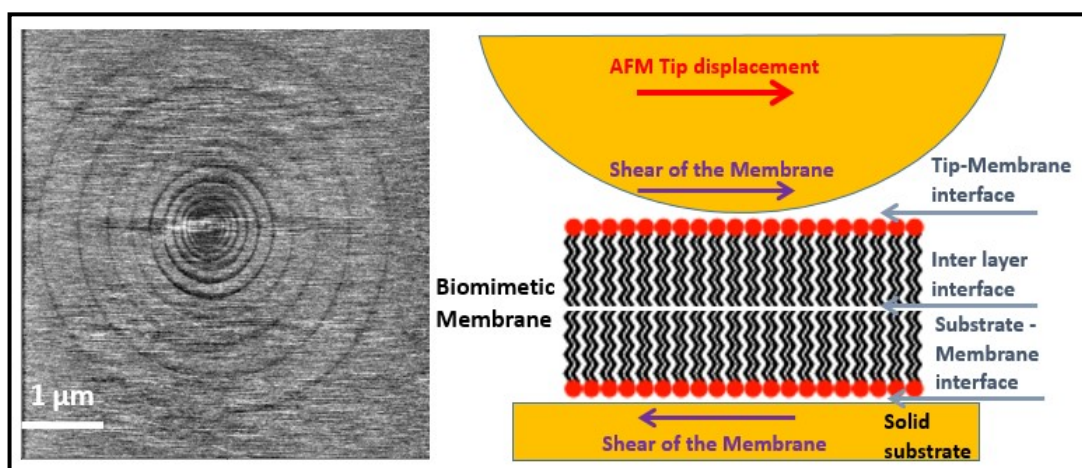
**HAL** is a multi-disciplinary open access archive for the deposit and dissemination of scientific research documents, whether they are published or not. The documents may come from teaching and research institutions in France or abroad, or from public or private research centers.

L'archive ouverte pluridisciplinaire **HAL**, est destinée au dépôt et à la diffusion de documents scientifiques de niveau recherche, publiés ou non, émanant des établissements d'enseignement et de recherche français ou étrangers, des laboratoires publics ou privés.

Par **Risa Nurin BAITI**

*Characterization of nano-mechanical properties of biological lipid membranes with circular mode atomic force microscopy*

Thèse présentée  
pour l'obtention du grade  
de Docteur de l'UTC



Soutenue le 28 novembre 2017

**Spécialité** : Biomécanique : Unité de Recherche Biomécanique  
et Bio-ingénierie (UMR-7338)

D2403



# THESIS

## Characterization of Nano-mechanical Properties of Biological Lipid Membranes with Circular Mode Atomic Force Microscopy

28 november 2017

by Risa Nurin BAITI

Under supervision of Pr. Karim EL KIRAT and Dr. Pierre-Emmanuel MAZERAN

### JURY

Denis	MAZUYER	Rapporteur
Touria	COHEN-BOUHACINA	Rapporteur
Marie-Christine	HO-BA-THO	Examineur
Olivier	NOEL	Examineur
Karim	EL KIRAT	Examineur
Pierre-Emmanuel	MAZERAN	Examineur

Thesis financed by Laboratoire of Excellence (LABEX) Control of Technological  
Systems-of-Systems (MS2T)

UMR CNRS 7338 - Laboratory of Biomechanic and Bio-engineering

Université de Technologie de Compiègne

# **Caractérisation des propriétés nanomécaniques des membranes lipidiques biologiques avec microscopie à force atomique mode circulaire**

**Par Risa Nurin BAITI**

**Soutenue le 28 novembre 2017**

**Spécialité : Biomécanique**

Sous la direction de Karim EL KIRAT et Pierre-Emmanuel MAZERAN

Unité de Recherche en Biomécanique et Bio-ingénierie (UMR-7338)

Université de Technologie de Compiègne



## **Characterization of Nano-mechanical Properties of Biological Lipid Membranes with Circular Mode Atomic Force Microscopy**

Cell membranes are involved in many cellular processes: drugs and ions diffusion, signal transduction, energy generation, cell development (fusion and fission). Phospholipid bilayers are the main components of cell membranes, they act as a dynamic barrier protecting cellular biochemical reactions. The determination of biochemical and mechanical properties of lipid bilayers and their evolution with environmental conditions is necessary to study the nature of cellular processes and the influence of external agents (mechanical resistance, permeability, and biological response). To conduct such characterizations, simplified biomimetic membrane models, such as supported lipid bilayers (SLBs), were developed.

Among the available characterization techniques, atomic force microscopy (AFM) has been widely used to study the nanoscale organization of SLBs under physiological conditions. AFM can yield high resolution images and it can also be used to quantify the mechanical resistance of SLBs by means of punch through experiments. For 30 years, AFM has been through many developments. Very recently, the Circular Mode AFM (CM-AFM) has been developed at the Université de Technologie de Compiègne. CM-AFM is able to generate a sliding movement of the AFM tip on the sample at high, constant and continuous velocity and to measure the lateral friction forces fast and accurately simultaneously with the vertical forces. For the first time CM-AFM is used to characterize biological samples under physiological conditions, allowing the simultaneous measurement of both the punch-through and the friction forces as a function of the sliding velocity. It offers for the first time the ability to describe the friction behavior of SLBs in complement of the punch-through force.

Due to the important need for quantitative measurement, optimization of the CM-AFM protocol has been done first. Protocol of scanner calibration has been successfully established to ensure the accuracy of sliding velocity. Besides, the protocol for tip calibration, based on wedge method and a scratched sample, is also made to determine the lateral force calibration constant. We have employed CM-AFM to measure the tribological properties of

solid samples to improve the equipment under liquid medium. Then, the mechanical properties (punchthrough and friction forces) of SLBs were measured as function of the sliding velocity. Pure and mixed SLBs were prepared by the vesicle fusion method. Various media were also used to study the effect of monovalent cations to the mechanical properties of SLBs. In all cases, the friction force increases linearly with the sliding velocity allowing us to deduce the friction viscous coefficient. As expected both the punchthrough force and the friction viscous coefficient are influenced by the composition of lipid mixtures, by the nature of cations in liquid medium, and by the length of hydrocarbon chains but not in a similar fashion.

The interpretation of the evolution of the viscous friction force coefficient with the studied system is particularly tricky as the friction force could be influenced by interface or volume properties. This problematic will be the challenge for the next studies. Nevertheless, our results illustrate how powerful the CM-AFM technique is and it opens wide opportunities to characterize other biological samples (cells and tissues) to gain a better understanding of the elementary mechanisms of friction.

## **Caractérisation des propriétés nanomécaniques des membranes lipidiques biologiques avec microscopie à force atomique mode circulaire**

Les membranes cellulaires sont impliquées dans de nombreux processus cellulaires: la diffusion des médicaments et des ions, la transduction des signaux, la génération d'énergie, le développement cellulaire (fusion et fission). Les bicouches phospholipides sont les principaux composants des membranes cellulaires, elles constituent une barrière dynamique protégeant les réactions biochimiques cellulaires. La détermination des propriétés biochimiques et mécaniques des bicouches lipidiques et leur évolution avec les conditions environnementales est nécessaire pour étudier la nature des processus cellulaires et l'influence des agents externes (résistance mécanique, perméabilité et réponse biologique). Pour mener de telles caractérisations, des modèles simplifiés de membrane biomimétique, tels que des bicouches lipidiques supportées (SLB), ont été développés.

Parmi les techniques de caractérisation disponibles, la microscopie à force atomique (AFM) a été largement utilisée pour étudier l'organisation nanométrique des SLB dans des conditions physiologiques. AFM peut produire des images à la haute résolution et peut également être utilisé pour quantifier la résistance mécanique des SLB au moyen d'expériences de perforation. Pendant 30 ans, AFM a traversé de nombreux développements. Très récemment, le Mode circulaire AFM (CM-AFM) a été développé à l'Université de Technologie de Compiègne. CM-AFM est capable de générer un mouvement de glissement de la pointe AFM sur l'échantillon à une vitesse élevée, constante et continue et de mesurer les forces de frottement latéral rapidement et exactement simultanément avec les forces verticales. Pour la première fois, le CM-AFM sert à caractériser les échantillons biologiques dans des conditions physiologiques, ce qui permet de mesurer simultanément les forces de poinçonnage et de frottement en fonction de la vitesse de glissement. Il offre pour la première fois la capacité de décrire le comportement de friction des SLB en complément de la force de perforation.

En raison du besoin important de mesure quantitative, l'optimisation du protocole CM-



AFM a été effectuée en premier. Le protocole d'étalonnage du scanner a été établi avec succès pour assurer la précision de la vitesse de glissement. En outre, le protocole d'étalonnage des pointes, basé sur la méthode de Wedge et un échantillon rayé, est également conçu pour déterminer la constante d'étalonnage de la force latérale. Nous avons utilisé CM-AFM pour mesurer les propriétés tribologiques des échantillons solides pour améliorer l'équipement sous milieu liquide. Ensuite, les propriétés mécaniques (forces de poinçonnage et de frottement) des SLB ont été mesurées en fonction de la vitesse de glissement. Les SLB purs et mixtes ont été préparés par la méthode de fusion des vésicules. Différents médias ont également été utilisés pour étudier l'effet des cations monovalents sur les propriétés mécaniques des SLB. Dans tous les cas, la force de frottement augmente linéairement avec la vitesse de glissement, ce qui nous permet de déduire le coefficient visqueux de frottement. Comme prévu, la force de poinçonnage et le coefficient visqueux de frottement sont influencés par la composition des mélanges de lipides, par la nature des cations en milieu liquide et par la longueur des chaînes hydrocarbonées mais pas de manière similaire.

L'interprétation de l'évolution du coefficient de force de frottement visqueux avec le système étudié est particulièrement délicate car la force de frottement pourrait être influencée par les propriétés d'interface ou de volume. Cette problématique sera le défi pour les prochaines études. Néanmoins, nos résultats illustrent la puissance de la technique CM-AFM et ouvre de nombreuses possibilités pour caractériser d'autres échantillons biologiques (cellules et tissus) afin de mieux comprendre les mécanismes élémentaires de friction.

Mots-clés: Mode circulaire AFM, bicouches lipidiques supportées, propriétés nanomécaniques

# Table of Content

---

<b>Abstract</b> .....	1
<b>Résumé</b> .....	3
<b>Table of Content</b> .....	5
<b>General Introduction</b> .....	11
 <b><i>LITERATURE REVIEW</i></b>	
<b>Chapter 1 Nanotribology</b> .....	17
1.1 Introduction.....	18
1.2 Macro- and Microscale Friction .....	19
1.2.1 Law of solid friction .....	20
1.2.2 Stick/Slip Friction .....	23
1.2.3 Lubrication .....	25
1.3 Nanoscale Friction .....	27
1.3.1 Single-asperity contact .....	28
1.3.2 Hertz Model .....	29
1.3.3 Effect of Adhesion .....	31
1.3.4 Friction Models.....	36
1.3.5 Effect of Velocity.....	38
1.3.6 Case example .....	39
1.4 Conclusion .....	41
<b>Chapter 2 Atomic Force Microscopy for Lipid Membrane Characterization</b> .....	43
2.1 History of AFM.....	44
2.2 Application of AFM.....	46
2.2.1 Imaging by AFM .....	46
2.2.2 AFM in Liquid .....	48
2.2.3 Force spectroscopy.....	49
2.2.4 Friction Force Microscopy (FFM).....	53
2.3 Sample Preparation for AFM.....	55

2.4 AFM verses other techniques .....	57
2.4.1 Surface Force Apparatus (SFA) .....	57
2.4.2 Micropipette Aspiration Technique .....	59
2.4.3 Optical Tweezer .....	60
2.4.4 Fluorescence Microscopy .....	61
2.4.5 Quartz Crystal Microbalance .....	62
2.5 Latest Development of AFM .....	62
2.6 Conclusion .....	64
<b>Chapter 3 Biological Membranes .....</b>	<b>65</b>
3.1 Cell Membranes .....	66
3.2 Model Membranes.....	67
3.2.1 Vesicles .....	69
3.2.2 Free-standing Membranes .....	73
3.2.3 Supported lipid bilayers (SLBs) .....	75
3.3 Lateral organization of cell membranes.....	78
3.4 Nanomechanical properties of cell membranes .....	79
3.4.1 Effect of temperature .....	79
3.4.2 Effect of medium composition .....	81
3.4.3 Effect of membrane composition.....	82
3.4.4 Effect of solid substrate.....	84
3.4.5 Friction, viscosity, and diffusion of lipid membranes.....	85
3.5 Conclusion .....	89
<b><i>MATERIALS AND METHODS</i></b>	
<b>Chapter 4 Materials and Methods .....</b>	<b>91</b>
4.1 Materials.....	92
4.1.1 Lipid .....	92
4.1.2 Mica surfaces.....	93
4.1.3 Gallium Arsenide (GaAs).....	93
4.1.4 Thiol-functionalized gold layer surface .....	94

4.1.5 Scratched Surfaces.....	94
4.1.6 Buffer solution .....	96
4.2 Methods .....	96
4.2.1 Preparation of lipid bilayers .....	96
4.2.2 Measurement of contact angle .....	97
4.2.3 Morphological characterization by AFM .....	98
4.2.4 Normal force calibration.....	99
4.2.5 Circular mode AFM .....	100
4.3 Conclusion .....	108

## **RESULTS AND DISCUSSION**

<b>Chapter 5 Calibration of the Circular Mode AFM.....</b>	<b>109</b>
5.1 Introduction.....	110
5.2 Lateral Force Calibration of AFM Tip.....	110
5.2.1 Principle of Method .....	114
5.2.2 Image acquisition.....	117
5.2.3 First Approach: Wedge Method .....	119
5.2.4 Second Approach: Scratch Method.....	121
5.2.5 Calibration line in different medium .....	129
5.3 Calibration of Piezoelectric Scanner .....	132
5.3.1 Initiation of Sliding.....	132
5.3.2 Resonance Frequency of Piezoelectric Scanner .....	133
5.3.3 Linearity of piezoelectric scanner.....	136
5.4 Conclusion .....	142
<b>Chapter 6 Friction Measurement on Solid Surfaces by CM-AFM .....</b>	<b>143</b>
6.1 Introduction.....	144
6.2 Characterization of bare mica surface .....	145
6.2.1 Morphology of mica .....	145
6.2.2 Data acquisition .....	145
6.2.3 Friction in air and water medium .....	147
6.2.4 Effect of environmental change .....	148

6.3 Characterization of bare glass surface (cover slip) .....	152
6.3.1 Morphology of the surface .....	152
6.3.2 Data acquisition .....	152
6.3.3 Effect of environmental change (addition of cations).....	153
6.4 Characterization of thiol-functionalized gold substrates.....	155
6.4.1 Contact angle of the surface.....	156
6.4.2 Morphology of the surface .....	156
6.4.3 Mechanical Characterization of Functionalized-Gold Layer.....	157
6.5 Discussion .....	160
6.6 Conclusion .....	162
<b>Chapter 7 Direct Measurement of Viscous Properties of Lipid Membranes by CM-AFM in The Case of Fluid SLBs .....</b>	<b>165</b>
7.1 Introduction.....	166
7.2 Optimization of CM AFM parameters .....	167
7.3 Morphology of fluid lipid membranes .....	168
7.4 Mechanical resistance of fluid lipid bilayers .....	169
7.5 Friction measurement of fluid lipid membranes .....	174
7.6 Discussion .....	175
7.7 Conclusion .....	181
<b>Chapter 8 Effect of Environment onto Nanomechanical Properties of Fluid Lipid Membranes.....</b>	<b>183</b>
8.1 Introduction.....	184
8.2 Results .....	185
8.3 Discussion .....	191
8.4 Conclusion .....	193
<b>Chapter 9 Effect of Lipid Composition on The Nanomechanical Properties of Bicomponents Membranes.....</b>	<b>195</b>
9.1 Introduction.....	196
9.2 Results .....	197
9.3 Discussion .....	203

9.4 Conclusion .....	206
<b>Chapter 10 Effect of Chain Length on Nanomechanical Properties of Pure SLBs .....</b>	<b>207</b>
10.1 Introduction.....	208
10.2 Results .....	209
10.3 Discussion.....	213
10.4 Conclusion .....	215
<b>Conclusions and Perspective .....</b>	<b>217</b>
<b>Annexe .....</b>	<b>221</b>
<b>References .....</b>	<b>237</b>
<b>Table of Figures .....</b>	<b>257</b>
<b>Table of Tables.....</b>	<b>267</b>
<b>Communications .....</b>	<b>269</b>

*(this page intentionally left blank)*

# General Introduction

---



## General Introduction

The advances of research in the fields of biomedical and bioengineering sciences contribute to the development of the next generation of therapies, devices, and diagnostics. Biomedical engineering itself is the application of engineering principles and design concepts to medicine and biology for healthcare purposes. This field fills the gap between engineering and medicine. It combines engineering skills with biological sciences to advance healthcare treatments, such as diagnosis, monitoring, and therapy. It recently emerged as a new field of research.

There are many topics discussed in the field of biomedical science and bioengineering. Drug delivery system is one of them. Drug is encapsulated inside biodegradable nanocapsules that will be released at designed places and times (Felice et al. 2014). It is well known to treat cancer cells because of its ability to target cancer cells specifically to release drugs thereby reducing side-effects. Indeed, targeting disease cells should prevent the healthy cells in the surrounding. There are various materials used to encapsulate drugs, such as biodegradable polymers (Mora-Huertas et al. 2010) and liposomes (Akbarzadeh et al. 2013). Liposomes are spherical vesicles with an internal aqueous compartment surrounded with at least one lipid bilayer. Due to their biocompatibility and biodegradability, liposomes were often chosen to encapsulate hydrophilic or hydrophobic drugs. To release the drug, liposomes will first attach then fuse with the membrane of target cell to finally reach cell interior. The mechanism of membrane fusion is a complex phenomenon for which the nanomechanical properties of lipid bilayers (in both the liposome and the cell envelope) play a crucial role. Therefore, understanding the influence of nanomechanical properties of lipid membranes is important to prepare lipid-based vehicles that can stimulate fusion with cell membranes.

Atomic force microscopy (AFM) coupled with force spectroscopy has been used frequently to characterize the nanomechanical properties (stiffness and punch-through force) of lipid membranes (Morandat et al. 2013). Modifications and developments were made to expand the capabilities of AFM. For example, the high-speed AFM (Ando 2014) with an imaging rate as high as 10 frames per second is developed to acquire video-like data. Besides, infrared coupled AFM (Fu & Zhang 2017) was developed to produce not only high

resolution topography images but also chemical maps to identify the chemical composition of the sample.

One of the most recent innovations is the Circular Mode AFM (CM-AFM) (Nasrallah et al. 2011) that has been developed at the Université de Technologie de Compiègne. It is able to generate circular horizontal displacement (relative to the sample plane) of the AFM probe. Therefore, the piezoelectric scanner has circular path rather than conventional linear path (raster scan - probe moves backward and forward). It offers great advantages such as, high scanning velocities, constant and continuous scanning (no rest period). For the first time, CM-AFM provides an access to friction forces simultaneously with punch-through forces of samples. It is very interesting because viscous friction of lipid membranes is very small and it is difficult; even if possible, to detect with conventional AFM which operates at low sliding velocity. Since lipid molecules have relatively high mobility, the displacement of the AFM probe in conventional AFM cannot sense their viscous properties. Thus, to detect viscous friction of biomembranes, it needs high sliding velocity which is possible with CM-AFM. Thanks to the circular displacement of scanning at high frequency, CM-AFM can keep a constant and continuous sliding velocity so that it is possible to access the viscous friction properties of the membranes.

Therefore, we held this research with several aims in mind: (1) to utilize CM-AFM in physiological medium in order to adapt it to the requirements for biological sample characterization; (2) to characterize quantitatively the friction behaviour of lipid membranes; (3) to gain a better understanding of membranes structure by interpreting their friction behaviour.

This thesis is a part of Labex *Maîtrise des Systèmes de Systèmes Technologiques* (MS2T) that focuses on multi-disciplinary scientific problems and applications. The labex MS2T is developed by three laboratories of the *Université de Technologie de Compiègne* affiliated to the *Centre National de la Recherche Scientifique* (CNRS). In the context of Labex MS2T framework, we concentrate on optimized design of technological systems of systems (SoSs) – multi-level and multi physical optimization of a set of complex systems. In our case, optimization of CM-AFM equipment and procedures of characterization is necessary to measure the nanomechanical properties of biological systems. Lipid membranes are considered as a system of systems. The elementary component is the lipid molecule and it can interact with other lipid molecules to generate emerging behaviours such as phase

separation. Thus, the bulk properties of lipid membranes are the result of systems of systems interaction. CM-AFM can be used to determine the lateral structure and dynamics of lipid membranes. CM-AFM can also probe the interaction between lipid membranes and proteins or any external agent. The knowledge of lipid membranes properties can be applied to improve and enhance the development of biomimetic lipid nano-systems designed for drug delivery purposes. CM-AFM is managed to address our multi-disciplinary problem that includes biological, mechanical, and chemical aspects.

This thesis consists of a general introduction, 10 chapters: a literature review, materials and methods, results, discussion, and a final chapter for the conclusion and perspectives.

In the literature review, there are three chapters: chapter 1, 2, and 3 that will explain respectively in detail the basic theory of nanotribology; the method of measurement: atomic force microscopy; and the object of this study: lipid membranes. It is important to distinguish nanoscale tribology from macro- and microscale tribology in order to set the proper interpretations. Furthermore, the basic working principle of AFM is given along with the comparison with some instruments which can measure friction forces. Recent development of AFM is also presented. Then, we review the preparation and properties of lipid membranes. Some examples of lipid membranes' characterization are given by pointing out several factors affecting their morphology, mechanical and frictional properties.

In chapter 4, the protocol of sample preparation and sample characterizations are developed. We introduce the principle of recently developed CM-AFM as our main instrument of characterization. The calibration procedure for AFM probe was also explained.

Chapter 5 – 10 will show all of the results acquired during 3 years of study accompanied by discussion. In chapter 5, we explain the protocol developed to adapt CM-AFM to our experimental conditions.

In chapter 6, we describe the preliminary experiments performed on various solid surfaces (mica, glass, and thiol-functionalized gold layer) to adapt the CM-AFM for measurements under in aqueous medium. These solid surfaces are commonly used as solid substrate in supported lipid membranes' preparation. Here, we are able to demonstrate for the first time the ability of CM-AFM to measure the mechanical resistance of normal and lateral forces in aqueous medium.

In chapter 7, we describe our results on biological samples: fluid SLBs of

dioleoylphosphatidyl choline (DOPC) lipid. We compare our results with previously published article for the same experimental condition to highlight the advantage of CM-AFM compared to conventional AFM. By measuring friction force at different sliding velocities, CM-AFM becomes the instrument that allows direct measurement of biomembranes' viscosity.

Chapter 8 demonstrates the effect of alkali cations to the mechanical and frictional properties of lipid membranes. LiCl, NaCl, and KCl were added to the aqueous medium. These monovalent cations have different ionic diameters. Among these ions, potassium is found to improve both the mechanical stability and the tribological properties of DOPC membrane.

In chapter 9, we studied the effect of lipid composition to the mechanical and frictional properties of lipid membranes. It is based on the idea that originally, cell membranes consist of heterogeneous types of lipids thus resulting in the formation of segregated lipid phases with different mechanical properties.

In chapter 10, we discuss the effect of the carbon chain length in lipid molecules to the mechanical properties of the resulting membranes. Dilauriloyl phosphatidylcholine (DLPC), dimyristoyl phosphatidylcholine (DMPC), and dipalmitoyl phosphatidyl choline (DPPC) with 12, 14, and 16 carbons per chain respectively were prepared and measured by CM-AFM separately. Then, we are able to demonstrate that the length of carbon tail chains affects linearly the viscous friction coefficient and the punch-through force.

For the last part, a short summary is given to conclude the three years of study on the characterization of nanomechanical properties of lipid membranes by using CM-AFM. Finally, the future perspectives are described because this study is only the first step from our long-term goal: to understand the mechanism of membrane dynamics in the process of natural membrane fusion in order to prepare lipid-based nano-vectors for drug delivery system and other dynamic properties of natural membranes.

| *(this page intentionally left blank)*

## Nanotribology

As quite recent discipline study, nanotribology is not yet very familiar. Therefore, in this chapter, brief explanation of nanotribology is given to differentiate it from macro- and microscale tribology. In general, tribology is a multidisciplinary study that involves contact between two surfaces. To begin with, laws of friction for solid friction are presented. They state that friction is proportional to normal, independent to contact area and sliding velocity. However, in nanoscale, frictional behavior of the surface is different than one in macro- or microscale and does not follow the classic friction law introduced by Coulomb and Amonton. To understand the contact at nanoscale, several reports of single-asperity experiments are given. Based on the published results, friction in nanoscale shows dependency on contact area and sliding velocity. Thus, it marks the special characteristic of nanotribology.

# Chapter 1

## Nanotribology

### 1.1 Introduction

The word « tribology » is derived from Greek word which means « rubbing ». So, literally tribology is the science of rubbing. It is considered as the mechanical interaction of bodies in contact with relative displacement. It can be defined as science of friction, adhesion, lubrication and wear on the length scale of micrometers to nanometers and the force scale of millinewtons (mN) to nanonewtons (nN) (Scherge & Gorb 2001). The term tribology was firstly proposed by Jost at 1964 (Bhushan 2011). In the dictionary, tribology is the branch of engineering that deals with the interaction of surfaces in relative motion. Understanding the surface interaction in tribology acquire multidisciplinary knowledge including physics, chemistry, solid mechanics, fluid mechanics, heat transfer, materials science, and rheology.

The development of technology, such the invention of hard disk drives, sensors, and processor; promote the miniaturization of technological devices (Gebeshuber 2005). It issues the necessity to understand the tribological phenomena at the micro- and nanoscale. Thus, the new term called *micro-* and *nanotribology* that separates the focus of discussion based on the working scale, is introduced. Scale difference in tribology poses specific characteristics. Nanotribology is usually characterized by single asperity contact and friction dependence to sliding velocity (Braun 2005).

In biological application, tribology can be also found in many systems at different length scale, such as: skin (Veijgen 2013; Derler & Gerhardt 2012), joints (Chernyakova & Goldade 2016), articular cartilage (Sotres & Arnebrant 2013), muscle connective tissues (Persson 2000), biological membranes (Merkel et al. 1989), etc. This topic refers to the term *biotribology*. More specific subject that discuss about biotribology in nanoscale is referred to bionanotribology. The aim of biotribology is to acquire information about friction, adhesion, lubrication, and wear of biological systems and then apply this knowledge for technological innovation either in biomimetic or bio-inspire systems (Gebeshuber 2005). The use of biological principles in material synthesis and assembly may become the path to develop molecular and nanoscale electronics (Sarıkaya 1999). For example, the information about frictional properties of lipid

bilayers is used to study interaction and adhesion forces between cells, and diffusion of phospholipids for therapeutic purpose (Oncins et al. 2005).

In short, this chapter will discuss the basic theory of tribology, including the characteristic of nanotribology. So, we are able to interpret the biological phenomena involving adhesion, friction, wear, and lubrication.

## 1.2 Macro- and Microscale Friction

Along with development of characterization technology, friction can be discussed based on the scale point of view. It is known that macroscopic friction behavior is determined by microscopic origins. However, this hypothesis was able to be proved after the invention of instrument that can do microscale measurement. The major different between macro and micro friction is located on the normal force ranges. The other differences are summarized on Table 1.1.

*Table 1.1 Macrofriction versus Microfriction (reproduced from Scherge & Gorb 2001)*

Parameter	Macrofriction	Microfriction
Normal force range	> 1 N	< 1 N
Ratio of real ( $A_R$ ) to geometric area ( $A_g$ )	$A_R \ll A_g$	$A_R \leq A_g$
Impact of wear	Large	Small, often negligible
Heat generation	Large	Small

The impact of each parameter depends on the investigated force and length scale. For example, the wear is commonly found in macrofriction but it is often negligible due to the presence of thin liquid film.

Tribology in macroscale often focuses on determining the friction coefficient and wear rate for the material of interest. However, both friction coefficient and wear rate are not materials' intrinsic physical properties and are depending on chemistry, elastic/plastic properties of the surfaces, chemical environment during measurement, and on the sliding history of the interface (Szlufarska et al. 2008).

In addition, relative motion of one surface on another surface may result in a continuous



sliding movement or discontinuous stick/slip movement depends on the roughness of both contacting surfaces (Tabor 1992) and also the sliding velocity (Braun & Röder 2002). In macrofriction, roughness causes mechanical interlock followed by an abrupt release of the force stick/slips. The frequency and amplitude of the stick/slip are a function of mechanical parameters such as mass and stiffness. The term stick/slip was created by Bowden at 1939 by describing movement of surface in which sliding occurs as a sequence of sticking and slipping as an oscillation at resonant frequency of the system. In the absence of wear, the asperities of one solid have to slide over the asperities of other solid. But, in the presence of wear, stick/slip tends to vanish due to the onset of rolling friction as part of a three-body effect. Asperities debris are formed on hard and brittle surface, while on softer surfaces, it gives the effect of ploughing (Bisson 1968; Kim & Suh 1991).

### ***1.2.1 Law of solid friction***

#### **A. Amonton-Coulomb laws**

The first record of scientific reports regarding friction was made by Leonardo da Vinci in the 15<sup>th</sup> century. For the first time he introduced the term of friction coefficient as the ratio of friction force to normal force by observing the sliding motion of rectangular block over a flat surface. However, his works were never published. Hundreds of years later, Guillaume Amontons (1699) and Charles-Augustin Coulomb (1781) formulated the dry friction laws which are still valid nowadays. Amontons presented the two friction laws after studying the sliding motion between two dry flat surfaces (Bhushan 2011). He observed the block slider made of wood down inclined planes by pulling the strings rolling over pulleys with weights hanging at the ends. The assumption is that there is no adhesion so the friction is load-controlled (Israelachvili 2013).

The first friction law, friction force is the force that resists the sliding at an interface and is directly proportional to the normal load. The second friction law, the amount of friction force is independent to apparent area of contact. Later, the works of Amontons were verified by Charles-Augustin Coulomb. He completed law of Amontons by adding the third friction law, friction force is also independent to the sliding velocity once the motion starts. Moreover, he also distinguishes static friction from kinetic friction. All three laws are known as Amontons'

law of friction (Persson & Tosatti 1995).

Figure 1.1 illustrates the block with mass  $m$  slides over a solid flat track. Normal force  $F$  is perpendicular to the solid-solid interface while the pulling force  $f$  is parallel to the interface. Magnification at interface shows that the effective contact area made of several localized patches is much smaller than the nominal area of contact  $\Sigma_0$ . In short, it has polyasperity contact.

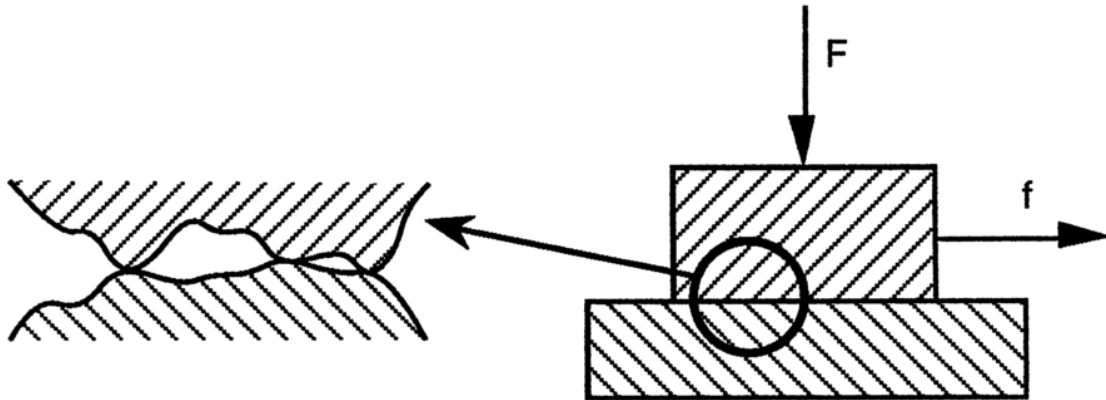


Figure 1.1 Scheme of sliding motion between rectangular block over a flat surface.  $F$  is the normal force while  $f$  is the pulling force. The left image showing the magnification of solid-solid interface (reproduced from Persson & Tosatti 1995)

At static condition, the friction force or the force to resist the pulling can be computed as,

$$F_s = \mu_s F_N \quad (1.1)$$

$\mu_s$  is the static friction coefficient. Static friction force corresponds to the minimum tangential force required to initiate the sliding.

When rectangular block starts to slide onto the flat surface with velocity  $v$ , friction force is

$$F_k = \mu_k F_k \quad (1.2)$$

Where  $\mu_k$  is the kinetic friction coefficient. The kinetic friction force  $f_k$  is the force needed to maintain the sliding at given velocity and it equals to the dissipative work done at the interface divided by the distance covered by the slider block (Gnecco & Meyer 2014).

The classical Amonton-Coulomb law of friction stated that both static and kinetic friction coefficient are independent of normal force and nominal contact area (Persson & Tosatti 1995).

### **B. Law of Bowden and Tabor**

Bowden and Tabor demonstrated the weaknesses of Amonton's law. They introduced the concept of the real contact area  $A_R$  (Tabor 1992). Real contact area is composed by big amount of small contact of asperities. At the interface, the atoms of the coupled surface are in contact. Thus the real contact between two solids is only a small fraction of the apparent contact area.

Moreover, Bowden and Tabor introduce the model that relates adhesive force and friction force by taking plastic junction into consideration. They postulated that friction force is proportional to the real contact area since it arises from force required to shear the adhesive junction. In other words, friction force is the force required to overcome adhesion between surfaces (Kumacheva 1998).

$$Ff = \tau A_R \quad (1.3)$$

$\tau$  denotes the shear stress at the interface. This model is known as plastic junction model which is based on the plastic deformation of the asperities due to friction mechanism (Bowden & Hughes 1939). However, this model is also known as adhesion model because adhesion is also proportional to the real contact area.

The total stress  $\tau$  is assumed to include the intrinsic material shear strength  $\tau_0$  or the stress at zero load and the compression stress  $\sigma_c$  or the normal pressure acting on limited unit area. Thus it can be understood that shear stress has linear relation with shear stress on the acting pressure.

$$\tau = \tau_0 + \alpha \sigma_c \quad (1.4)$$

$$\sigma_c = \frac{F_N}{A_R} \quad (1.5)$$

$\alpha$  is a constant determined by the atomic smoothness of the surfaces and the dimensions and shape of molecules in the gap between sliding surfaces (Homola et al. 1990).

So, the dependence of friction force to the normal force can be derived by combining equation 1.3; 1.4 and 1.5.

$$F_f = \tau A_R = (\tau_0 + \alpha \sigma_c) A_R = (\tau_0 A_R + \alpha F_N) \quad (1.6)$$

### 1.2.2 Stick/Slip Friction

Friction means loss of energy and work against the relative motion of contacting surfaces. For basic friction experiments (see Figure 1.2), the flat silicon sample is moved in the x-direction with velocity  $v_1$  to scrub the silicon ball which is attached to a spring (silicon model system). Flat sample's position is parallel to the spring. Tangential force  $F_t$  of the spring can be quantified by Equation 1.7.  $k_x$  is the spring constant and  $\Delta x$  is the elongation of spring.

$$F_t = -k_x \Delta x \quad (1.7)$$

There isn't any relative motion between the ball and the flat sample at  $x = 0$  and  $x = x_s$ . In this state which is called stiction, the ball and the flat sample are stick to each other and move together at the same velocity. At  $x = x_s$ , the ball starts to slide and the static friction  $F_{fS}$  is recorded. Then, the ball continues to slide on the flat sample at further sliding distance. In this state, the velocity of the ball becomes zero for the case of fluctuation-free sliding in which the relative sliding velocity of the ball  $v_{rel} = v_1$ . If there is fluctuation,  $v_{rel}$  is in the range between  $v_1$  and  $v_2$ .  $F_{fd}$  is the dynamic friction or the average tangential forces during sliding.

$$F_s = -k_x x_s \quad (1.8)$$

$$F_{fd} = -\frac{1}{N} k_x \sum_{i=1}^N x_i \quad (1.9)$$

$N$  is the number of samples taken between  $x_s$  and  $x_{max}$ .

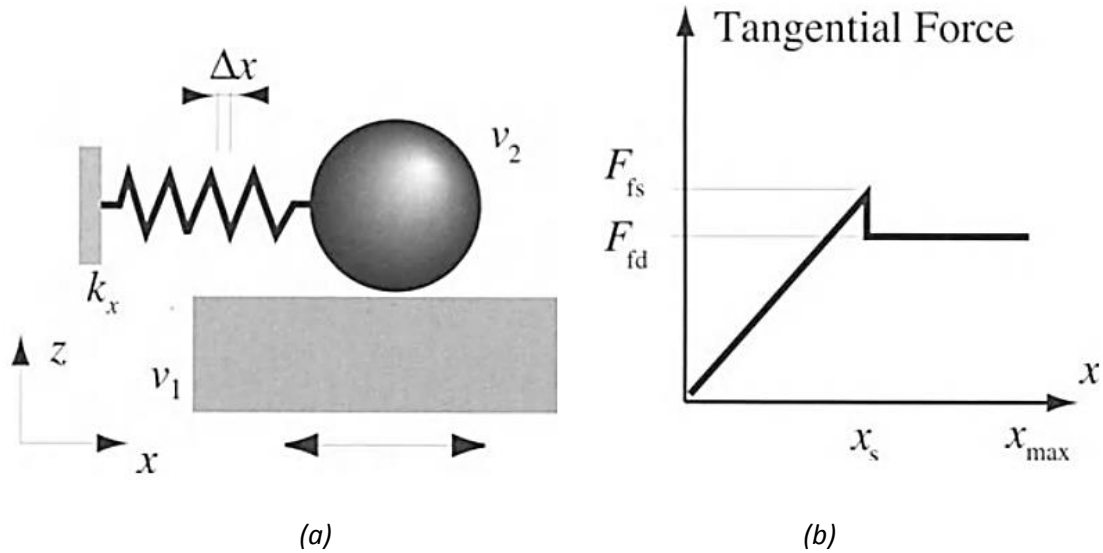


Figure 1.2 (a) Basic setup for friction experiments using silicon model system and (b) ideal tangential force curve (reproduced from Scherge & Gorb 2001)

The basic model of Coulomb friction describes global relationship between static friction force and velocity. The friction coefficient is independent on sliding velocity. As stated in the friction law of Amonton-Coulomb, friction force is independent of sliding velocity. The dimensionless static friction coefficient is  $-1 \leq \mu_s \leq 1$  (Stark et al. 2004). Moreover, this model of friction only applies for dry sliding contact (Geffen 2009).

Coulomb friction can be modeled as elastic and plastic deformation forces of microscopic asperities in contact. Each asperity has a part of  $f_i$  of the normal load  $F_N$ . The assumption is that plastic deformation of the asperities has grown large enough and becomes contact junction. The contact area  $A_i$  of each asperity junction can be computed as,

$$A_i = \frac{f_i}{H} \quad (1.10)$$

where  $H$  is the hardness of the weakest bulk material bodies in contact. So, the total contact area (plastic junction) is

$$A_R = \frac{F_N}{H} \quad (1.11)$$

The tangential deformation of each asperity is elastic until the applied shear pressure exceeds the shear strength of the surface materials because at this point it becomes plastic. Thus, the friction force can be calculated by Bowden and Tabor's formula as:

$$F_{fT} = \tau_y A_R \quad (1.12)$$

friction coefficient can be calculated with the following equation and it does not depend on normal load.

$$\mu = \frac{F_T}{F_N} = \frac{\tau_y}{H} \quad (1.13)$$

### **1.2.3 Lubrication**

At most frictional processes, both surfaces are damaged and produced debris particles in the case of brittle materials. For more ductile surfaces, the damage remains localized at nanoscale. When there is a lubricating layer that separates the mating surfaces, this condition is known as interfacial sliding or **boundary friction** or **viscous friction** (Bushan 1995).

The presence of a lubricating layer reduces friction by a factor of  $\mu_v$ , which is lower than Coulomb friction coefficient  $\mu_C$  (Virgala & Kelemen 2013). The slope of linear friction law is given by the viscous contribution.

$$F_{fv} = \mu_v F_N v \quad (1.14)$$

At low velocities, lubricants act as a surface film in which the friction is determined by shear strength. However, at high velocities and low pressure, a fluid layer of lubricant is built up in the interface due to hydrodynamic effects. Then, the shear forces which depend on the viscous character of the lubricant, determine the friction (Olsson et al. 1998).

The thickness (related to viscosity) of the lubricating layer played a huge role in controlling the friction between smooth surfaces. As the lubricant becomes thinner, its physical properties are changed quantitatively and qualitatively (Granick 1991; Hu & Granick 1992; Dhinojwala & Granick 1997). Quantitatively, there is an increase of viscosity, the

appearance of non-Newtonian flow behavior, and the presence of glass transition temperature instead of melting point but the film remains as a liquid. This regime is known as “**mixed lubrication**” regime as the rheological properties of film is between the bulk and boundary properties. Qualitatively, thin film undergoes first-order phase transitions to solid or liquid-crystalline phase whose properties are difficult to characterize (Gee et al. 1990; Klein & Kumacheva 1995).

At certain film thickness in which lubricant is able to completely separate the coupled surface, the friction coefficient increase with velocity as hydrodynamic effect becomes significant. This regime is known as **hydrodynamic lubrication** in which Stribeck effect takes place in which the separation between contacting surfaces is comparable to their roughness. Stribeck concept is only applied at high velocity because at low velocity the film thickness can decrease. At this case, the asperities can have contact and causing wear and high friction. Stribeck curve describes the variation of friction coefficient  $\mu$  with the parameter  $\frac{\eta v}{F_N}$  (see Figure 1.3) (Gnecco & Meyer 2014).

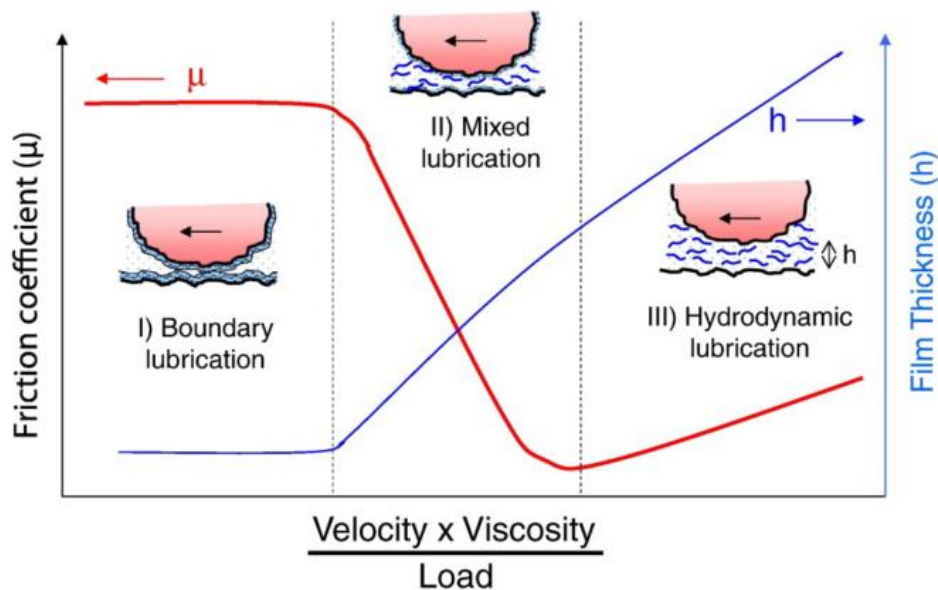


Figure 1.3 Stribeck curve (reproduced from Coles et al.2010)

Stribeck curve is popular to differentiate which type of sliding regime is occurring: boundary lubrication, mixed lubrication, or hydrodynamic lubrication. The thickness of lubricant film is proportional with the fluid viscosity and the relative velocity, and inversely with the applied load. It is clear already that lubrication is highly dependent on the viscoelastic properties of both lubricant and the adsorbed lubricant films. For boundary lubrication regime,

friction decreases with increasing velocity until mixed or full film lubrication is achieved, after which the friction force can either be constant or increase with increased sliding velocity due to viscous and thermal effect (Andersson et al. 2007; Maru & Tanaka 2007). The fluid-film lubrication regime will prevail at high loads for high viscosity lubricant and vice versa. Meanwhile, in the boundary lubrication regime, the friction force is also dependent on viscoelasticity and plasticity of the lubricant films as these properties will determine the real contact area.

Stribeck friction model covers everything from Coulomb friction to viscous friction (see Figure 1.4) depending on the choice of parameter values. Since the most basic friction models contain Coulomb friction and linear viscous damping, Stribeck curve can provide good representation of the friction between sliding surfaces.

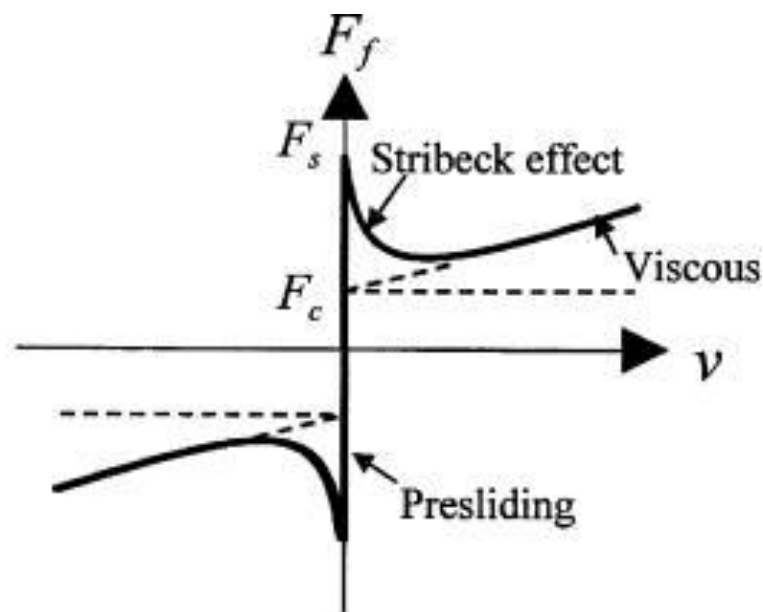


Figure 1.4 Relation between friction force and sliding velocity based on Stribeck model (reproduced from Ha et al. 2005)

### 1.3 Nanoscale Friction

Nanoscale friction can be found on the interaction between the top atom of cantilever and the surface atom of the sample. Stick/slip is presented because the AFM tip has to climb up the potential hill of surface atom followed by sudden drop due to down motion at the other



side potential hill. The stick/slip pattern depends on the sliding direction of the tip and the surface lattice because probe tip prefers to jump to the nearest atom. Lateral force is detected when the tip is not exactly above on the preferred atomic position (Bennewitz 2005). Thus, either a straight path (one dimension stick/slip) or zigzag path (two dimensions stick/slip) can be found. At higher sliding velocity, the stick/slips' amplitude is decreased since the relaxation time (time needed to bring the tip back to its initial position) decreases. Surprisingly, the Tomlinson model is still fit for atomic friction as dynamic friction numerical simulation reveals the existence of two regimes in contact mode AFM: steady sliding and stick/slip, depends on the sliding velocity and interfacial friction force between tip and sample. The tip and sample surface undergo stiction and kinetic friction to generate continuous sliding and stick/slip motion respectively (Stark et al. 2004).

The most important difference between friction at nanoscale and friction at macro- or microscale is the fact that nanoscale friction is dependent to the contact area and sliding velocity. Friction force is increasing with the increase of normal force as well as sliding velocity due to the results of atomic scale stick-slip. This is the result of thermal activation of the thermal activation of the irreversible jumps of the AFM probe that arise from overcoming the energy barrier between adjacent atomic positions (Bhushan 2008).

It is obvious that Amonton's law is not applied for friction at the nanoscale due to the independency of friction to normal force, sliding velocity, and contact area. The later theory proposed by Bowden and Tabor takes contact area into consideration since the real contact area is different with the apparent contact area. They assumed that contact area is based on plastic deformation. However, Israelachvili found that friction does not simply depend on plastic deformation as it is still proportional to the contact area even in the absence of wear (Falvo & Superfine 2000). Then, Hertzian model of contact can be incorporated into the elastic deformation.

### ***1.3.1 Single-asperity contact***

The term tribology is used when there are two surfaces in contact and move at relative velocity. At most surface interfaces, the contact occurs at numerous asperities. Thus, in macroscale tribology involves multiple asperities. However, study of tribological properties at

the nanoscale requires experiments at well-defined interfaces that provide single-asperity contact (Szlufarska et al. 2008). The understanding of single asperity contact is very important to study the mechanism and the nature of contact. Nanotribology can be characterized by the presence of monoasperity on the interfaces that provides continuous contact area. It is to avoid any ambiguities arose from the interaction of multiple asperities. Since tribological behavior of an interface depends not only on the material composition, but also on the contact geometry, the presence of single asperity contact can facilitate the comparison between theory, experiment, and simulation (Szlufarska et al. 2008).

The invention of probe microscopy (scanning tunneling microscope and atomic force microscopy) whose atomic resolution has opened new access to address the interfacial problems (Bhushan 2008). The tip used in such microscopy has curvature 20 – 100 nm (Bushman 1995) allowing up to atomic scale investigation of mechanical processes such as friction, adhesion, wear, and lubrication. Therefore, since then the development of micro- and nanotribology has progressed very fast.

### ***1.3.2 Hertz Model***

The contact mechanic between two elastic curved bodies is firstly described by Hertz at 1896 (Hertz et al. 1896). When two curved surfaces are in contact, the surface is deformed under the applied force and it develops a localized stresses in the contact area known as Hertzian contact stress.

The contact area between two surfaces can be deformed due to compression. Contact mechanic is defined as study of deformation of coupled surfaces which are in contact at one (mono asperity) or more points (poly asperities). The main components of contact mechanic are the normal pressure and adhesion acting perpendicularly to the body surface and the friction force acting between surfaces in lateral direction (Johnson 1985). For the contact between two smooth spheres with radius of  $r_1$  and  $r_2$ , it is often assumed that the radius of curvature  $R$  defined as

$$\frac{1}{R} = \frac{1}{r_1} + \frac{1}{r_2} \quad (1.15)$$

Classic Hertz theory described the non-adhesive contact mechanic between two elastic bodies. The dimension of contact area is much smaller than the dimension of both contacting bodies. This model assumes that the material is homogenous and isotropic. Besides, this theory works in the condition where the strains are small and within the elastic limit. The contact is illustrated on Figure 1.5.

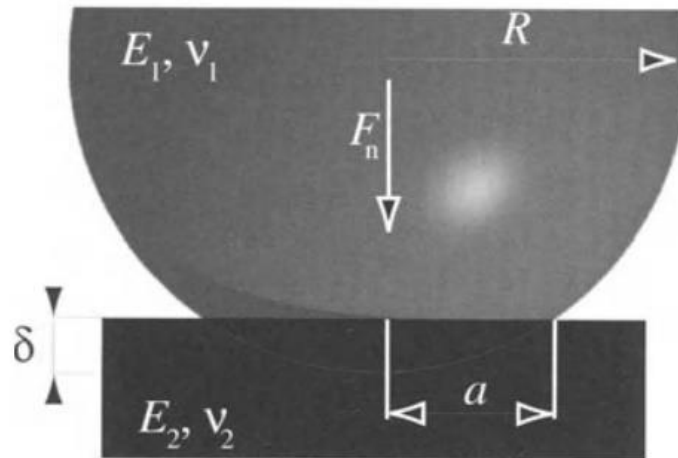


Figure 1.5 Scheme of Hertz model of contact (reproduced from Scherge & Gorb 2001)

The contact area  $A_c$  can be calculated as:

$$A_c = \pi \left( \frac{RF_n}{K} \right)^{\frac{2}{3}} \quad (1.16)$$

and  $K$  is the effective elastic modulus and is defined as:

$$\frac{1}{K} = \frac{3}{4} \left( \frac{1 - \nu_1^2}{E_1} + \frac{1 + \nu_1^2}{E_2} \right) \quad (1.17)$$

where  $\nu_i$  is the Poisson ratios and  $E_i$  is the modulus Young of the materials. The Hertz model applies on dry air where adhesion is neglected. The figure 1.5 illustrates the Hertz model of contact in which  $a$  is the radius of contact and  $\delta$  is the depth of indentation, expressed by:

$$\delta = \frac{a^2}{2R} \quad (1.18)$$

### 1.3.3 Effect of Adhesion

Adhesion force can be defined as a state of minimum energy that is attained when two solids are brought into contact (Scherge & Gorb 2001). However, Hertz contact model does not consider adhesion force. The presence of adhesion force can be quantified by doing simple experiment of silicon ball facing a flat silicon sample. This system is called silicon model system. The silicon ball is attached onto spring with spring constant  $k_z$ . Flat sample is perpendicular to spring and is moving forward and backward in  $z$ -direction. The scheme of the experiment can be seen at Figure 1.6. Distance between the ball and the flat sample is measured in  $z$ -direction. At  $z_{max}$ , the ball and flat sample are separated at certain distance. They are in contact at  $z_0$ . Further compression (flat sample moves forward approaching the ball) of the spring is done at negative  $z$ -distance and is referred as indentation. At this region, normal force is increasing and can be described as,

$$F_n = -k_z \Delta z \quad (1.19)$$

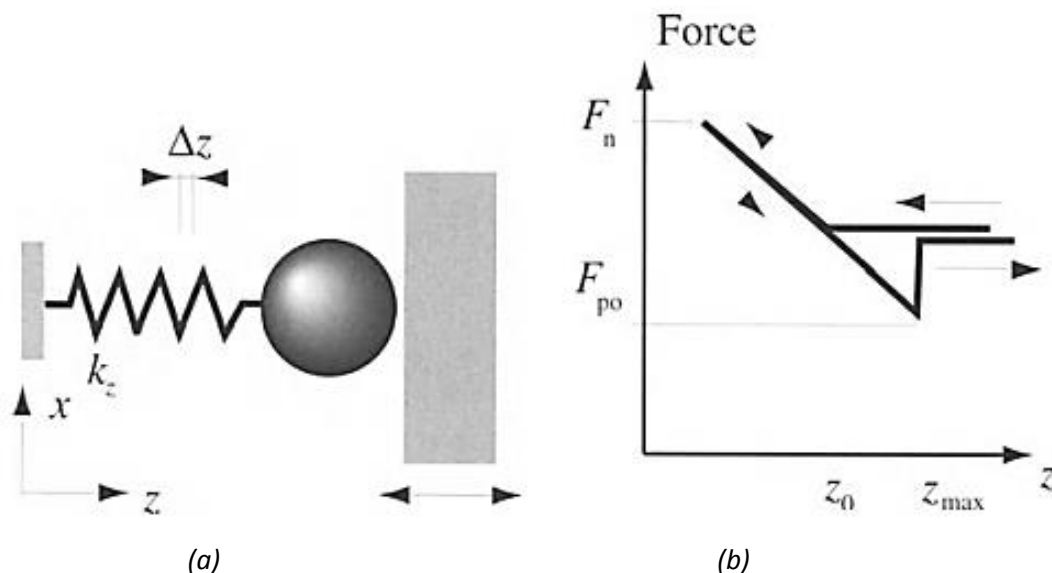


Figure 1.6 (a) Basic setup for adhesion and indentation experiments and (b) force-indentation curve to measure adhesion force and indentation (reproduced from Scherge & Gorb 2001)

$\Delta z$  is the elongation or shortening of the spring during compression and retraction. The negative sign is given for compression test.

When the flat sample moves away from the ball (retracting), the force normal is decreasing into negative value. Expansion of the spring is due to adhesion force between the ball and the flat sample that keep them in contact. This contact breaks  $z_{max}$ . The negative force needed to break the contact is referred as adhesion force  $F_{ad}$ , or also is commonly known as pull-off force  $F_{po}$ . This region describes the adhesion properties of the materials.

$$F_{ad} = F_{po} = -k_z(z_{max} - z_o) \quad (1.20)$$

There are four main contribution to adhesion forces: molecular interaction, electrostatic interaction, capillarity, and action of excess charge. Molecular and electrostatic interaction are caused by quantum mechanical interaction. Whereas, capillarity and forces due to excess charges are continuum quantities. Based on this definition of adhesion force, other contact models were proposed.

### A. Johnson-Kendall-Roberts Model (JKR Model)

Research group of Johnson et.al found some contradictive facts on the classic Hertz model when the low loads are applied. Even though Hertz model works very well on large loads application, the contact area is larger than predicted value by Hertz theory on low loads application. Besides, the contact area is not zero when the load is removed. Moreover, there is adhesive force acted on the surfaces even though it is clean and dry (Johnson et al. 1971). Thus, they developed different contact model in which they incorporate adhesion in the model. This theory considers the effect of contact pressure and adhesion only inside the contact area. The contact area increases due to interfacial energy minimization. This is obviously in the contrary with Hertz model.

$$A_c = \pi \left[ \frac{R}{K} \left( F_n + 6\pi\gamma R + \sqrt{12\pi\gamma R F_n + (6\pi\gamma R)^2} \right) \right]^{\frac{2}{3}} \quad (1.21)$$

$A_c$  is the contact area,  $\gamma$  is the interfacial energy, representing the adhesion.

Figure 1.7 shows the scheme of JKR contact model that there is adhesion neck generated at the edge of contact. Moreover, the indentation can be expressed as:

$$\delta = \frac{a^2}{R} - \sqrt{\frac{16\pi\gamma a}{3K}} \quad (1.22)$$

Due to adhesion, the ball still sticks to the surface in the absence of normal force. The negative normal force is found when the contact breaks, referred by pull-off force as defined as:

$$F_{po}^{JKR} = -3\pi\gamma R \quad (1.23)$$

It should be noted that pull-off force is independent to the moduli of both contacting bodies.

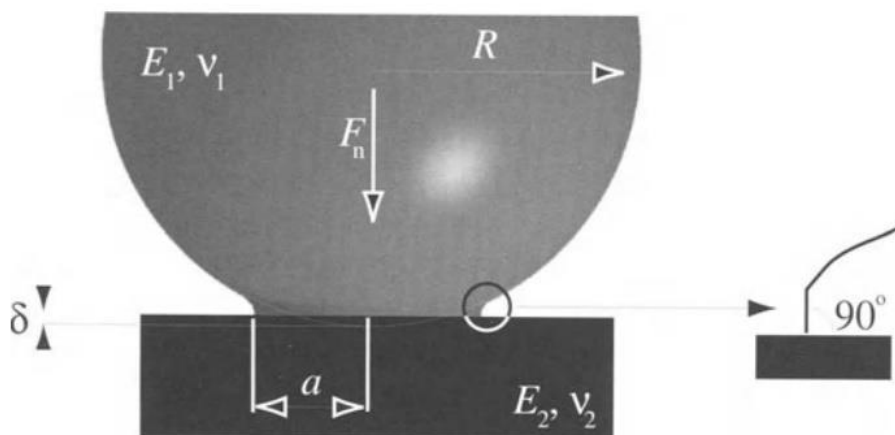


Figure 1.7 Scheme of Johnson-Kendall-Roberts model of contact (reproduced from Scherge & Gorb 2001)

One of the systems that follows JKR model is the single-asperity contact between platinum-coated AFM tip and muscovite mica surface (Carpick, Ogletree, et al. 1996; Carpick, Agrait, et al. 1996). Friction force at the tip-surface interface measured by ultra high vacuum AFM varies with load in the proportion to the contact area predicted by JKR theory of elastic contact (Carpick, Agrait, et al. 1996). Moreover, the prediction of the tip shape is consistent with predicted friction behavior. Thus, interfacial surface energies and shear strengths can be estimated by using JKR model.

## B. Derjaguin-Muller-Toporov Model (DMT Model)

Given the weaknesses of Hertz contact model, Derjaguin et.al also developed their theory with taking adhesive force into consideration (Derjaguin et al. 1975). However, they are using different adhesion theory that Johnson et.al. This model takes adhesion with long-range forces into consideration. It assumes that the deformation of the contact is due to attractive interaction outside the contact area. Meanwhile, the contact profile in this theory is the same as hertzian contact profile. The pull-off force of the contact can be described by:

$$F_{po}^{DMT} = -4\pi\gamma R \quad (1.24)$$

DMT model is applicable only for undeformable flat with equal adhesive properties for both surfaces. Thus, when the pull-off force is reached or the loads are removed, the contact area becomes zero and there is not singularity in the contact stress at the edge of the contact area. A couple of tungsten-carbide AFM tip and hydrogen-terminated diamond (111) examined by ultra high vacuum AFM, gives an ideal single asperity-contact that follow DMT model. It is one of the hardest and the stiffest known heterocontact (Enachescu et al. 1999)

## C. Maugis Transition

Maugis (Maugis 1992) proposed a transition mechanism between theory of JKR and DMT by using a model of Dugdale. In this model, the contact radius  $c$  that surrounds the contact area  $a$  is taken into consideration. The attractive forces are working on the contact radius. Then, he introduced parameter  $\lambda$ :

$$\lambda = 2\sigma_0 \sqrt[3]{\frac{9R}{16\pi w E^*2}} \quad (1.25)$$

where  $\sigma_0$  is the maximum stress that is equal to:

$$\sigma_0 = \frac{16}{9\sqrt{3}} \frac{w}{\xi_0} = 1.03 \frac{w}{\xi_0} \quad (1.26)$$

Parameter  $\lambda$  is similar to parameter  $\mu$  introduced by Pashley ( $\lambda=1.157\mu$ ). Maugis

explained the relation between contact radius, forces, penetration, and parameter  $\lambda$  by inputting  $m = \frac{c}{a}$ .

$$\begin{aligned} \frac{\lambda \bar{a}^2}{2} \left( \sqrt{m^2 - 1} + (m^2 - 2) \operatorname{atan} \left( \sqrt{m^2 - 1} \right) \right) \\ + \frac{4\lambda^2 \bar{a}}{3} \left( \left( \sqrt{m^2 - 1} \right) \operatorname{atan} \left( \sqrt{m^2 - 1} \right) - m + 1 \right) = 0 \end{aligned} \quad (1.27)$$

$$\bar{F} = \bar{a}^3 - \lambda \bar{a}^2 \left( \sqrt{m^2 - 1} + m^2 \operatorname{atan} \left( \sqrt{m^2 - 1} \right) \right) \quad (1.28)$$

$$\bar{\delta} = \bar{a}^2 - \frac{4}{3} \lambda \bar{a} \left( \sqrt{m^2 - 1} \right) \quad (1.29)$$

where  $\bar{a}$ ,  $\bar{F}$ ,  $\bar{\delta}$  are the dimension of contact radius, normal force, and indentation respectively.

$$\bar{a} = a \sqrt[3]{\frac{\frac{4}{3} E^*}{\pi w R^{*2}}} \quad (1.30)$$

$$\bar{F} = \frac{F_N}{\pi w R^*} \quad (1.31)$$

$$\bar{\delta} = \delta \sqrt[3]{\frac{\frac{16}{9} E^{*2}}{\pi^2 w^2 R^*}} \quad (1.32)$$

Based on the parameter  $\lambda$ , it is possible to determine the relation between  $a$ ,  $F$ ,  $\delta$  that intermediate the DMT theory and JKR theory. If  $\lambda \ll 1$ , Maugis transitions tends to belong to DMT theory. Meanwhile if  $\lambda \gg 3$ , Maugis transition has a tendency to belong to JKR theory. In between, Maugis transition should be applied. For AFM, numerical application showed that in the case of ceramic and metal, the parameter  $\lambda$  is much smaller than 1, thus DMT theory is applied. In the case of polymer,  $\lambda$  is in the order of 1 or in the domain of Maugis transition. And, for elastomer whose  $\lambda$  is larger than 10, JKR theory is used.

So, at the nanoscale, Hertzian model of contact is not valid due to the absence of



adhesion. So this theory is failed for friction at nanoscale. In this case, JKR, DMT, and Maugis transition model are possible to be used since they incorporate adhesive force in the formula. The relationship between applied load and contact area for different model of contact can be seen at Figure 1.8.

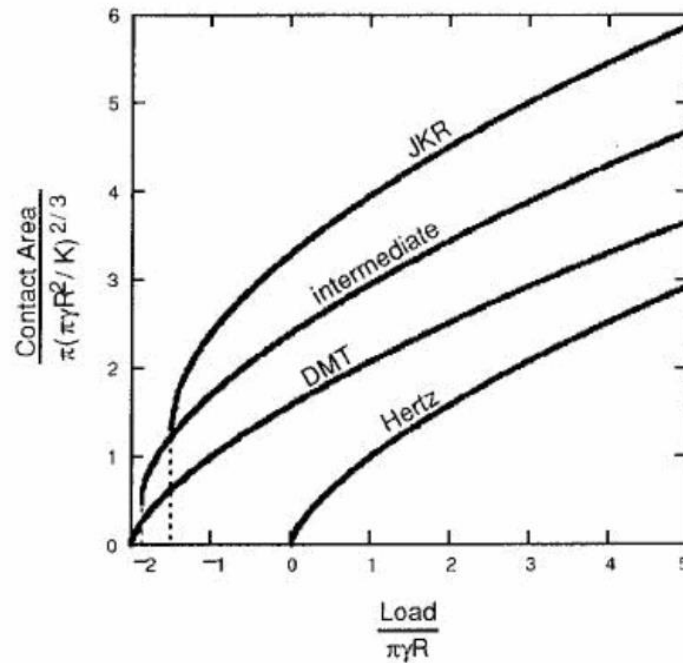


Figure 1.8 Relationship between applied load and contact area for various model of contact (reproduced from Carpick & Salmeron 1997)

### 1.3.4 Friction Models

There are two well-known models of friction at atomic scale: The Tomlinson model and Frenkel-Kontorova model. Both models illustrate movement of single atom which is placed into the external periodic potential assumed to be sinusoidal function (Braun & Naumovets 2006).

#### A. Tomlinson Model

Prandtl and Tomlinson introduced a mechanism for wearless friction at 1929. It is based on the idea that a molecule at one surface can be plucked by the other surface as illustrated on Figure 1.9. The atom of tip probe is dragged by a spring over a corrugated energy landscape.

A frictional parameter  $\eta$  is defined as ratio between the energy corrugation and the elastic energy stored in the spring:

$$\eta = \frac{4\pi^2 V_0}{k\alpha^2} \quad (1.33)$$

where  $k$  is the spring constant,  $\alpha$  is constant of surface roughness and  $V_0$  is the amplitude of sinusoidal potential.

Due to inhomogeneity of molecules between two contacting surfaces, the molecule is pinned at the other surface. Then, the molecules vibrates and this vibration is damped because the vibrating molecule excites electronic or elastic waves into the bulks of the sliding bodies. This friction mechanism is wearless because plucking the molecule does not change its equilibrium position (Persson & Tosatti 1995)

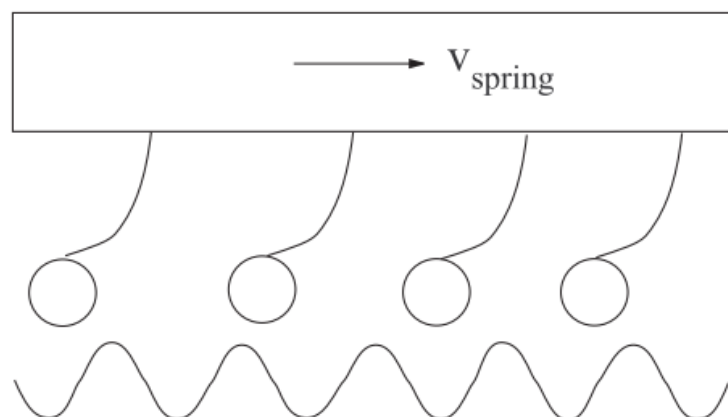


Figure 1.9 The Tomlinson Model (reproduced from Braun & Naumovets 2006)

### B. Frenkel-Kontorova Model

The Frenkel-Kontorova model (FK model) describes a chain of interacting atoms (for example adsorbed lubricant atom), placed in the external periodic created by surface atoms of substrate (Braun & Naumovets 2006) (see Figure 1.10). It has also been a standard model in the study on mobility of charge density waves. The infinite range of the harmonic interaction in the model leads to a disordered fluid state very different from the conventional one. In this model, the hysteresis loop tends to disappear with the increasing of microscopic friction. The

advantage of this system is that the equilibrium property of the commensurate-incommensurate transition is well understood (Persson & Tosatti 1995).

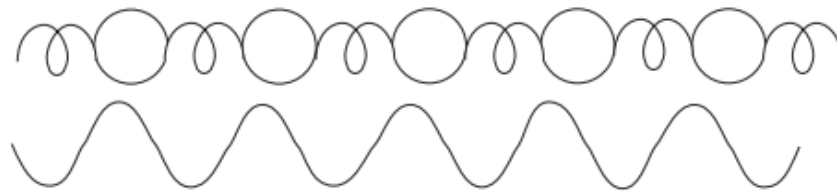


Figure 1.10 The Frenkel-Kontorova Model (reproduced from Braun & Nauvometts 2006)

### **1.3.5 Effect of Velocity**

For the contact between hydrophobic surfaces, the friction force increases linearly with a logarithmic increase of sliding velocity (Noel et al. 2012). In the contrary, for contact involving hydrophilic surfaces such as tip and sample made of silicon nitride, friction force and contact radius decrease with sliding velocity (Mazeran 2006). This decrease is due to capillary nucleation: the formation of water bridge on the asperities between surfaces. The growth of capillary meniscus is a thermal-activated process. The schematic of water bridge formation which is time-dependent is illustrated on Figure 1.12. The depression of capillary meniscus can yield adhesive force that is proportional to the contact area and can act as additional normal load. Thus, during sliding at higher sliding velocity, the capillary force is disappearing causing decrease on friction, adhesion, and contact radius (Mazeran 2006).

However, the velocity dependence behavior of friction can change during pump-down in a vacuum system from air to ultra high vacuum at  $10^{-8}$  mbar (Opitz et al. 2005). Opitz et al described the three distinct friction regimes on hydrophilic contact between sharp silicon tip and flat Si (100): (1) friction is dominated by capillary force due to the presence of water films, (2) water removal due to vacuum desorption; the remaining water is now an ordered water double layer that dominate the friction, and (3) complete water desorption resulting solid-solid contact. Regime 3 gives the lowest friction among all.

In the case of polymer confined film whose thickness  $\approx 3$ nm, the frictional shear stresses increase with sliding velocity (Sivebaek et al. 2010). However, the type of increase (linearly or logarithmically) depends on the length of its hydrocarbon chain. The mechanism

of frictional behavior on confined film relays on the kinetic phase transition.

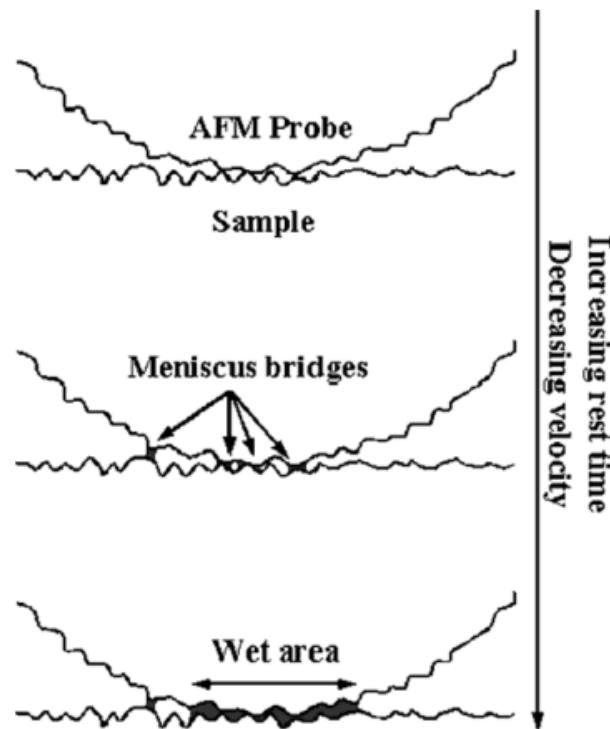


Figure 1.11 Schematic of capillary water bridges formed in the contact area of hydrophilic surfaces. The asperities act as nucleating site for capillary condensation. (reproduced from Mazeran 2006)

### 1.3.6 Case example

Since the invention of scanning probe microscopy (SPM) and atomic force microscopy (AFM); and the advancement of computational method, single-asperity contact measurement has progressed a lot (Szlufarska et al. 2008). SPM allows force measurement and characterization of tribological properties at nanometer scale contact in various environments for a wide range of materials. Meanwhile, atomistic simulations based on molecular dynamics (MD) technique have been used to model single-asperity contacts and their dynamic during sliding.

AFM provides a single asperity contact between the tip and the sample surface. Observation of frictional force that was done on the interface of platinum-coated tip and muscovite mica surface in ultra high vacuum AFM reported that friction for solid-solid nanocontacts, below the threshold force of visible wear, is proportional to the true contact area (Carpick, Ogletree, et al. 1996; Carpick, Agrait, et al. 1996). Furthermore, the scanning of

the tip also showed decrease of adhesion due to the structural and chemical changes of the AFM tip (Carpick, Ogletree, et al. 1996). The proportionality of friction force to the contact area was also found in friction measurement done in humid atmosphere (55% relative humidity) at the interface of silicon nitride tip and cleaved mica surface (Carpick et al. 1997).

AFM is able to quantify the loads and stresses that cause wear and to characterize the changes in asperity shape. The main challenge in AFM measurement is to control the composition, shape, and size of the tip because it represents half of the interface. AFM tip can undergo shape change due to wear. It is the result of the substantial stresses which are generated in small contact area at typical loads then it exceeds the strength of the tip (Bloo et al. 1999; Larsen et al. 2002). A pyramidal silicon nitride tip can undergo flattening at the top of the tip during silicon surface imaging in contact mode because the contact pressure approaches the critical stress (Bloo et al. 1999). Furthermore, Chung et al found that the fracture of the silicon tip can be caused by the impact during approach process and the wear of silicon tip is happened gradually under low normal load (Chung et al. 2005). The wear of silicon tip can increase the tip radius and adhesion between tip and sample thus reducing image resolution and causing the appearance of artifact (Tao & Bhushan 2006). In addition, contamination of the tip due to material transfer from sample surface can also modify the shape of the tip (Bloo et al. 1999). It is also called as adhesive wear and it is happened at the part of the tip that has contact with sample. The damage of the tip can be discovered from SEM image of the tip or from analyzing the cross section of AFM image before and after wear. The tip flattening and material transfer are able to be detected (see Figure 1.13). In order to decrease the friction, adhesion, and wear at the tip-sample interface, the tip coating can be applied. Coating the tip with liquid lubricant or self assembled monolayer (SAM) or polymer can improve the quality of the image (Tao & Bhushan 2006). However, the humidity of the environment can affect the tip chemical modification (Qian et al. 2000).

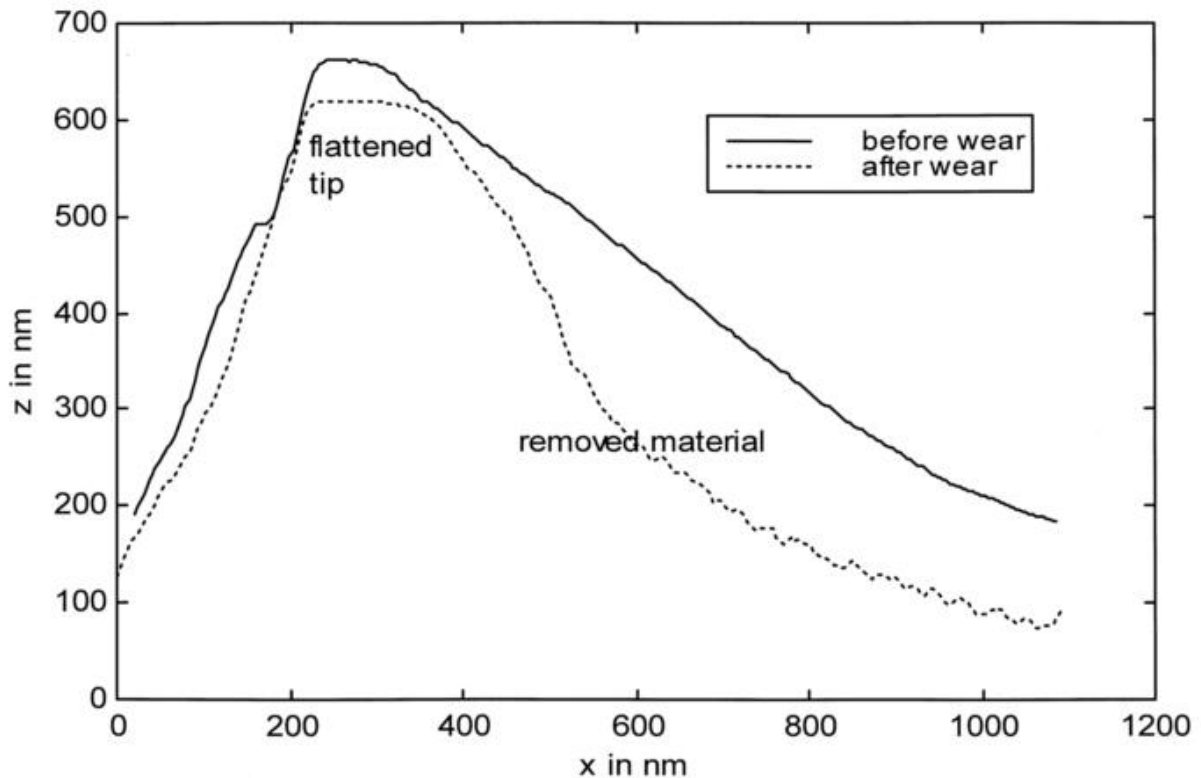


Figure 1.12 Cross section of AFM image before and after wear experiment (reproduced from Bloo et al. 1999)

## 1.4 Conclusion

The main characteristics of nanotribology are that it depends on sliding velocity and contact area and it considers a single asperity contact. Nanotribology can be found in the single asperity contact between two atomically smooth surfaces that are often seen in miniaturized electronic device. Meanwhile, for macro- and microscale tribology, it assumes polyasperity contact due to the roughness of the surfaces in contact. In biological system, nanotribology is used to understand the molecular interactions that control the cellular process and the function of system as a whole unit (Bhushan 2007; Discher 2005). Due to the complex nature of nanotribology, it is important to choose the proper assumptions to explain the nature of contact between surfaces. More importantly in biological system, the intrinsic properties and the environment during measurement should be taken into consideration before discussing the tribological properties of biomaterials of interest.

*(this is page intentionally left blank)*

## Atomic Force Microscopy for Lipid Membrane Characterization

Now, in this chapter, author will review the atomic force microscopy (AFM) that is widely used to characterize biological membrane. Firstly the history of AFM invention and development are presented. Then the detail about AFM components and work principles are given. Some comparison between AFM and other instruments are done to point out the strength of AFM as our reason to use AFM in our study. However, author also highlights some challenges faced on AFM. Recent development of AFM is also presented.



# Chapter 2

## Atomic Force Microscopy for Lipid Membrane Characterization

### 2.1 History of AFM

The idea about electron tunnelling was firstly introduced by Giaever at 1960. He proposed that a current will flow when potential difference is applied to two metals separated by a thin insulating film (Bushan 1995). Maximum distance between two metals is 10 nm. More than decade passed by, Binnig et al. (1982) introduced vacuum tunnelling combined with lateral scanning and he named it as scanning tunnelling microscopy (STM). This technique allows sample imaging with high resolution; 1 nm for lateral resolution and 0.1 nm for vertical resolution. STM can be operated in either the constant-current mode or constant-height mode. Main requirement of STM is it needs electrically conductive surface sample to generate current channel between tip and sample surface. Thus, careful sample preparation is necessary to characterize non-conductive sample.

In order to address the challenge of STM to image non-conductive sample in its native condition (minimum sample preparation), atomic force microscopy (AFM) is invented by Binnig et al at 1986(Binnig et al. 1986). Soon, it becomes a new weapon to characterize biological sample since it does not need or less sample treatment and it permits to characterize sample in wet condition (in liquid medium). It is very suitable for biological sample which cannot be dehydrated. Major privilege of AFM is it can give real time and nano scale resolution of image and it can perform mechanical measurement with precision of pN.

Since its first design proposed by Binnig et al, AFM was going through continuous development. Two years later, McClelland et al. and Erlandsson et.al propose their design of AFM with some advancement in high-sensitivity fiber-optic displacement sensor. Later, Kaneko et al. (1992) proposed some modification that a piezotube scanner was used to hold the sample and the tip was supported on a single-leaf spring. They incorporated a new tube scanner and an optical multifunction sensor (Bushan 1995). To date, there are many commercial AFMs available on the market. The most commonly design of AFM nowadays is the multimode AFM that allows measurement using contact and tapping mode. Figure 2.1

illustrates design of commercial AFM/FFM where sample is mounted on a piezoelectric tube scanner.

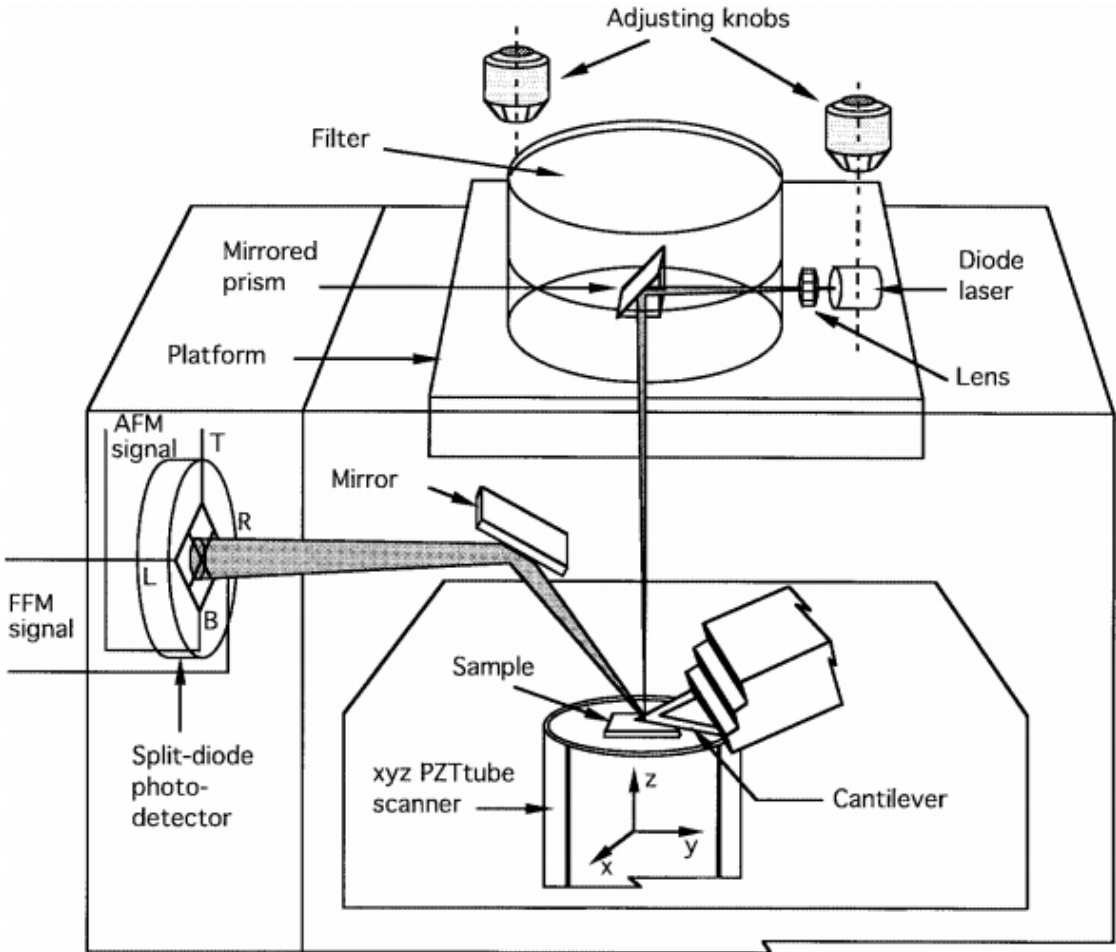


Figure 2.1 Design of commercial AFM/FFM (reproduced from Bushan 1995)

In term of AFM application, Figure 2.2 shows how development of AFM for the last 30 years has broaden the function of AFM, especially to cell and molecular biology. Advancements were done not only in imaging technique but also in force measurement.

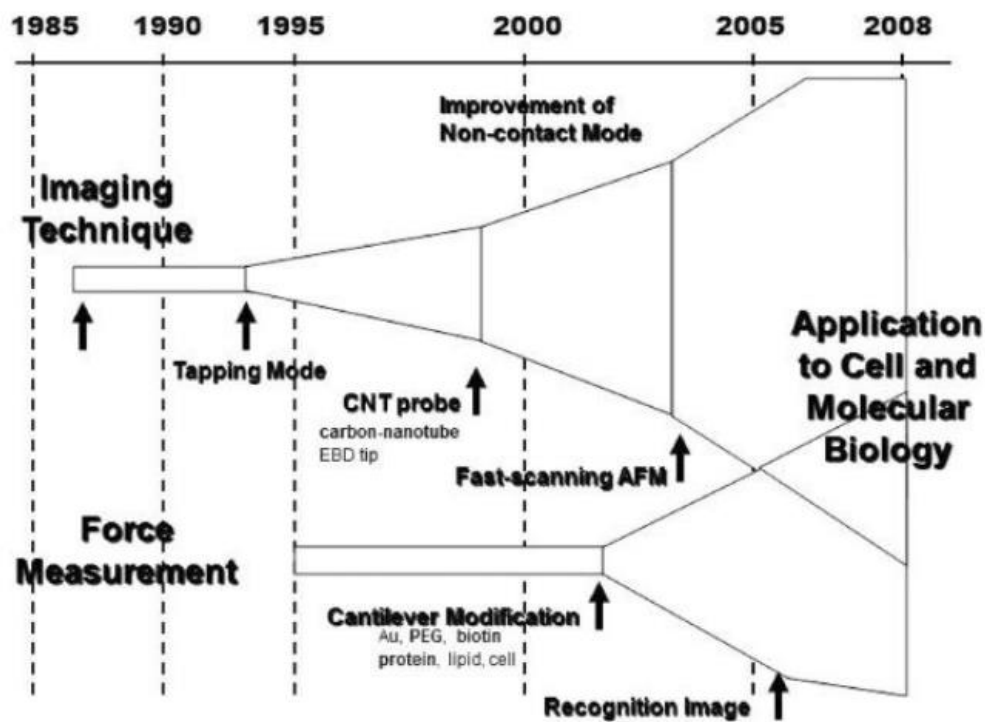


Figure 2.2 Development of AFM techniques in biology domain (reproduced from Takeyasu 2014)

## 2.2 Application of AFM

### 2.2.1 Imaging by AFM

To generate an image, AFM uses a tip probe which is located at the edge of cantilever to scan sample surface then maps the selected area of sample. Sample is mounted on piezoelectric tube scanner which can move upward and downward to keep constant interaction force between sample and tip surface (Picas et al. 2012). Sample is scanned precisely in X-Y plane in a raster pattern (see **Error! Reference source not found.**). The sharp tip is brought into contact with the surface. The topography of the surface causes deflection of cantilever in the vertical direction and torsion of cantilever in the lateral direction. A laser beam generated from a diode laser is directed by a mirror onto the back of cantilever. The reflection beam is directed onto four quadrants photodiode detector producing scanner deflection signal. The differential signal from the top and bottom photodiodes gives the AFM signal which is a sensitive measure of the cantilever vertical deflection (see Equation 2.1).

Whereas, the differential signal from the left and right photodiodes gives a sensitive measure of the torsion of cantilever, referred to friction force measurement in friction force microscopy (FFM); it also can give friction image. During imaging, this AFM vertical deflection signal is used as the feedback signal to control the vertical position of the scanner and the sample. Thus, the interaction force between tip and sample surface will remain constant as the displacement of tube scanner relates directly to the topography of the sample surface. So, the AFM signal can be mapped as function of scanner displacement to generate a 3 dimension morphology image of sample surface.

### A. Contact Mode

In contact mode imaging, the tip at the end of cantilever is put in contact with the sample surface by moving the scanner. During contact, the tip maintains weak repulsive inter-atomic force with the sample surface. The force applied causes cantilever deflection which is measure by laser interferometry (Bushan 1995). Figure 2.3 illustrate the contact mode imaging of AFM. Imaging by using contact mode results high resolution image, however the tip has high chance to perturb the sample surface, especially for biological sample which is very fragile. Therefore, non contact mode is developed to minimalize the physical change in surface due to tip-sample interaction.

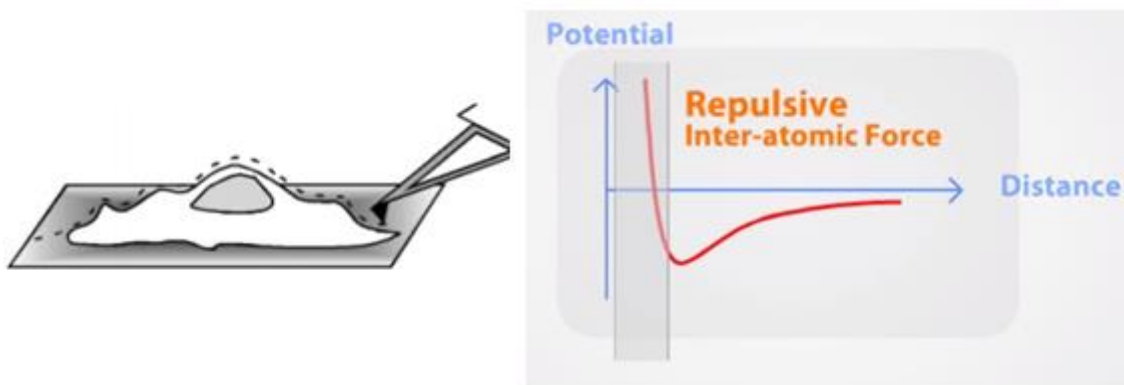


Figure 2.3 Illustration contact mode AFM

### B. Tapping Mode

In the tapping mode, the tip is maintained the attractive inter-atomic force detected at distance of several nm. Van der Waals attractive force presents at the tip-sample interface. The tip is oscillating on the sample surface (see Figure 2.4) at its resonance frequency (about 300

kHz) with a 20 – 100 nm amplitude in the vertical direction. The amplitude of oscillation is relatively always big in order to avoid the tip get stuck to the sample because of adhesive attraction between tip and sample surface. Oscillation to the cantilever beam is provided by oscillating a biomorph mounted on the beam(Bushan 1995).

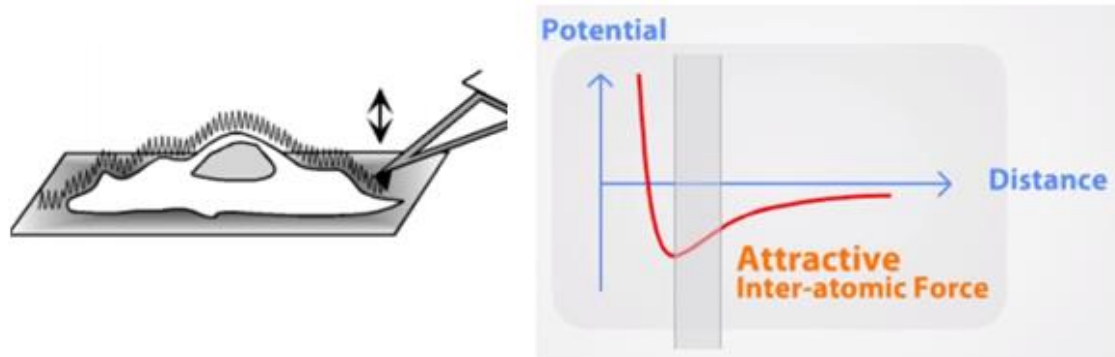


Figure 2.4 Illustration of tapping mode AFM

### C. Non-contact Mode

Non-contact mode was developed a year after AFM invention, at 1987, based on the idea that biological samples were very fragile that they can be easily damaged even by small forces applied. Non-contact mode allows examination on biological samples without touching them, resulting high resolution image. However, the major drawback for this mode is that it needs to be operated under vacuum condition(Bushan 1995). Thus it limits its use in biology. Only few biological samples that can meet the experimental condition, can be imaged. In contrary, numerous efforts have been doing to develop imaging in liquid by non-contact mode.

### 2.2.2 AFM in Liquid

Basically the principle of imaging and force measurement (explain later) in ambient atmosphere and in liquid are the same. However, some modifications are needed to protect the electrical components from liquid drop. Firstly, piezoelectric scanner where the sample is mounted, should be covered. Then, the sample holder and tip holder (liquid cell) must be big enough to accommodate the sample and the liquid medium. Small quantity of liquid used has risk of evaporation that can change the concentration of medium thus affect the sample's properties. Then, special design of liquid cell is created to avoid scattering of laser beam in the liquid surface. The liquid cell is featured by well-defined solid-liquid interface with a

transparent window. Usually, in air-liquid interface, the rise of surface wave in the liquid scatter the laser beam producing a noisy spot that can disrupt the detection of cantilever's deflection (see Figure 2.5). In order to have liquid exchange during experiment, some liquid cells are featured with input and output inlet. However, liquid flow may cause turbulence in the surrounding of the cantilever, increasing the risk of tip damage. So, it is recommended to withdraw the tip during liquid exchange (Baro & Reifenberger 2012).

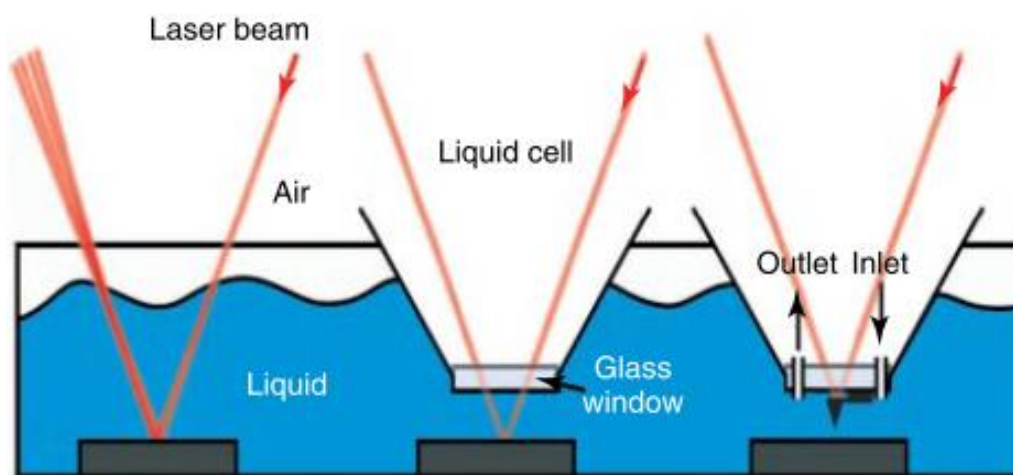


Figure 2.5 Reflection of laser beam through air-liquid interface; (left) without liquid cell, (middle) with liquid cell, and (right) with liquid cell whose input and output inlet for liquid exchange (reproduced from Baro & Reifenberger 2012)

### 2.2.3 Force spectroscopy

AFM coupled with force spectroscopy can give a new insight in mechanical properties and can correlate force and topology of biological membrane. Indentation of SLB by AFM tip gives a picture about the mechanical stability of SLB. This feature of AFM is also can be used to quantify the mechanical resistance between two different component attached on lipid substrate and coated tip (Morandat & Kirat 2010) and also the interaction between lipid layer and its solid support since is able to detect normal and lateral force in both air and liquid condition (Grant & Tiberg 2002). In fact, AFM measures the interaction force between tip and lipid surface and also van der Waals then converts it into mechanical unit. There are two interaction force governed when AFM tip approach the sample surface: electrostatic force detected in longer interaction's range and steric force detected in shorter interaction's range (Figure 2.6). In neutral pH, the repulsion force is yielded when the zwitterionic head group

interact with water layer covering the surface. Besides, the no-charge sample surface develops van der Waals force which can be counter-balanced by electrostatic force. While, the steric force is very useful to estimate thickness of bilayer using the transition between electrostatic regime to steric regime (Leonenko et al. 2004). The tip should be in certain distance to feel the short-range interaction with sample surface, either attraction or repulsion. Instead of constant distance, AFM keeps constant interaction force between two surfaces in which tip slightly touch membrane surface (Morandat et al. 2013).

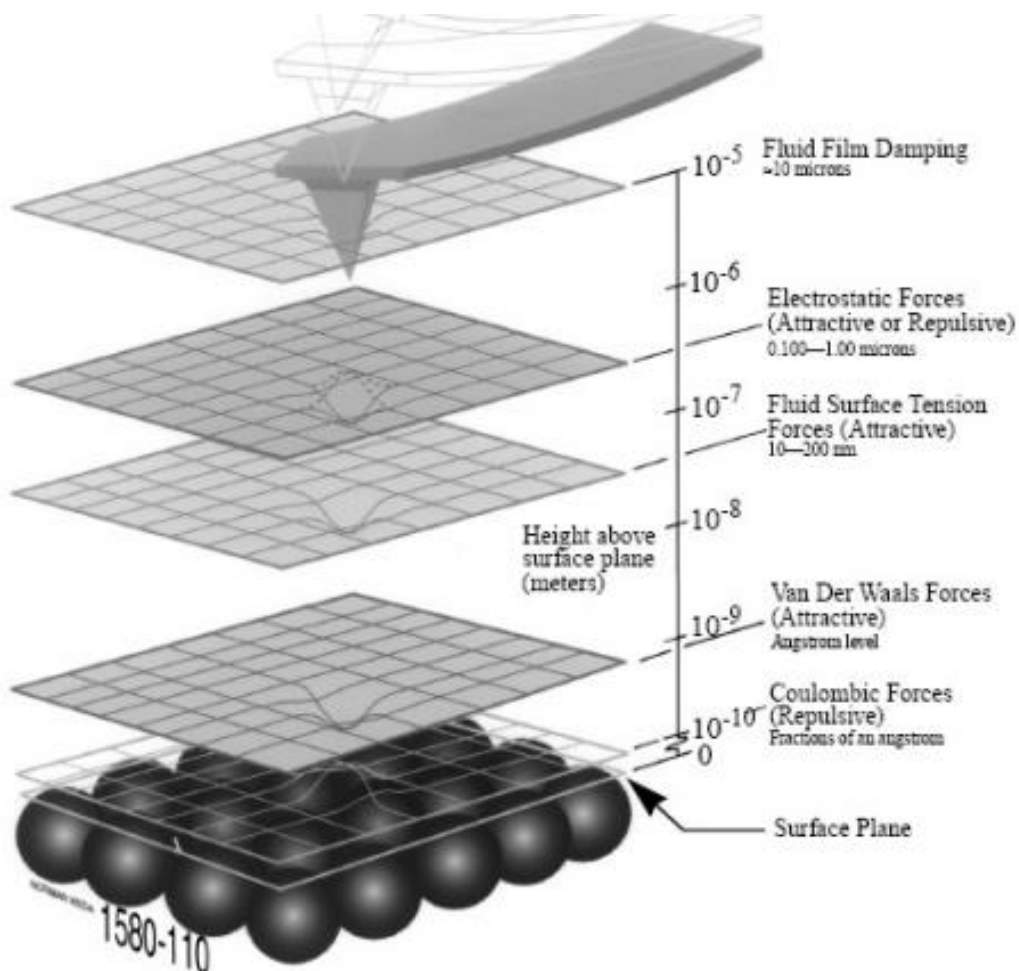
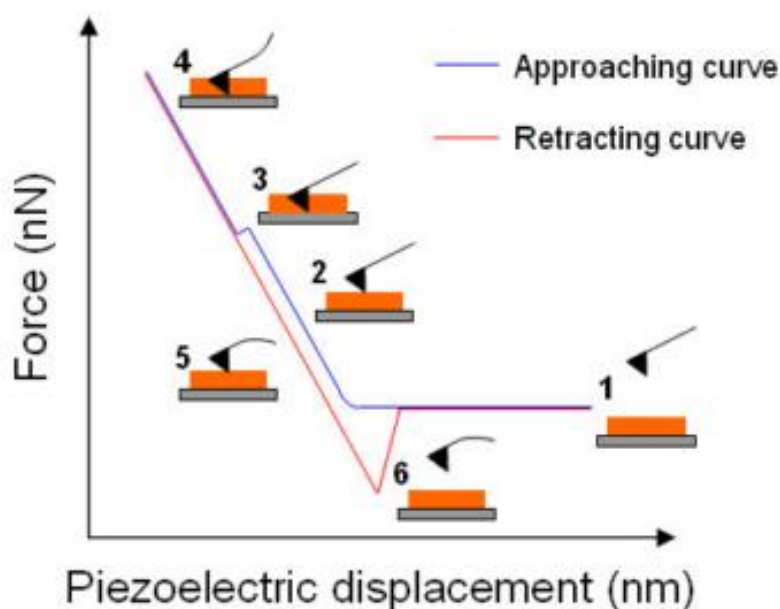


Figure 2.6 Illustration of tip-sample surface interaction force (reproduced from Anon 1998)

Mechanical measurement by using force spectroscopy on supported lipid bilayer gives typical force-distance curve that represent the deflection of cantilever. Figure 2.7 shows the position of tip and the deflection of cantilever during indentation. At position (1), tip is still far

from sample surface then it does not sense any forces. (2) As the force is increasing, the tip approaches the surface and it detects the short-range tip-sample interaction (Derjaguin-Landau-Verwey-Overbeek (DLVO) forces, hydration forces, or steric forces. When the tip is in mechanical contact with surface, the sample starts to elastically deformed. (3) A jump can be observed when the tip reaches the threshold value as it breaks the lipid bilayer. (4) The next event identifies the onset of the plastic regime. After the tip reaches the maximum applied force, the cantilever is retracted as the force is gradually decreasing. (5) However, the bonds between tip and surface are still remained causing the cantilever to bend towards the surface. (6) Later, cantilever will snap up when the tip-sample bonds are broken. The force needed to break the bond can be calculated through this snap (Morandat & Kirat 2010).



*Figure 2.7 Schematic of a typical force curve obtained on AFM measurement on supported lipid bilayers (reproduced from Morandat & Kirat 2010)*

One of the quantification of nano-mechanical properties of supported lipid bilayers (SLB) is the value of yield threshold force or breakthrough force detected by force curve. It is the maximum normal or vertical force that bilayer can withstand before breaking. It can be found in approaching curve. This parameter is related to membrane stability because it is also described the lateral interaction between phospholipid molecules (Garcia-Manyes et al. 2005). Then, the force curve is used to explain the mechanical behaviour of supported lipid bilayers (elasticity and plasticity)(Morandat et al. 2013)as illustrated in Figure 2.8. Elastic region can be



found when the force applied is smaller than breakthrough force and plastic region is when the force applied is higher. By converting the piezoelectric displacement into vertical separation between tip and sample (see Figure 2.9), we can observe electrostatic and hydration clearer. And also it is possible to measure the thickness of lipid bilayers (horizontal distance of jump). In addition, by analysing the retract curve, we can get information about adhesion force as explained in previous paragraph. It is useful in single molecule AFM force spectroscopy to study the protein unfolding process (Cao et al. 2015).

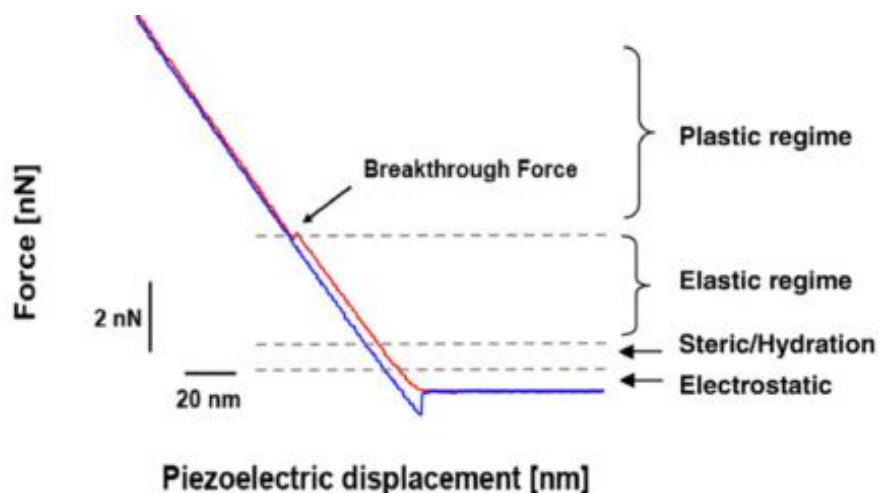


Figure 2.8 Example of force curve (reproduced from Garcia-Manyès & Sanz 2010)

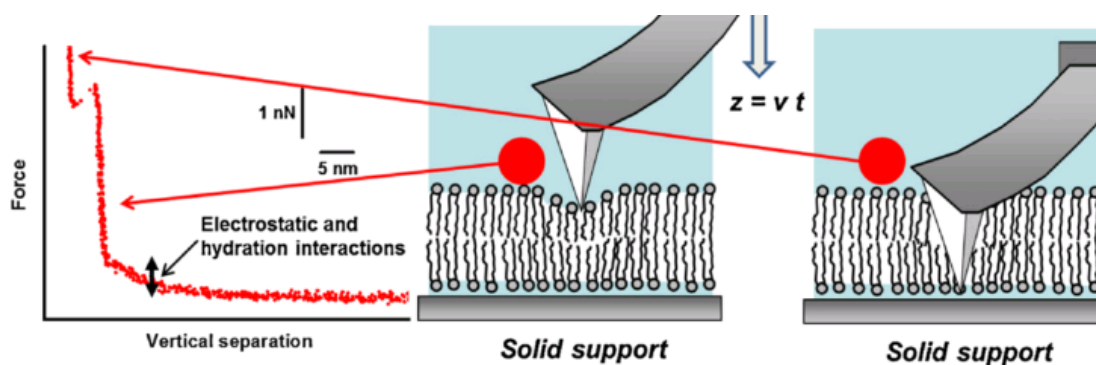


Figure 2.9 Indentation of lipid bilayer by AFM tip (reproduced from Morandat et al. 2013)

Furthermore, force spectroscopy is also used to study frictional properties of lipid membrane by measuring lateral force. The instrument used is often called as Lateral Force Microscopy (LFM) or Friction Force Microscopy (FFM). Friction force is measured by recording the change of torsion of cantilever through horizontal deflection of the laser beam. It focuses

more on modulation in X direction. It could be friction between two assemblies of head group observed in supported-double-lipid-bilayer (Grant & Tiberg 2002) and between hydrophobic domains in single lipid bilayer (Oncins et al. 2005). It can be used to determine the phase state of lipid mixture membrane (Oguchi et al. 2010) (explained in later part). It is because the force applied during normal and lateral force measurement is nearly similar. In addition, rectangular cantilever is preferred because it offers linear relationship between lateral force and torsion angle (Grant & Tiberg 2002).

### ***2.2.4 Friction Force Microscopy (FFM)***

The principle of friction force microscopy (FFM) or lateral force microscopy (LFM) is basically the same with atomic force microscopy. FFM can be considered as one of the type of AFM that is especially dedicated for friction measurement. FFM is often compared with SFA as both of them are popular in bio-tribology. Both can be used to quantify the tribology of thin layer. Table 2.1 gives the comparison of operating parameter between SFA and FFM (Bhushan 2011b).

Atomic force microscopy coupled with force spectroscopy is used to measure normal force through analysis the deflection signal of the cantilever. In FFM, we are more interested on the left and right sets of quadrants of the photodetectors which are used to detect the torsion of the cantilever. Friction force on the tip-sample interface cause twisting of the cantilever that cause change in laser beam intensity in the left and right quadrants of photodetector. The difference intensity between left and right per total intensity is proportional to the torsion of lever and also the magnitude of the friction force. In the end, FFM can produce three-dimensional maps of friction force. In order to convert the friction force to force unit, a lateral force calibration of the tip is mandatory (see chapter 2). The coefficient of friction can be obtained by calculating the slope of the friction force data plotted as a function of normal force (Bhushan 2011a).

Friction measurement is done in contact mode while tapping mode, referred as dynamic AFM, is used for surface roughness measurement. In this mode, the tip is sinusoidally vibrated at its resonant frequency by slightly tapping the surface. The feedback loop controls the scanner to maintain constant oscillating amplitude and constant average normal force. The

signal of feedback to the z-direction piezoelectric scanner (to keep the set point constant) is a measure of surface roughness. Before touching the sample, the tip-cantilever vibrates at certain amplitude called free amplitude. When the tip engages to the surface, the oscillation amplitude is influenced by contact with the sample. The setpoint is defined as ratio of the vibration amplitude after engagement to free amplitude before engagement (Bhushan 2011b). The computer records height to measure surface roughness and a phase angle which is a function of the viscoelastic properties of the sample. The amplitude is maintained large enough to avoid the tip not get stuck to the sample due to adhesion force. Additionally, the force applied in tapping mode is smaller than force applied in contact mode.

*Table 2.1 Comparison between SFA and FFM (reproduced from Bhushan 2011b)*

Parameter	SFA	AFM/FFM
Radius of mating between two surfaces	$\approx 10$ mm	5-100 nm
Radius of contact area	10-40 $\mu$ m	0.05-0.5nm
Normal load	10-100 mN	$\leq 0.1$ -500 nN
Sliding velocity	0.001-100 $\mu$ m/s	0.02-200 $\mu$ m/s Scan size 1nm $\times$ 1 nm to 125 $\mu$ m $\times$ 125 $\mu$ m Scan rate $\leq 1$ -122 Hz
Sample limitations	Atomically smooth surface	Smooth surface

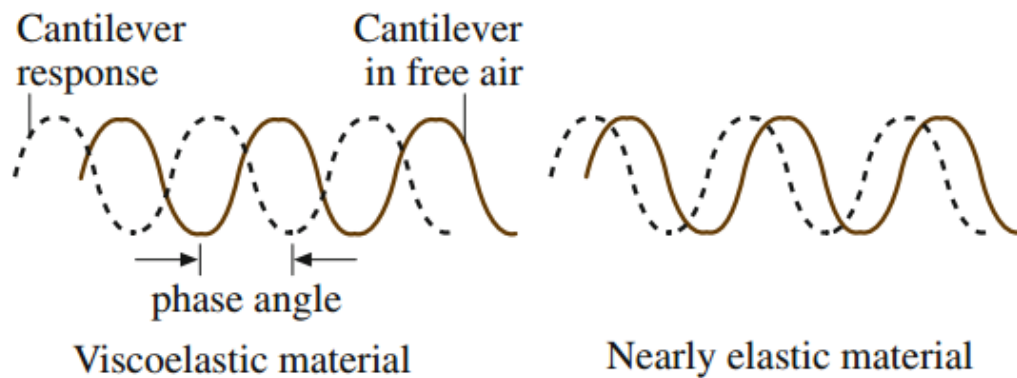


Figure 2.10 Illustration of the tip oscillation (reproduced from Bhushan 2011b)

## 2.3 Sample Preparation for AFM

One of advantages of AFM is that the ability to characterize biological sample in its native condition. The only requirement is that the samples should be well attached onto solid substrate by using nondestructive method (El Kirat et al. 2005). Therefore, the selection and preparation of solid substrate is as important as immobilization protocols for biological samples in order to assure samples attachment.

An atomically flat substrate is necessary to deposit the samples with strong adhesion to the substrate. Samples which are not well attached can be easily swept by the AFM tip resulting numerous artifacts in the AFM images (Lyubchenko 2012). Muscovite mica, glass, and silicon oxide have been often used as it shows excellent performance as solid substrate for AFM sample (El Kirat et al. 2005). Mica  $KAl_2(OH)_2AlSi_3O_{10}$ , is layered mineral whose has 1nm of thickness each. To produce clean and smooth surface, an easy cleavage process can be done by an adhesive tape. The cleaved surface has negative charged and can be modified with silanes to improve surface adsorption (Lyubchenko et al. 1992).

Another option for solid substrate is glass cover slip. The roughness of the surface is appropriate to immobilize cells or other large structure but it is too rough for adsorbed molecules. Additional step of rinsing with concentrated acidic solution; is needed to result clean glass surface as it is always coated with contaminants. Then ultrasonification in water solutions is done to remove to excess of acidic solution. Besides mica and glass, silicon oxide wafers are also possible to be used as solid substrate. Despite of their drawbacks; more complicated to handle and more expensive, they provide smoother surface than glass.

Moreover, silicon has conductive surface unlike mica. Therefore, to achieve good dispersion of polymeric nanoparticles suspension on silicon, glow discharge treatment is needed (Souza et al. 2015).

Later, to have selective characteristic of substrate, surface modification procedure can be done. Coating of highly oriented pyrolytic graphite (HOPG), carbon, or polymers (polystyrene, poly (methyl methacrylate)) produces hydrophobic surface which favors the adsorption of DNA. For specific application, gold coating is used as intermediate layer for self-assembled monolayers (SAMs). Gold surface can be acquired by thermal evaporation onto mica, glass, or silicon oxide substrates.

Various methods have been used to immobilize biomolecules such as DNA, RNA, and proteins onto solid substrate to be imaged in air. One can deposit a drop of suspension of biomolecules and let it evaporate. Another option is immersing the substrate in the suspension for certain given time and then rinsing and air-drying. To improve the attachment of DNA, pre-treatment of substrate is necessary such as chemical functionalization (silane and amino group) and addition of cation ( $Mg^{2+}$ ) in the buffer (Lyubchenko 2012). The adsorption of bio-particles from buffer solution is controlled by the concentration of electrolyte and pH of the buffer (Starostina & West 2006).

It is necessary to optimize the protocol of sample fixation as it can provoke changes in the cells. Different methods of cell fixation: air-drying directly from water or air-drying following immersion in ethanol dehydration series; gives different images. In addition, the fixation agents can also alter the topography image. Fixation agent is applied after adsorption. Immersion of cells in 3% glutaraldehyde results in intact and uniform surfaces with better structural integrity than 4% paraformaldehyde (Francis et al. 2010).

Furthermore, supported lipid bilayers (SLBs) have been widely used to mimic the biological surfaces to study cellular processes. The preparation of SLBs will be explained in detail in the following chapter concerning biological membranes. In short, there are two common techniques to prepare SLBs: Langmuir-Blodgett technique and vesicle fusion technique.

Another interesting biological object to be observed under AFM is two-dimensional protein crystal. The most frequent preparation protocol is based on physical adsorption in aqueous solution. The typical procedure is following dilution of membrane in buffer and deposition a drop of solution on the freshly cleaved mica. After certain given time to let the

membrane be adsorbed on the substrate, the sample is rinsed with water to remove unattached membrane (Jena & Horber 2002).

## **2.4 AFM versus other techniques**

There are several instruments that can be used to quantify mechanical properties of SLB. Micropipette aspiration technique, optical tweezer, surface force apparatus, fluorescence microscopy, and quartz crystal microbalance have been used to characterize lipid vesicles as it is the original form of SLB. But, those techniques are limited to big vesicle. While, surface force apparatus (SFA) open an opportunity to see the process happened during lipid bilayer adhesion, fusion, and recovery. It also has been used to measure the interaction force between symmetric and asymmetric lipid bilayer. But, it is limited to two bilayers on two opposing mica substrate (Garcia-manyes et al. 2010). The appearance of scanning tunnelling microscopy (STM) gives an enlightenment to dig more information of SLB's morphology. As one of STM's development, atomic force microscopy (AFM), invented in 1986 (Binnig et al. 1986), becomes a new weapon to characterize biological sample since it does not need or less sample treatment and it permits to characterize sample in wet condition (in liquid medium). It is very suitable for biological sample which cannot be dehydrated. Otherwise, a conductive dry sample is necessary in STM because it uses current channel generated from tip and sample surface electrical interaction. Another privilege of AFM is it can give real time and nano scale resolution of image.

### ***2.4.1 Surface Force Apparatus (SFA)***

Surface force apparatus is firstly introduced by Tabor and Israelachvili to measure the forces between two surfaces in air, vacuum, or liquid environment while changing their distances at the angstrom level. Figure 2.11 shows the scheme of SFA. The distance between surfaces and refractive index in the medium are measured interferometrically (Fallis 1995). SFA measures the force between two cylindrically curve which is molecularly smooth at 90° (mostly mica due to its planar surface) (Baro & Reifenberger 2012). An optical multiple-beam interference technique is used to measure the separation between curves with an accuracy of

a few Å. The optical part produce colored fringes or commonly known as FECO (fringes of equal chromatic order) which represents cross-sectioned view of the contact, to monitor the surface shape.

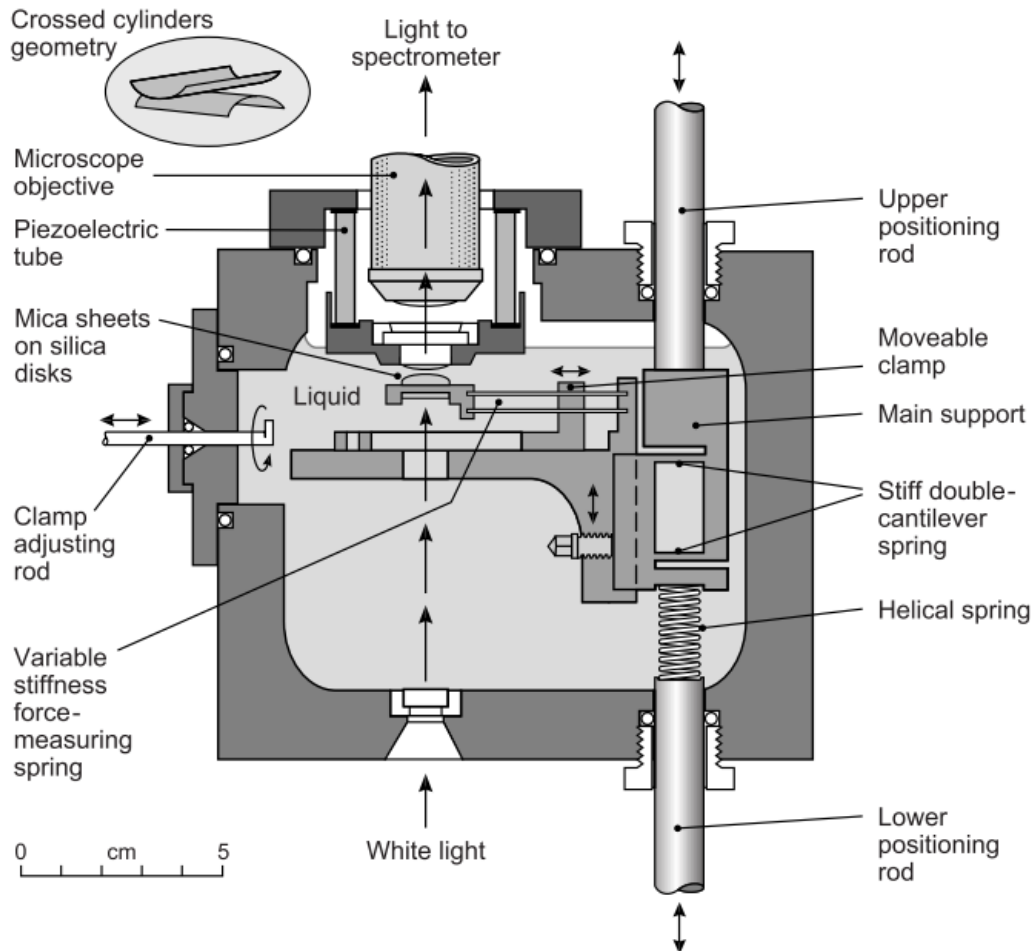


Figure 2.11 Illustration of surface apparatus (reproduced from Israelachvili 2013)

Two surfaces in contact result elastic deformation and small circular contact area, see Figure 2.12. The surfaces are separated by lubricant film which could be as thin as monolayer. The thickness of lubricant film can be varied by changing the load. Thus, SFA can be used to study sliding friction for given thickness of lubrication film (Persson 2000).

SFA can be used to measure forces between lipid bilayers and stability of symmetrical and asymmetrical lipid bilayers. In SFA, lipid bilayers are compressed and tested for occurrence of hemifusion. Hemifusion or monolayer fusion is the process of two bilayers fusing into one. Hemifusion can be induced by the presence of defect on lipid bilayers. By modulating the pressure of deposition in Langmuir-Blodgett instrument during membrane preparation, the

number of defects is evolved. The type of defect can be varied to monolayer deep than can evolve to bilayer deep due to decreasing of deposition pressure. Lipid bilayers that have more defects need less force for hemifusion. The drawback of SFA is that it is not adapted to characterize single bilayers even though SFA works well to quantify the stability and thickness of two interacting bilayers and to study the kinetics of lipid bilayers adhesion, fusion, and healing. It is because it requires interaction of two surfaces (the use of two curves). Furthermore, it uses relatively stiff spring constant that causes difficulty to sense short-range interactions such as, steric hydration and Van der Waals forces (Benz et al. 2004).

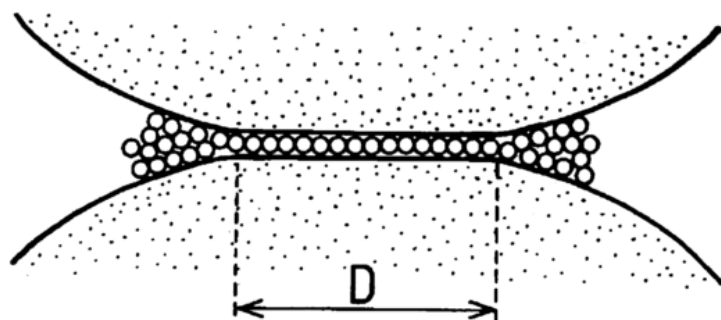


Figure 2.12 Contact area between two curved surfaces in SFA (reproduced from Persson 2000)

### **2.4.2 Micropipette Aspiration Technique**

This method pressurizes vesicles to measure elastic bending and area stretch moduli on fluid-like phosphatidylcholine (PC) membranes in the form of giant vesicle. The suction pressure applied is smaller than osmotic pressure in order to keep constant volume during area expansion test. The suction pressure produces a uniform membrane tension which is described as geometric relation based on pipet diameter and diameter of vesicle in the exterior part. Thus, the data of aspiration length versus pipette pressurization is converted to apparent area expansion versus tension properties of lipid bilayer. Later, lipid area expansion and bending moduli can be obtained by deriving from apparent area expansion. It was found that unlike stretch moduli which is relatively constant (10% variation), bending moduli was increasing on longer alkyl chain in saturated and monounsaturated lipid (Rawicz et al. 2000). This technique is also applied with any spherical biological molecule, such as nucleus. Understanding of nuclear mechanics and deformation is obtained by measurement of stress



transition. However, the pores on nucleus envelope should not be neglected because they can affect the mechanical properties. Pores cause fluid leakage which depends on pressure and time (Vaziri & Mofrad 2007). Consequently, morphology of experimental object using micropipette technique should be highly considered if mechanical properties are the main interest of study.

In the beginning, micropipette aspiration technique was used to prepare lipid bilayers from two monolayers by monitoring electrical response during formation. Contact between monolayers is monitored by applying a sinusoidal voltage during downward movement of the pipette (pipette was put vertically with opening part is at the bottom). Sudden increase in output signal can be found when contact formation is achieved. However, bilayers prepared with this method only last for less than a minute (Nag & Keough 1993). By using the same principle of electrical monitoring, modification on micropipette technique with ITIES (interface between two immiscible electrolyte solutions), allows measurement of ion rate transfer on monolayers. We can observe the current transient consisted of a capacitive and faradaic current component. The rate of ion transfer is enhanced due to lowered interfacial tension (Kontturi et al. 1997).

### ***2.4.3 Optical Tweezer***

Line optical tweezers is used to observe state transitions and transformation on giant vesicles. Optical forces cause sub-micrometer deformation in GUV to measure bending rigidity and shear modulus. Liposomes were stretched along the line optical trap due to the laser tension resulting membrane shape transformations from spherical to tubular. Thus, it induces dynamic shape deformation and yield budding transition, fission, and peristaltic transition on liposomes. Those transformations are obtained due to osmotic rise of surface (Spyratou et al. 2009). To ease morphological observation during deformation, fluorescence agent and/or silica bead are encapsulated inside the liposome. Furthermore, by using dual-beam optical tweezers, similar shape transformation is obtained. But, an intermediate shape, lemon-like shape, was seen before reaching final shape, tubular. In this case, surface tension and bending rigidity are acquired from the measured force-expansion curve which can explain the movement and the expansion of liposome. For one phase liposome, surface tension increases

with an increase of electrically-charged component while the bending rigidity is relatively constant. Different characteristic is found in two-phase liposome as they need spatial rearrangement to form specific shape (Shitamichi et al. 2009). In short, this technique works well to characterize lipid bilayer in the form of GUV.

#### ***2.4.4 Fluorescence Microscopy***

Fluorescence microscopy is able to visualize coexisting phase in molecule mixture by giving different contrast on ordered-phase and ordered phase or in fluid-phase and gel-phase (Shitamichi et al. 2009). For example, the presence of cholesterol in lipid system has proven to induce lateral phase segregation on lipid monolayer which depends on surface pressure and cholesterol concentration. Cholesterol decreases the liquid-condensed ( $L_c$ ) phase in dipalmitoylphosphatidylcholine (DPPC) while it has no effect in palmitoyl-oleoylphosphatidylcholine (POPC) (POPC is remained at liquid-expanded ( $L_E$ ) phase) (Worthman et al. 1997). In order to visualize coexisting domain and lateral structure of membrane, it uses environmentally insensitive fluorescent probe. Therefore, it is possible to construct lipid phase diagrams for artificial lipid mixtures from fluorescence images. Since partition of the fluorescent probe depends more on the local chemical environment of the lipid domain, it does not always provide information about the local physical properties of each coexisting domains in the membrane. Therefore, the fluorescence intensity image limits the information about shape, size and morphology of lipid domain. Another drawback of fluorescence microscopy is that there is necessity to find pairs of fluorescent probes that specifically label each lipid domains presented on membrane (Bagatolli 2006).

Besides constructing the phase diagrams, fluorescence microscopy can also be used to characterize the osmotic properties of lipid vesicles. By encapsulating self-quenching fluorescence dye (ex. carboxyfluorescence) in unilamellar vesicles ( $D = 100\text{nm}$ ) prepared by extrusion, it is possible to observe the change in structure and dynamics of biological membranes which are exposed to trans-membrane osmotic gradients. Dilution of medium external of vesicles causes leakage and lysis. Leakage is gradual loss of osmolytes from the vesicle lumen without alteration in gross vesicle structure. Whereas, lysis is the rupture of vesicle due to transient alteration in gross vesicle structure. It is available to measure time and pressure of osmotic lysis by quantifying the release of fluorescence dye (Ertel et al. 1993).

Furthermore, fluorescence microscopy is also used to observe the morphological change due to addition of cations on giant vesicle (Haverstick & Glaser 1987; Haverstick & Glaser 1988).

#### ***2.4.5 Quartz Crystal Microbalance***

Quartz crystal microbalance with dissipation monitoring (QCMD) is used to monitor the adsorption of biological molecules onto surface and also their structure at solid/liquid interface. It is also useful to study self-assembly of layers or multilayers at surfaces. Layer deposition brings change in the resonant frequency of the quartz crystal. Therefore, it is possible to monitor the formation of biological film. The calculation of value for change in resonant frequency results hydrated mass and thickness of deposited film. However, this model of calculation is based on assumption that molecules adsorbed form homogeneous, rigid elastic layer. While in nature, the layer likely has viscoelastic behavior. Thus, QCMD should be accompanied with probe microscopy. Despite its ability to produce three-dimensional morphology image, probe scanning microscopy has limited range in z-direction. Given that QCMD uses coated quartz crystal (by gold or silicon dioxide) whose higher roughness compared to bio-macromolecule size, there is a need to modify the substrate to have simultaneous characterization of QCMD and scanning microscopy. Moreover, deposited layer is sensitive to roughness and physicochemical nature of substrate. So, it is important to prepare the sample on atomically flat surface, such as hydrophilic mica and hydrophobic graphite (Westwood et al. 2012).

### **2.5 Latest Development of AFM**

We have demonstrated the performance of several characterization tools that can be used to characterize organic layer. For mechanical characterization of planar lipid membrane, AFM has shown its strength to yield high resolution image and to have mechanical measurement at nano scale compared to other techniques. Micropipette aspiration technique, and optical tweezer are more suitable for bilayers vesicles characterization. While surface force apparatus acquired two organic bilayers deposited onto two surfaces which is facing to each other, thus characterization of single bilayers is not possible. Furthermore, fluorescence microscopy does not have direct measurement of mechanical properties and are

more specific for morphological studies under environmental change. Meanwhile, the usage of QCMD is highly recommended to be accompanied by probe microscopy. So, AFM is the most appropriate tool to address the mechanical properties and the structure of biological sample under physiological conditions in real-time with nano resolution (Morandat & Kirat 2010).

However, there are still some challenge remained for further development of AFM. For example, observation of the activity of single protein molecules has a complex procedure because we have to infer the protein function from the static snapshots of their structures and dynamic behaviour of optical markers attached to the molecules (Ando et al. 2013). It arouses the necessity of high-resolution AFM to study dynamic of protein without the use of protein-attached markers. Thus, high-speed AFM has been develop for a decade to observe single molecules at submolecular spatial resolution and sub-100 ms time resolution (Ando 2014). The imaging rate of HS-AFM is higher than 10 frames per second resulting video-like data. In addition, the high velocity acquisition is not disturbed by the tip force acting on biological sample. The movement of myosin V when it is walking on actin filament is successfully observed by HS-AFM (Kodera et al. 2010). For further advancement, it is possible to couple HS-AFM with fluorescence microscopy as it is already done with conventional AFM. This technique allows us to study not only the structure of biological sample but also the components of the sample by specific labelling of molecules with different colour of fluorescence dyes (Uchihashi et al. 2016).

Infra-red-coupled AFM which is developed at 2010 by Dazzi and friends allows us to obtain not only high resolution topography image but also chemical maps to identify the chemical composition of the sample (Dazzi et al. 2015). Infrared absorption causes heating on sample resulting thermal expansion of sample. Due of that, the oscillation of AFM cantilever is increasing and is detected by optical system of conventional AFM. The local absorption is proportional to the cantilever oscillation so the infrared spectrum can be obtained by collecting the amplitude and the wave length.

In friction force measurement, the tip must be calibrated for normal and lateral force applied. Besides, another problem arose due to inconstant sliding velocity during friction measurement. As explained before, the scanner moves in raster pattern during scanning causing the presence of rest periods when the scan direction of the scan is inverted (shown by dashed line on the **Error! Reference source not found.**). During the rest period, the characteristics of the nanoscale tip-sample interaction may change significantly (Nasrallah et

al. 2011). It has been demonstrated that adhesion (Noel et al. 2012) and capillary forces (Mazeran 2006) depend on sliding velocity. So, the circular mode is firstly introduced to address this problem to yield constant and continuous sliding velocity (Nasrallah et al. 2011). The Circular Mode AFM will be explained in the next chapter.

Next, a challenge on imaging function is encountered for study with interest in height of defects on lipid bilayers membrane, it is difficult to precisely measure defect whose height is in the range of the diameter of the cantilever tip. It is because cantilever probe interacts with single or few molecules which can lead to pushing down the lipids and/or the tip can penetrate into the sample. Thus, tip can modify the shape and size of defects (Benz et al. 2004).

## 2.6 Conclusion

The invention of atomic force microscopy (AFM) has opened a new insight in characterization of biological samples that require minimum pre-treatment. Equipped with sharp tip, laser equipment, and piezoelectric scanner, AFM is the only technique that allows imaging under physiological conditions at nanoscale. The loop system controls the interaction force between the tip and the sample surface to avoid any damage to both tip and sample. For imaging purpose, there are several mode of scanning available: contact, tapping, and intermittent mode. Compared to other imaging instrument, the samples of AFM do not need complex preparation. However, several cautions are still given to obtain high resolution image. Furthermore, coupled with force spectroscopy, AFM is able to quantify the molecular interactions forces, elasticity, chemical properties, and receptor sites on the molecular scale. By comparing AFM with other available technique for force measurement of biological membrane, we have highlighted the strength of AFM to measure the mechanical properties of lipid bilayers with piconewton sensitivity. But, it does not mean that AFM stop developing. Some recently modified AFMs were introduced to acquire more information about the properties of lipid membranes. Now, AFM is used to obtain the morphology, mechanical and chemical properties of the biological samples.

## Biological Membranes

In this chapter, we will discuss about lipid membrane as it is the main component of cell membrane envelope. Then, various membrane models available are presented for lipid bilayer characterization, including their strengths, weaknesses, and method of preparation. Later, we will focus more on biomimetic models of supported lipid bilayers (SLBs) and discuss the several factors influencing the mechanical properties of lipid bilayers. Besides, we also put some interest on frictional and flow behavior of lipid membranes. Some examples are shown, mostly using AFM as the most appropriate tool to study SLBs.

# Chapter 3

## Biological Membranes

### 3.1 Cell membranes

Cell membranes are built by two leaflets of lipids supported by cytoskeleton and combined with glycolipids and proteins. It maintains cell's shape and protects the cell interior by giving clear boundary between extracellular environment and cytosol. Half of cell membrane's mass is accounted for lipid molecules. Most of them are phospholipids which are amphiphilic: they have a polar headgroup (hydrophilic) and two nonpolar hydrocarbon tails (hydrophobic). On the basis of the level of saturation of their acyl chains, lipids can be classified into two classes: saturated lipid containing only single C-C bonds and unsaturated lipids containing at least one cis-double bond (C=C). The effect of each lipid type onto the physico-chemical and mechanical properties of membranes will be discussed later but structurally it is clear that double bonds introduce a kink among the acyl chains in the hydrophobic part of membranes (see Figure 3.1). Moreover, lipid membranes give basic fluid structure (Albert et al. 2002) and are involved in many crucial cellular processes, such as drugs and ions diffusion, transduction of signal, energy generation (Garcia-Manyes & Sanz 2010) and cell exchanges and development (fusion and fission) (Picas et al. 2012). Cell membrane protect cell interior from the external environment by controlling the transportation of ions, molecules, or other exogenous factors.

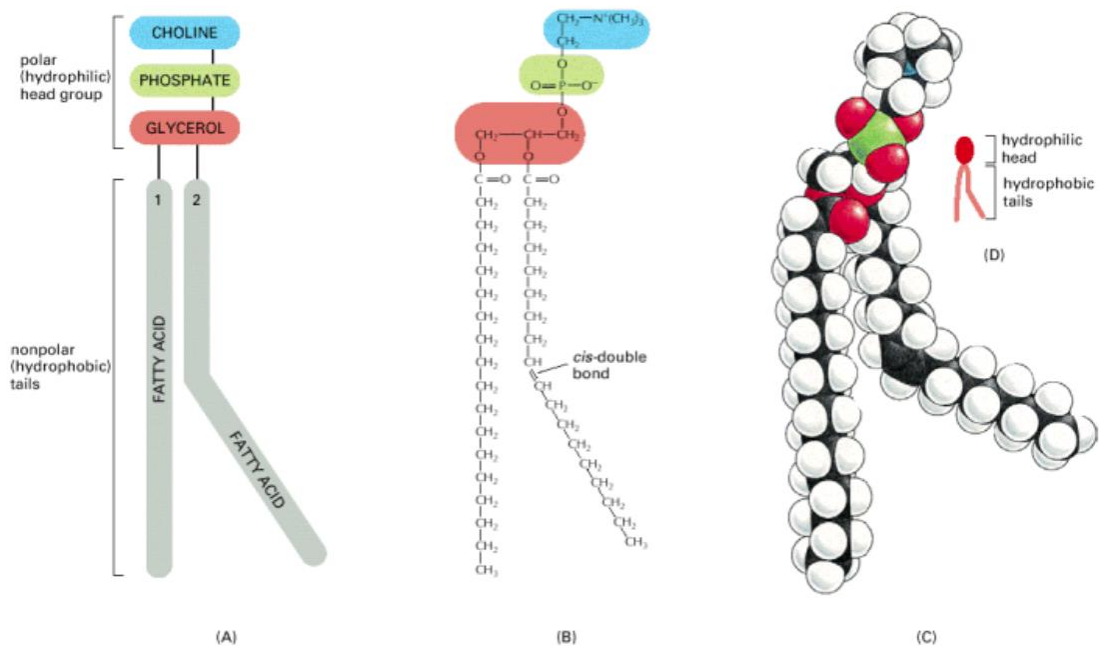


Figure 3.1 Phospholipid molecule (A) schematically, (B) by semi-developed formula, (C) as a space-filling model, and (D) as a symbolic cartoon (reproduced from Albert et al. 2002)

## 3.2 Model Membranes

Model membranes can be categorized according to their shape and origin as summarized in Table 3.1. Based on their origin and their method of preparation, model membranes can be classified into two different approaches; bottom-up that uses synthetic lipid molecules or top-down when membranes purified from biological material (Figure 3.2) (Takeyasu 2014). Biomimetic membranes are prepared by the bottom up approach and are available in various model membranes: vesicles, planar membranes, and nanodiscs. In water, phospholipid molecules can self-assemble into bilayer vesicles spontaneously. The vesicle structure is called “liposome” and it can be classified based on its size into small, large, giant unilamellar vesicles and multilamellar vesicles. Studies of lipid membranes based on the use of vesicles are highly influenced by the size and shape of vesicles. However, vesicles cannot give the information about the effect of cytoskeleton to the structure and dynamics of biomembranes as they are existed freely in the medium without support. Indeed, cell membranes are supported by cytoskeleton in nature. Thus, preparation of membrane bilayers deposited onto solid support was developed because bilayers can better mimic the conditions of lipids in membranes in contact with cytoskeleton (Seeger et al. 2009).



Table 3.1 An overview of model membrane systems (reproduced from Takeyasu. 2014)

Structure	Origin		
	Synthetic		Cell-derived
	From bilayers	From monolayers	
Vesicles, nm range <i>for binding assays, biochemistry</i>	SUVs by sonication LUVs by extrusion		Nanopatches
Vesicles, $\mu\text{m}$ range <i>for microscopy</i>	GUVs by electroformation	GUVs by microfluidic jetting, double emulsion	Giant plasma membrane vesicles (GMPVs)
Flat supported membranes <i>for microscopy, AFM</i>	SLBs by vesicle fusion	SLBs by Langmuir-Blodgett	Supported cell-membrane sheets (SCMS) by coverslip rip-off or sonication
Tethered lipid bilayers by combination of techniques			
Flat suspended membranes <i>for electrophysiology</i>		Free-standing membrane or Black lipid membranes (BLMs)	Patch clamp rip-off
Nanodiscs <i>for biophysics, biochemistry</i>	Nanodiscs: flat, scaffolded bilayer patches		

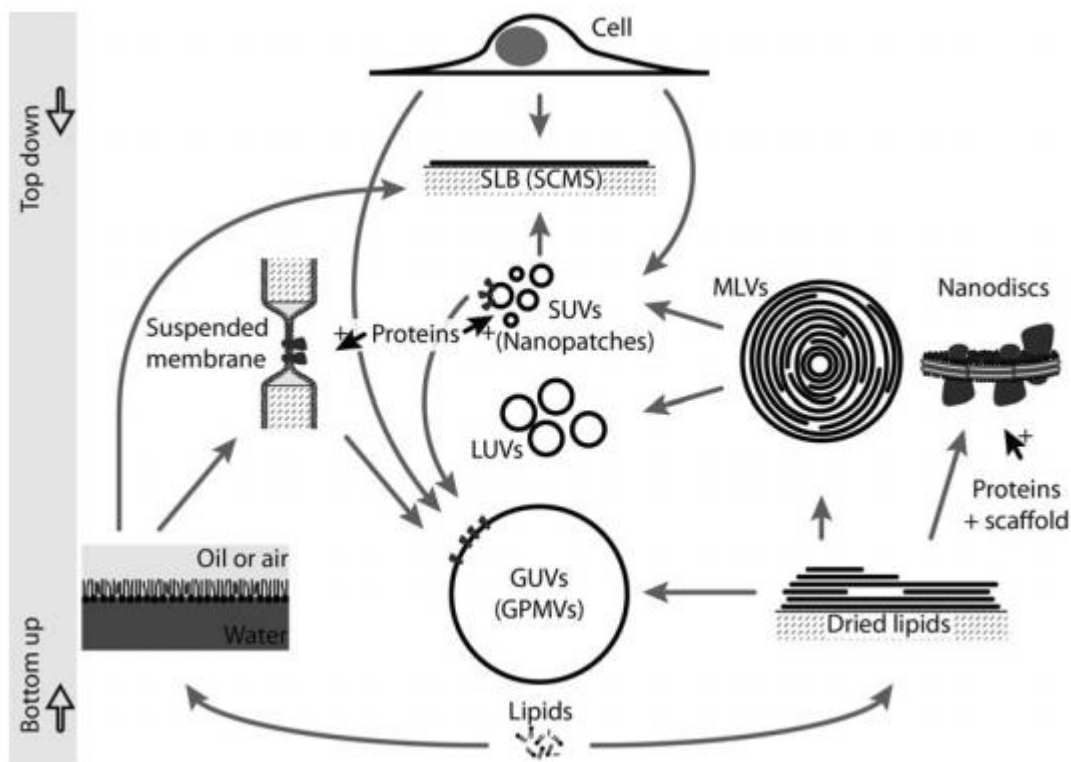


Figure 3.2 Model membrane systems (abbreviation are available in table 4.1) (reproduced from Williams & Daviter 2013)

### 3.2.1 Vesicles

The mechanism of lipid self-assembly in liquid medium can be explained by the concept of the « optimal surface area » per head group in which the total interaction free energy per lipid molecule is at minimum. Free lipid molecules are attracted to each other through hydrophobic interaction among hydrocarbon tails. It induces the congregation of molecules while, the hydrophilic headgroups remain in contact with water (Israelachvili et al. 1977). The geometry of vesicles depends on the optimal surface and the hydrocarbon chain volume and is limited by the maximum length hydrocarbon chain can extend. Liposomes are used widely to study the properties of permeability (Van Bambeke et al. 1993) and fluidity (Parasassi et al. 1991) of lipid membranes. Besides, recently they have been developed to encapsulate the drugs, proteins, or enzymes (Peetla et al. 2009) in the domain of pharmaceuticals and cosmetics.

Based on the preparation method, different structures of liposomes can be obtained as listed below.

### **A. Small Unilamellar Vesicles (LUVs)**

SUVs are the vesicles with a diameter in the range of 20 – 50 nm (Peetla et al. 2009). In order to prepare SUVs, the lipids are dissolved in organic solvents which then are evaporated to result thin film of lipid. The dried lipid films are rehydrated in buffered medium and later are subjected to vortexing until complete dissolution of lipid film. Then, the lipid suspension is sonicated to clarity using a titanium probe sonicator in an ice bath. The last, the suspension is filtered to eliminate titanium particles (El Kirat et al. 2005). They are suitable for biochemical or biophysical characterization. For example, encapsulation of fluorescent dye inside the vesicle which is exposed to osmotic gradients as one of the methods to study osmotic properties of lipid bilayers (Ertel et al. 1993). SUVs can be prepared by sonication and are osmotically insensitive (Johnson & Buttress 1973). SUVs give high membrane surface area per volume. One of the important drawbacks is the high bending of the membrane due to the small diameter that alters their stability and dynamics compared to natural biomembranes.

### **B. Large Unilamellar Vesicles (LUVs)**

Diameter range of LUVs is between 100-500 nm (Laouini et al. 2012). The difference between SUVs and LUVs relies on their strategy of preparation in which LUVs are produced through a controlled two-step processes. The preparation of LUVs includes the evaporation of organic solvent and extrusion. The early steps of preparation method are similar with one to prepare SUVs until the obtaining of lipid suspension. From here, the suspension are subjected to 3-5 freeze-thaw cycles for the uniformity of liposome size (Peetla et al. 2009). Then, LUVs are acquired from multiple consecutive extrusion through polycarbonate filters with pore size 100 – 200 nm (Polozov et al. 2001). Compared to MLVs, LUVs are preferred to use to study osmotic properties of such vesicles because the absence of multiple internal aqueous compartments (Mui et al. 1993). LUVs has single internal compartment that can simplify the study of lysis and solute release. Furthermore, for the encapsulation of ketoprofen-cyclodextrin drug complex, LUVs give higher encapsulation efficiency and slower permeation rate than SUVs (Maestrelli et al. 2006). It is due to the fact that LUVs have bigger volume of aqueous compartment, greater density and viscosity. Both LUVs and SUVs are consisting PhosphatidylCholine and cholesterol (60:40, w/w). The permeability study was done by using artificial lipophilic membranes that simulate the skin behavior.

### C. Giant Unilamellar Vesicles (GUVs)

GUVs are prepared efficiently by electroformation (Okumura et al. 2007). The diameter of GUVs is in the range of 10 – 100  $\mu\text{m}$  which is close to actual cell size (Peetla et al. 2009). Furthermore, among the vesicles classes, GUVs is the only vesicle that can give direct measurement of mechanical properties of lipid bilayer by micropipette aspiration technique (Rawicz et al. 2000) and optical tweezers (Shitamichi et al. 2009). Under micropipette pressurization, GUVs are deformed thus elastic bending and area stretch moduli could be acquired directly. While, optical tweezers deform the vesicle from the inside resulting in shape change. Due to their large size, membrane curvature and presence of free-standing bilayers, GUVs are especially useful for microscopic studies on the micrometer scale. The early studies of phase separation in lipid-mixtures were done by using fluorescence microscopy on GUVs (Haverstick & Glaser 1987). The composition of lipid phase domains can result in different fluorescent dye-partitioning thereby helping in the identification of structures and segregations in GUVs. For example in DPPC/DLPC GUVs, Dil-C20:0 which favors DPPC-rich phases over fluid phases and Bodipy-PC which favors fluid phase are added to visualize the coexisting phases (Feigenson & Buboltz 2001). Figure 3.3 gives the fluorescence image of Dil-C20:0 (upper right), fluorescence image of Bodipy-PC (upper left) and the color-merged image (below). Orange fluorescence given by Dil-C20:0 indicates the DPPC-rich ordered phase while green fluorescence given by Bodipy-PC indicates the DLPC-rich fluid phase.

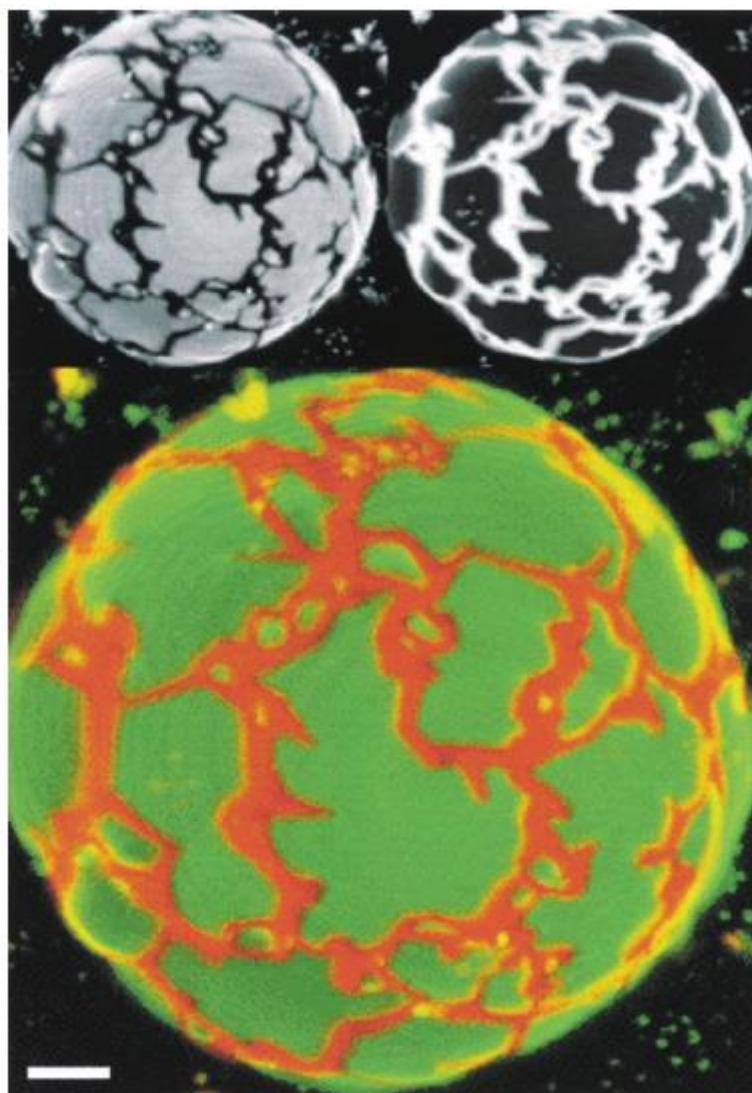


*Figure 3.3 Confocal fluorescence images of GUV of DPPC/DLPC 1:1; with Dil-C20:0 and Bodipy-PC dyes at mole fraction  $\sim 0.001$ . Excitation was at 488 nm. The upper right image is the fluorescence emission through a 585 nm LP filter (exclusively from Dil-C20:0). The upper left image is the emission through a 522/35 nm BP filter (exclusively from Bodipy-PC). The bottom image is the merger colorized image.*

*The bar represents 5  $\mu\text{m}$ . (reproduced from Feigenson and Buboltz. 2001)*

#### **D. Multilamellar Vesicles (MLVs)**

MLVs can be obtained by hydrating thin film of lipids resulting from evaporation of organic solvent. The MLVs produced from this method give some drawbacks: low encapsulation efficiency, elimination of large molecules, possible degradation of phospholipids and compounds to be encapsulated (Akbarzadeh et al. 2013). Thus, the preparation technique of reverse-phase evaporation (through water/oil emulsion) is preferred (Pidgeon et al. 1986).

The diameter of MLVs can go approximately from 0.3 to 2  $\mu\text{m}$  (Olson et al. 1979) with bilayers number >15 layers (Pidgeon et al. 1986). The difference between LUVs and MLVs is that LUVs only have one bilayer wall while MLVs are made of several bilayers embedded in each other with a structure resembling to an onion. The general disadvantage of MLVs as membrane model is their shape is not fully spherical (onion-like shape) with multiple internal aqueous compartments thus it complicates studies of lysis and solute release. Thus, the non-equilibrium distribution of solutes within internal aqueous compartments (Mayer et al. 1985) can cause different osmotic gradient at different internal lamellae when MLVs are exposed to hypoosmotic or hyperosmotic media (Mui et al. 1993). In contrary, the advantage of MLVs is that they can carry more than one component. For example, with some modifications, interbilayer-crosslinked MLVs are stably entrapped protein antigens in the vesicle core and lipid-based immunostimulatory molecules in the vesicle walls under extracellular conditions as synthetic vaccines (Moon et al. 2011). They are formed by crosslinking headgroups of lipid bilayers within MLVs. Thus, this type of MLVs can address the problem of toxicity and antivector immunity in production of vaccines.

### ***3.2.2 Free-standing Membranes***

Free-standing membranes are also called as black lipid membranes (BLM). BLM are widely used to study the physiological and pharmaceutical functions of the ion channel under chemically controlled condition (Miller 1986). Compared to supported lipid bilayers (SLBs), BLM is preferred for these purposes because SLBs have close surface proximity giving difficulty to incorporate large membrane-spanning protein (Hirano-Iwata et al. 2008). In addition, they are more suitable for electrical characterization of lipid bilayers to monitor electrical resistance and capacitance (Ichinose 2010).

These membranes can be prepared by immersing a microporous hydrophobic substrate into water. Then, the inside of the pore is coated by organic solvent containing lipids. Since the substrate is wet with organic solvent, the lipid molecules are reassembled in the micro-sized pores while the outermost surface of the liquid film will be covered by phospholipid monolayer. After the evaporation of organic solvent, the BLM is formed in substrate porous surrounded by a thick annulus (Ichinose 2010). The main problem with this system is the

instability of lipid membrane due to the presence of residual solvent causing insufficient electrical, temporal, and mechanical stability for broader application (Hirano-Iwata et al. 2010). Among the available technique to prepare BLM, the patch-clamped technique is more widely used due to their tolerance of solution exchange (Hirano-Iwata et al. 2008). Hirano-Iwata et al designed a microfabricated aperture with nanometer-scale smoothness (Figure 3.4) to prepare reduced-solvent BLM that are stable for solution exchanges (Hirano-Iwata et al. 2010).

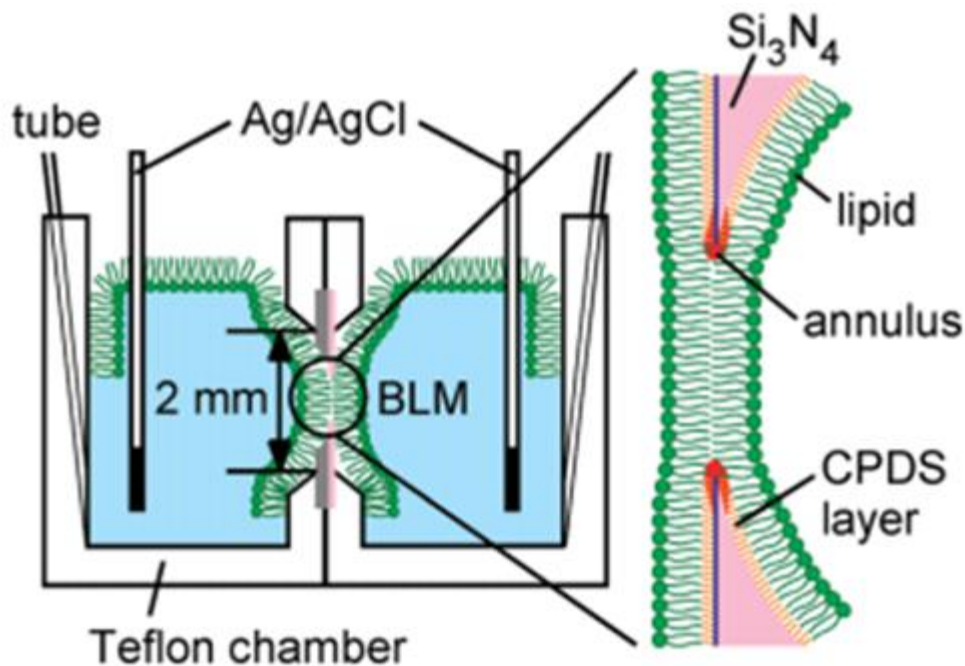


Figure 3.4 Example of apparatus of BLM. BLM is formed across an aperture of silicon ( $\text{Si}_3\text{N}_4$ ) chip that has been silanized with 2% (v/v) 3-cyanopropyltrimethylchlorosilane (CPDS) (reproduced from Hirano-Iwata et al. 2010)

BLM has an important role in the development of biosensors by incorporating synthetic and inorganic channels. Umezawa et al demonstrated an ion-channel proteins biosensor by incorporating membrane protein GluR ion channels into artificial lipid bilayers (Uto et al. 1990; Minami et al. 1991). GluR is a receptor protein for major excitatory neurotransmitter L-Glutamate in the central nervous system. The sensor will produce rectangular-shaped current pulses, referring to transition between the opening and the closing of the channel. Besides that, Hirano et al have incorporated unmodified gramicidin as molecular signal transducer (Hirano et al. 2003). The gramicidin-based lipid bilayers sensor includes lipid bilayers containing receptor sites (e.g., biotin-labeled phosphatidylethanolamine –biotin-PE) and dinitrophenyl (DNP)-PE) and gramicidin. The bilayers structure will be distorted and the

monomer/dimer kinetics of gramicidin will be modulated when biotin catches avidin (or DNP-PE catches anti-DNP antibody). In this system, the receptor sites and signal transducer gramicidin are separately embedded into bilayers. Figure 3.5 illustrates the principle of ion-channel based lipid-bilayer biosensor by incorporating biological channel (membrane protein) or natural channel (gramicidin).

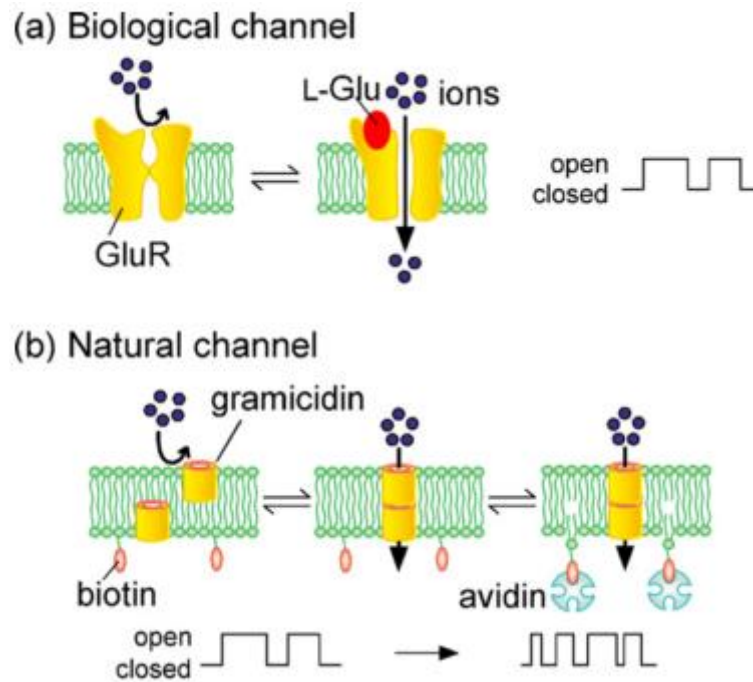


Figure 3.5 Example of ion channel-based lipid-bilayer sensors: (a) GluR receptor in channel and (b) gramicidin (reproduced from Hirano-Iwata et al. 2008)

### 3.2.3 Supported lipid bilayers (SLBs)

Another biomimetic model system that is often used in biophysical research to assess physico-chemical properties of cell membrane is supported lipid bilayers (SLB) or supported planar bilayers (SPB) (Sackmann 1996). More precisely, SLBs can be defined as thin lipid films supported on a solid substrate (mica, glass, silicon oxide, or polymer cushion). One of their advantages is that they can apply to a broad range of supports especially to conduct analytical characterization. SLBs model are often considered to be more similar to natural lipid membranes because, in fact the natural cell membrane is not floated in aqueous medium but it is supported by the cytoskeleton network (Garcia-manyes et al. 2010) Furthermore, many



cellular processes such as molecular recognition, enzymatic catalysis, cell adhesion and membrane fusion can be observed with SLBs. The development of molecular recognition is possible due to SLB's ability to become a substrate for anchoring biomolecules (Kirat et al. 2005). However, the major shortcoming of SLBs comes from their close surface proximity (Hirano-Iwata et al. 2008). The distance between SLBs and the support is only several nanometers which is not enough to incorporate trans-membrane protein. Even if it is possible, it can yield loss of lateral mobility and function of the SLBs.

As shown in Figure 3.6, SLBs are deposited onto solid supports but lipid headgroups are not in direct contact with the solid support. Instead, there is thin water layer in between. Lipid layer which is closer to solid support is called proximal leaflet, while the layer that is far from solid support is called distal leaflet.

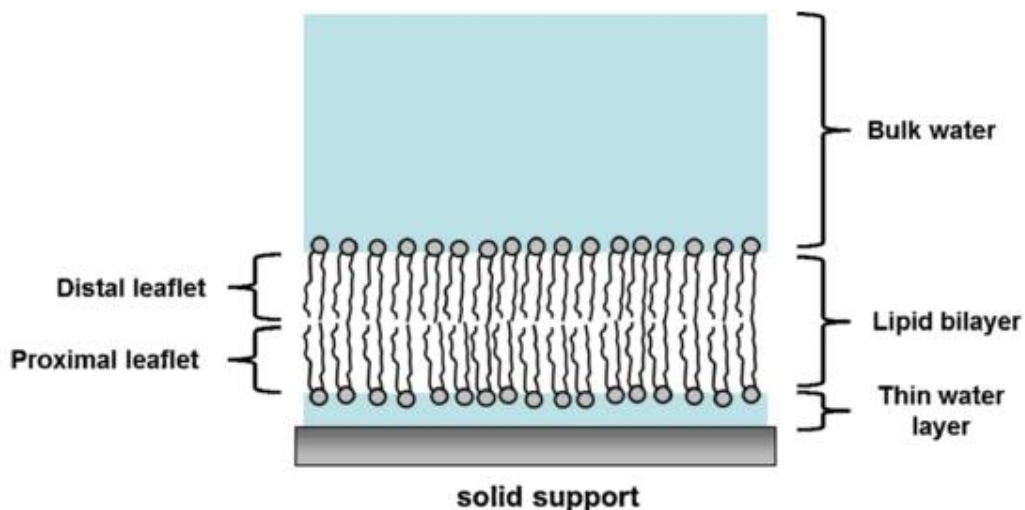


*Figure 3.6 Cartoon of the structure of a supported lipid bilayer (reproduced from Alessandrini & Facci 2012)*

There are two common methods to prepare SLBs: Langmuir-Blodgett technique and fusion of lipid vesicles as illustrated in Figure 3.7. One of the methods is by using Langmuir-Blodgett (LB) apparatus. This technique allows transfer of monolayer onto solid support at constant surface pressure and constant speed (Figure 3.7 A). Then, SLBs are formed by two vertical transfers of lipid monolayers from the air-water interface of a liquid.

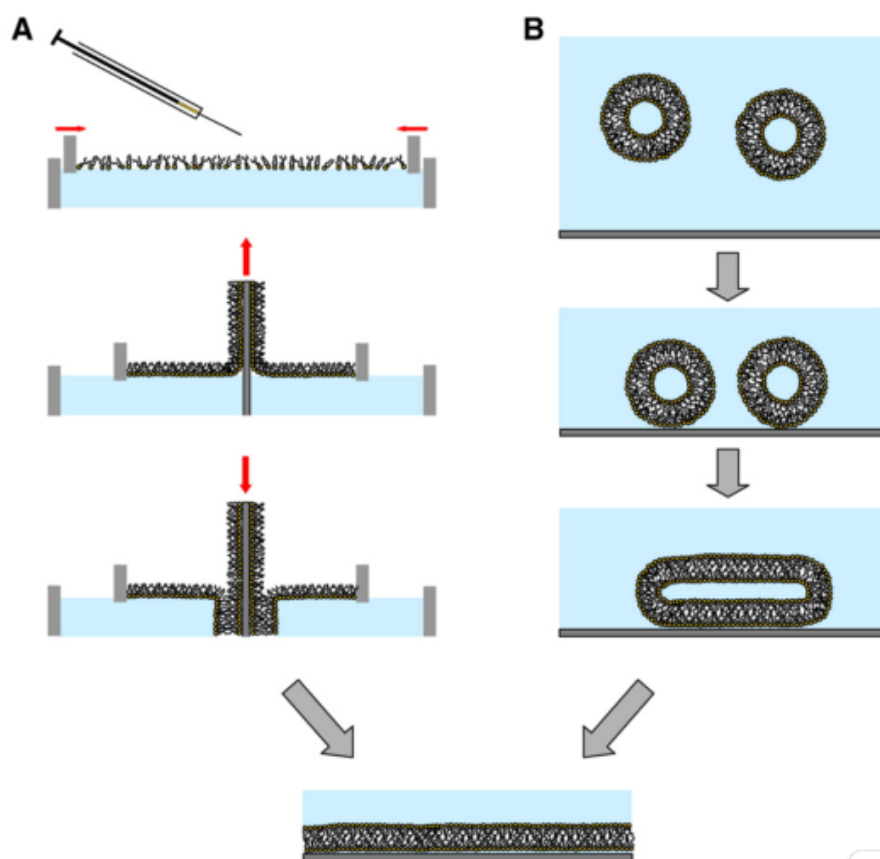


Figure 3.7 Preparation methods for the formation of SLBs (reproduced from El Kirat et al. 2010)

Usually, lipid molecules are spread at the air/water interface in hexane/ethanol or chloroform/methanol mixtures (Figure 3.7 A) (El Kirat et al. 2010). The Teflon barriers control the area available for lipids spreads at the air/water interface, and lipid packing is monitored by the surface pressure. Hydrophilic solid support, such as mica, will expose the lipid tails to the environment since the headgroups will interact with the support. Such monolayer is more stable in air and therefore it should be examined in air, not in aqueous medium (El Kirat et al. 2005). SLBs can be prepared by transferring a second lipid layer onto the first mica supported lipid monolayer (Figure 3.7 A). Thus, the first lipid leaflet is formed by pulling the solid support vertically through the lipid monolayer formed at the air/water interface. The second lipid leaflet is then transferred by dipping the solid support covered with the first monolayer either vertically (LB-transfer) (Figure 3.7 A) or horizontally (Langmuir-Schaefer, LS-transfer) (Morandat et al. 2013). A tensiometer is used to record the surface pressure at the air/water interface since careful control of surface pressure is important to avoid defect formation or feature alignment of the deposited structure (Vié et al. 1998). Compression/decompression isotherms are obtained by plotting the surface pressure versus interfacial area. This isotherm

is useful to determine the physical state, the packing, and the organization of the lipid molecules (El Kirat et al. 2010).

Another method to prepare SLBs is vesicles' fusion that is often chosen because of its simplicity (Alessandrini & Facci 2012). But, it is impossible to prepare asymmetric bilayers in which each leaflet has its own properties. This is an important drawback because the natural plasma membrane of cells is asymmetric to maintain a surface potential that is crucial for example to the ionic stability of the living cells. And also, this method lacks control of the lateral pressure in lipid bilayers.

To prepare SLB using the vesicle fusion method, firstly lipids are dissolved in organic solution which is then evaporated under a nitrogen gas flow. After drying the lipid under vacuum in desiccators, aqueous buffer solution is poured to form a suspension. Then MLVs are produced by strong agitation. To generate SUVs, a sonication step is needed. SLBs are then made from adhesion, flattening and rupture of SUVs on a solid support (Figure 3.7 B). These steps are induced by incubation at a temperature above the melting point of lipids as it is considered to be the optimum condition (El Kirat et al. 2005). The fusion temperature can decide the nanomechanical properties of SLB as it has a great influence on the domains' size of each phase in the lipid mixture (Garcia-Manyes et al. 2005b; Beauvais et al. 2013). The higher the fusion temperature, the more gel domains are found in large size, this is due to the fact that gel lipids at a temperature above the transition are in a fluid state so they mix with fluid-state lipids and diffuse in all the SLBs before they can nucleate and form large domains. The adhesion of vesicles on solid substrate involves electrostatic interactions between both surfaces. Meanwhile, the rupture of vesicles to yield bilayers is affected by the size of vesicles, lipid concentration, and the presence of cations (Morandat & Kirat 2010).

### **3.3 Lateral organization of cell membranes**

For years, the organization of lipid molecules in cell membranes was believed to follow the two dimensional fluid mosaic model proposed by Singer and Nicholson in 1972 (Singer et al. 1972). Fluid mosaic model refers to an analogous to a two-dimensional oriented solution of integral proteins in the viscous phospholipid bilayers solvent. This model states that the proteins which are integral to the membrane are heterogeneous set of globular molecules.

These globular molecules are partially and randomly embedded in a matrix of phospholipid. The bulk of the phospholipid is organized as discontinuous fluid bilayers that serve as a solvent for membrane proteins (Singer et al. 1972). However, this model does not consider lipid compositional heterogeneity as an important factor in dynamic of biological membranes (Bagatolli 2006). Later, the founding of stable phase separation in biological membranes has changed the fluid mosaic model because it proves the existence of lateral diffusion highlighting heterogeneity of membranes (Shimshick & McConnell 1973). For thermodynamic reason, biological membranes whose coexistence of gel and fluid should have high lateral compressibility that can facilitate the insertion of newly synthesized protein into the membranes. Later, the theory of lipid raft was introduced based on dynamic clustering of sphingolipids and cholesterol to form rafts that move within the bilayers (Simons & Ikonen 1997). The sphingolipids and cholesterol form a moving platforms or rafts onto which specific proteins attach within the bilayers. The function of these microdomains is for the transportation of selected membranes or as relay stations in intracellular signaling. The lipids in these assemblies are thought to be enriched in saturated and longer hydrocarbon chains and hydroxylated ceramide backbones (Simons & Sampaio 2011).

### **3.4 Nanomechanical properties of lipid membranes**

Understanding the factors influencing the nanomechanical properties of SLBs is necessary to study the interaction between cells and between cell and exogenous agents, such as proteins, drugs, and nanoparticles (El Kirat et al. 2010). It has been proved that the maximum force needed to penetrate lipid bilayers is influenced by temperature, ionic strength, lipid nature, tip chemistry, and tip's approaching velocity (Garcia-manyes et al. 2010). It is also worth noting that the type of solid substrate underneath the SLBs affects phase segregation (Seeger et al. 2010).

#### ***3.4.1 Effect of temperature***

Concerning the temperature effect, lipids are known to undergo phase transition. The temperature-related study can be done thanks to temperature-controlled AFM (Leonenko et al. 2004). With the change in phase, nanomechanical properties changes can be expected. It

is evident that gel or Lo phases need more force to be penetrated than liquid Ld phase due to more compactness and/or order. Thus, increasing the temperature softens the lipid membrane (see Figure 3.8) as the broadening of liquid phase is able to be seen in AFM morphology. The origin of membrane softening is related to the enhancement of steric repulsion causing decrease of order among phospholipid molecules. Although the effect of temperature can be seen for Lo, gel and liquid phases of lipid bilayers, the impact is more prominent for Lo and gel phases. Surprisingly, AFM images during heating of DMPC SLBs from 19° - 37,5°C gave two phase transitions (Garcia-Manyes et al. 2005b). The first phase transition corresponds to gel to fluid phase transition ( $L_{\alpha} \rightarrow L_{\beta}$ ) and it is confirmed by Differential Scanning Calorimetry (DSC) experiment. However, to explain the nature of the second phase transition, there are two hypotheses proposed: (1) the formation of interdigitated or partially interdigitated lipid chains, but this new phase is not be confirmed or (2) each transition belongs to each leaflet of bilayers (Garcia-Manyes et al. 2005b). In this article, more evidences support for the second hypothesis. It was found that the proximal leaflet has higher lipid density thus it needs higher temperature to undergo the phase transition compared to the distal leaflet (Seeger et al. 2010).

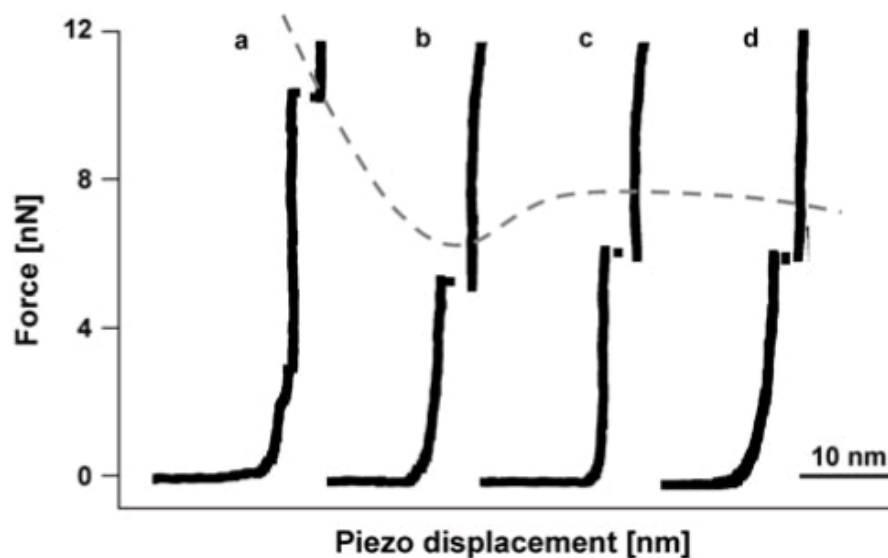


Figure 3.8 Punchthrough force curve of a DiMyristoyl PhosphatidylCholine (DMPC) SLB measured with conventional AFM at (a) 20.1 °C, (b) 29.5 °C, (c) 40.9 °C, and (d) 52.4 °C in 10mM Hepes/NaOH containing 150mM NaCl and 20 mM MgCl<sub>2</sub> pH 7.4(reproduced from Garcia-Manyes et al. 2005b)

### ***3.4.2 Effect of medium composition***

Before AFM, molecular dynamics showed the effect of electrolytic medium to the assembly of phospholipid molecules. The presence of sodium and calcium ions can give higher degree of membrane organization. It is because the interaction between cations and carbonyl oxygen on lipid forms tight ion-lipid complexes with lower mobility (Bockmann et al. 2003). The higher the concentration of cations, the higher the breakthrough forces. It is applied for phospholipids with zwitterionic headgroups, including phosphatidylcholine (PC) and phosphatidylethanolamine (PE). Interestingly, this trend is the same for natural lipids, *E. coli* polar lipid extract, with a composition of 67% PE; 23,2% phosphatidylglycerol (PG), and 9,8% cardiolipin. Even though, the increase in the breakthrough force is small (Garcia-Manyes et al. 2005a). Friction measurement by FFM on DiMyristoyl PhosphatidylCholine (DMPC) SLBs was also showing an increase of breakthrough force in the presence of sodium ions in the medium (Oncins et al. 2005).

Furthermore, the size of cations and their number of electron valencies also affect the mechanical resistance of lipid bilayers (Redondo-Morata et al. 2012). Several cations in the alkaline group IA ( $\text{Na}^+$ ,  $\text{Li}^+$ ,  $\text{K}^+$ ,  $\text{Cs}^+$ ) and IIA ( $\text{Ca}^{2+}$ ,  $\text{Sr}^{2+}$ ) were added in the aqueous medium of lipid bilayers separately. Figure 3.9 shows the effect of cations present in the medium to the punchthrough force of DLPC (12:0) and DPPC (16:0). The presence of cations increases the punchthrough force in both fluid-like and gel-like lipid SLBs. Cations reduce the intermolecular distance between lipid headgroups. Thus they increase the compactness of lipid bilayers. Cations with bigger ionic size are able to amplify the punchthrough force more. However, very big cations, such as  $\text{Cs}^+$  and  $\text{Sr}^{2+}$ , are not able to increase the compactness of lipid bilayers. Thus, it is more likely due to the optimum relationship between the real cationic size and the distance between polar headgroups of lipids.

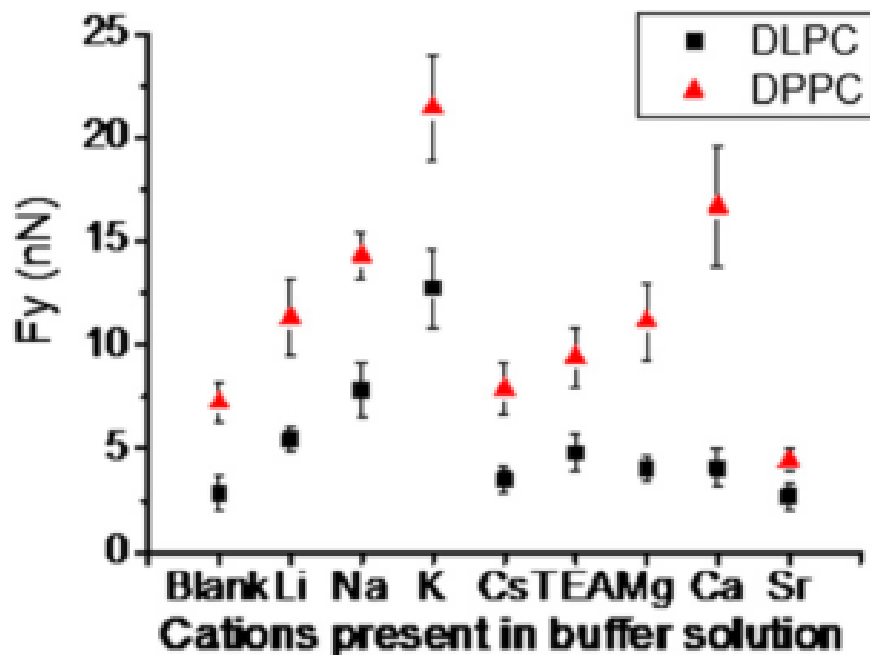


Figure 3.9 Effect of cations on the punchthrough force of SLBs. Force measurement was done by conventional AFM at 25°C in 20mM HEPES/XOH containing 150mM XCl (X is the monovalent ion present in the buffer) pH 7.4 (reproduced from Redondo-Morata et al. 2012)

### 3.4.3 Effect of membrane composition

Not only the external stimuli such as temperature and ionic strength can affect stability of the membrane, but also its internal characteristic such as chemical group function in the lipid headgroup, length of hydrophobic tails, the presence of branched groups along acyl chains, and the degree of unsaturation. The mechanical resistance of SLB is related to the effective packing molecule which can be probed directly by measuring its line tension. This parameter defines the interaction between two neighbour lipid molecules. Before, it was only known that head group affect the mechanical resistance of membrane since it faces not only solid support but also buffer solution. An experiment with different headgroup functions but the same tail chain length (16 Carbon) was held by who Garcia-Manyes et al (Garcia-manyes et al. 2010). It was found that the breakthrough force increased in the order Phosphatidic (PA) < Phosphatidylethanolamine (PE) < Phosphocholine (PC) < Phosphatidylserine (PS) < Phosphatidylglycerol (PG). Later, it is found that tail acyl chains also contribute to the packing order. It enhances the interaction among lipid headgroups, thus the line tension is affected by

the whole lipid structure. The longer the acyl chains, the higher the breakthrough force of lipid membranes in the same headgroup function (Figure 3.10 A). In addition, molecular branching decreases drastically the breakthrough force since the existence of methyl branched groups increase the area per lipid molecule thus it weakens molecular packing of SLBs. Moreover, the same effect was shown with high degree of unsaturations for lipids (Figure 3.10 B). The presence of cis double bonds in the acyl chains increases lipid mobility thus it induces fluidity. Then, it needs lower force to break lipid membrane (Garcia-manyes et al. 2010).

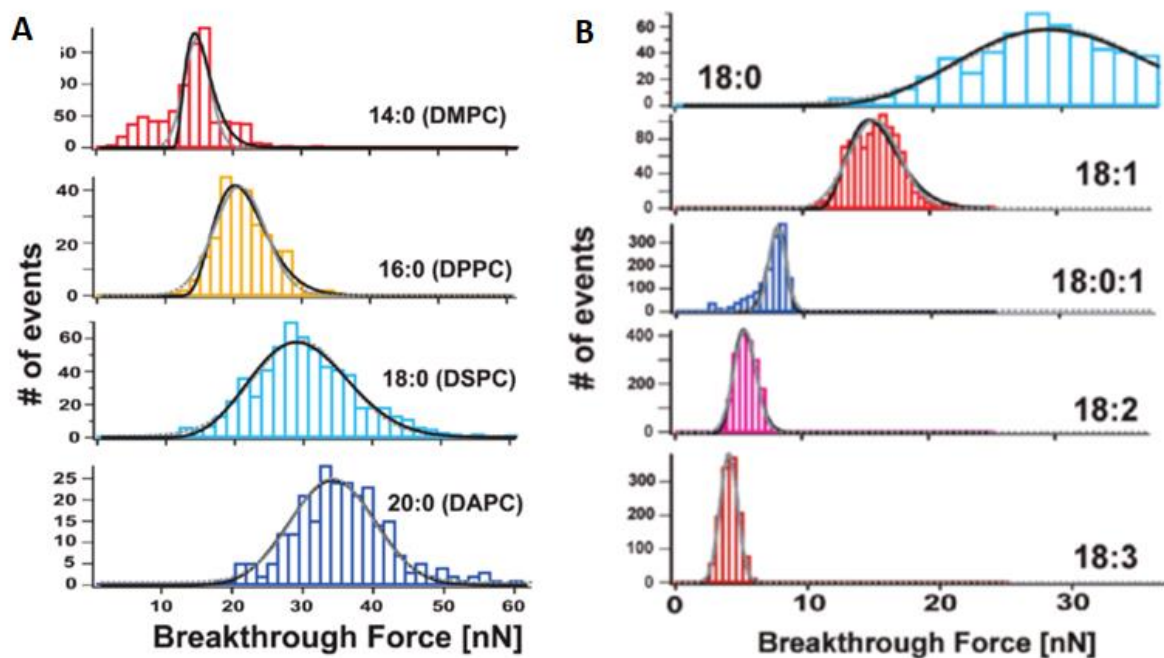


Figure 3.10 The effect of (A) tail chain length and (B) lipid saturation level to mechanical resistance of lipid bilayers. All SLBs were prepared in 10Mm Hepes/NaOH pH 7.4 containing 150mM NaCl and 20mM MgCl<sub>2</sub>. Force measurement was done on DiMyristoyl PhosphatidylCholine 14:0; DiPalmitoyl PhosphatidylCholine 16:0; Distearoyl PhosphatidylCholine 18:0 and DiArachidoyl PhosphatidylCholine (20:0) to study the effect of tail chain length. While, measurement was done on DSPC 18:0; 18:1; 18:0:1; 18:2; and 18:3 to determine the of lipid saturation level (reproduced from Garcia-Manyes et al. 2010)



### ***3.4.4 Effect of solid substrate***

The use of solid substrate raises another issue since it provokes changes in the thermodynamical state of SLBs compared with unsupported lipid membranes. In living cells, lipid membranes are always in contact with other components, both in the interior and the exterior sides. Inside, it faces cytoplasmic components while outside, there are other molecules attached to the membrane, such as proteins and ligands. Each contact can influence the membrane's structural and functional characteristics. Since each side of bilayers membranes encounter different elements, the properties of a lipid layer close to a solid substrate (proximal leaflet of SLBs) and lipid layer in contact with the environment (distal leaflet) can have different properties (Seeger et al. 2010). The finding of two transition temperatures in pure bilayers of DMPC (Garcia-Manyes et al. 2005b) support this idea (see Figure 3.11). But the use of mica as substrate can give single transition temperature if the fusion temperature during the process of vesicles fusion is higher than the main phase temperature of lipids (Seeger et al. 2010). It is related to its interleaflet coupling strength. Higher fusion temperature induces stronger coupling. Consequently, the coupling strength can be nearly similar with the interaction forces between proximal leaflet and substrate then both leaflets show similar properties (Seeger et al. 2010). By contrast, it cannot happen on silica oxide supports on which the two leaflets maintain their differences. Thus, temperature-induced phase transition for SLBs on silicon oxide is independent of fusion temperature during preparation (Seeger et al. 2010). In addition, an appropriate substrate is necessary since SLBs must be well attached to resist the lateral forces developed by the scanning tip of AFM. Therefore, smooth surfaces with low roughness are generally recommended (El Kirat et al. 2005).

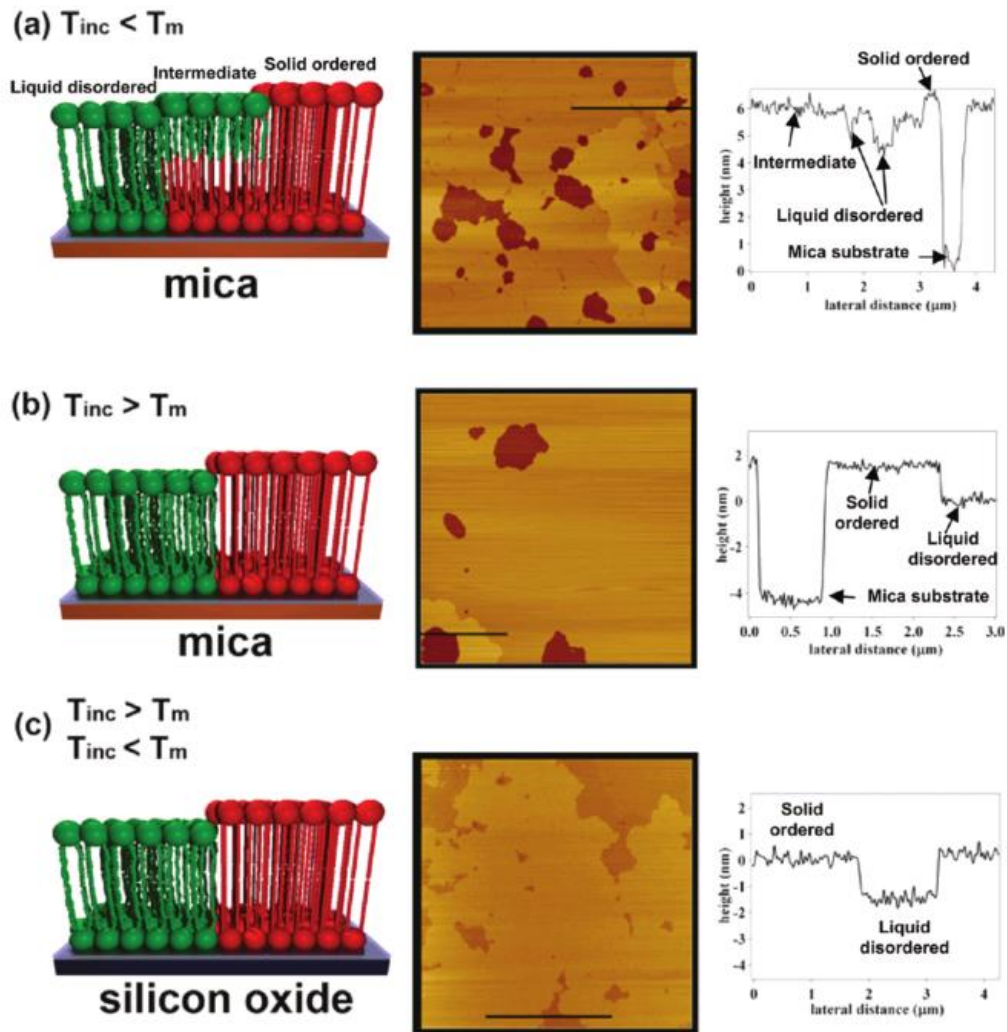


Figure 3.11 Schemes, topography images, and line sections of mixtures of lipids 1-palmitoyl-2-oleoyl-*sn*-glycero-3-phosphoethanolamine (POPE) and 1-palmitoyl-2-oleoyl-*sn*-glycero-3-phospho-(1'-*rac*-glycerol) (POPG). POPE/POPG SLBs was prepared on mica at temperature (a) below and (b) above melting point. (c) POPE/POPG SLBs was prepared on silicon oxide. Regardless the fusion temperature, SLBs prepare on silicon oxide give coupled transition. AFM imaging was done in 10mM potassium dihydrogen citrate, 150mM KCl at pH 7. ( $T_{inc}$  = fusion temperature,  $T_m$  = melting temperature) (reproduced from Seeger et al. 2010)

### 3.4.5 Friction, viscosity, and diffusion of lipid membranes

Friction measurement on Dimyristoyl PhosphatidylCholine (DMPC) showed that low friction was found at small vertical force even at high concentration of cations ( $\text{Na}^+$ ) (see Figure 3.12) due to electrostatic repulsion between the AFM tip and the polar head of lipids (Oncins

et al. 2005). It indicates that lipid molecules are suitable for boundary lubrication and it confirms their role in joint lubrication (Grant & Tiberg 2002). Friction measurement in pure water showed that lipid bilayers are able to restructure after rupture due to the high mobility of lipid molecules. In the presence of sodium chloride, lipid bilayers are more compact so they are less prone to self-healing as illustrated in Figure 3.13 (Oncins et al. 2005). Interestingly, the adsorption of ions to zwitterionic lipid bilayers influences the mechanical and tribological properties in different ways (Dekkiche et al. 2010). Better resistance to normal indentation is achieved by the increase in bilayers cohesion. Meanwhile, higher lubrication is due to an increase in the repulsion between lipids within the membrane. Ions in solution can also escalate the zeta potential values of both the lipids and the solid substrate, which accelerates the adhesion of liposomes and their fusion on the solid substrate (Garcia-Manyes et al. 2005a).

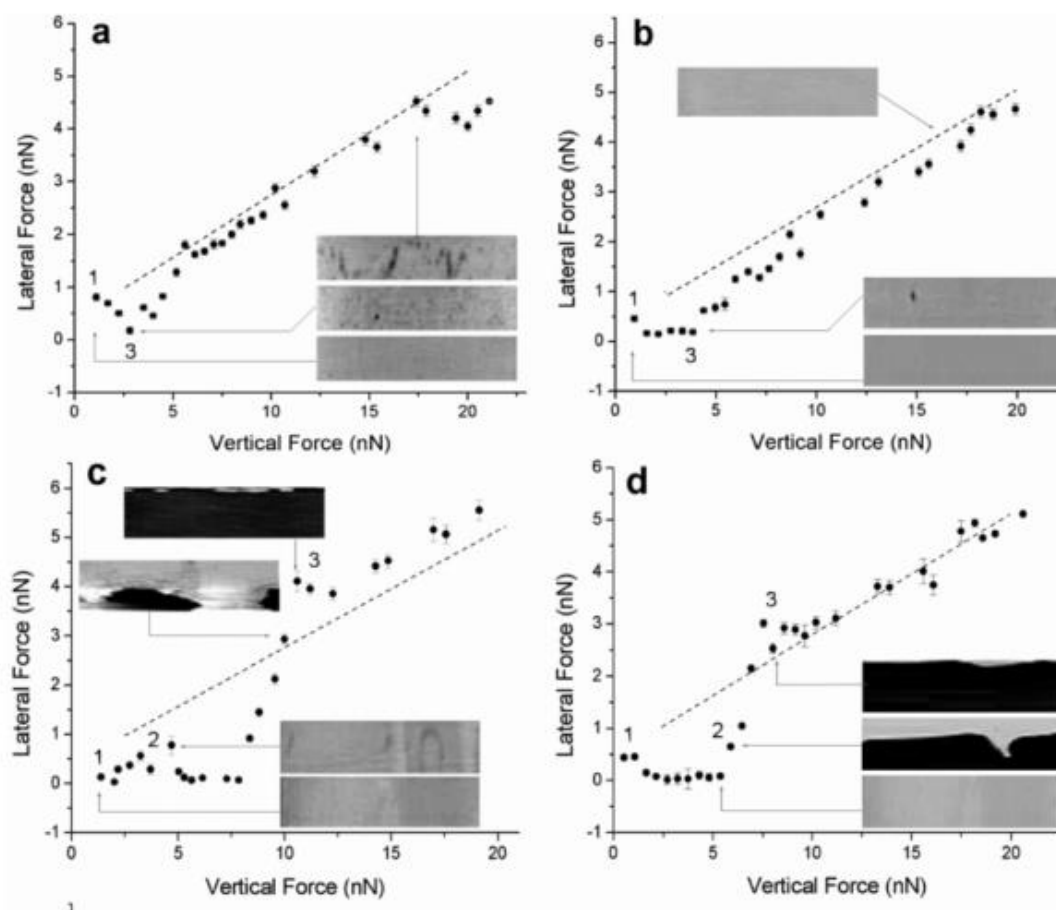


Figure 3.12 Vertical force versus lateral force curves obtained for DiMyristoyl PhosphatidylCholine (DMPC) SLBs characterized by conventional AFM in Tris buffer pH 7 containing NaCl with concentration (a) 0 M, (b) 0.01 M, (c) 0.05 M, and (d) 0.1 M (reproduced from Oncins et al. 2005)

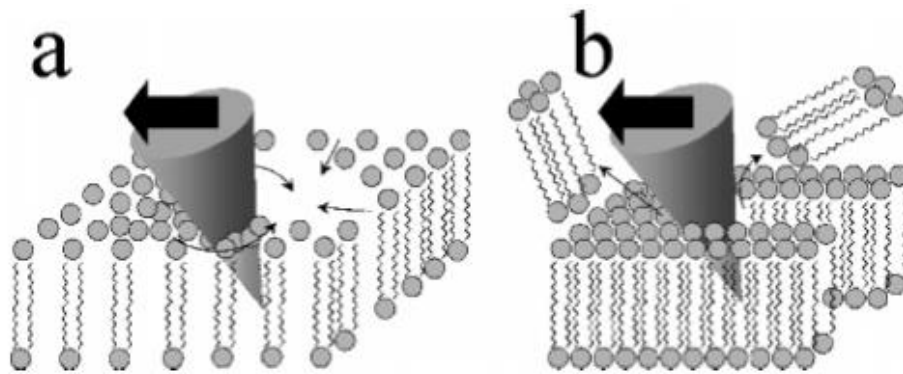


Figure 3.13 Mechanical interaction between tip and lipid bilayer during friction measurement (a) in pure water and (b) in the presence of sodium chloride (reproduced from Oncins et al. 2005)

Another study was done to demonstrate the effect of temperature to the friction force of lipid membranes. Monolayer films of DSPC and DLPC were prepared by the Langmuir-Blodgett technique at the air/water interface and they were characterized at different temperatures by Friction Force Microscopy (FFM). The influence of temperature is more obvious on gel-phase DSPC than on fluid-phase DLPC. Measurement on a binary mixture of DSPC/DLPC (50:50) %mol at room temperature shows that the friction force of DSPC domains is higher than for DLPC as expected (see Figure 3.14). In general, lipid gel phases give better resistance to tangential and normal stresses.

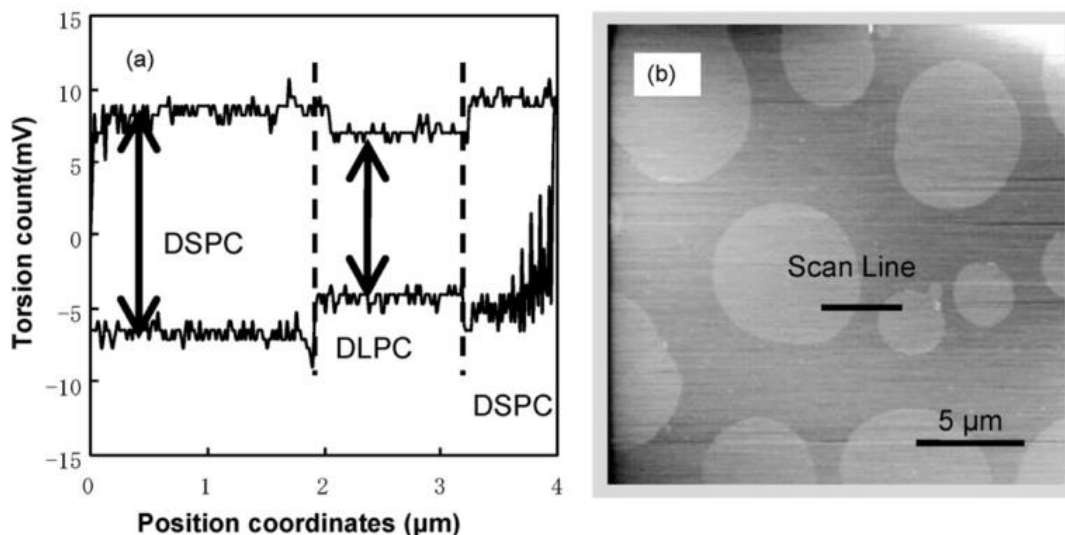


Figure 3.14 (a) Friction forces on mixture of DSPC/DLPC monolayer(50:50) %mol, measured on along the scan line shown in (b) AFM topographic image. DSPC/DLPC monolayer was transferred onto a cleaved mica surface by horizontal lifting method. (reproduced from Oguchi et al.2010)

Further observation on pure monolayers of DSPC and DLPC displays that as the temperature is increasing, the friction force of both the DSPC and the DLPC is decreasing. However, the decrease for DSPC is greater and is finally reaching the same values as DLPC when it passes the phase transition temperature (see Figure 3.15); it is around 70-80°C (theoretically  $T_m$  of DSPC is 58°C). Above the melting point, DSPC undergoes gel-to-liquid phase transition.

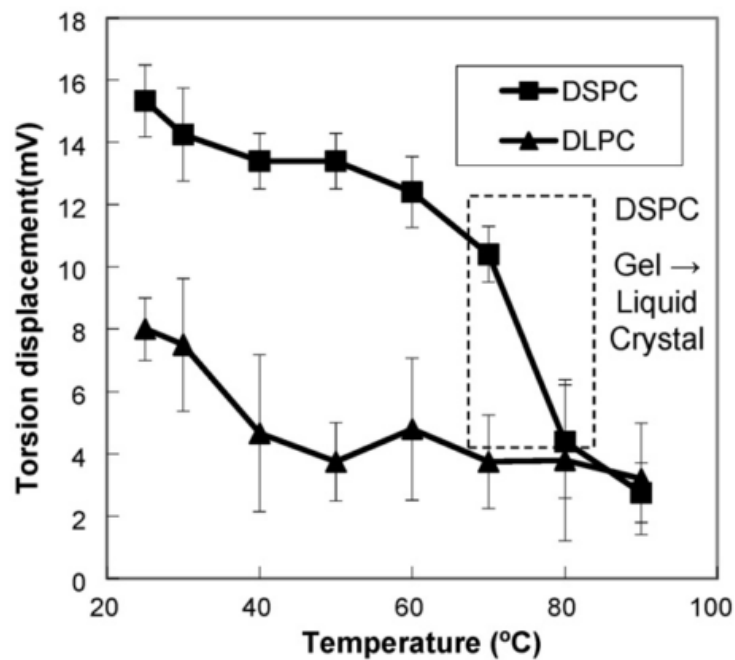


Figure 3.15 Torsion displacements of pure monolayers of DSPC and DLPC as function of temperature. Each monolayer was prepared by horizontal lifting method in which the hydrophobic chains of the lipids face the outer surface of the substrate. (reproduced from Oguchi et al.2010)

It was established that cell membranes are viscoelastic by using magnetic bead microrheometry to locally measure the viscoelastic parameters (friction coefficient and viscosity) of fibroblasts (Bausch et al. 1998). Even though the origin of this viscous flow regime is still unknown since it results from the complex relations among the components of the cell envelope.

Molecular dynamic simulation of surface viscosity for in-plane shear deformations and an intermonolayer friction coefficient for slip between leaflets on a bilayer was done to have better insight into flow behavior of lipid membranes. The term surface viscosity defines the resistance of a lipid bilayer assumed to be a two dimensional fluid, against shear deformation (den Otter & Shkulipa 2007). It is based on the theory of Saffman who relates the surface viscosity with translational diffusion coefficient of a tracer particle confined to a membrane

(Saffman 1976).

$$D = \frac{k_B T}{4\pi\eta_s} \left[ \ln \left( \frac{\eta_s}{R\eta_w} \right) - 0.577 \right] \quad (3.1)$$

$D$  is the lateral diffusion coefficient,  $k_B$  is the Boltzmann constant,  $T$  is temperature (K),  $\eta_s$  is the surface viscosity of the membrane (surface poise),  $\eta_w$  is the surface viscosity of solvent (surface poise), and  $R$  is the radius of the tracer particle. The analysis of membranes' frictional properties is developed into fluid mechanical theory for particle mobility of membrane deposited on solid substrate introduced firstly by Saffman and Delbrück (Saffman & Delbrück 1975).

Prior to molecular dynamic simulation, an experimental study was done using microfluorescence methods to observe the flow behavior (coefficient of viscous friction and coefficient of diffusion) in monolayers and in bilayers (Merkel et al. 1989). Coefficient of viscous friction can be called as surface viscosity and is defined as division product of interfacial shear stress and interfacial slip velocity. Meanwhile, the coefficient of lateral diffusion is derived from half-time of fluorescence recovery. Viscous friction between monolayers depends on surface packing density, substrate-monolayer rigidity, and the degree of interdigitation between lipid tails. Moreover, by measuring the frictional coefficient between the bilayer and the substrate, it is possible to predict the thickness of the water thin film and it was found to be 1-50nm in the case of DMPC and DOPC deposited on glass surface. It highlights the importance of substrate properties onto membranes' properties. Thus it is predicted that large viscous drag can be provoked by friction between the substrate and the proximal leaflet of a SLB. This phenomenon is related to the coupling between the plasma membrane bilayers and the subsurface cytoskeleton in living cells.

### 3.5 Conclusion

Cell membrane is component of the cell that protects the interior of the cell from the environment. It has important role in many cellular functions, such as ionic exchange (Minami et al. 1991), signal transduction (Simons & Ikonen 1997), drug transport, tissue development (Picas et al. 2012) and so on. The main composition of cell membrane is lipid molecules which

have hydrophilic headgroup and hydrophobic tail group. In order to facilitate the study of cellular processes involving cell membranes, several membrane models are developed: liposomes, free standing membranes, and supported lipid bilayers (SLBs). Each has strengths and weaknesses thus the choice of membrane model is depending on the focus of study and the instrument available. Measurement of membranes' mechanical properties has been an interesting topic as they reflect the structure of the membranes and provide information about cellular processes. SLBs are widely used to study the topology and mechanical properties of membranes by atomic force microscopy (AFM). By now, there have been many evidences of the factors influencing mechanical properties of lipid bilayers. Temperature (Garcia-Manyes et al. 2005b), solid support (Seeger et al. 2010), composition of membranes (Shimshick & McConnell 1973) and medium (Garcia-Manyes et al. 2005a) have been reported as factors affecting membranes' properties. Thus, by collecting such information, it will help us to unravel the complexity of biological membranes.

## Materials and Methods

In this chapter we describe the materials and methods used during this PhD study. We listed all samples used for calibrations experiments. All surface samples are subjected to pre-treatment process to have flat and clean surface that are proper for AFM measurement and/or deposition of another molecules. The technique of lipid synthesis is explained in detail. Besides, we also describe the characterization method used, including contact angle measurement, AFM imaging, and force measurement by circular mode AFM. The calibration procedure for AFM probe was also explained to obtain spring constant of the cantilever.



# Chapter 4

## Materials and Methods

### 4.1 Materials

#### 4.1.1 Lipid

All type of lipid used in this study were in pure condition (99%) and were used without further purification. They were purchased from Sigma Aldrich (St. Louis, MO). The lipids are in form of powder, were dissolved in chloroform with concentration of 5 mM and then were stocked at -20°C prior of membrane synthesis. The chemical structure of the lipids used can be seen at Figure 4.1 and the melting point and molecular weight for each lipid are listed in Table 4.1. Other chemicals such as ethanol, isopropanol, dichloromethane, chloroform were obtained from VWR International (France). MillQ water was used during experiment.

Table 4.1 Properties of lipid used in this study

Lipid	Abbreviation	a <sup>1</sup>	b <sup>2</sup>	Melting temp (°C) <sup>3</sup>	Molecular weight <sup>4</sup>
DiLauryloyl PhosphatidylCholine	DLPC	12	0	-2	621.83
DiMyristoyl PhosphatidylCholine	DMPC	14	0	24	677.93
DiPalmitoyl PhosphatidylCholine	DPPC	16	0	41	734.04
DiOleoyl PhosphatidylCholine	DOPC	18	1	-17	786.11

<sup>1</sup> Number of carbon in each tail chain of lipid

<sup>2</sup> Number of double-bond in each tail chain of lipid

<sup>3</sup> Data acquired from Avanti Lipid

<sup>4</sup> Data acquired from Sigma Aldrich

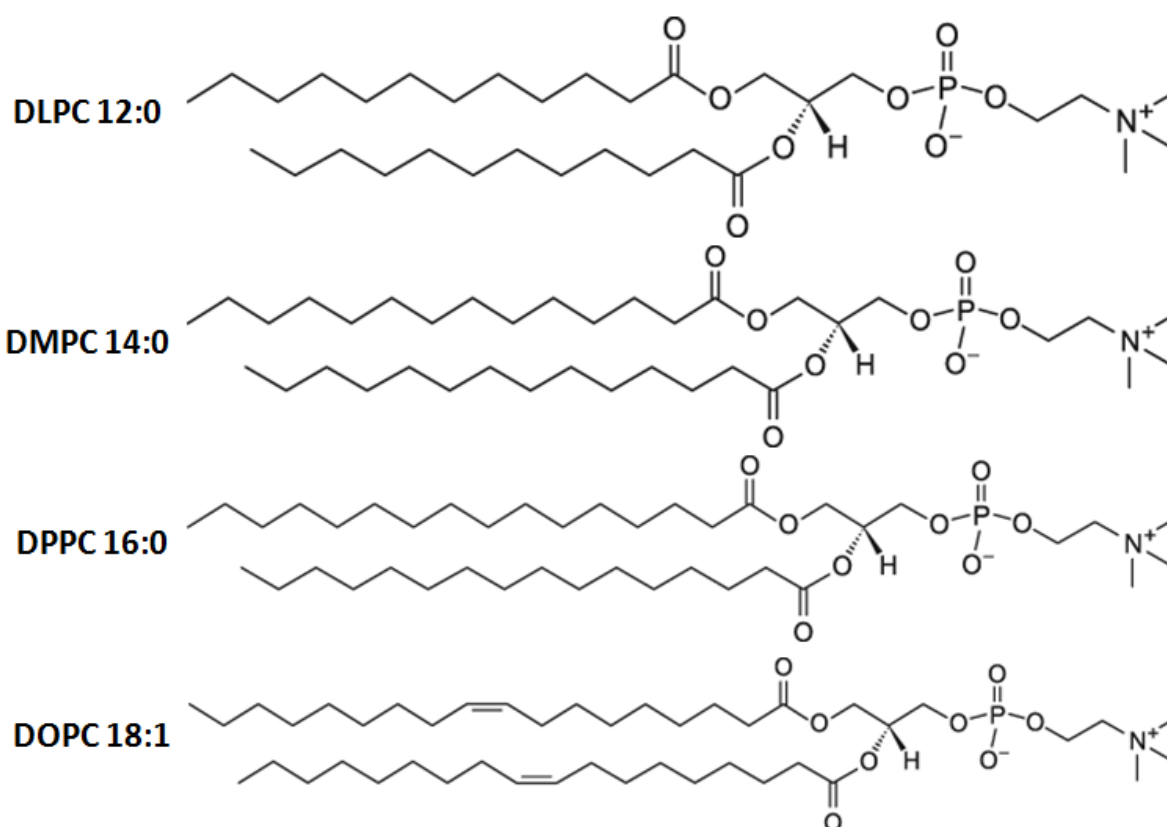


Figure 4.1 Chemical structure of lipids used in this study: DiLauryloyl PhosphatidylCholine (DLPC) 12:0, DiMyristoyl PhosphatidylCholine (DMPC) 14:0, DiPalmitoyl PhosphatidylCholine (DPPC) 16:0, and DiOleoyl PhosphatidylCholine (DOPC) 18 :1 (reproduced from [www.avantilipids.com](http://www.avantilipids.com))

### 4.1.2 Mica surfaces

Multiple layers flat mica surfaces  $\text{KAl}_2(\text{OH})_2\text{AlSi}_3\text{O}_{10}$ , were cut into circle shape with diameter of 5 mm. Each layer has thickness of 1 nm. Epotek 377 (Polytec, France) was used to glue mica sheet on steel disc (Agar Scientific, England) to maintain stable position on AFM sample stage. Before use, the surface is freshly cleaved with the help of adhesive tape to produce clean and negatively charged surfaces (El Kirat *et al.*, 2005).

### 4.1.3 Gallium Arsenide (GaAs)

Surface of gallium arsenide (GaAs) was prepared for calibration of piezoelectric scanner. GaAs surface was chosen because of its softness at room temperature (Wasmer *et al.*, 2008) and it is sensitive to wear and/or plastic deformation after undergoing mechanical contact. The sample was cut into size that can fit with the scanner head and was attached onto

steel disk using double-sided tape.

#### ***4.1.4 Thiol-functionalized gold layer surface***

In order to study the effect of sliding velocity to adhesion force on hydrophobic and hydrophilic surfaces, we functionalized the gold layer surface with thiol molecules. First of all, glass surface was cut into the size of 5  $\mu\text{m}$  x 5  $\mu\text{m}$  so that it can fit on the AFM scanner head. Then, it underwent cleaning routing with ethanol and dichloromethane. After drying the sample, it was put in thermal evaporator Edwards E306A with pressure under vacuum of  $2 \times 10^{-6}$  mbar. The physical vapor disposition process resulted thin layer of chrome with 2 nm thickness and 47 nm thick of gold layer on top of it. The velocity of deposition was 1 nm/s.

After the deposition of gold layer, the sample was cleaned with UV ozone cleaner for 15 minutes then was rinsed with water, ethanol, and dichloromethane. Separately, 1 mM of 1-Undecanethiol ( $\text{C}_{10}\text{CH}_3$  98%) and 11 Mercapto-1-undecanol ( $\text{C}_{11}\text{OH}$  97%) from Sigma Aldrich were prepared in ethanol respectively.  $\text{C}_{10}\text{CH}_3$  has alkaline group at the end of its chain so that it can generate hydrophobic surfaces. In contrary,  $\text{C}_{11}\text{OH}$  has alcohol group at the end of its chain to yield hydrophilic surfaces. The clean glass sample was then immersed overnight in either  $\text{C}_{10}\text{CH}_3$  or  $\text{C}_{11}\text{OH}$  solution. Later, it was rinsed 0.1 M NaOH continued with water and ethanol. The sample should be dried before examination.

#### ***4.1.5 Scratched Surfaces***

For lateral force calibration, we developed a calibration procedure from wedge technique (Ogletree, Carpick and Salmeron, 1996) that is based on known slope of surface. Therefore, several adapted samples were prepared and tested: gold layer, diamond layer, aluminum, polycarbonate, glass (cover slip), and pure silica; to select the proper sample that can fit our proposed-technique of calibration. Gold and diamond layer were prepared by depositing gold and diamond onto clean glass surface through physical vapor deposition (PVD) procedure (see section 4.1.4). Before deposition, flat glass plate is cut into size which is fitted on steel disk ( $\varnothing$  15mm), approximately 5 $\mu\text{m}$  x 5 $\mu\text{m}$ . Gold and diamond layer were tested because they show obvious local variation of topography.

The other surfaces were prepared by using nano-indentation instrument. Before, all surfaces were running through liquid cleaning routines by rinsing three times with water and ethanol and were air-dried. The cleaning procedure was finished by using UV ozone cleaner for 15 minutes. Each surface was scratched by nano-indentor G200 Agitech with Berkovich indenter which is three shapes pyramid face forward to make a triangular scratch whose constant slope between ascending and descending part, as illustrated on Figure 4.2. To assure a stable position during calibration, it is then attached on steel disk for AFM imaging by using epoxy glue, polymerized at  $T=140^{\circ}\text{C}$ . Before calibration, sample has had cleaned with flowing water, alcohol, and finishing with UV ozone cleaner for 30 minutes. For examination in dry condition, sample can be used directly. While in liquid condition, millQ water drop is put on top the sample.

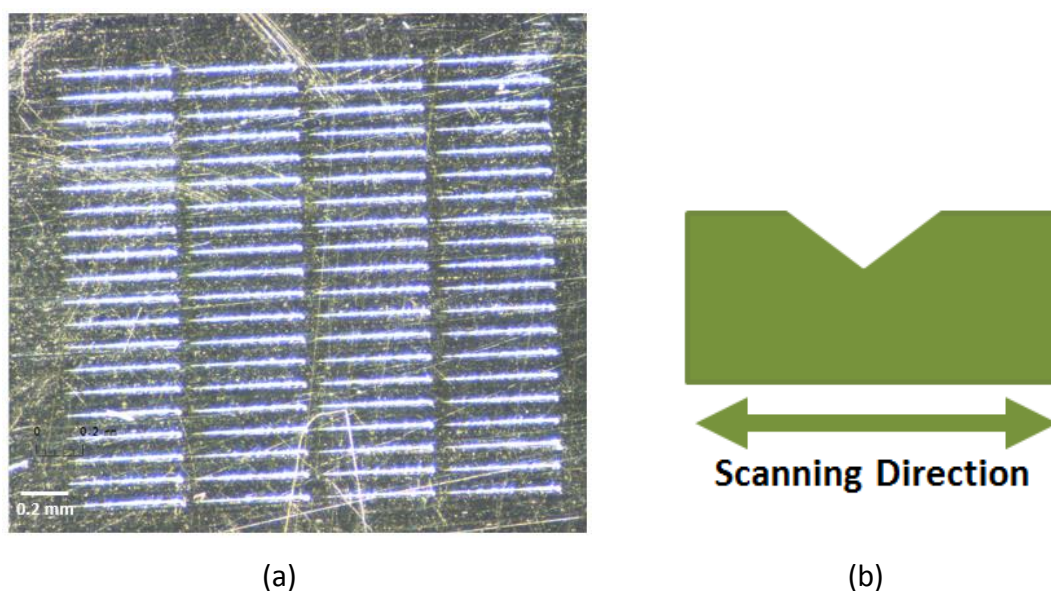


Figure 4.2 (a) Image of scratched surface taken by optical microscope (the scale bar refers to 0.2 mm) and (b) illustration of side view of scratch making on flat glass making (arrow shows the scanning direction)

The four surfaces mentioned above: mica, gallium arsenide (GaAs), thiol-functionalized gold layer, and scratched surfaces; are used in calibration processes. Since we require several steps of calibration, each sample surface is dedicated to specific procedure. Mica surfaces are used in normal force calibration to obtain spring constant of AFM cantilever. GaAs surfaces are used in calibration of AFM piezoelectric scanner to verify its linearity in regards to circular

displacement. Meanwhile, gold layer and scratched surfaces are used in lateral force calibration to acquire the constant that allow quantification of friction forces.

#### ***4.1.6 Buffer solution***

Buffered medium was selected in order to mimic physiological condition. The general buffer solution used in this study is 10 mM Tris-NaCl buffer containing 150 mM NaCl. It was prepared in water millQ and has pH of 7.4. To study the effect of cations in the liquid medium, different salts were used to replace NaCl. LiCl and KCl were added in Tris buffer instead of NaCl. The pH adjusted for all buffer solution is 7.4.

## **4.2 Methods**

### ***4.2.1 Preparation of lipid bilayers***

Pure SLBs was prepared based on vesicle fusion method (El Kirat, Morandat and Dufrière, 2010) with final concentration of 1 mM. This preparation method is chosen because of its simplicity and good reproducibility. Upon the synthesis, all lipids were dissolved in chloroform with concentration of 5mM and stored at -20°C. First, some amount of lipid suspension was put onto separated flask then was evaporated by using nitrogen gun and was desiccated under vacuum for 2 hours to result lipid thin layer. To study the effect of lipid composition, a binary mixture of DOPC/DPPC 50:50 %mol was prepared by mixing both lipids.

10 mM Tris buffered saline (TBS) pH 7.2 containing 150 mM NaCl and 3 mM CaCl<sub>2</sub>, was added to storage with lipid thin layer in order to obtain multilamellar vesicles (MLVs) with final concentration of 1 mM. It is necessary to vortex the sample to detach the lipid layer from the bottom of storage and re-assembly into MLVs. Small unilamellar vesicles (SUVs) were obtained by sonicating using a 500 W, 13 mm diameter probe sonicator (Fisher Bioblock Scientific, France) for 3 cycles with 2.5 minutes each. 35 % of power was used to prevent over heating on sample. Lipid suspension is placed on ice bath during sonication to avoid temperature increase. Then, it was filtered on 0.2 µm Acrodisc® (Pall Life Science, USA) to remove titanium particles.

Separately, glass surfaces were prepared to be lipid substrate. Epotek 377 (Polytec,

France) was used to glue glass on steel disc (Agar Scientific, England). Before using, glass surface was wiped by sulphuric acid and was rinsed with water and ethanol bath. Then, it was dried on the air and was put in UV ozone cleaner for 15 minutes to avoid any organic component left on the surface. Later, A 150  $\mu\text{L}$  SUVs suspension was deposited onto freshly cleaned glass surface. Lipid fusion was done at 60°C for 1 hour (70°C and 1.5 hours for DSPC pure SLBs). Then, sample was rinsed with 3 mL of 10 mM Tris-HCl buffer pH 7.2 containing NaCl 150 mM and slowly cooled to room temperature. Samples were incubated overnight at 21°C to reach thermodynamic equilibrium of SLBs before characterization.

### ***4.2.2 Measurement of contact angle***

Measurement of contact angle is referred to the ability of liquid to spread out on the surface. It is very useful in wettability testing, stability of surface films, and detergency (Israelachvili, 2013). Among variety of measurement technique, we used direct static Sessile drop method (McClements, 1999). In this method, a drop of liquid was deposited on the solid surface of interest. Therefore, three phases system occurs: solid, liquid, and gas (see Figure 4.3).

Contact angle  $\theta$  is the angle of tangent drawn at the point where the liquid contact the surface. This angle is measured from the side of the droplet. The drop's profile depends on physic-chemical properties of the solid force, adhesion forces at the solid-liquid interface, and the cohesion forces of the liquid. Any change will affect the contact angle value revealing the surface state and the different forces occurred are linked together according to Young's equation (equation 5.1) (Lotfi, Nejib and Naceur, 2013). Thus, the profile of the droplet can be predicted by knowing the contact angle: smaller contact angle gives tendency for liquid to spread over the surface (McClements, 1999).

$$\cos \theta = \frac{\gamma_{SG} - \gamma_{SL}}{\gamma_{LG}} \quad (4.1)$$

where  $\gamma_{SG}, \gamma_{SL}, \gamma_{LG}$  are referred to surface tension at the interface of solid-gas, solid-liquid, and liquid-gas respectively.

Measurement of contact angle was done by depositing 5  $\mu\text{L}$  of water or diiodomethane onto the surface sample by using a syringe. Liquid droplet on the surface was observed by

using the instrument equipped with a computer (DSA-10, kruss, GmbH, Hamburg) at room temperature (21 – 24°C). Contact angle was determined from digital image acquired by camera which is connected to the computer. Associated software allowed the digitations the droplet profile through image treatment. By applying the Young's equation and interpolation method, contact angle can be easily determined.

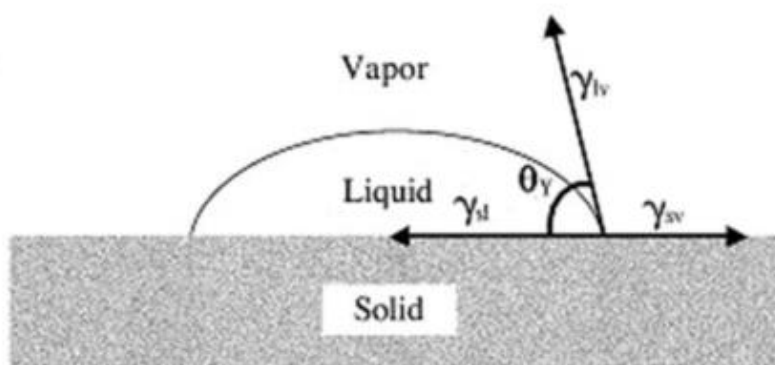


Figure 4.3 Force balance of a droplet at a solid-gas interface (reproduced from Lotfi, Nejib, and Naceur, 2013)

### 4.2.3 Morphological characterization by AFM

Supported lipid bilayers were characterized by using a commercial AFM (Nanoscope III Multimode AFM, Veeco Metrology, Santa Barbara, CA) equipped with a J scanner (125  $\mu\text{m}$  x 125  $\mu\text{m}$  x 5  $\mu\text{m}$ ). Morphological images were acquired by using oxide-sharpened microfabricated  $\text{Si}_3\text{N}_4$  cantilevers (Microlevers, Veeco, Metrology LLC, Santa Barbara, CA) with spring theoretical spring constant of 0.01-0.03 N/m. The nominal spring constant of each cantilever was calibrated for normal and lateral force. The curvature radius of silicon nitride was  $\sim 20\text{nm}$ . Images were recorded with minimal applied force (<200 pN) and resolution of 256 x 256 pixels in contact mode at room temperature of 21°C. In this document, all AFM topography images shown are flattened raw data.

#### ***4.2.4 Normal force calibration***

Normal force calibration is required to obtain the spring constant or the stiffness of the cantilever. Spring constant and sensitivity of normal deflection are necessary to quantify the normal force signal in force measurement of AFM. The cantilever is subjected to normal and torque force causing normal and torsional deflection. There are various methods to calculate the normal spring constant with 90 % accuracy, such as shift in resonant frequency with added mass and static deflection under load. Burnham et al (Burnham *et al.*, 2003) did a comparison study of different normal calibration technique based on each uncertainties, advantages, and disadvantages.

It was Cleveland et al (Cleveland *et al.*, 1993) who is the research team that investigates the normal force calibration. Their method is based on added mass method. Resonance frequency of the cantilever is varied as function of added end mass with mass resolution to be 0.5 ng (nanograms). The advantage of this method is that this method is universally acceptable, regardless of geometry or material properties of the cantilever. In the contrary with Cleveland's method, Sader et al (Sader, Chon and Mulvaney, 1999) determined the spring constant based on unloaded resonance technique. Stiffness of the tip relies solely on the measurement of the resonant frequency quality factor on the cantilever in air, and also information about tip's dimension. This technique is nondestructive, noninvasive and allows rapid determination of normal spring constant of rectangular cantilever. Both Cleveland and Sader calibration technique can be extended to calibrate the torsion of the cantilever to quantify the friction force between tip and sample surface (Green *et al.*, 2004).

Besides, spring constant of AFM tip can be determined by measuring the motion of a tip above a sample. If the tip is far from the sample, its motion is solely due to thermal fluctuations (Hutter and Bechhoefer, 1993). It evaluates the power spectrum of thermal noise. However, this technique neglects the mass of the tip which may comprise 50% or more the effective mass of the cantilever (Allen, Sumali and Penegor, 2009). Thus the probe tip can have significant effect on the spring constant and introduce error in calibration as much as 10-20 %.

In our study we prefer the thermal method as proposed by Hutter and Bechhoefer (Hutter and Bechhoefer, 1993). One of its strength is that this method is based on standard physics and so it is independent of material properties and geometry of cantilever.



## 4.2.5 Circular mode AFM

### A. Basic principle of circular mode AFM

Following the basic principle of atomic force microscopy, the basic of circular mode lies onto three main components: AFM probe whose direct contact to sample surface, photodiode detector that captures the changes of reflected laser's angle due to cantilever's deflection, and piezoelectric scanner that maintains constant force through feedback loop. The movement of scanner is due to voltage application that allows scanner to expand or to compress. The scanner has five electrodes in a hollow piezoelectric tube (see Figure 4.4): X, Y, and Z. Each electrode has responsibility for the movement in each direction axis. X and Y define the horizontal planar axes, while Z defines the vertical axis. The opposite voltages are applied to the  $-X$  and  $-Y$  electrodes.

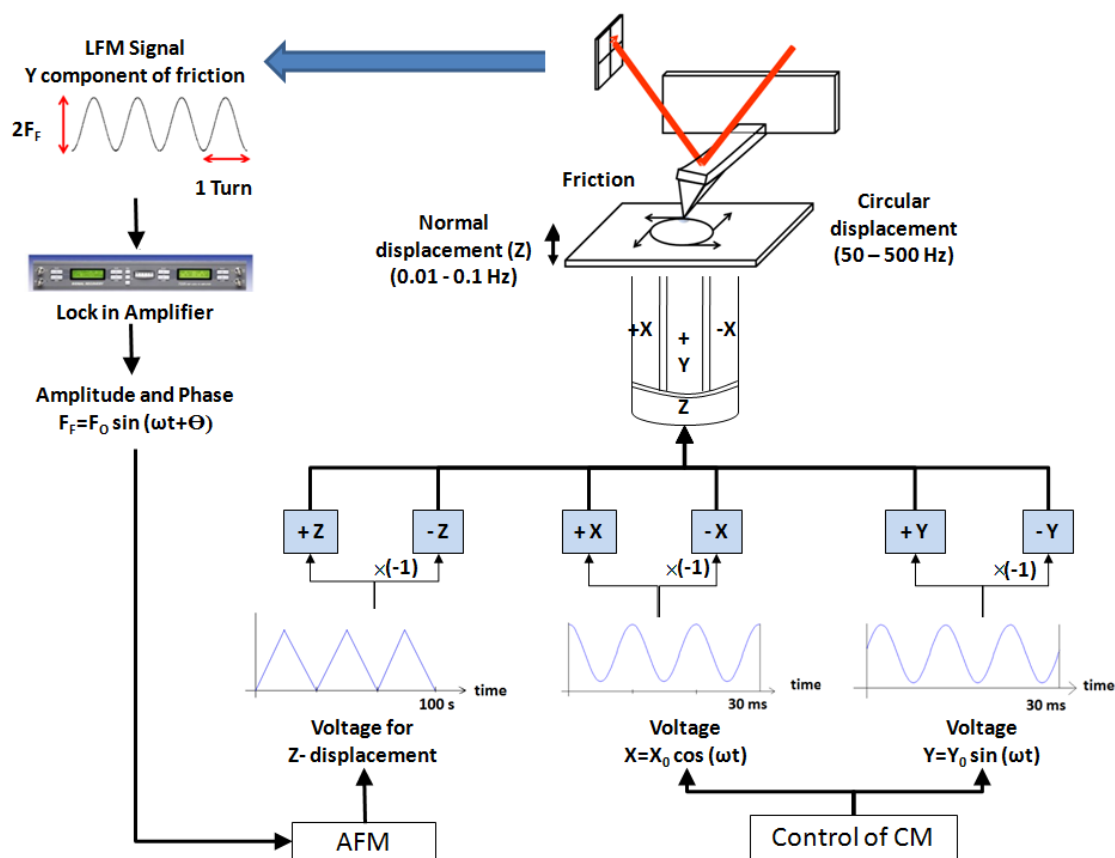


Figure 4.4 Scheme of circular mode AFM

In order to generate circular displacement of the scanner, several additional accessories are necessary to complete the configuration of AFM. There are Signal Access Module (SAM),

Digital to Analog Converter (DAC) device and Lock in Amplifier (LiA). Combination of LiA and DAC device is used to generate two sinusoidal voltage signals whose phase shifted by  $\pi/2$  to be applied to horizontal (X and Y axes) electrodes (Nasrallah, Mazeran and Noël, 2011). The voltages applied are defines as:

$$V_X = V \cos \omega t \quad (4.2)$$

$$V_Y = V \sin \omega t \quad (4.3)$$

$$V_{-X} = -V_X \quad (4.4)$$

$$V_{-Y} = -V_Y \quad (4.5)$$

$V$  is the voltage half-amplitude and  $\omega$  is the angular frequency. The instruction of voltage generation is programmed digitally in our software. LiA has a role in signal conditioning to limit the noise so the signals. The output analog signals are then sent to SAM box which allows us to manipulate the internal AFM signals. When the toggles are switched to “input”, the AFM signals are interrupted by external commands (application of sinusoidal voltage signals). Therefore, the scanner can move in circular pattern instead of raster scan pattern.

In our laboratory, we combined AFM with force spectroscopy for force measurement. In real experiment piezoelectric scanner displace in XY place to create circular displacement. The tip slides on the sample surface and generate friction force as surface response. At the same time, it moves vertically to gradually increase the normal force for indentation. Thus, the movement of scanner looks like a spring. With this configuration, the friction and normal force measurement are done simultaneously (see Figure 4.5).

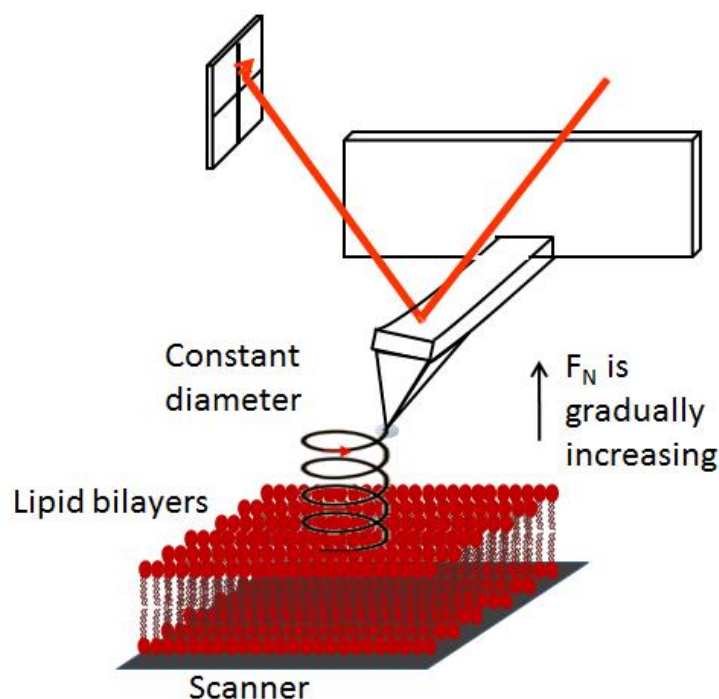


Figure 4.5 Schematic of circular mode AFM for characterization of lipid bilayers

## B. Advantages of circular mode AFM

Recently developed Circular Mode AFM offers many advantages. First, it provides constant and continuous sliding velocity (Nasrallah, Mazeran and Noël, 2011). Modification of scanning pattern from raster scan to circular displacement allows AFM tip to avoid rest period. In the case of conventional AFM, the tip goes back and forth causing moment of pause due to change of scanning direction. Additionally, it also causes inconstant velocity due to acceleration and deceleration. This condition is not favorable for friction measurement. Therefore, the invention of CM-AFM can solve this problem by performing measurements in a stationary state.

Second, CM-AFM increases the limit of sliding velocity in friction measurement. Usually the maximum sliding velocity of conventional AFM is up to  $100 \mu\text{m/s}$  while with CM-AFM it can reach  $100,000 \mu\text{m/s}$ . Actually, the limit of sliding velocity is highly dependent on the capacity and characteristic of piezoelectric scanner. In our condition of experiment, we used J-type scanner with resonance frequency of  $950 \text{ Hz}$  (discussed on the latter section) and maximum scan range of  $75 \mu\text{m}$ . However, our configuration has limited the voltage amplitude to  $10 \text{ Volt}$ . Thus, the technical maximum sliding velocity is  $11.424 \mu\text{m/s}$  with circular displacement as big as approximately  $450 \text{ nm}$  and frequency of  $400 \text{ Hz}$ . More detail

explanation about the calculation is given in sub chapter 5.1.1. Even though the size of the circle is much smaller than the maximum scan range, the sliding velocity has increased almost two orders of magnitude than the ones obtained with conventional AFM (Nasrallah, Mazeran and Noël, 2011). However, a proper calibration of scanner's linearity is needed to verify the safe range of frequency and amplitude that is adapted to our instrument.

Third, CM-AFM simplifies the calibration of piezoelectric scanner. In conventional AFM, the scanner has two axes called fast and slow axes. Slow axes are perpendicular to the scanning direction and are stacked to form an image. Fast axis is parallel to scanning direction. Due to non-linearity and creep of the piezo-actuator, the voltages applied on both directions of scanner follow a complex equation to generate a voltage function that conducts the linear scan (Elings and Gurley, 1991). In contrary, calibration of scanner in circular mode eliminates the differential between low and fast scanning directions. It is supported by the fact that voltage sent to the piezo-actuator is sinusoidal in both X and Y directions. Practically, the calibration of piezoelectric scanner can be done by measuring circular tracks resulted from wear of the surface obtained with CM-AFM at various voltage amplitude and voltage frequency. This method relatively simple, fast, and reliable and will be explained in the next section. This method is adapted when the scanner tube is used at high frequencies. The drawback of this method is that it can damage both tip and surface.

Fourth, CM-AFM is possible to be combined with classical mode to measure simultaneously friction, adhesion, and normal force. Thus, more mechanical information about the surfaces can be acquired in shorter time. The last but not least, CM-AFM widens the access of surface characterization for surfaces who need high velocity displacement or require stationary state measurement (constant sliding velocity).

### **C. Mechanical Systems**

For our experiment, the lipid bilayers are deposited on the solid substrate and have contact with AFM tip during friction measurement, as illustrated in Figure 4.6. Based on this mechanical systems, there are interfaces: AFM tip – lipid headgroups interface, lipid tails – lipid tails interface, and lipid headgroups – solid substrate interface. The lateral displacement of AFM tip during friction measurement can cause shearing in the lipid bilayers. However, at this moment, there are not clear explanation about the characteristic of friction at each interface. Two possibilities are remained, whether it has solid-like friction characteristic or

viscous friction characteristic.

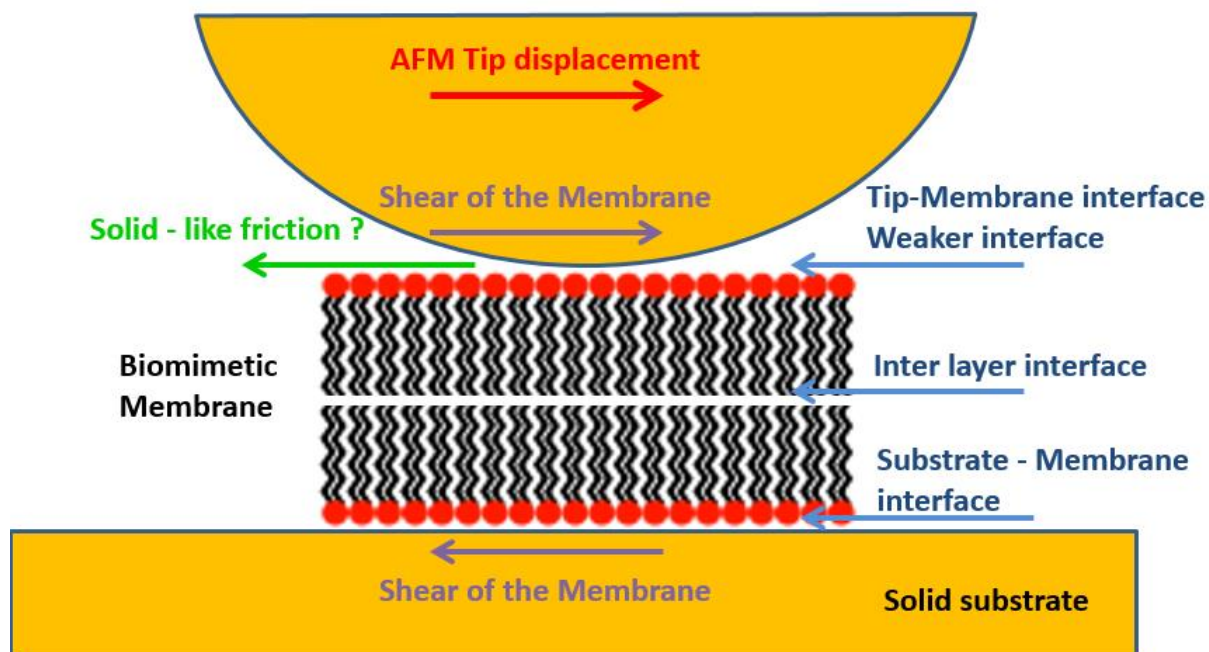


Figure 4.6 Illustration of mechanical systems between AFM tip, lipid membranes, and solid substrate during friction measurement

### C. System components of circular mode AFM

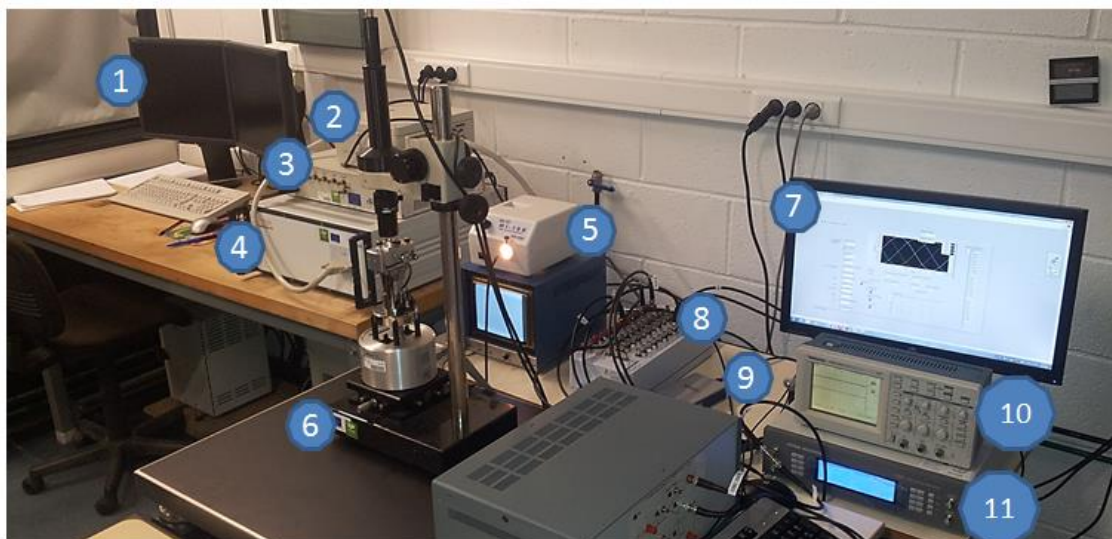


Figure 4.7 Components of circular mode AFM in our laboratory

We present all the components of our circular mode AFM as shown in Figure 4.7. There are:

1. Screen and computer to control the AFM through software *Nanoscope*
2. Quadrex
3. Picoforce
4. Nanoscope controller
5. Screen and light source for microscopy to monitor the real-time condition of the tip and the surface
6. Atomic Force Microscopy set-up
7. Screen and computer to control circular movement by using self-developed program in LabView
8. Signal Access Module
9. Data acquisition device
10. Oscillator
11. Lock in Amplifier

Each component has specific function in order to have complete run of circular mode AFM. In general, it consist the same components as conventional AFM except there is addition of several accessories (components number 8 – 10). All components are connected by using cable. The scheme of the cable network is shown in Figure 4.8.

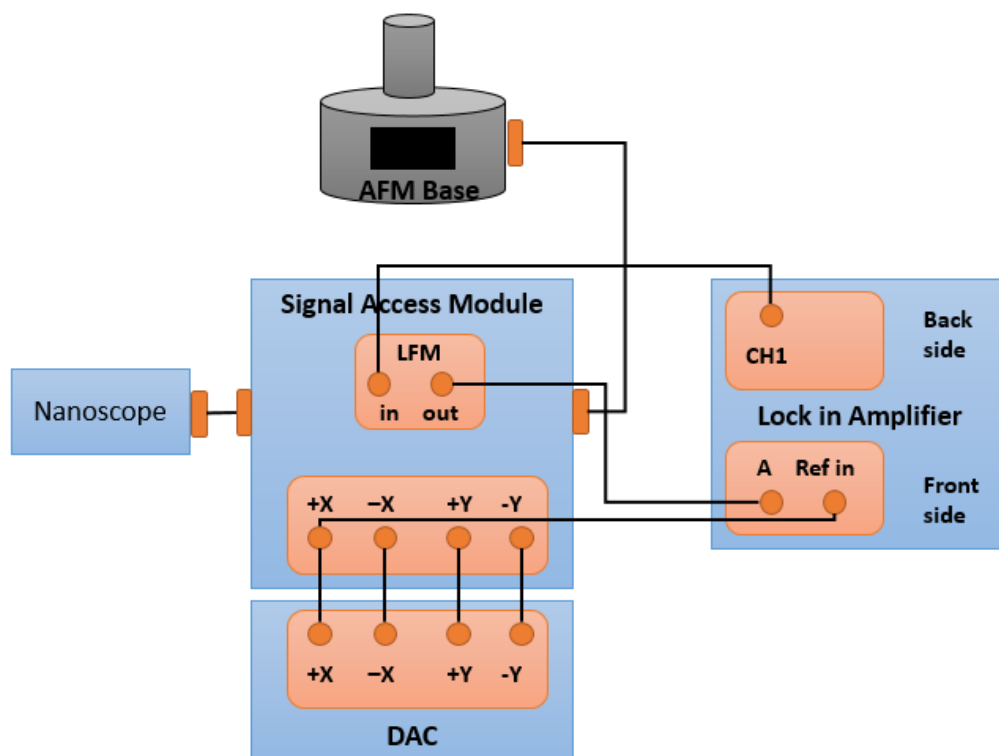


Figure 4.8 Scheme of cable connection between components of AFM in our laboratory

## D. Signal Access Module

Signal access module (SAM) is an optional attachment to the AFM that allows user to gain access to internal AFM signals. Therefore, for normal experimental condition, AFM can work well without SAM. Besides, external signals can be injected to the AFM for controlling or processing the signals by connecting the signals sources through SAM box. BNC connectors interface are used to connect SAM with other component in circular mode AFM configuration. By switching the toggle, it is possible to switch each line separately between a normal, uninterrupted configuration, and an external input signal. Output BNC connectors allow monitoring of both conditioned and uninterrupted signals for use in experiment.

Signal connectors are classified into five groups and are positioned on top and two sides of the box.

1. Low voltage inputs to nanoscope controller (data signals) – on top panel
2. Low voltage outputs from nanoscope controller (control signals) – on top panel
3. High voltage outputs from nanoscope controller (piezo drive signals) – on top panel
4. Low voltage inputs to application module – on side 1 panel
5. Low voltage outputs from application module – on side 1 panel

On top panel, there are individual pairs of input and output signal connectors. In the last row (high voltage outputs), X and Y refer to scan position while Z refers to probe position with respect to the sample plane (Figure 4.9). This row of connectors is used to manipulate the signal resulted from piezoelectric movement due to tip-surface interaction. For example, it is useful to retrieve the friction data of a sample. Additionally, when all toggles are switched to “output”, AFM signals are in the normal position or uninterrupted operation (no signal manipulation). On side 2 panel, there are connectors to connect SAM to AFM set up and nanoscope controller.

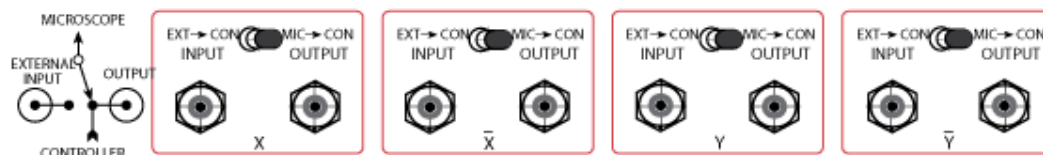


Figure 4.9 High voltage outputs panel on signal access module (SAM)

## **E. Digital to Analog Converter (DAC)**

In data acquisition system, there are three main components: a sensor, DAQ measurement device and a computer whose programmable software. In our case, piezoelectric scanner acts as sensor to monitor AFM tip-surface interaction during measurement. DAQ device is the interface between AFM signal and computer. It has roles for signal conditioning, and analog-to-digital converter (ADC). AFM signals passed from SAM to DAQ device are conditioned by lock in amplifier that include amplification, filtering, and isolation of signals because they have a lot of unspecific frequency noises, so they are not measurable. Harmonic wave signals as the output of lock in amplifier become the input to DAQ device. Then, DAQ device acts as analog-to-digital converter to convert analog signals from sensors to digital in order to be manipulated by computer software.

ADC is a chip that provides a digital representation of an analog signal at an instant in time. Then, computer bus is the interface of communication between DAQ device and computer to pass instruction and measured data. Using our self-developed software in LabView, the converted signals are manipulated. Inversely, it is possible to send digital instruction from software to manipulate the sensor (the movement of piezoelectric scanner). In this case, DAQ device acts as digital-to-analog converter.

## **F. Lock in Amplifiers**

Lock in amplifiers or phase sensitive amplifiers are used to detect and measure AC signals, down to a few nano volts. It uses a phase sensitive detection method to single out the component of the signal at specific frequency and phase even though the signal has signals whose other frequencies. The components of signals at other frequencies are rejected and neglected from the measurement. With using amplifier with a phase-sensitive detector (lock in amplifier), it can detect signal at high frequency (10 kHz) with a very narrow bandwidth (up to 0.01 Hz). Thus it decreases the signal-to-noise ratio and an accurate measurement is possible. During experiment, signals are generated at fixed frequency (from an oscillator or function generator). Lock in amplifiers can detect it at reference frequency.

There are two types of lock in amplifier: analog and digital. The role of phase sensitive detector is different among the two. In our case, we use digital lock in amplifier which multiplies the signal with the reference sine waves digitally; phase sensitive detector acts as



linear multipliers. The signal is multiplied by a single reference sine wave, resulting harmonic signal.

The advantages of lock in amplifiers are their ability to narrow the bandwidth and to adjust important parameters, such as time constant and sensitivity. Time constant defines the frequency to filter the signal. The output from phase sensitive detector passes through low pas filter. By increasing the time constant, the output becomes more steady and easier to measure. Besides, the sensitivity parameter can be used to maintain the output between 30 % and 100 % of the full scale.

### **4.3 Conclusion**

All of the materials used and methods applied in this PhD study have been mentioned and explained in this chapter. Proper sample handling and measurement protocol are necessary to assure reproducibility of the results. Moreover, we used lipid membranes as samples that are very sensitive to any chemical and physical changes in its surrounding. Besides, it is important to be more careful when working at the nanoscale because it is not visible with naked eye. In general, this PhD study can be divided into two parts: optimization of CM-AFM in liquid medium, including calibration of piezo and AFM cantilever; and nanomechanical measurement on lipid membranes, once the CM-AFM is ready to use. In short, this chapter becomes our guideline to do the experiment in laboratory.

## Calibration of the Circular Mode AFM

This chapter is exclusively dedicated to discuss the implementation and adaptation of circular mode AFM for measurement in liquid medium. In circular mode AFM, the displacement pattern of scanner is modified. Thus, the aim of this chapter is to establish protocols of calibration of lateral forces and piezoelectric scanner at the condition of high sliding velocity. Given that AFM employs harmonic signal to result circular displacement, the experimental condition is different with conventional AFM. In addition, we propose a new method adapted from “wedge” method to calibrate the lateral force of the cantilever. Several materials were tested to select the proper sample for lateral force calibration

# Chapter 5

## Calibration of Circular Mode AFM

### 5.1 Introduction

There are two elements that have to be calibrated before doing measurement with CM-AFM: the AFM probe and the piezoelectric scanner. Normal force calibration is done by applying the established thermal method (Hutter & Bechhoefer 1993) to obtain the spring constant of AFM cantilever which is necessary to quantify its deflection. This method has been explained in the previous chapter (see section 4.2.4). In order to do friction measurement, lateral force calibration is also needed to quantify the torsion of AFM cantilever. We propose a new method adapted from wedge method (D F Ogletree et al. 1996) which is the easiest among the existing methods of lateral force calibration with the same accuracy. Both normal and lateral force calibration are done by conventional AFM.

Besides cantilever's calibration, the AFM scanner should be also calibrated. Circular displacement in CM-AFM is generated by injecting the harmonic voltage in X and Y axis of the piezo electrode. Consequently, it has constant, continuous, and high sliding velocity. Moreover, CM-AFM is only working with single frequency of solicitation that is a few hundred Hertz. Those characteristics do not exist in conventional AFM whose scanner with raster scan pattern at low frequency. Thus, an adapted protocol of scanner's calibration is in need to be established. In addition, the fact that calibration of piezoelectric scanner is known to be complex and not linear due to creep effect, should be keep in mind.

### 5.2 Lateral Force Calibration of AFM Tip

There is a great challenge to calibrate the lateral force of AFM probe. It is obligatory to do lateral force calibration as addition of normal force calibration in friction measurement in using AFM to ensure the reproducible result (D. F. Ogletree et al. 1996). To exploit information from force curve through force spectroscopy coupled with AFM, a calculation of force and friction coefficient is mandatory. But it is difficult because it highly depends on cantilever

thickness and tip height. Since its dimension is very small, it is difficult to control the fabrication and measure its dimension even by using scanning electron microscopy. The tip position is often not in the middle of cantilever, it has an offset value. The calibration system is decided by precise alignment of deflection sensor where optical detection is used. Furthermore, a significant variation is found in cantilevers from the same wafer. Thus, instead of using given force constant to measure the friction and adhesion of lipid membranes, the force calibration of each cantilever is highly recommended.

Lateral force calibration is obligatory to convert the friction forces of the sample which is usually given on Volt unit by AFM instrument to force unit Newton. That is the only way to quantify friction force for further analysis. Lateral force calibration is not as straightforward as normal force calibration. There are two methods proposed to calibrate the lateral force of the tip: the two-steps calibration method (Xie et al. 2008) and direct calibration method (D F Ogletree et al. 1996).

One of the early method **was two-steps calibration**, proposed by Ruan and Bushan (Ruan & Bhushan 1993). Two-step calibration is composed by measurement of lateral stiffness of cantilever and the lateral photodiode response (torsion sensitivity). They measured the friction force by using 'height' mode where the scanning direction of the sample is parallel to Z-direction. This method can result the absolute value of friction coefficient that can be used as an internal means to calibrate the data obtained by 'aux' mode. 'Aux' mode is based on the perpendicular scanning on X-direction of the sample and the output of cantilever torsion is measured. However, this technique assumes that deformation by friction force can be compensated by normal force. Since friction force applied on cantilever causes different distribution of bending moment, normal force generated deflection geometry (Cain et al. 2000). Thus, it breaks the precedent assumption.

Later, Liu et al (Liu et al. 1996) was physically moving the four quadrants photodetector in lateral direction to measure lateral deflection sensitivity. They used an optical geometry approach and require calculation of elasticity of the cantilever. Relation between normal bending signals (normal force) and torsion signals (lateral force) was used to derive formula to determine the lateral force perpendicular to the cantilever major axis. For their exemplary study, the used triangular cantilever, the same shape with cantilever that we used in our studies. This was the first method proposed that gives direct measure of the lateral sensitivity of the photodiode. However, this technique is sensitive to any change on the optical path.

However, with the technique invented by Bogdanovic and friends (Bogdanovic et al. 2000), their value of torsional spring constant tends to be larger than calibration method that considers the cantilever dimensions. It is because the uncertainty of cantilever's thickness and length which have big influences on lateral calibration.

In other hands, Carpick et al (Carpick et al. 1997) used different approach to quantify the friction and shear strengths on FFM. They determined the lateral stiffness which is proportional to contact radius, formed by elastic contact of tip and sample surface. They stated that the tip is attached on cantilever which has its own normal spring constant. Thus the contact and cantilever are two springs in series in lateral stiffness model on FFM.

To simplify and to advance the two-steps calibration by Ruan and Bushan (Ruan & Bhushan 1993) and all precedent studies, the **direct calibration** with wedge method (D. F. Ogletree et al. 1996) was introduced and it becomes one of the reliable calibration technique until now. Direct calibration assesses the calibration factor in single step produce thus it has better time efficiency. It requires sample whose known slopes because the technique is based on comparison of lateral force signal on each surface's slope. Later, an improvement was made by Varenberget al (Varenberg et al. 2003) by using flat facets on the calibration grating to decrease error. However, this technique showed increase of lateral force calibration factor with the increase of applied load, unlikely with friction coefficient. Thus, despite the advantages offered, such as simpler calculation of calibration factor and usage of calibration grating; separate lateral force calibration is necessary for every given applied load. To address this problem, the contact factor which is derived from the contact stiffness between the tip and sample, is added to the calculation (Wang & Zhao 2007). Thus, repeating the calibration factor can be valid for any given load.

Feiler et al (Feiler et al. 2000) presented different approach of direct calibration by measuring torsion spring constant. This method simultaneously calibrates the response of scanner to the angular deflection of the cantilever. This method requires simultaneous measurement of the vertical and lateral deflection of the AFM cantilever. The best results of calibration obtained if the adhesion force between the tip and the surface is minimized. Later, Reitsma (Reitsma 2007; Reitsma et al. 2008) adapted this method on his self-modified AFM cantilever that enables the user to select acceptable measurement precision via calibration measurement across the full working range of photodiode detector. At almost the same time, Quintanilla and Goddard (Quintanilla & Goddard 2008) applied Feiler's method to calibrate the

colloidal probe cantilever. Feiler's one-step calibration method is able to address the problem of misalignment of probe particles. Misalignment is shown to badly affected the cantilever torsion stiffness but not on the lateral photodiode sensitivity. Thus cantilever should be perpendicular to the photodiode detector. However, Liu and friends have successfully calibrated an off-axis tip that has T-shape cantilever and minimized the Abbé error which is involved due to misalignment between the cantilever width axis and the scanning line (Liu et al. 2011).

Cannara et al (Cannara et al. 2006) introduced calibration method that does not require contact between tip and sample surface. Their calculation is based on Sader's technique (Green et al. 2004). They determined the lateral signal sensitivity by loading the colloidal sphere. Laser intensity distribution was assumed to be the same for test cantilever and cantilever of interest whose integrated-tip. This method called test probe method is in good agreement with wedge method.

Further advancement and modification of the calculation mode is still going on to address the rest of problems in lateral calibration. Anderson and friends (Anderson et al. 2011) emphasized the character of typical lateral calibration which is time consuming, expensive and can cause wear of the tip. Their proposed method only requires one set of images to minimize the time, cost, and wear of the tip. While, Gao and friends (Gao et al. 2014) used molecular dynamic simulations to determine the stiffness of the tip by simulating tip apex subject to shear or sliding over a substrate surface. Their model is based on a multi spring model in order to simplify the system.

In our study, we design lateral calibration method based on wedge method which is proposed by Ogletree at 1996 (D. F. Ogletree et al. 1996) due to its simplicity, time efficiency, and accuracy. Compared to the original wedge method, our method which is based on the strong correlation lateral signal and the surface slope, is more practical. We use scratched-fused silica surface as sample. In addition, all the experiments of calibration were done in liquid environment. We put a lot of attention to align the sensor beam as the optical system to avoid any errors due to misalignment.

### 5.2.1 Principle of Method

Figure 5.1 shows the scheme of contact between tip and slope's surface. LFM images show a correlation with topography image. However, both images are not similar; there is indirect relation between topography and LFM signal. In contrary, LFM images have strong correlation with slope image in X direction. The slope image is derived from topography,

$$\theta = \frac{dz}{dx} \quad (5.1)$$

where a slope ( $\theta$ ) is resulted from height difference divided by difference of x distance. Therefore, topography and LFM image are physically coupled though it is more related with surface's slope than surface's topography. This assumption is valid only if the friction coefficient ( $\mu$ ) of the surface is constant.

Total force  $F$  is taken from addition of normal force  $N$  and lateral force  $L$  applied on AFM tip. Referring to axis  $x$  and  $z$  and surface slope angle  $\theta$ . Therefore, the mathematical equations of force action on tip during trace movement (tip is going) can be derived as shown below:

$$F_{x-trace} = N \sin \theta + L \cos \theta \quad (5.2)$$

$$F_{z-trace} = N \cos \theta - L \sin \theta \quad (5.3)$$

while when the tip has retraced movement (tip is changing its direction of scanning):

$$F_{x-retrace} = N \sin \theta - L \cos \theta \quad (5.4)$$

$$F_{z-retrace} = N \sin \theta + L \cos \theta \quad (5.5)$$

$F_x$  is recorded as LFM signal while  $F_z$  is topography signal. In AFM experiment, the vertical force  $F_z$  is maintained to be constant during trace and retrace scanning by the servo loop. Thus,  $F_{z-trace} = F_{z-retrace} = F_z = constant$ .

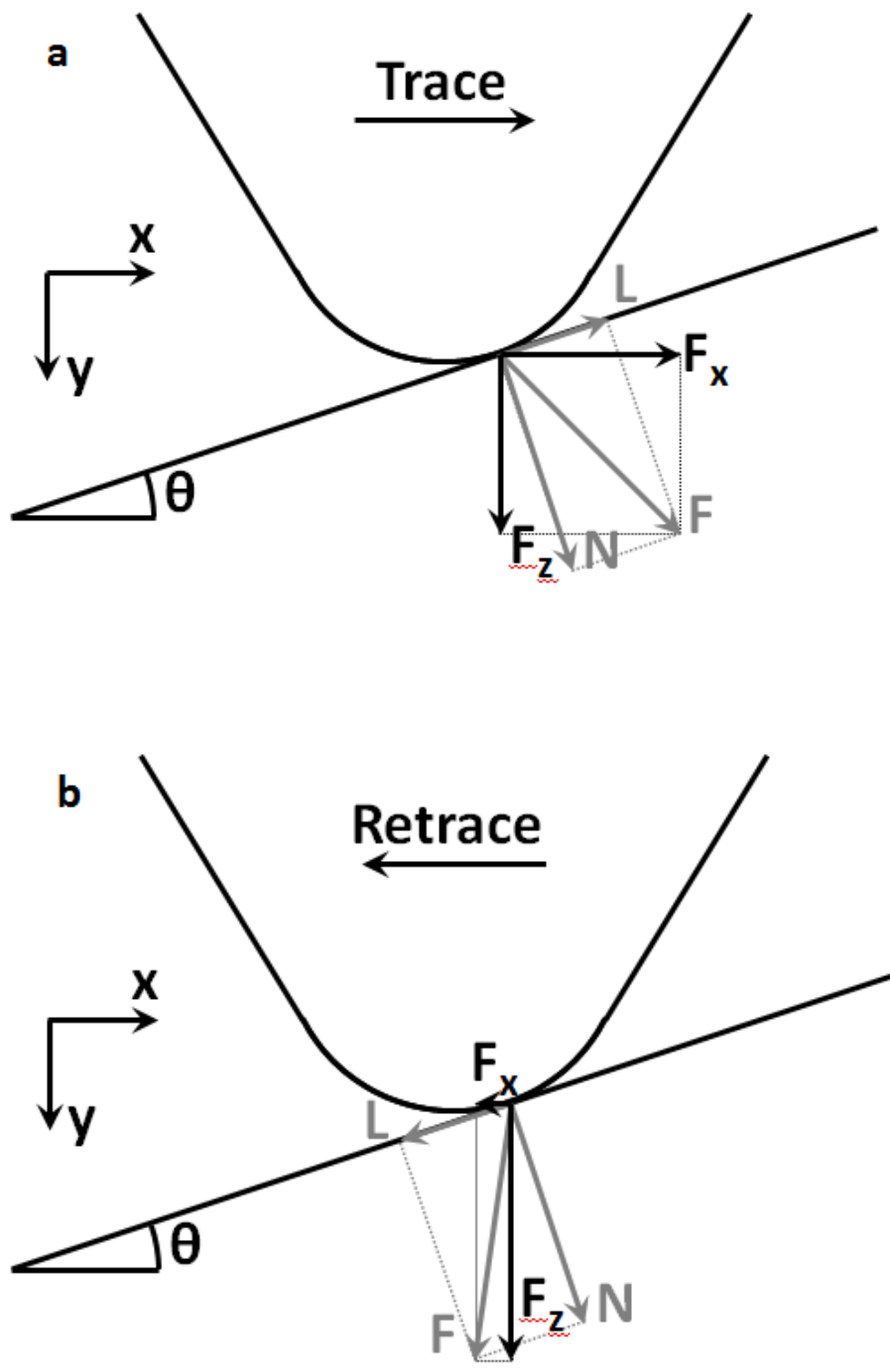


Figure 5.1 Model of contact of AFM tip on tilted surface (a) during ascending and (b) during descending the slope

Given that friction factor  $\lambda$  is the division of friction force by normal force,

$$\lambda = \frac{L}{N} \tag{5.6}$$



it can be obtained that for trace signal:

$$\frac{F_{x-trace}}{F_z} = \frac{\tan \theta + \lambda}{1 - \lambda \tan \theta} \quad (5.7)$$

and for retrace signal:

$$\frac{F_{x-retrace}}{F_z} = \frac{\tan \theta - \lambda}{1 + \lambda \tan \theta} \quad (5.8)$$

The friction factor  $\lambda$  is different with friction coefficient  $\mu$  because in nanoscale  $\lambda$  is not always proportional to the normal force, unlike  $\mu$ .  $\mu$  is the ration of difference of friction force to the difference of normal force and is constant.  $\lambda$  is similar to  $\mu$  if  $\lambda$  is constant in which Amonton's law is applied.

$$\mu = \frac{\Delta F_f}{\Delta F_N} \quad (5.9)$$

In local scale, for the first approach, generally surface's slope is very small ( $\ll 0.5$ ), then the value of  $\mu \tan \alpha$  could be neglected. So, the equation of lateral force during trace and retrace scanning becomes:

$$F_{x-trace} \approx F_z \tan \theta + F_z \lambda \quad (5.10)$$

$$F_{x-retrace} \approx F_z \tan \theta - F_z \lambda \quad (5.11)$$

Now, it is clearly seen that LFM signal is composed by slope  $F_z \tan \alpha$  and friction factor  $F_z \mu$ . The friction part is theoretically constant for surface from the same material composition. By subtraction and addition of LFM signal trace and retrace, it can be obtained:

$$F_{x-trace} - F_{x-retrace} \approx 2F_z \lambda \quad (5.12)$$

$$F_{x-trace} + F_{x-retrace} \approx 2F_z \tan \alpha \quad (5.13)$$

## 5.2.2 Image acquisition

Friction image (LFM image) is required by engaging the AFM tip on one of the scratch. The AFM parameters should be optimized before imaging. Integral and proportional gain, scan velocity, and z limit should be minimized. At least 128 scanning lines and 512 points per line are necessary to obtain good resolution of image.

The friction imaging is conducted with multiscreens appeared on the nanoscope interface. There are three channels: Topography image (trace), friction (trace), and friction (retrace). Our AFM set up is only capable to produce three images at the same time. It should be noted that for friction image, it is necessary to not use fit line.

In ideal condition of AFM, LFM signals are always proportional to normal force. By using an assumption that LFM signal is direct function of lateral force through calibration parameter  $C$ , it can be expressed as:

$$LFM = C_{LFM}F_x + C_0 \quad (5.14)$$

Knowing that lateral force  $F_x$  has two terms; slope and friction coefficient, the equation above becomes:

$$LFM_T = CF_z \tan \alpha + CF_z \mu + C_0 \quad (5.15)$$

$$LFM_R = CF_z \tan \alpha - CF_z \mu + C_0 \quad (5.16)$$

where the sign  $T$  and  $R$  indicates the trace and retrace scanning direction respectively.

Thus the half difference and total of lateral signals are:

$$\Delta F_x = \frac{F_{x-trace} - F_{x-retrace}}{2} = F_z \lambda C_\Delta \quad (5.17)$$

$$\Sigma F_x = \frac{F_{x-trace} + F_{x-retrace}}{2} = \tan \alpha F_z C_\Sigma \quad (5.18)$$

$C_{\Delta}$  and  $C_{\Sigma}$  are the correcting factors for the difference and the total of lateral signals respectively. Thus,  $C_{\Delta}$  and  $C_{\Sigma}$  can be obtained by:

$$C_{\Delta} = \frac{\tan^2 \theta + 1}{1 - \lambda^2 \tan^2 \theta} \quad (5.19)$$

$$C_{\Sigma} = \frac{1 + \lambda^2}{1 - \lambda^2 \tan^2 \theta} \quad (5.20)$$

where  $C_{LFM}$  is the calibration factor that converts lateral signal from Volt to nanonewton, and  $C_0$  is the LFM offset.

Thus, it can be obtained:

$$\Delta_{LFM} = F_z \lambda C_{\Delta} C_{LFM} \quad (5.21)$$

$$\Sigma_{LFM} = \tan \alpha F_z C_{\Sigma} C_{LFM} + C_0 \quad (5.22)$$

Imaging was done in liquid condition on glass plate sample prepared following the protocol explained in part B. It is crucial to calibrate the lateral calibration factor in the medium as the experiment will be employed (Pettersson et al. 2007). It is possible to determine the change of sensitivity in the case of medium change (calibration in air but experiment in liquid) if the geometry of the tip and refractive index are well known. Thus, to avoid error due to uncertainty of geometry and refractive index, calibration is conducted in liquid as our experiment is mostly done with biological materials.

There are three images acquired for this lateral calibration method: height image, lateral force image-trace ( $LFM_T$ ), and lateral force image-retrace ( $LFM_R$ ). The same type of images is acquired for different applied load. We recommend that a minimum of five different normal forces are necessary to have enough precision.

In addition, this method is sensitive to linearity of piezoelectric scanner. Nonlinear piezo can cause hysteresis and shift of the images. It is important to be at the same position during image acquisition for a series of voltages in order to maintain constant proportion of positive and negative slopes.

### 5.2.3 First Approach: Wedge Method

First, we have tried to apply the wedge method to calibrate AFM probe by testing gold and diamond layers. Both surfaces contain some slopes that come from the gold and diamond particles attached respectively. We compared the results based on the quality of AFM height image and friction image (trace and retrace signal of LFM).

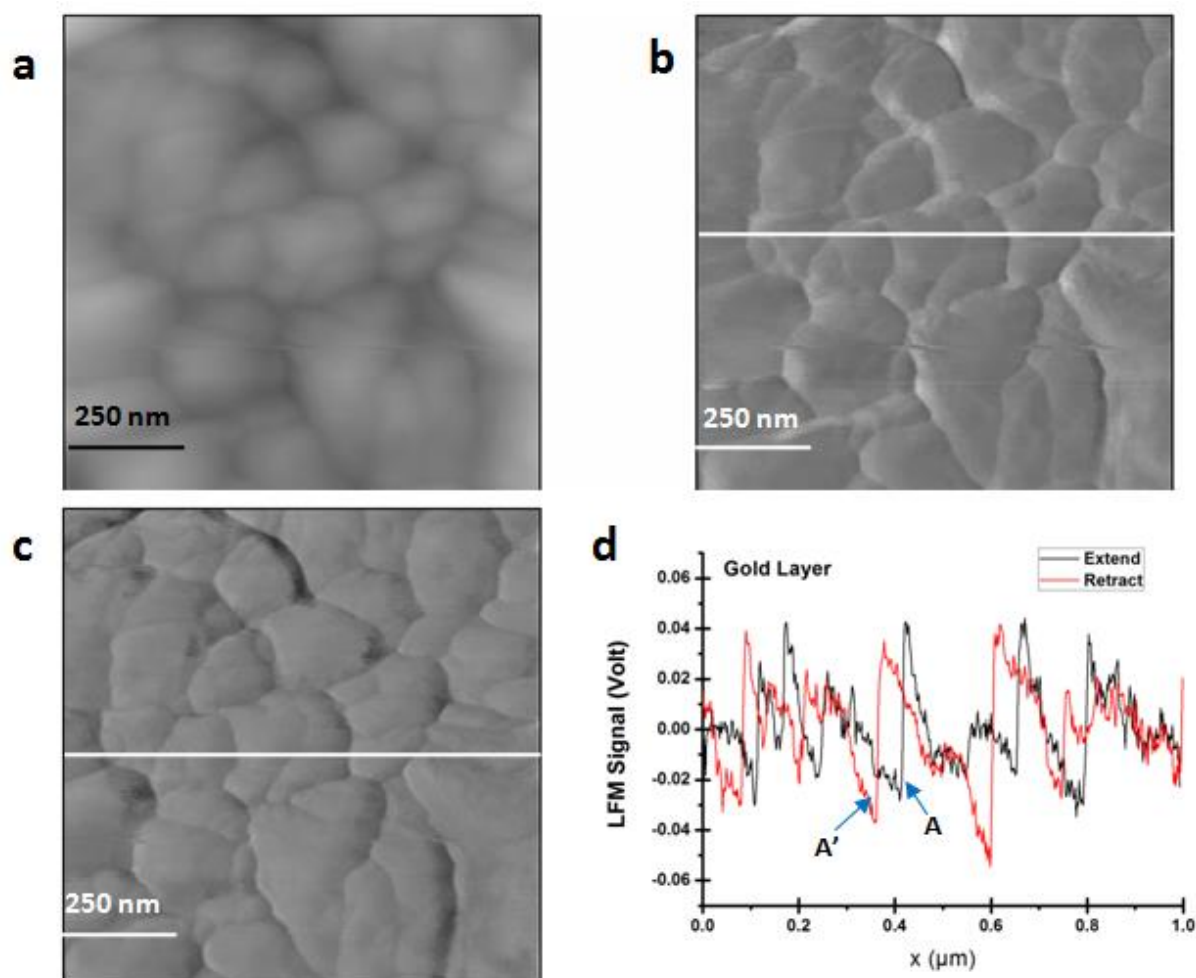


Figure 5.2 Image of (a) topography (z-range = 100 nm) and friction image: (b) trace and (c) retrace (z-range = 0.5 Volt) of gold layer surface. Size 1  $\mu\text{m}$  x 1  $\mu\text{m}$ . (d) Line profile analysis along the white straight line

Gold is a noble metal that presents local variation on topography. Without further surface treatment, gold layer is hydrophilic. Individual atomically flat Au grain separated by steps and deep channels (dark area) can be observed on Figure 5.2 (a). SEM images done by other research group showed that the sides of the gold islands are sharp. However, the

topography image taken by AFM gives smoother dark channel due to the finite radius of curvature (Koutsos et al. 1998). We intended to use the slope of gold islands that might fit to our requirement of constant surface slope. Figure 5.2 (b-c) showed the friction image for trace and retrace scanning direction. The line profile of both LFM signals is compared in Figure 5.2 (d).

The second material tested is diamond layer deposited onto glass surface through PVD process. Diamond is a wide band gap semiconductor with electronic properties that can be varied from insulating to conductive. There are two types of diamond: boron-doped (p-type) and phosphorus-doped (n-type). Figure 5.3 (a) showed the topography image of smooth diamond layer along its friction image (trace and retrace). The crystal of diamond has separated by a clear barrier.

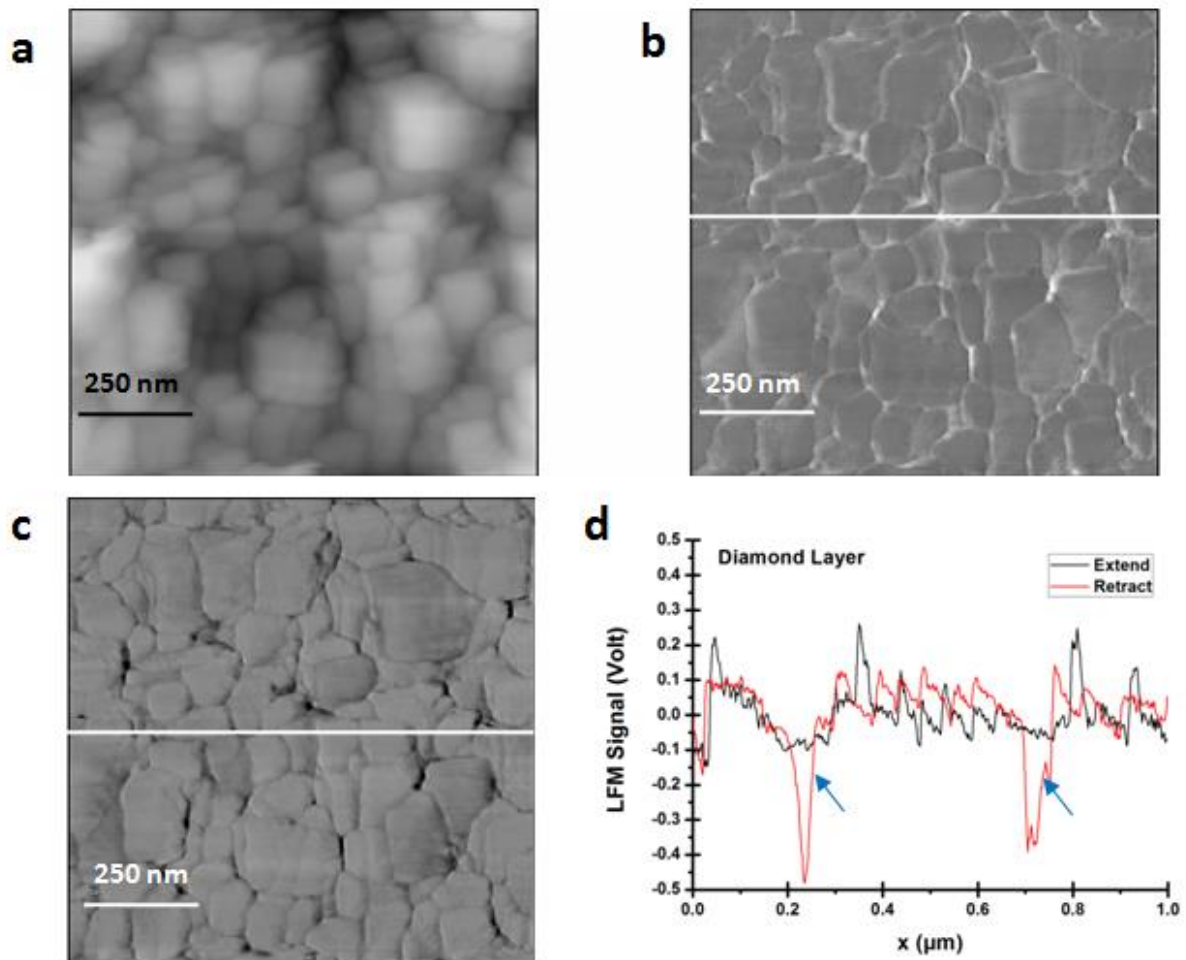


Figure 5.3 Image of (a) topography (z-range = 100 nm) and friction image: (b) trace and (c) retrace (z-range = 0.5 Volt) of diamond layer surface. Size  $1\ \mu\text{m} \times 1\ \mu\text{m}$ . (d) Line profile analysis along the white straight line

For gold surfaces, there is horizontal shifting of LFM signals. The peak A pointed by the blue arrow (see Figure 5.2) is displaced to peak A' even though the overall signals of LFM trace is similar with signals of LFM retrace. It is related to the tip-sample interaction which directly linked with frequency shift. A resonance between scan speed and time constant of the system can describe the spatial shift and the image resolution (Gauthier et al. 2002).

We have intended to benefit the slope of diamond crystal to fit our method of calibration. However, diamond surfaces present LFM trace and retrace images which are not corresponding to each other. The blue arrow in Figure 5.3 points the valleys which are not existed in the trace signals.

Friction force of the surface is half of vertical hysteresis between trace and retrace LFM signals. However, the LFM signals of both surfaces are overlapping (no hysteresis). It is complicated to compute the lateral calibration factor when the LFM signals are not identical and do not possess vertical hysteresis. The friction images of both surfaces indicate that there might be influences from outside AFM set up. We assume that LFM signals are very sensitive to any external disruption (small vibration produced by talking, walking, etc). Moreover, the Multimode AFM that we used is an open AFM in which the sample stage is uncovered and exposed to room air. So, to address this problem, it is recommended to use stiffer cantilever (Giessibl et al. 2004). Since we are working with biological samples, softer cantilevers are used and. Thus, the wedge method is not adapted perfectly for our condition of experiment.

#### ***5.2.4 Second Approach: Scratch Method***

Since we have not succeeded measuring the lateral calibration factor by using Wedge method, we have developed the so-called Scratch method. Scratches have been made onto the surface by nanoindentation onto produce constant slopes. The vertical incision of the scratch showed inverse triangular profile with positive slope in one side and negative slopes in another side (see Figure 5.2). The sample of calibration should have constant friction coefficient. Several surfaces were examined: aluminum, polycarbonate, glass, and fused silica. We compared the results based on the quality of AFM height image and friction image (trace and retrace signal of LFM).

From previous experiment, we have learnt that using the surfaces whose slopes given by the crystal barrier, are not adapted to our proposed method of lateral force calibration.

Thus, we changed our strategy to prepare the surface with man-made slope. For that, we use a Berkovich indenter of nanoindentati onto make a scratch on a flat surface resulting triangular scratch. Nanoindentation technique is usually used to examine the local deformation and hardness at micro scale to reveal the elastic and plastic properties of materials at small indentation depth (Sumomogi et al. 2005; Ogura et al. 2011). It simplified the number of slope measured. In spite multiple surface slopes from each crystal, a scratch whose two slopes: ascending and descending will be images and be analyzed.

**A. Aluminum and Polycarbonate**

First material that we have tested to apply the scratch method of calibration is aluminum. Figure 5.4 showed the topography and friction image of aluminum scratch.

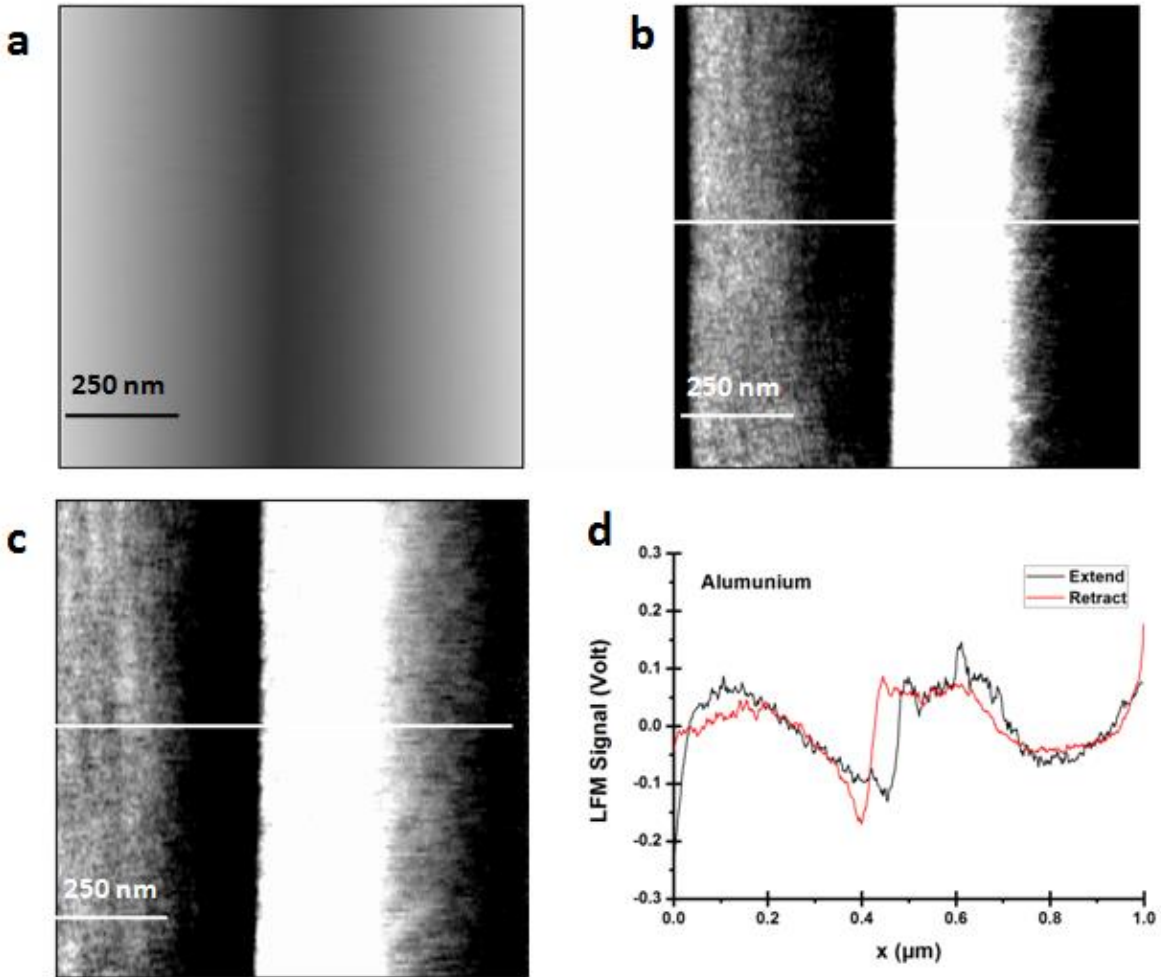


Figure 5.4 Image of (a) topography (z-range = 100 nm) and friction image: (a) trace and (c) retrace (z-range = 0.1 Volt) of aluminum surface (on the triangular scratch). Size 1 μm x 1 μm. (d) Line profile analysis along the white straight line

We positioned the scratch, visualized as straight black line in the middle of the image,

to be at the middle in order to have equal proportion of positive and negative slope. However, we did not acquire the friction image as we have expected. We have expected that the friction of the descending slope (left side of the scratch) is lower than one on ascending slope.

We also have tested polycarbonate which is a viscoelastic materials in which the effective elastic modulus and the hardness values are dependent on applied load, hold times, and loading rates (Fang & Chang 2004), as calibration sample. It yields ripple-like structure on the scratch (see Figure 5.5). It was found that the increase of applied force during scratching increases the roughness of the surface (Fang et al. 2005) as shown in Figure 5.5. The deformation on the surface was also promoted by pile-up which occurs at large deformation due to localization effects (Pelletier 2008).

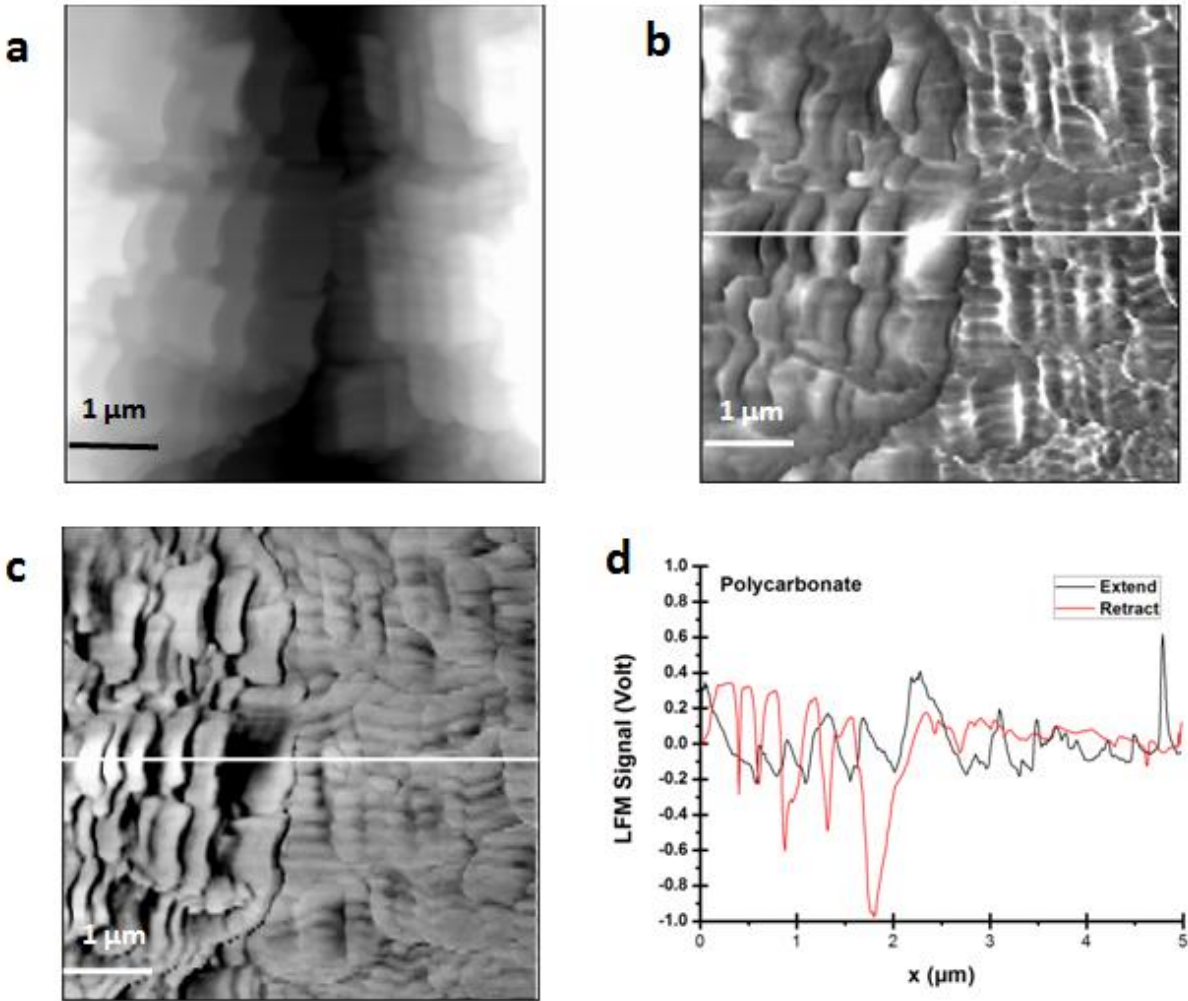


Figure 5.5 Image of (a) topography (z-range = 250 nm) and friction image: (a) trace and (c) retrace (z-range = 0.5 Volt) of polycarbonate surface (on the triangular scratch). Size 5 μm x 5 μm. (d) Line profile analysis along the white straight line

Unfortunately, we cannot determine the lateral calibration constant by using aluminum and polycarbonate sample. Aluminum sample does not have vertical hysteresis even though



LFM trace and retrace signals are nearly identical. Meanwhile, polycarbonate surfaces are deformed resulting rough surfaces. Both samples showed variation of slope which is problematic in lateral force calibration. Thus, the friction coefficient of the surfaces is not constant that might be due to anisotropy, surface deformation, etc. This problem can be solved by having two height images to compare. However, both images should have recorded simultaneously to avoid shifting. But our AFM set up can only produce three images at one time. So, it is not possible have one more image during acquisition. Having sample with constant slope is the requirement in scratch method.

For aluminum, its plastic nature might have a role in yielding this result. The release of compression beneath the indenter and the aluminum surface causes crystal dislocation during micro plastic deformation. The rotation of the lattice during nanoindentation scratching may account for the pile up of the material (Rathinam et al. 2009). In addition, anisotropy of friction coefficient of aluminum were found to be depended on its crystal orientation, scratching direction, and the plane of indentation (Komanduri et al. 2000) which we did not put more attention about it. Without information about crystal orientation of our aluminum surface, it is difficult to produce scratch with constant slope.

## **B. Glass (cover slip) and Fused Silica**

The next material tested with scratch technique was glass (cover slip) surface. Glass is hydrophilic surface and is often used as solid substrate to deposit the biological molecules, cells, etc (El Kirat et al. 2005). The mechanical characterization of glass surfaces by nanoindentation indicates that its mechanism of crack nucleation is influenced by the angle and the crystalline structure (Morris et al. 2004).

Figure 5.6 shows the topography and friction (trace and retrace) images of glass surface. The section line of friction image shows the stabilized LFM signal of approaching and retraction. The difference between LFM signals trace and retrace allows measurement of surface friction. Constant slope of ascend and descend is also pictured on the height and LFM images. Despite of the appearance of small artifact on the edge of the image, the quality of the image is promising. Thus, we continued to analyze the images required to compute the lateral calibration factor.

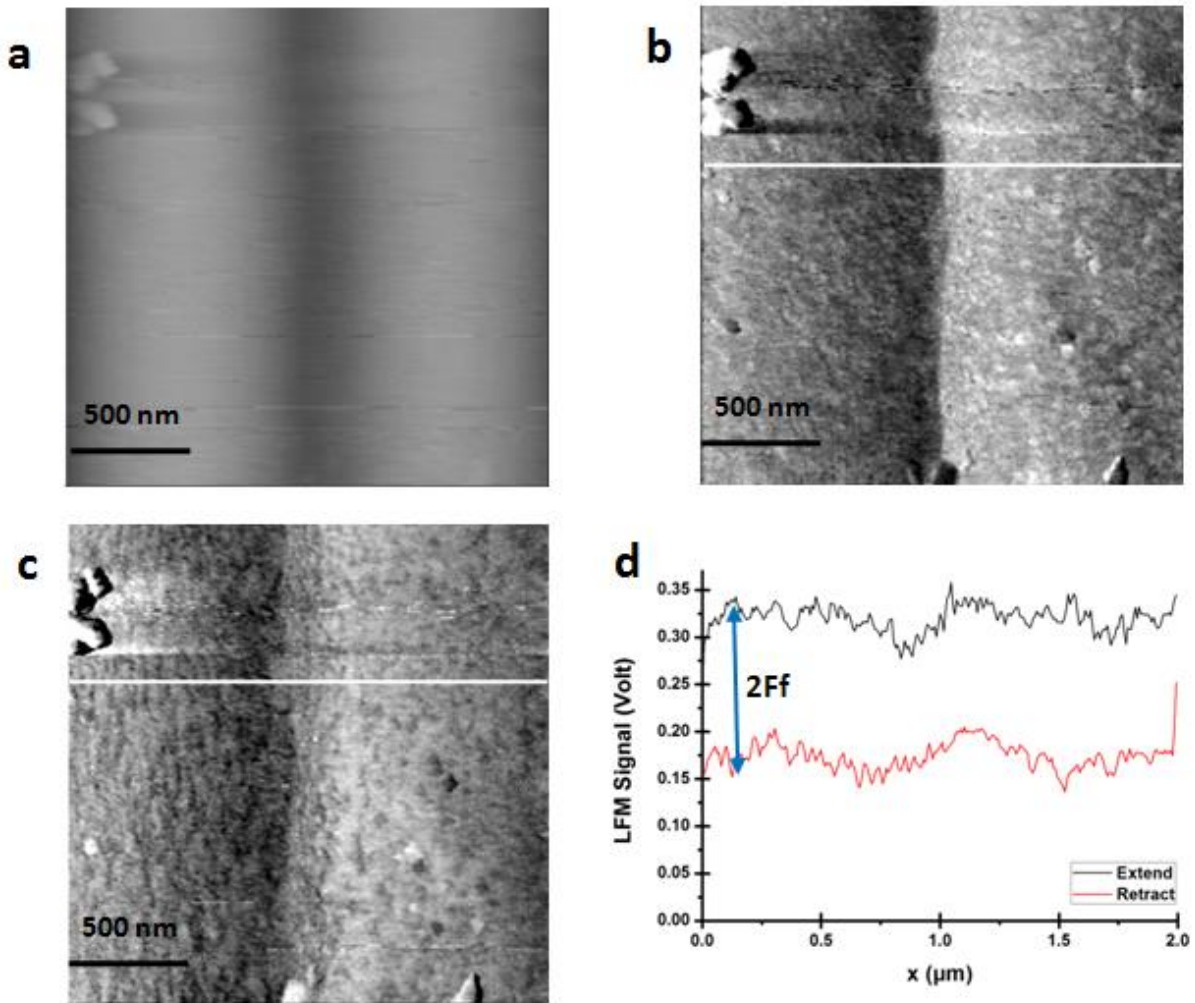


Figure 5.6 Image of (a) topography ( $z$ -range = 60 nm) and friction image: (a) trace and (c) retrace ( $z$ -range = 0.1 Volt) of cover slip glass surface (on the triangular scratch). Size  $2\ \mu\text{m} \times 2\ \mu\text{m}$ . (d) Line profile analysis along the white straight line

Figure 5.7 showed the result of signal analysis by computing the surface slope, total and difference of LFM signal along with their histogram respectively. The computation is based on Equation 6.6. We used a program created by Pierre-Emmanuel Mazeran in LabView software, to transform the image and later determine the lateral calibration factor.

Contrast given in surface slope image shows the decline (negative slope) and incline (positive slope) on the scratch. Later, surface slope image will be used to validate the total of trace and retrace lateral force signal ( $LFM_{T+R}$ ) based on their similarity. It should be noted that in the latter explanation, the term  $LFM_{T+R}$  and  $LFM_{T-R}$  refers to the value of  $\frac{LFM_{T+R}}{2}$  and  $\frac{LFM_{T-R}}{2}$  found in mathematical equation.

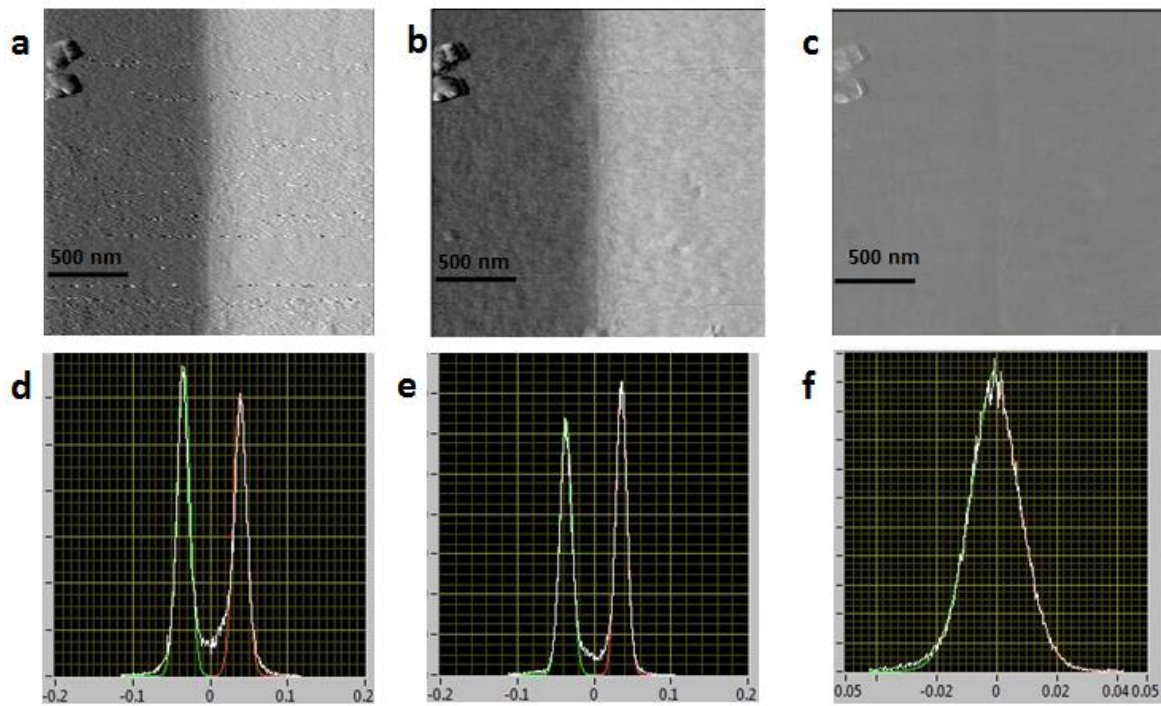


Figure 5.7 Cover slip glass image of (a) surface slope, (b) total friction ( $T+R$ ) and (c) difference of friction ( $T-R$ ). Size  $3\ \mu\text{m} \times 3\ \mu\text{m}$ . (d-f) Histogram of the surface slope, total friction ( $T+R$ ) and difference of friction ( $T-R$ ) respectively.

Then, we computed the addition and the subtraction of lateral force signal to later determine the friction coefficient  $\mu$  and the lateral calibration coefficient  $C$ . Figure 5.7 shows the image of lateral force after addition and subtraction. The image of total lateral force shows similarity with image of surface slope with the appearance of two drastic contrast indication incline and decline slope. It also proves our assumption that there is correlation between topography of the surface with lateral force response (see Equation 5.18). In the contrary, the image of difference lateral force shows relatively uniform contrast as it indicates the constant friction force. The relationship between difference lateral force signal and friction force is shown on Equation 5.17. In order to qualify this correlation, a histogram is made and is shown on Figure 5.7 (d-f).  $LFM_{T+R}$  gives two histogram peaks which correspond to incline and decline slope respectively, in agreement with surface slope image and its accordance with surface topography. Meanwhile,  $LFM_{T-R}$  only has one single peak indicating its uniformity and constant friction force. It implies that our glass surface is homogeneous and has single friction coefficient.

Even though the result of glass surface is better as it fits to our concept of lateral force calibration, we still have some doubt about the quality of the result. The histogram  $LFM_{T-R}$  still contains noise on the peak. Thus, we put glass surface on hold and tested the last material: fused silica.

Fused silica is smoother (El Kirat et al. 2005) and has less additive than glass surface. Figure 5.8 gives the image of topography and LFM trace and retrace. The section line of LFM signals shows clear difference between LFM trace and retrace to measure the surface friction. In addition, the LFM signals have considerably low noise.

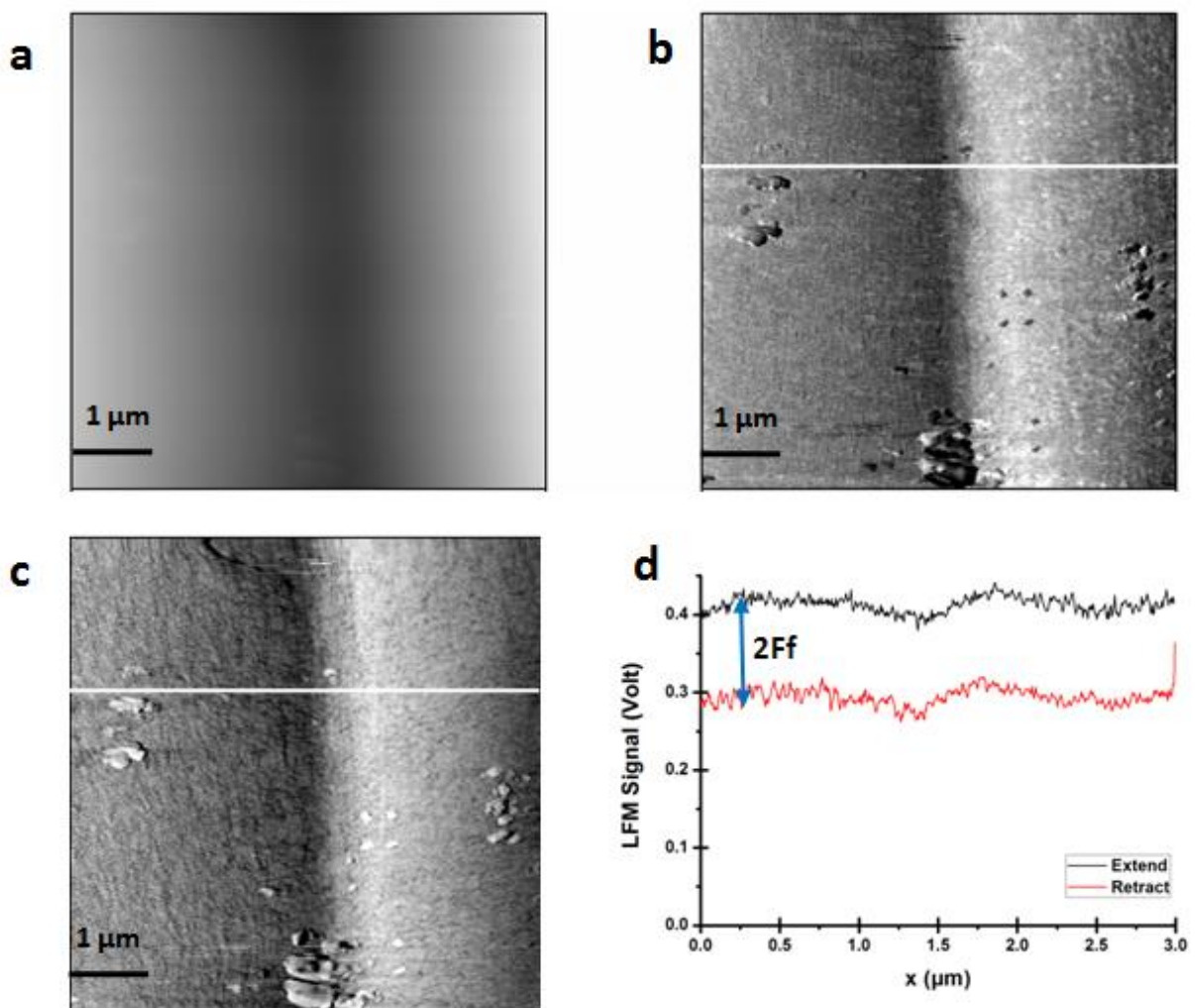


Figure 5.8 Image of (a) topography (z-range = 100 nm) and friction image: (a) trace and (c) retrace (z-range = 0.1 Volt) of fused silica surface (on the triangular scratch). Size  $3 \mu\text{m} \times 3 \mu\text{m}$ . (d) Line profile analysis along the white straight line

Later, we applied our calibration calculation to analyze the image acquire as we have done with glass surface. Figure 5.9 shows the result of image analysis together with the histogram to quantify the images. The results of fused silica are similar with the ones acquired with glass sample. However, with fused silica, the histogram of surface slope and total LFM signals have small width indicating smaller standard deviation and more contrast friction coefficient. In addition, the difference between the peak values of two data populations is larger than ones found in glass surface. Thus, it eliminates the ambiguities in differentiating positive and negative population. The standard deviation value of fused silica is much smaller than the difference of slopes. In other words, there is wider gap between decline and incline slope or large variation of surface slope. In contrary, glass surface has smaller variation that might be caused by surface defect, oscillation, and normal variation of the surface. The two population curves are intersecting resulting uncertainty of the results. Moreover, on fused silica, the histogram of LFM signals difference also has less noise on the peak. In conclusion, we select fused silica as our lateral force calibration sample among other options because it has the least uncertainty.

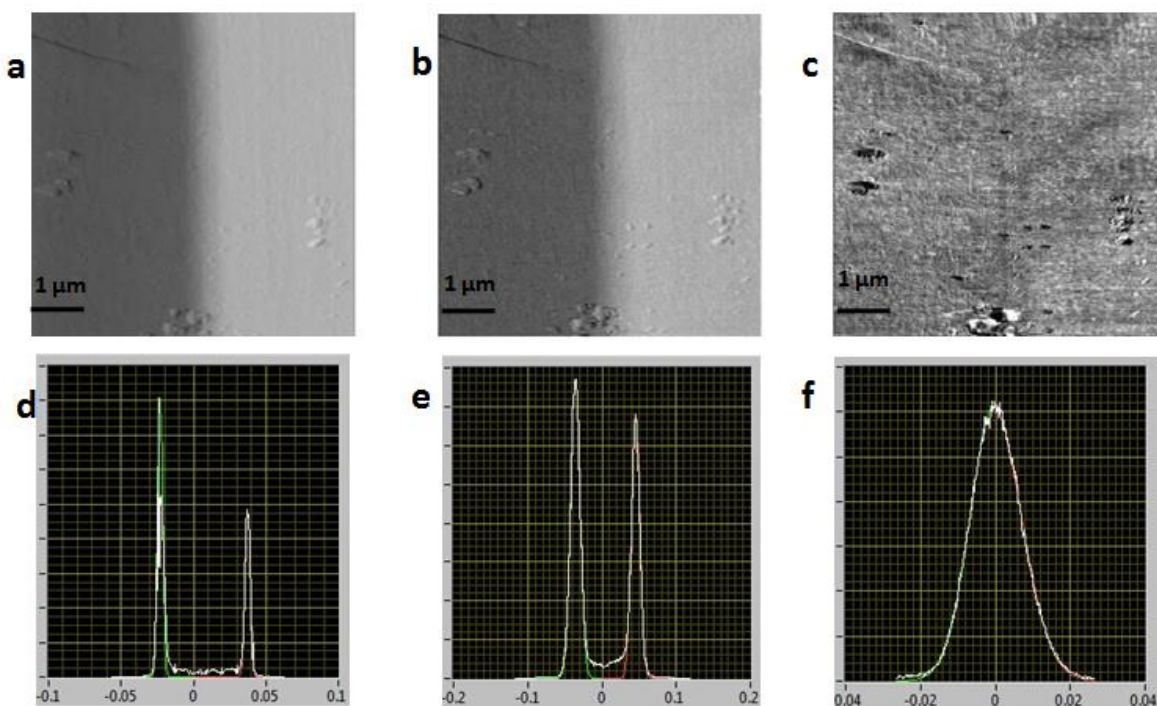


Figure 5.9 Fused silica image of (a) surface slope, (b) total friction ( $T+R$ ) and (c) difference of friction ( $T-R$ ). Size  $3 \mu\text{m} \times 3 \mu\text{m}$ . (d-f) Histogram of the surface slope, total friction ( $T+R$ ) and difference of friction ( $T-R$ ) respectively.

### 5.2.5 Calibration line in different medium

Another requirement of our lateral calibration technique is the quantification of normal force in which the determination of normal spring constant is obligatory. We have used the thermal oscillation technique to measure the stiffness of the cantilever. With accurate information of normal force applied, the lateral calibration constant can be determined as shown on Figure 5.10 and Figure 5.11. The calculation is based on Equation 5.18. Here, the constant is defined as the inverse of the slope of linear regression line and is given in nN/Volt unit which perfectly fit to convert the recorded friction force into force unit.

A microlevier whose six cantilevers with different spring constants was calibrated in air and in millQ water to study the influence of medium to the calibration constant. However, only three cantilevers were tested with spring constant of: L2= 0.0592 N/m; L3= 0.1314 N/m; and L4= 0.456 N/m. Those are the cantilevers that we plan to use on the latter experiment with biological membrane. The values of spring constant were obtained through normal force calibration- thermal oscillation technique.

Figure 5.10 gives the calibration line measured in air medium. Meanwhile Figure 5.11 shows the calibration line acquired in the presence of millQ water. The term  $Fn.C$  refers to the relationship between total LFM signals and surface slope, mathematically explained by Equation 5.19. Each calibration line gives linear relationship between  $Fn.C$  and normal force applied with value of  $R^2$  range 0.95-0.99.

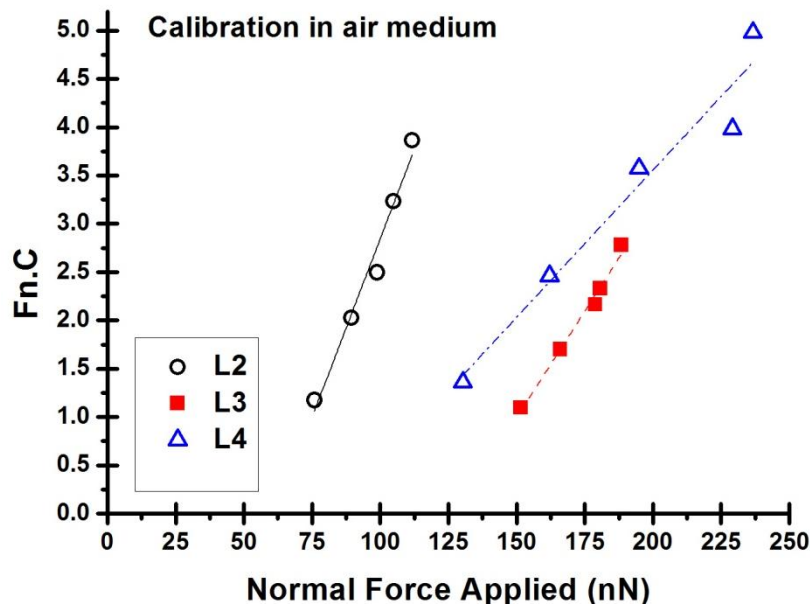


Figure 5.10 Determination of lateral calibration coefficient from LFM signal measured in air atmosphere

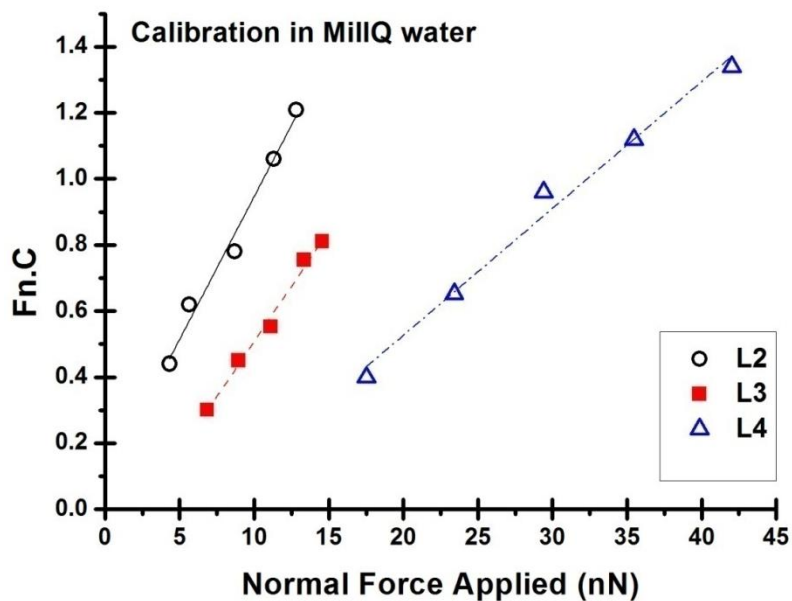


Figure 5.11 Determination of lateral calibration coefficient from LFM signal measured in MillQ water medium

Furthermore, the values obtained in millQ water were lower than those obtained in air medium for the same cantilever. The reason behind this difference is due to different interaction between tip and sample. In air imaging, capillary forces play a central role in the tip-surface interaction due to the formation of water bridge (Mazeran 2006). Meanwhile, in liquid imaging, electrostatic interactions has bigger role because of the presence of electric double layer (Israelachvili 2013). Solution consists of mobile ions that surround the probe, cantilever, and also the sample surface. Ions with the same sign of charge are repelled to each other while the ions with different sign of charge are electrostatically attracted. Electric double layer is the result of arrangement of screening charges around the object. Its structure has major impact on interactions between tip and sample. Moreover, due to low van der Waals forces and the absence of capillary forces, the applied forces decrease by several magnitudes. In air imaging, forces of hundreds of picoNewton are induced by the presence of strong adhesion forces arising from van der Waals and capillary forces. Thus, the calibration should be done in the respective medium, depend on the environment of measurement of interest.

We compared the lateral calibration constant for three cantilevers measured in air and millQ water. All the values obtained during lateral calibration are listed on Table 5.1. Figure 5.12 shows that there is an increasing tendency of lateral calibration constant as function of normal spring constant in both medium. However, there is not enough data to explain the type of the relationship (linear or logarithmic).

Table 5.1 Comparison of lateral force calibration constant measured in different medium for several AFM tips whose different stiffness

	L2	L3	L4
<b>Spring Constant (N/m)</b>	0.0592	0.1314	0.456
<b>In air</b>			
<b>Linear Fitting</b>	$y = 0.08x - 4.55$ $R^2 = 0.97$	$y = 0.04x - 5.61$ $R^2 = 0.98$	$y = 0.03x - 2.54$ $R^2 = 0.94$
<b>C (nN/Volt)</b>	13.52	22.72	32.89
<b>In water</b>			
<b>Linear Fitting</b>	$y = 0.09x + 0.08$ $R^2 = 0.98$	$y = 0.07x - 0.16$ $R^2 = 0.99$	$y = 0.04x - 0.24$ $R^2 = 0.98$
<b>C (nN/Volt)</b>	11.55	14.95	26.06

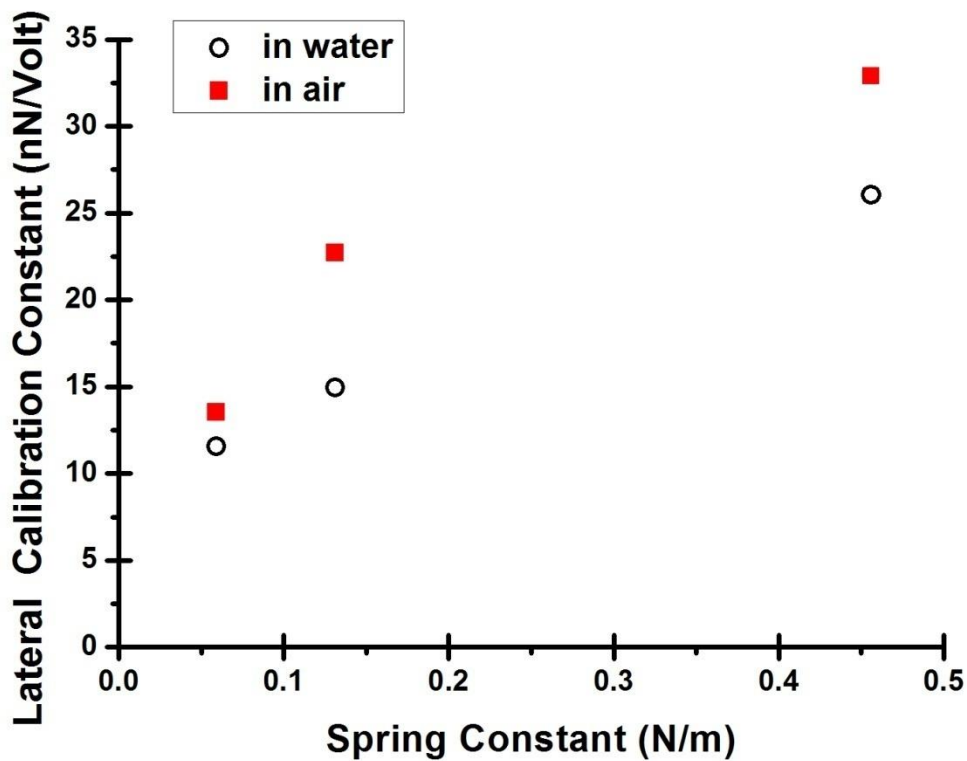


Figure 5.12 Comparison of lateral calibration force for the same cantilever measured in different medium: air and water



## 5.3 Calibration of Piezoelectric Scanner

There are several parameters affected the circular displacement. To control the sliding velocity, it is possible by modifying the voltage amplitude  $V$  (Volt) and the voltage angular frequency  $f$  (Hertz) that sets the constant radius per amplitude voltage  $R$  ( $\mu\text{m}/\text{Volt}$ ). Voltage controls the diameter of circular track while frequency controls interval of time to complete one circle. In order to define the important parameters of circular mode, calibration procedures were done. The sliding velocity  $v$  is determined by the following equation:

$$v = 2\pi RfV \quad (5.23)$$

Therefore it is important to define the working range of frequency and amplitude. To give the first idea about the parameter, we have conducted experiment to determine the resonance frequency of piezoelectric scanner and the amplitude of displacement.

### ***5.3.1 Initiation of Sliding***

Oscillator amplitude is a parameter of injected sinusoidal voltage signal from lock in amplifier to generate circular displacement of the scanner. There is maximum oscillator amplitude to allow AFM tip slides on the surface. In simple way, the experiment about initiation of sliding adapts the principle of friction silicon model experiment explained on chapter 4. This experiment was done by conventional AFM (circular mode was turned off). The oscillator amplitude is gradually increasing from 0 to 0.5 Volt to modify the sliding distance. At short distance (very low amplitude) there isn't motion between the tip and the flat sample as the tip shears the sample. In this state which is called stiction, tip and surface are stick to each other and move at the same velocity. When the tip slides at certain amplitude, it starts to slides resulting friction on the surface (Scherge & Gorb 2001). Then, the tip continues to slide on the sample at further sliding distance.

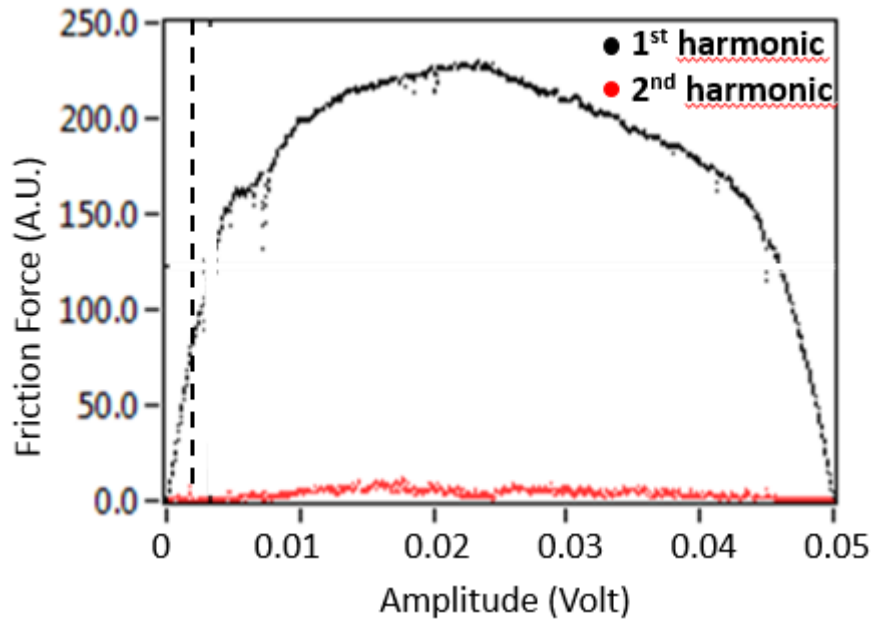


Figure 5.13 Scanning as function of voltage amplitude: 0 - 0.5 Volt

Figure 5.13 showed the curve of tip sliding with voltage amplitude increasing and decreasing gradually. The minimum voltage amplitude is given when the curve is no longer linear. During shearing at very low amplitude, it has linear behaviour in which the amplitude is proportional with voltage applied. At higher amplitude, it loses linearity and forms curve which is also an indication that friction depends on sliding velocity. Therefore, increase and decrease experiment are necessary to ensure the reproduction both linear and non-linear curve. By using 1000 points of data experiment, we found out that the voltage applied should be lower than 0.001 Volt. Since it is important to avoid modulation of friction force, the amplitude applied should be lower than the maximum limit.

### ***5.3.2 Resonance Frequency of Piezoelectric Scanner***

We have scanned GaAs surface with gradually increased frequency to determine the resonance frequency of piezoelectric scanner which is indicated by the peak point of amplitudes. GaAs surface is selected because of its nature as soft material that is sensitive to wear. The frequency defines the time needed to complete one sliding track and amplitude defines the sliding distance. Besides, this experiment was done to determine the working frequencies of CM-AFM because it should not be close to resonance frequency of piezo. Based

on simple harmonic motion, the resonance frequency of AFM cantilever  $f$  depends on the intrinsic properties of cantilever: spring constant  $K$  and the mass  $m$ . The change in tip can shift the curve resulting elliptical displacement due to difference of spring constant and mass. Thus, the working frequencies should be in the linear part of the curve to avoid any effect due to change of AFM cantilever's type.

$$f = \frac{1}{2\pi} \sqrt{\frac{K}{m}} \quad (5.24)$$

Several ranges of frequency were chosen to ensure the correct value found. Number of points is the amount of frequencies used. It should be noted that the experiment was done in liquid environment (millQ water medium) and resonance frequency of cantilevers are 7 ; 15 ; 38 ; and 125 kHz for triangular cantilevers number 1, 2, 3, and 4 respectively. This experiment was done with conventional AFM.

### **A. Frequency 1-100 Hz**

Scanning between frequencies of 1 – 100 Hz does not give any significant peak of amplitude. It simply means that resonance frequency of piezoelectric scanner is higher than 100 Hz. Figure 5.14 illustrates the signals resulted from the experiment. We have plotted the two harmonic signals recorded; however our point of interest is the first harmonic. The first harmonic signal shows a tendency of linear increase, indicating possible of working frequency range.

### **B. Frequency 100-2000 Hz**

Scanning between frequencies of 100-2000 Hz results harmonic peak at approximately  $f = 1000$  Hz as shown in Figure 5.15. When the curve reach  $f=1000$  Hz, it starts decreasing. In addition, during the increase, the slope of increase is changed at  $f=600$  Hz and becomes steeper. It is indicating that 600 Hz is the limit of working frequency. However, this range should be verified again at the calibration of piezo.

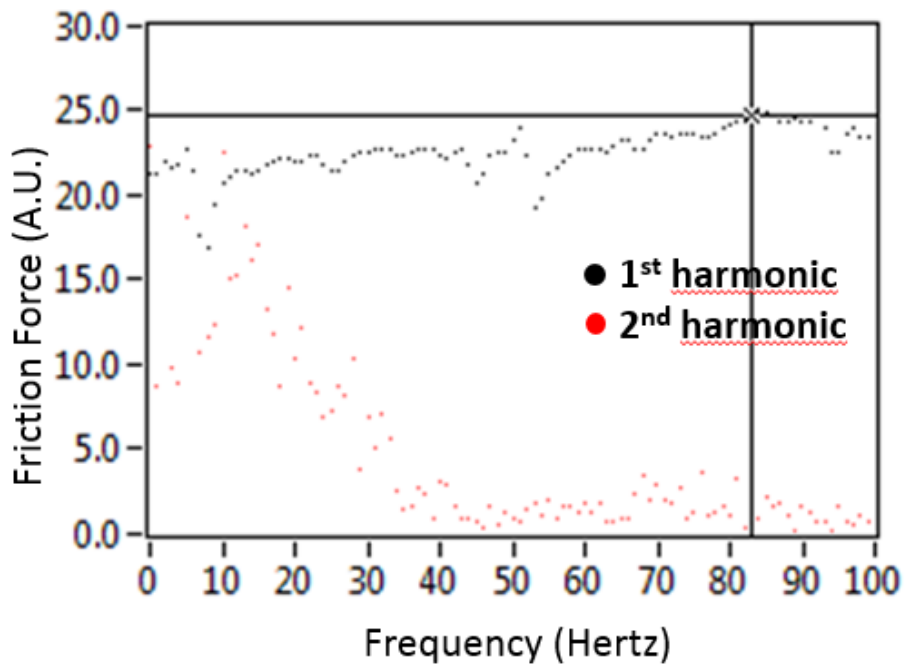


Figure 5.14 Scanning as function of frequencies: 1 – 100 Hz

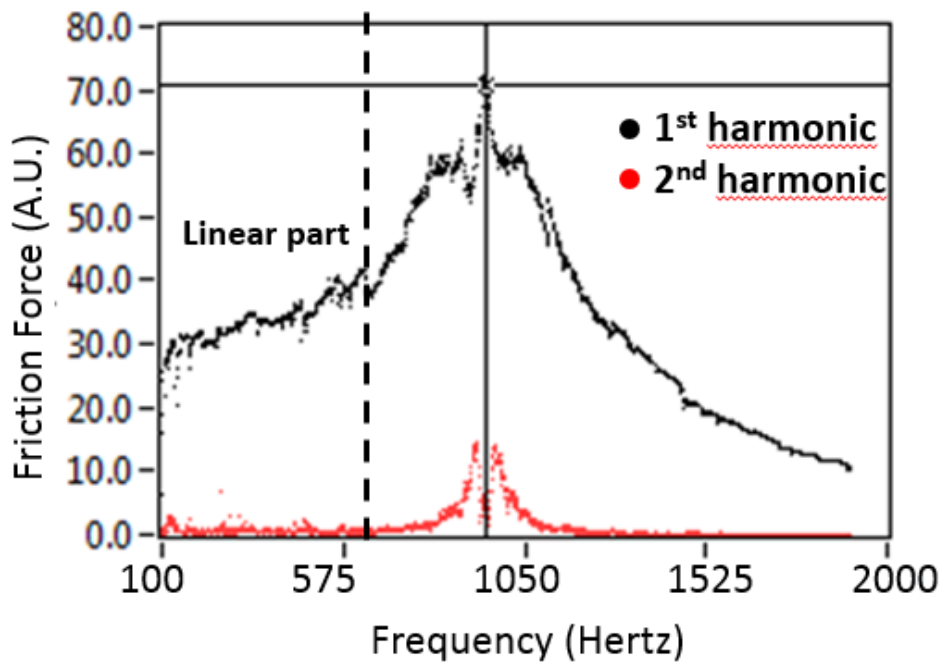


Figure 5.15 Scanning as function of frequencies: 100 – 2000 Hz

### C. Frequency 1000-10000 Hz

Scanning at higher range of frequency (1000 – 10000) was done look for the possible second harmonic peak. However, at frequency above 2000 Hz, the signals form a flat basic line. It supports the fact that resonance frequency of scanner tube is between 950 -1000 Hz as there is only single harmonic peak is found (see Figure 5.16).

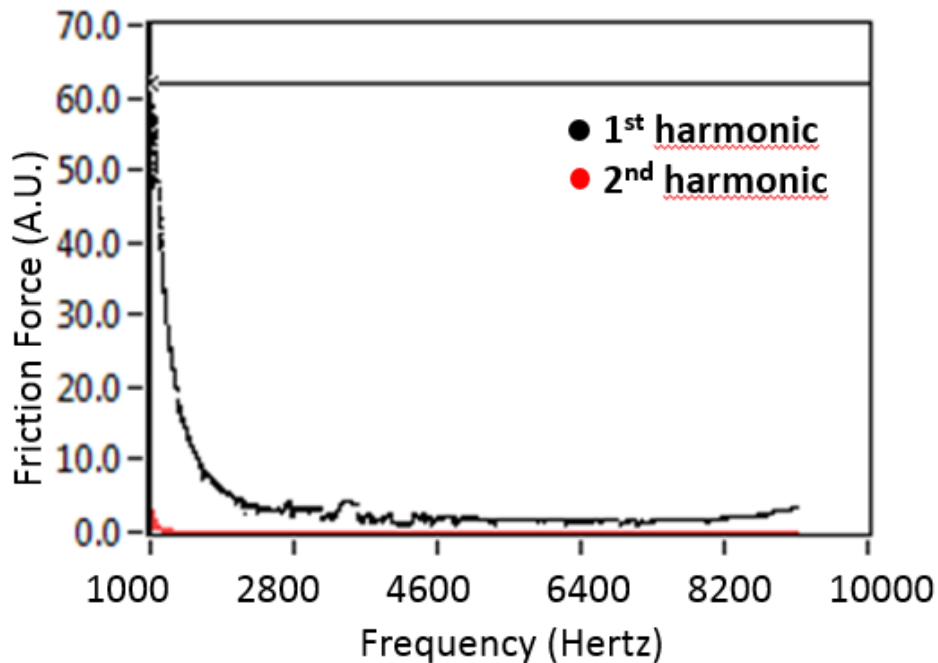


Figure 5.16 Scanning as function of frequency: 1000 - 10000 Hz

### 5.3.3 Linearity of piezoelectric scanner

In order to define the radius of circular track per applied voltage, series of experiment were done. It is important to verify the linearity response of piezoelectric scanner for any change of applied voltage amplitude and voltage angular frequencies. For simpler explanation, the term of amplitude (instead of voltage amplitude) and frequency (instead of angular frequency) will be used in the later part.

Circular displacements as many as 30.000 cycles were made onto gallium arsenide (GaAs) surface with silicon nitride tip (spring constant = 0,456 N/m). Experiments were done in liquid condition to avoid any influences of different environment as this technique will be applied for characterization of lipid bilayers. GaAs is known in microelectronics industry as semiconductor materials that is often scratched and indented to characterize mechanical properties

(Parlinska-Wojtan et al. 2008).

Gallium-arsenide (GaAs) is a soft material that is unfortunately not only producing necessary defect but also particles from AFM tip scratching. Experiments with various sliding velocity do not give significant differences of the circular tracks and the chips produced. It showed that sliding velocity has only little influence in chips (Wasmer et al. 2000). TEM observation showed that circular defect on the surface was induced by slip bands and perfect dislocations. During scratching, the deformation occurs in front of the tip and the sliding velocity allows perfect dislocations to propagate (Parlinska-Wojtan et al. 2008; Pouvreau 2007a). The usage of AFM sharp tip gives uneven depth of the tracks in which the stress concentration appeared due to plugging of the tip (Wasmer et al. 2008).

Firstly, various voltages were applied on several location points of the surface. Constant frequency was maintained at  $f = 200$  Hz. Diameter of circular track was measured by using software Nanoscope in three different axes: vertical, horizontal, and diagonal to address possibility of elliptical trace (see Figure 5.17. In addition, measurements were done by taking the outer circle because the width of the wear can becomes the source of uncertainty. Integral and proportional gain value used was 0.01. Low values were preferred to avoid tip oscillation. Diameters of circular traces were measured and were compared with the quasi-statical value (given from previous calibration of piezoelectric scanner for normal usage).

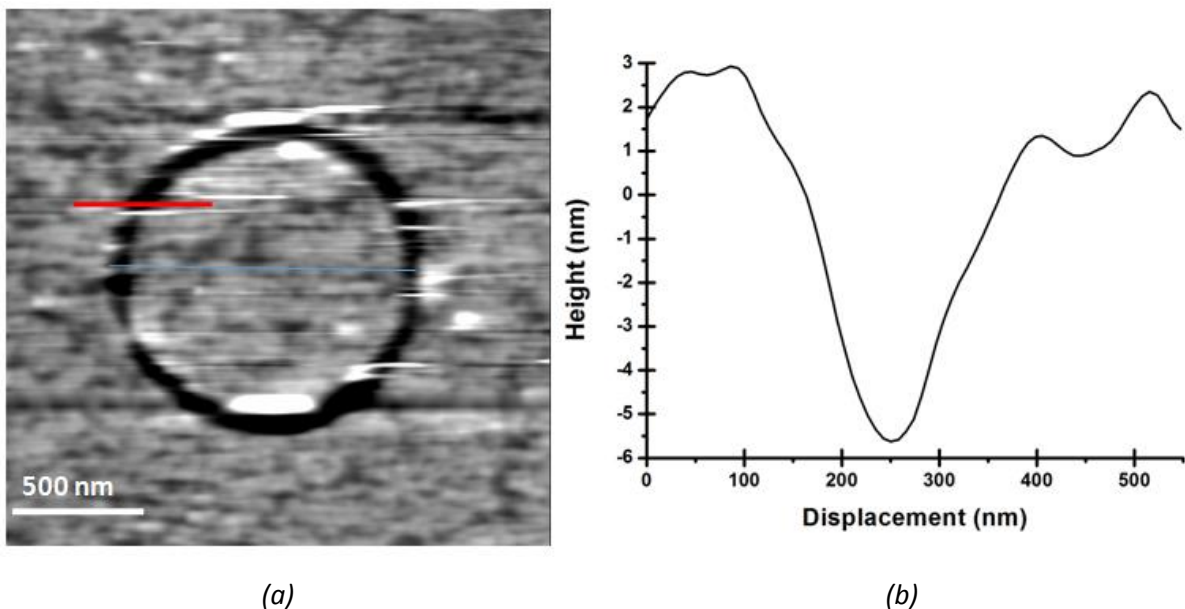


Figure 5.17 (a) Friction image of GaAs surface after circular AFM with sliding velocity of  $786 \mu\text{m/s}$  for 2.5 minutes ( $z\text{-scale} = 10\text{nm}$ ). (b) Section curve along the red line to visualize the width and the thickness of wear due to sliding of AFM tip

We have tested several frequencies ranging from 10 to 500 Hz. This range is based on the result of previous experiment explained in section 5.3.1 and 5.3.2. The change of circular trace diameter caused by various frequencies is given on Figure 5.18. Constant amplitude of 3 Volt was applied to generate approximately 1 μm diameter of circles, guided by quasistatic value of scanner displacement on X and Y direction plotted as diameter at 0 Hz). However, all circles generated from any range of frequencies give larger diameter. We assumed that the differences come from different mode of scanning, thus the scanner gives different response and shifts further. Quasistatic values were acquired for raster scan pattern, while we use circular scan pattern. For the frequency range from 10 to 500 Hz, we obtained partially linear response of circular diameter between 50 and 400 Hz. Thus, a linear fitting line was only made at the range of 50-400 Hz to determine the circular track diameter at untested frequencies in between. It is  $y (\mu m) = 1.147 + 5.315 \cdot 10^{-4}x$  for data of Z-axis with  $R^2 = 0.93$ . Circular traces at lower or higher frequencies than the permitted range are too far from our guidance value, consequently they are not recommended to be applied during experiment.

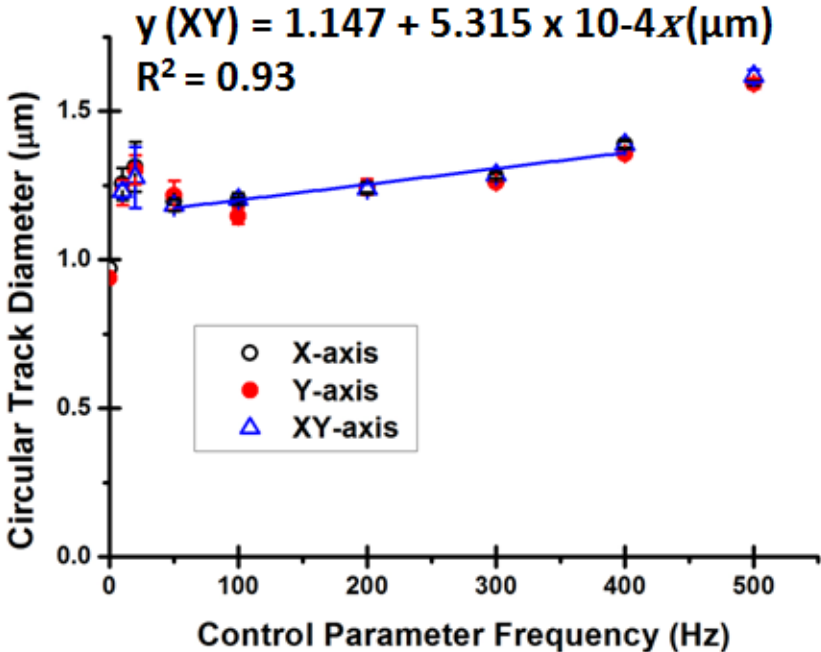


Figure 5.18 Circular trace diameter as function of frequencies at constant amplitude of 3Volt, quasistatic values are given at 0 Hz frequency. The linear regression line is made on limited frequency ranging from 50 to 400 Hz.

The summary of circular track diameter constant at nm per amplitude voltage is listed on Table 5.2. The values are simply acquired from the data of Figure 5.18 divided by three because they were measured at 3 volt of amplitude. Thus, the fitting line equation becomes

$(nm/Volt) = 380.848 + 0.185 x$  , for Z-axis whose the highest R<sup>2</sup> values.

Table 5.2 Constant of circular track diameter per amplitude voltage

Frequency	Circular track diameter per voltage amplitude nm/Volt		
	X-Axis	Y-Axis	XY-Axis
Quasistatic	323	313	N/A
10	418	409	410
20	438	434	426
50	399	405	394
100	401	382	401
200	415	415	413
300	426	420	428
400	463	452	463
500	531	531	539

The change of circular trace diameter caused by various frequencies and amplitudes is given on Figure 5.19 and Figure 5.20 that plots the data as function of frequency and amplitude respectively. The change of diameter for each set of amplitude maintains at the same pattern at different frequency (see Figure 5.19). It confirms the working range of frequency 50 – 400 Hz as discussed previously. Mean while, for all frequency, the evolution of diameter maintains in linear response as function of amplitude (see Figure 5.20 and Table 5.3 for the detail regression line equation for each set of frequency). Consequently, calibration constant can be defined as circle diameter in nm generated per voltage amplitude applied in Volt (nm/Volt). It is given that the amplitude defines the diameter of circular track. Even though on higher amplitude the diameter value gets further from quasistatic value, it does not perturb the linearity of amplitude. Thus, any values of amplitudes from 0.2 to 10 V can be applied. Amplitudes below 0.2 Volt have risk to induce tip shifting because the diameter of circular track is close to or smaller than tip radius (50 nm).



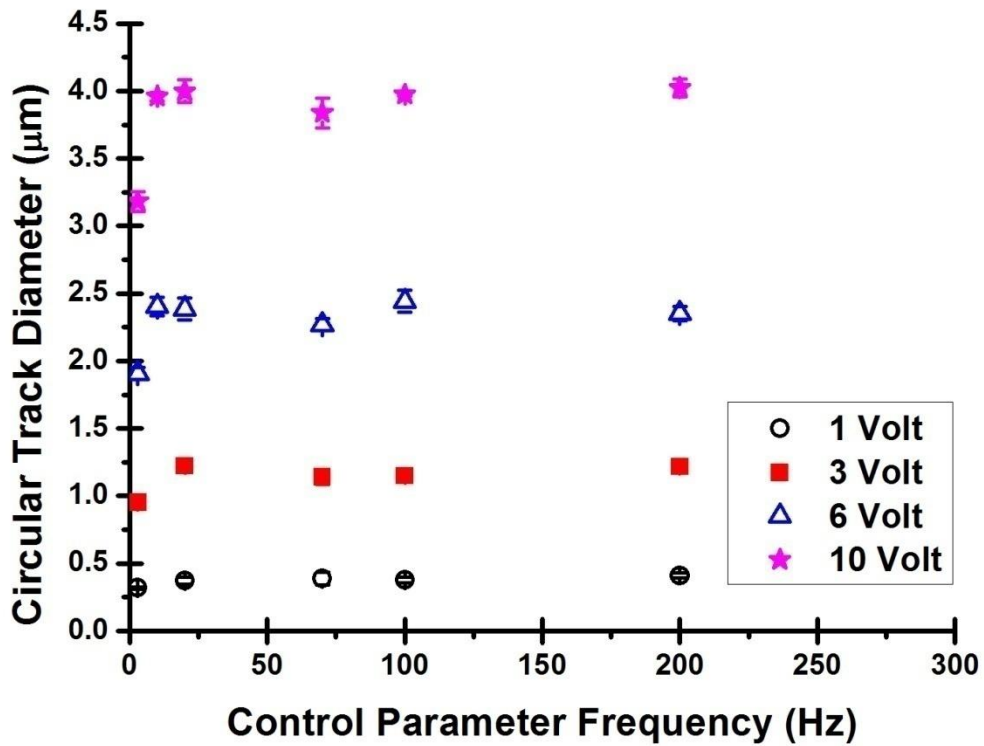


Figure 5.19 Circular trace diameter measured by CM-AFM at various amplitudes plotted as function of frequencies

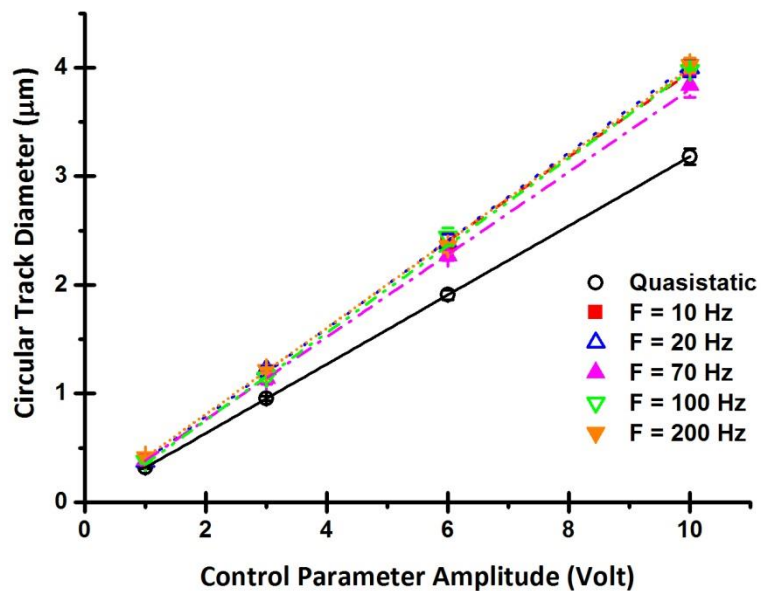


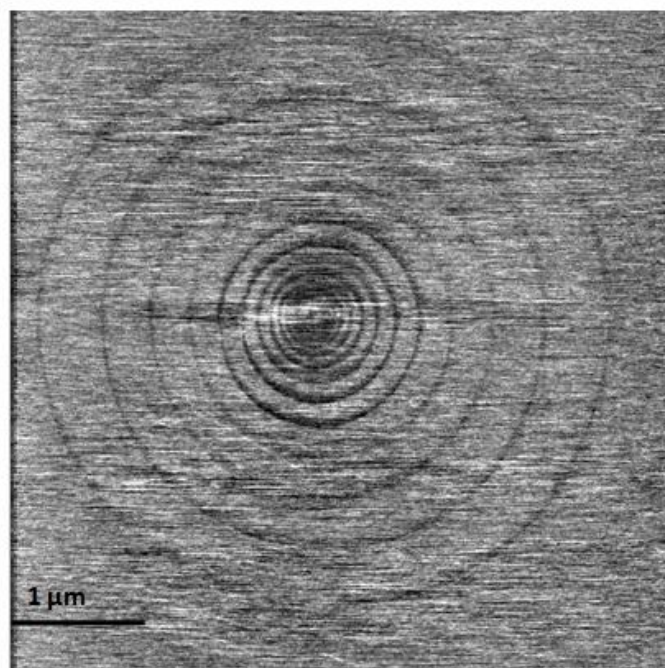
Figure 5.20 Circular trace diameter measured by CM-AFM at various frequencies plotted as function of amplitudes

Table 5.3 Regression line fitting of the curve in the Figure 5.20

Frequency (Hertz)	Linear Fitting	R <sup>2</sup>
Quasistatic	$y = 0.32x$	1
10	$y = 0.39x + 0.07$	1
20	$y = 0.41x - 0.2$	0.99
70	$y = 0.38x + 0.003$	0.99
100	$y = 0.41x - 0.05$	0.99
200	$y = 0.4x + 0.02$	0.99

By acquiring the range of both parameters, it is possible to calculate the maximum sliding velocity for our set up of CM-AFM by inputting the maximum frequency (400 Hz) and amplitude (10 Volt). The distance of sliding is the length of the circumference. So, we obtain 5,172  $\mu\text{m/s}$  of sliding velocity at  $f = 400$  Hz and  $A = 10$  Volt.

Later, several voltages were applied in the same location point in the surface. It is to investigate the possibility of nonlinearity of scanner due to change of voltages. Non linearity of piezoelectric scanner can cause shifting, especially during magnifying. Consequently, several circular traces were visualized with different diameter which respects each voltage. All circles appeared as ecocentric circle or have the same center point. This experiment was done on mica surface. At low applied voltage, the shifting is visible as the smaller circles (lower applied voltage) are leaning to top-left direction (see Figure 5.21). Thus, we propose to displace the AFM tip in every change of voltages to avoid cross point between circles because of shifting.



*Figure 5.21 Friction image of mica surface after circular AFM: amplitude = 0.1 - 10 Volt; frequency = 300 Hz (size 5x5 μm, z-scale = 0,1 Volt)*

## 5.4 Conclusion

The development of circular mode AFM requires optimization on the components of atomic force microscope. Special characteristics of CM-AFM: circular displacement, constant, continuous, and high sliding velocity require adapted protocol of calibration. Thus, the protocol for conventional AFM is not valid.

Calibrations were done to measure AFM probe's lateral force calibration constant which is needed in friction measurement and to verify the linearity of piezoelectric scanner. The tip's calibration was done based on our Scratch method. The conventional AFM was used for data acquisition. The main principle of this method is that there is correlation between surface slope and friction coefficient of the surface. This method requires constant slope of sample surface and constant friction coefficient. After some trials and errors, fused silica sample works the best with scratch method to fit our experimental condition. In addition, calibration factor can be influenced by medium of measurement.

Furthermore, we conclude that there are two parameters of CM-AFM to control sliding velocity: frequency and amplitude. The working frequency ranges from 50-400 Hz while the working amplitude ranges from 0.2-10 Volt. Thus, the limit sliding velocity in CM-AFM is 10 – 6,000 μm/s.

## Friction Measurement on Solid Surfaces by CM-AFM

This chapter discusses our early experiments to adapt CM-AFM in liquid environment. Friction and adhesion force measurements were done on surfaces such mica, glass, and thiol-functionalized gold layers in liquid medium. We are able to observe the dependency of friction and adhesion force with sliding velocity. The effect of ion in medium was also studied. It is found that the nano mechanical properties of the surfaces are influenced by the environmental change.

# Chapter 6

## Friction Measurement on Solid Surfaces by CM-AFM

### 6.1 Introduction

One of the advantages of AFM is that it allows characterization of the sample with minimum sample preparation procedure. Compared to STM which requires conductive materials, AFM can work on functional materials and biological samples in their native environment (Bhushan 2008). The development of friction force microscopy from the original atomic force microscopy adds the possibility to measure tribology at nano scale. Circular mode AFM was recently developed for nanomechanical characterization (Nasrallah et al. 2011). Friction measurement on several solid surfaces was done by CM-AFM as pre-eliminatory tests before the technique can be adapted to membranes' characterization. The selected surfaces are the usual solid supports of lipid membranes: mica, glass (cover slip), and thiol-functionalized gold layer as it was known that type of support can influence the properties of lipid bilayers(Seeger et al. 2010).

Mechanical measurement was also done in various medium as many researchers proved that mechanical response is sensitive to the environment ((Hauser & Shipley 1983; Garcia-Manyes et al. 2005; Cordoní et al. 2008; Gurtovenko & Vattulainen 2008; Vácha et al. 2009)). Examination in dry air medium results in the formation of a thin water layer due to ambient humidity. Consequently, the attractive capillary forces were present (Noel et al. 2012). However, in liquid environment, the capillary forces are absent and the dispersion interactions are reduced. Thus, the resolution of the image is improved (Leiro et al. 2017).

Moreover, the effect of ion in liquid medium was also studied as ionic strength can also alter the surface interaction forces. In acidic water (pH 5,5), the molar concentration of  $\text{H}_3\text{O}^+$  is higher than  $\text{OH}^-$ . For muscovite imaging, it has been proposed that  $\text{H}_3\text{O}^+$  could replace  $\text{K}^+$  ions in some sites of the mica surface due to energy lowering (Raviv et al. 2002). It means that the distances between surface features of the AFM images would be twice of those measured in air (Leiro et al. 2017). In addition, by dipping mica surface onto acidic solution, this ion-exchange process appears as surface cleaning process from the adsorbed contaminants

resulting higher adhesion forces than native mica surface (Christenson 1993). In addition, the lipid membranes that will be deposited on the solid mica support, are sensitive to the presence of cations. The change in cation type and their concentration affect the mechanical properties of lipid membranes (Garcia-Manyes et al. 2005). So, we aim to measure the mechanical response of solid supports as function of medium, cations, and ionic concentration.

## 6.2 Characterization of bare mica surface

### 6.2.1 Morphology of mica

Figure 6.1 shows the topography image of mica surface after examination by CM-AFM with two tips with different spring constants. Both images do not show a clear circular track indicating that plastic deformation is not happened on the surfaces.

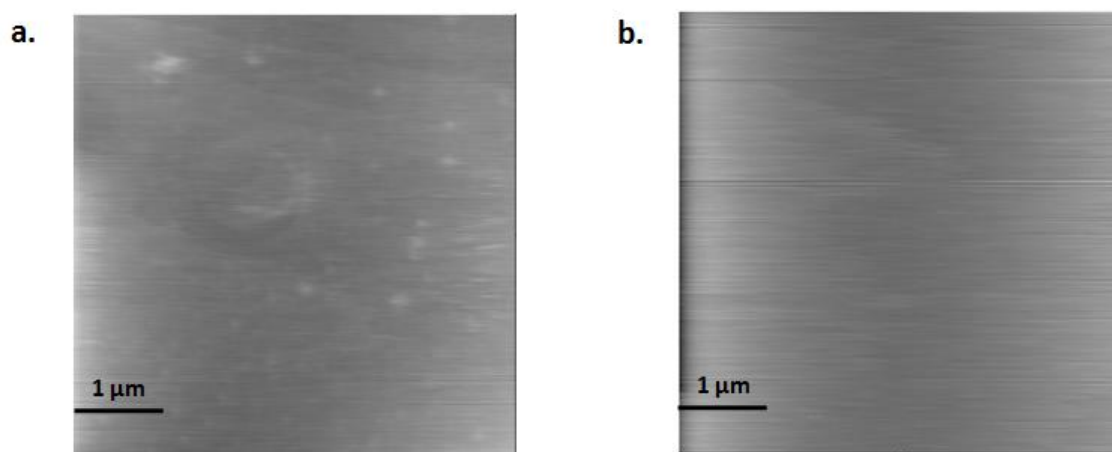


Figure 6.1 Topography image of mica surface after experiment by CM-AFM in air at sliding velocity  $1000 \mu\text{m/s}$ . Size  $5 \mu\text{m} \times 5 \mu\text{m}$ ;  $z$ -range =  $10 \text{ nm}$ . The tip used has a spring constant of (a)  $0.2 \text{ N/m}$  and (b)  $0.05 \text{ N/m}$ .

### 6.2.2 Data acquisition

The force measurement by CM-AFM generates two curves simultaneously: deflection and friction. Deflection refers to normal deflection of cantilever while friction refers to torsion or lateral deflection of the cantilever. Both signals were recorded in voltage units. By

converting these data with the calculated value of spring constant and lateral calibration constant, we can easily plot the friction force as function of the normal force (see Figure 6.2).

The typical friction curve of mica surface measured in liquid medium (water) is seen on Figure 6.2. When the tip approaches the surface, it detects the short range interaction force causing a small increase in the friction force. As the applied force is increased, the tip finally contacts the mica surface, which provokes an abrupt increase of friction. Later, the friction force increases proportionally with the normal force. It shows that friction measurement of mica in water follows the Amonton's law of solid friction (Persson & Tosatti 1995).

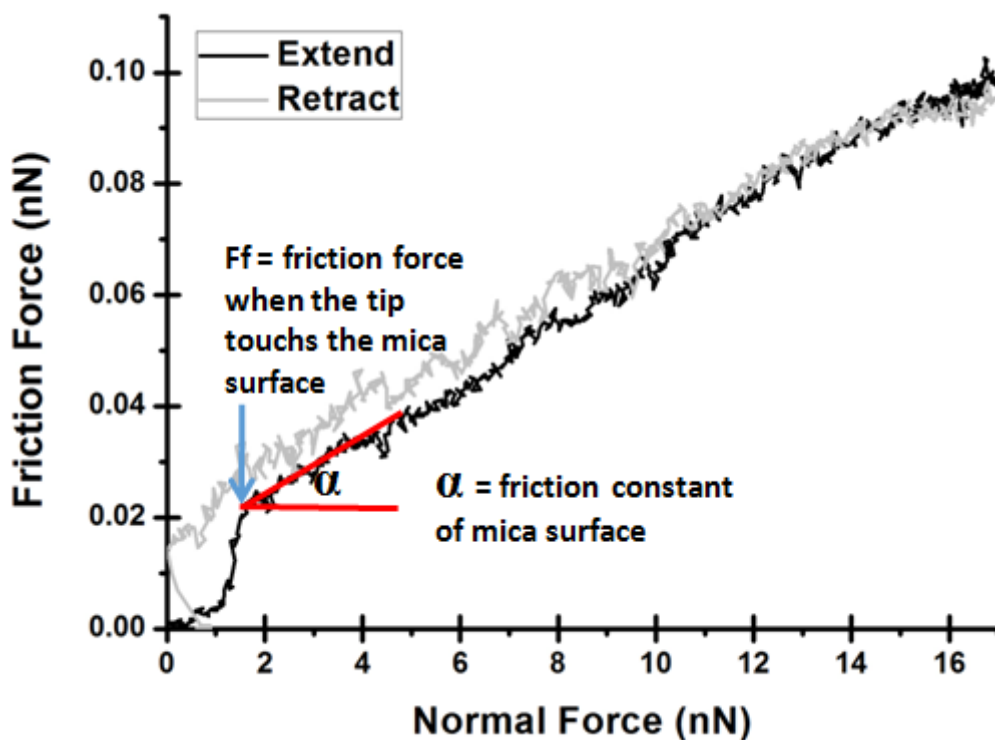


Figure 6.2 Example of curve of friction force versus normal force measured on mica (measured by CM-AFM in water medium; sliding velocity = 215  $\mu\text{m/s}$ ). The important values recorded are the initial friction force  $F_f$ , indicated by the arrow, and friction coefficient  $\alpha$  (slope).

There are two values that can be obtained from the force curve: the initial friction force and the friction coefficient. The initial friction force  $F_f$  is the friction value recorded when the tip contacts the sample as shown by blue arrow in Figure 6.2. Given that the friction force varies linearly with the applied normal force, then the friction coefficient  $\alpha$  of the sample surface can be calculated as the slope of the curve. With tip-approaching velocity of 15 nm/s, each curve was recorded within 33 seconds. Later, it is possible to plot the evolution of both

$F_f$  and  $\alpha$  as function of the sliding velocity. Minimum ten curves were acquired for each sliding velocity.

### 6.2.3 Friction in air and water medium

In the beginning, a friction measurement test under ambient condition ( $T=21^\circ\text{C}$ ) was done on a mica surface (see Figure 6.3). A constant circular mode frequency of 300 Hz was used with modulation of circular mode amplitude between 0.1 – 10 V (circular radius of 20 – 2,000 nm). With the interface program we have, it is possible to increase the amplitude automatically without withdrawing the AFM tip. Here, we can highlight one of the main advantages of CM-AFM: its high sliding velocity (up to 2500  $\mu\text{m/s}$ ).

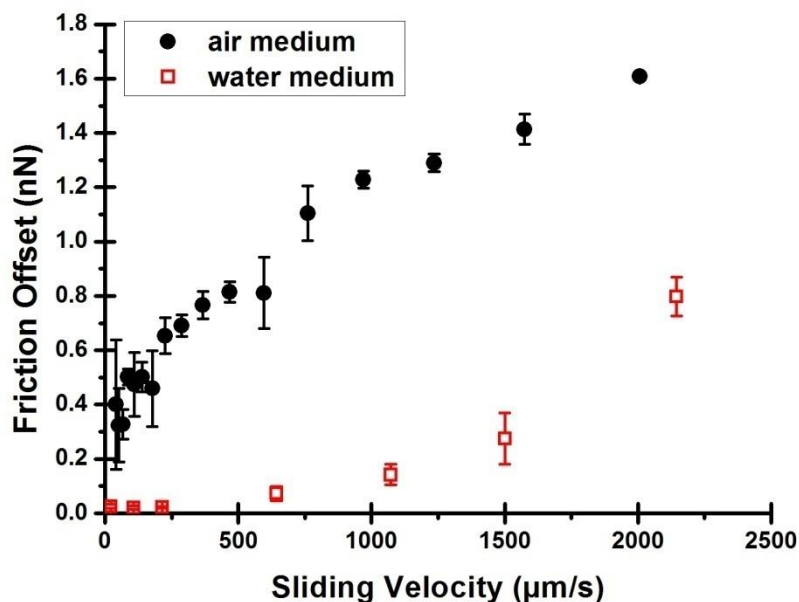


Figure 6.3 Friction force versus sliding velocity of mica surface examined by CM-AFM in air (sliding velocity = 20 – 2200  $\mu\text{m/s}$ ), in ultrapure water, and in Tris-NaCl buffer (sliding velocity = 20 – 2000  $\mu\text{m/s}$ )

Figure 6.3 shows the comparison between friction measurement in dry air and in water. Generally, the friction measured in air is higher than the friction measured in liquid. In both medium, friction force of mica increases with sliding velocity. However, it increases in different pattern. In air, friction increases drastically at low sliding velocities ( $>215\ \mu\text{m/s}$ ) then it rises linearly. However in water, friction slowly increases at low sliding velocities. The fact that adhesion force is time dependence due to surface adsorption may be related to this result



(Christenson 1993). Besides, the presence of capillary forces due to humidity under air condition may also contribute to this behavior (Mazeran 2006). Since, it is not linearly increasing; it is complicated to measure the viscous friction coefficient.

At increasing sliding velocity, the friction coefficient is also increasing (see Figure 6.4). Moreover, the difference of increase pattern between measurement in air and in liquid is also found in the case of friction coefficient. Friction coefficient increases until certain sliding velocity then it becomes relatively constant. Surprisingly, considering the previous graph (Figure 6.3), friction coefficient of mica measured in liquid was higher than those measured in air.

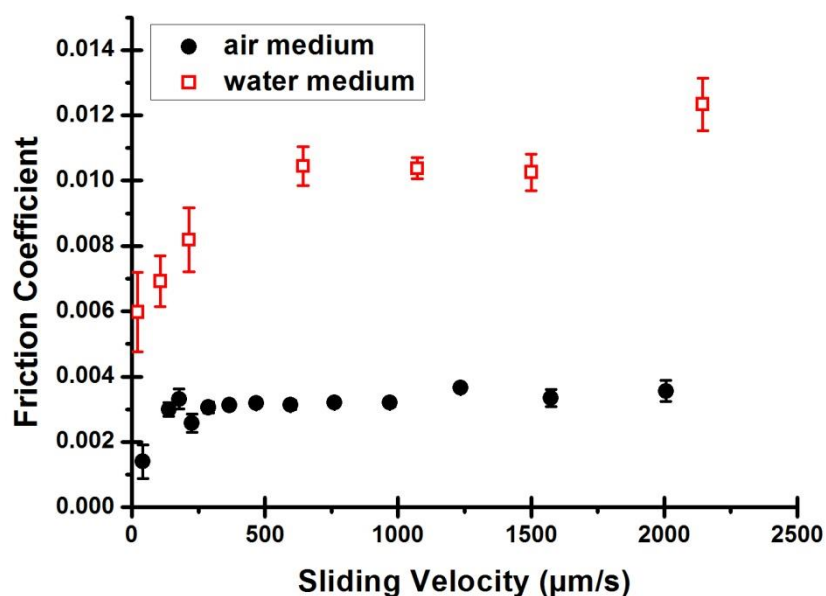


Figure 6.4 Friction coefficient versus sliding velocity of mica surface examined by CM-AFM in air (sliding velocity = 20 – 2200  $\mu\text{m/s}$ ), in ultrapure water, and in Tris-NaCl buffer (sliding velocity = 20 – 2000  $\mu\text{m/s}$ )

#### 6.2.4 Effect of environmental change

Biological membranes are prepared and measured under physiological conditions so it requires Tris-NaCl buffered medium. In order to study the effect of environmental changes on the frictional properties of mica surface, we modified the content of liquid medium. Figure 6.5 shows the comparison of friction measured in air, water, and Tris buffer (pH 7.4). We have already shown that the friction force is increasing significantly with sliding velocity when the

measurement was done in air and water. In buffered liquid medium, the friction force of mica also increased with sliding velocity but to a considerable lower extent (up to 0.13 nN at maximum with velocity of 2150  $\mu\text{m/s}$ ). Given that buffered medium has higher concentration of ions, the van der Waals attraction dominates the forces between surfaces and overcomes the weak repulsion, causing a jump into strongly adhesive contact (Raviv et al. 2002). Moreover, the presence of ions can increase the distance of tip-substrate due the ion adsorption by the surface. Thus, at buffered medium, there are more ions shielded the surface causing decrease of shear stress and friction force (Guegan et al. 2016) compared to measurement in ultrapure water.

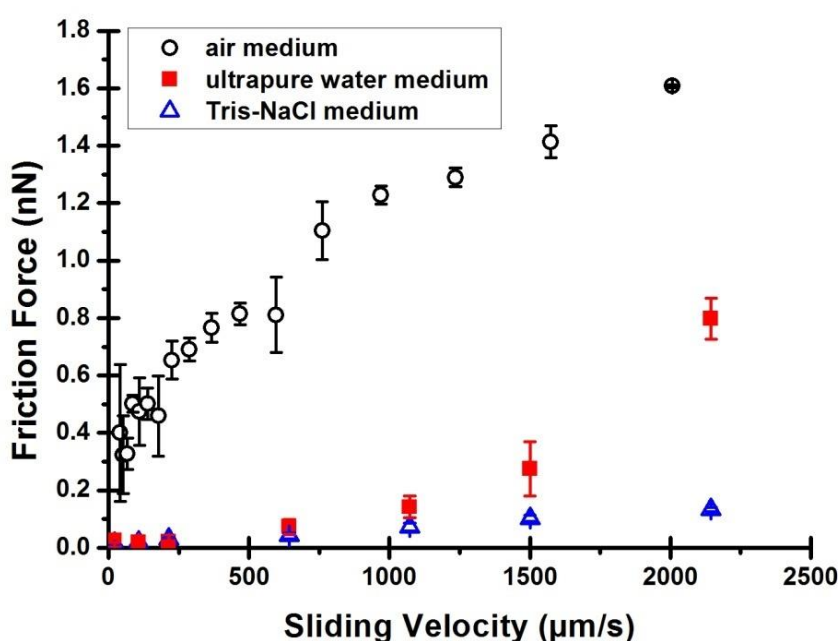


Figure 6.5 Friction force versus sliding velocity of mica surface examined by CM-AFM in air (sliding velocity = 20 – 2200  $\mu\text{m/s}$ ), in ultrapure water, and in Tris-NaCl buffer (sliding velocity = 20 – 2000  $\mu\text{m/s}$ )

Following, the same trend found for measurements in air and water medium, the friction coefficient of mica increases until a certain limit of sliding velocity (<215  $\mu\text{m/s}$ ). At higher sliding velocity, it is relatively constant (see Figure 6.6).

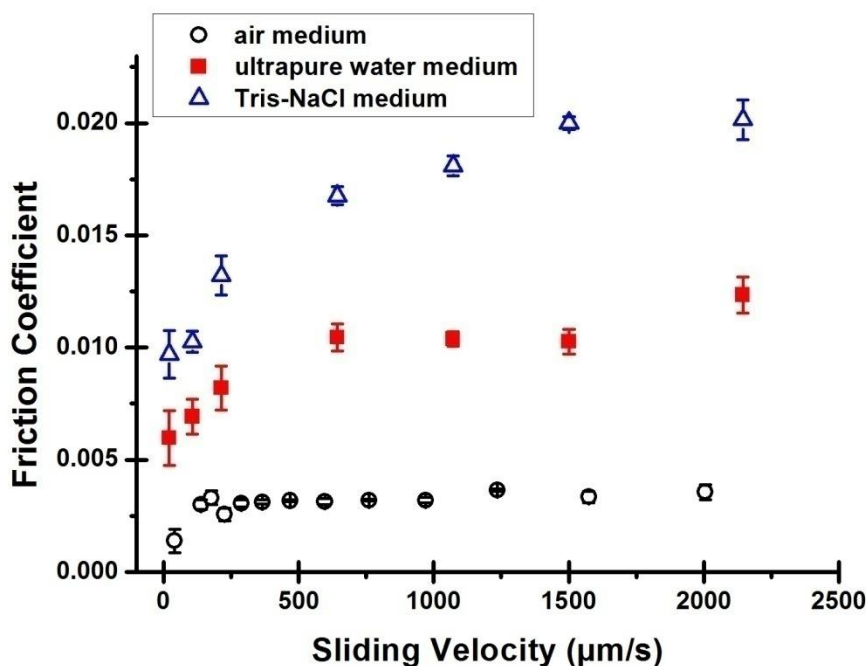


Figure 6.6 Friction coefficient versus sliding velocity of mica surface examined by CM-AFM in air (sliding velocity = 20 – 2200  $\mu\text{m/s}$ ), in ultrapure water, and in Tris-NaCl buffer (sliding velocity = 20 – 2000  $\mu\text{m/s}$ )

In the previous experiments, we have compared the mechanical properties of mica surface measured in dry and wet environments. In liquid medium, we have compared the medium with and without salts (buffer solution and ultrapure water). The next experiment was done to observe the effect of cations concentration in the buffered medium. Figure 6.7 and Figure 6.8 shows the evolution of friction force and friction coefficient of mica at various sliding velocities in three different concentration of calcium. Calcium has been proved to improve the fusion mechanism in preparation of SLBs and the lateral organization of SLBs. Calcium at 3 mM did not give significant effect compared to pure Tris buffer. However, with the concentration of 150 mM, calcium increases the friction force of mica by approximately five folds from 0.13 nN in 10 mM Tris buffer to 0.75 nN in 10 mM Tris + 150 mM calcium. These results are in agreement with previous study held by (Xu & Salmeron 1998b). They found that even at high humidity,  $\text{Ca}^{2+}$  increases the friction forces of mica compared to the presence of  $\text{K}^+$  or  $\text{H}^+$ . It is because of several reasons:  $\text{K}^+$  or  $\text{H}^+$  ions are more easily displaced by AFM tip than the divalent ions; and the tip detect rougher surface when it slides over the less mobile  $\text{Ca}^{2+}$ .

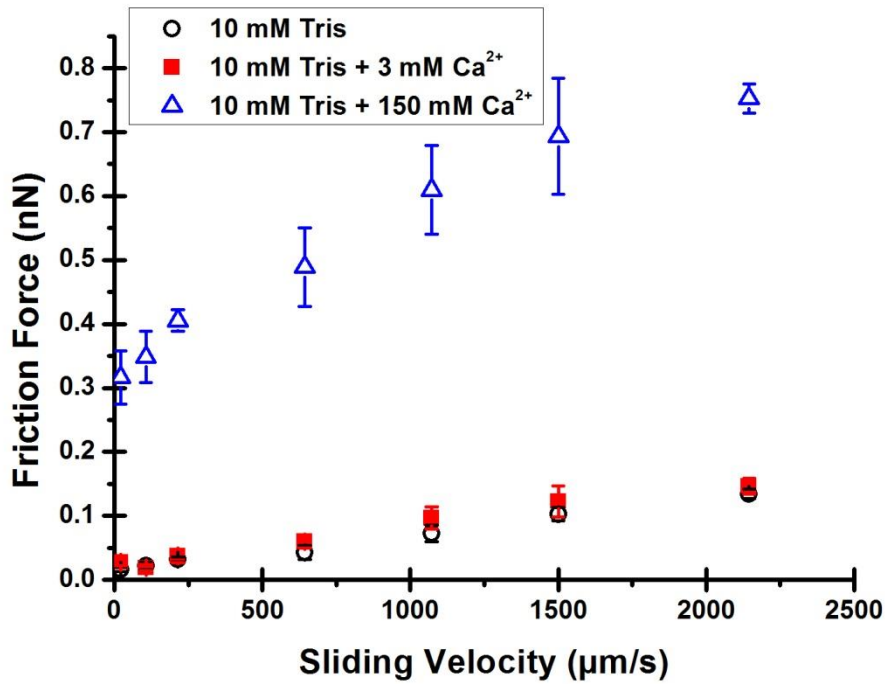


Figure 6.7 Friction force versus sliding velocity of mica surface examined by CM-AFM (sliding velocity = 20 – 2200  $\mu\text{m/s}$ ) in different liquid composition measured at  $f = 175$  Hz and  $A = 0.1 - 10$  V. The viscous friction coefficient ( $\eta$ ) for mica in Tris is  $54.94 \pm 3.47$  nN.s/m ( $R^2=0.99$ ); in Tris+3mM  $\text{Ca}^{2+}$  is  $60.45 \pm 5.48$  nN.s/m ( $R^2=0.95$ ); and in Tris+150mM  $\text{Ca}^{2+}$  is  $188.45 \pm 13.57$  nN.s/m ( $R^2=0.98$ )

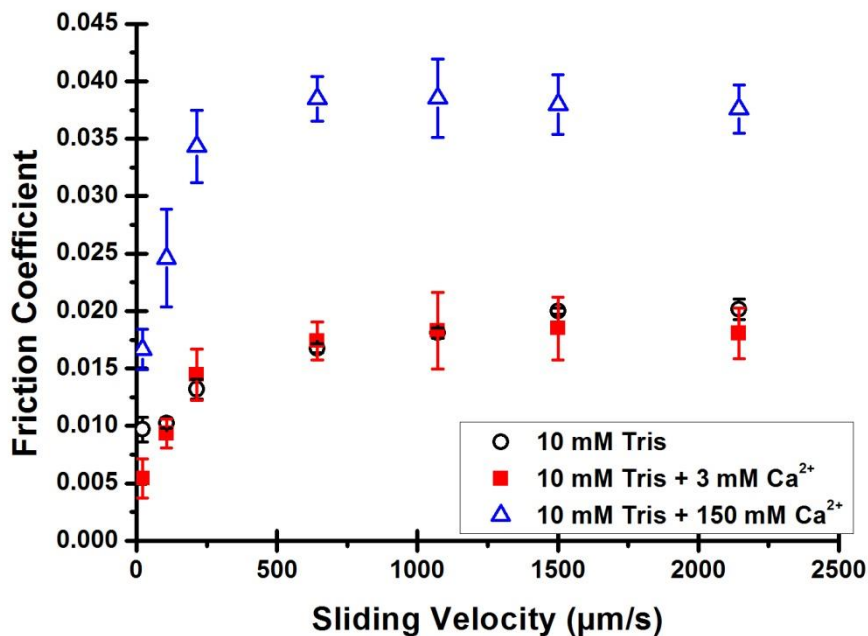


Figure 6.8 Friction coefficient versus sliding velocity of mica surface examined by CM-AFM in different ionic compositions measured by CM-AFM; sliding velocity 20 – 2200  $\mu\text{m/s}$ )

## 6.3 Characterization of bare glass surface (cover slip)

### 6.3.1 Morphology of the surface

Figure 6.9 gives the morphology image of bare glass surface before and after mechanical characterization by CM-AFM in water medium. A microlever tip (spring constant = 0.2 N/m) was used to measure both mechanical resistance and friction response of the surface. We do not spot the circular trace on the surface implying that plastic deformation of surface did not occurred.

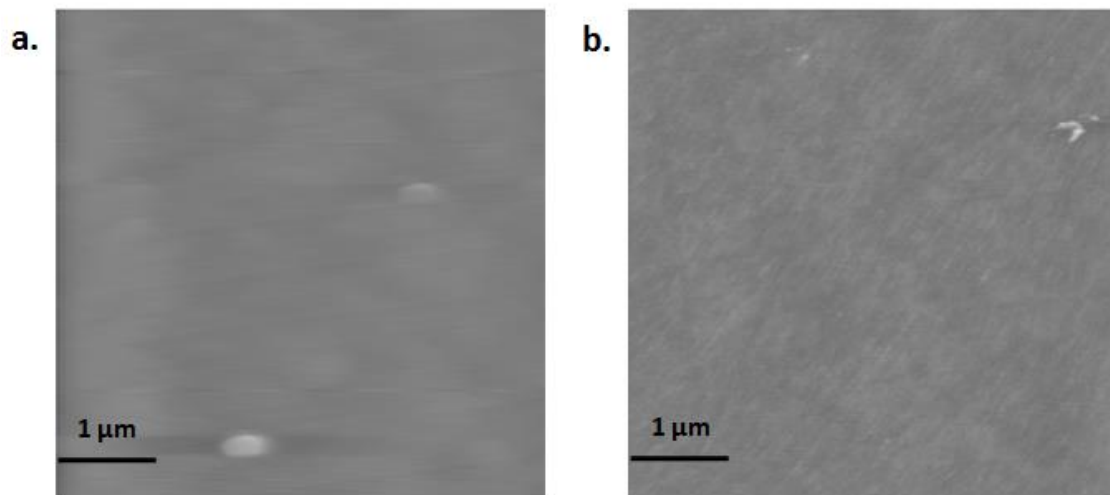


Figure 6.9 Bare glass surface (a) before and (b) after circular mode AFM examination (amplitude = 10 V; frequency= 175 Hz). Size = 5  $\mu\text{m}$  x 5  $\mu\text{m}$ , z-range = 10 nm

### 6.3.2 Data acquisition

The tip-approaching velocity (vertical velocity) used was 15nm/s. Consequently, raw force curves: deflection and friction forces, were recorded every 33 seconds. Both curves were combined resulting friction force curve as a function of the normal force. Typical friction curve of glass surface is shown on Figure 6.10. The extent and retract curves were similar to each other. An abrupt jump of friction force was recorded when the AFM tip contacted the glass surface. Then, it increased linearly with the increase of normal force. The slope of friction force is referred to viscous friction coefficient  $\alpha$  of glass surface.

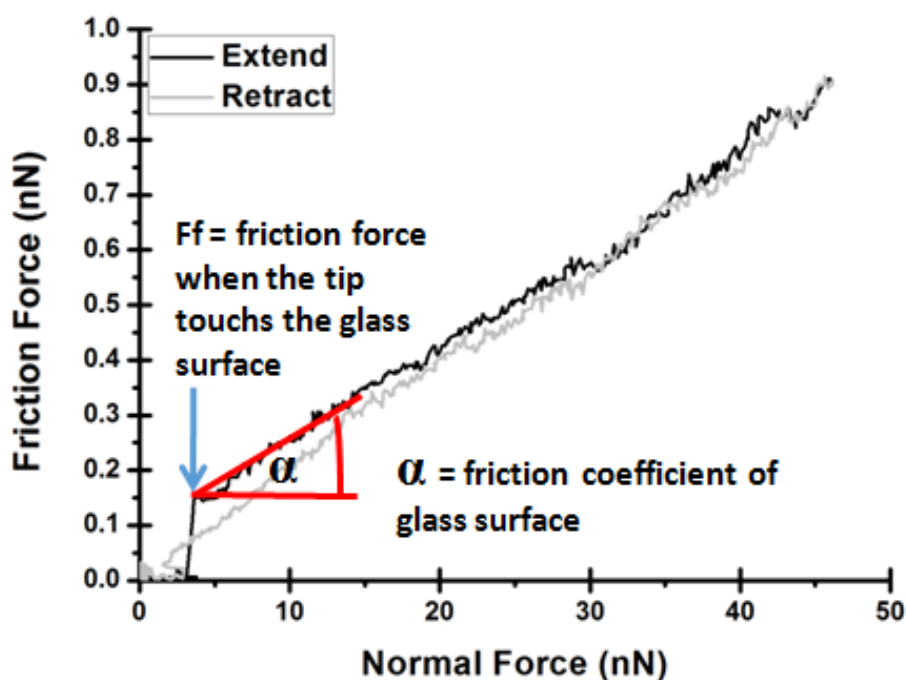


Figure 6.10 Example of curve of friction force versus normal force measured on glass (Measured by CM-AFM in water medium; sliding velocity = 215  $\mu\text{m/s}$ ). The important values recorded are the initial friction force  $F_f$  indicated by the arrow and friction coefficient  $\alpha$  (slope)

### 6.3.3 Effect of environmental change (addition of cations)

The presence of ions in the medium can alter the mechanic response of the sample because it affects the interaction force between AFM tip and surface sample.

The effect of cations present in the medium to the friction force of glass surface is shown on Figure 6.11. In all cases, the friction force is linearly proportional with the sliding velocity. The friction force in ultrapure water is significantly higher than in the presence of salts. By comparing the friction of glass in different media, it can be assumed that the ionic size of the cations plays a role in the friction mechanism of the surface. Measurement in the presence of potassium ions whose ionic size is 1.52  $\text{\AA}$  (Shannon 1976) gives the lowest friction value and the smallest slope of regression line among the series of alkali used. Lithium and sodium ion whose ionic sizes are respectively 0.9 and 1.16  $\text{\AA}$ , yield lower friction values. Interestingly, viscous friction coefficient of the glass is inversely proportional with the ionic size of the cations (see Figure 6.12).

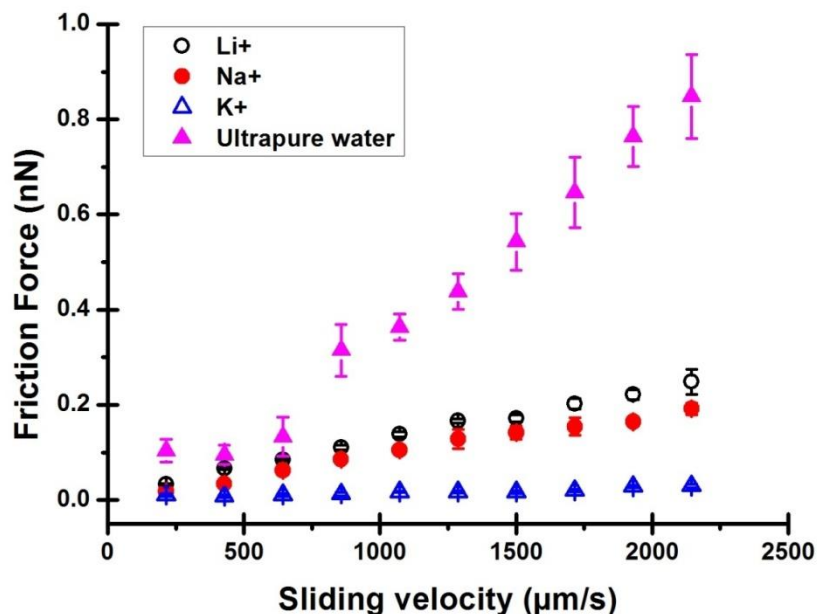


Figure 6.11 Friction force as function of sliding velocity for bare glass measured in 10 mM Tris buffer containing 150 mM salts. The viscous friction of glass friction measured in water, buffer containing lithium, sodium, or potassium is  $383.6 + 22.17 \text{ nN}\cdot\text{m/s}$  ( $R^2=0.95$ );  $161.11+2.62 \text{ nN}\cdot\text{m/s}$  ( $R^2=0.98$ );  $91.04+2.93 \text{ nN}\cdot\text{m/s}$  ( $R^2=0.98$ ); and  $10.44+1.42 \text{ nN}\cdot\text{m/s}$  ( $R^2=0.85$ ) respectively. Measurements were done by CM-AFM with sliding velocity 200 – 2000  $\mu\text{m/s}$ .

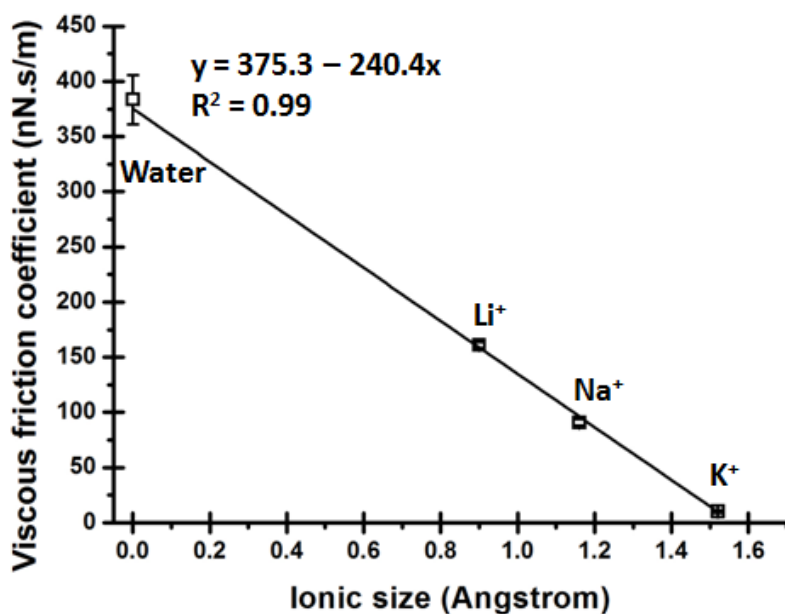


Figure 6.12 Viscous friction coefficient of bare glass surface in the presence of different cations as function of their crystalline ionic size respectively (Shannon 1976). ( $\text{Li}^+ = 0.90 \text{ \AA}$ ;  $\text{Na}^+ = 1.16 \text{ \AA}$ ; and  $\text{K}^+ = 1.52 \text{ \AA}$ ). The zero point of ionic size refers to the measurement in ultra pure water. Measurements were done by CM-AFM with sliding velocity 200 – 2000  $\mu\text{m/s}$ .

Surprisingly, contrary to the friction force, the friction coefficient of the glass surface seems to be independent of the ionic composition in water (see Figure 6.13). However, the cause is still unknown.

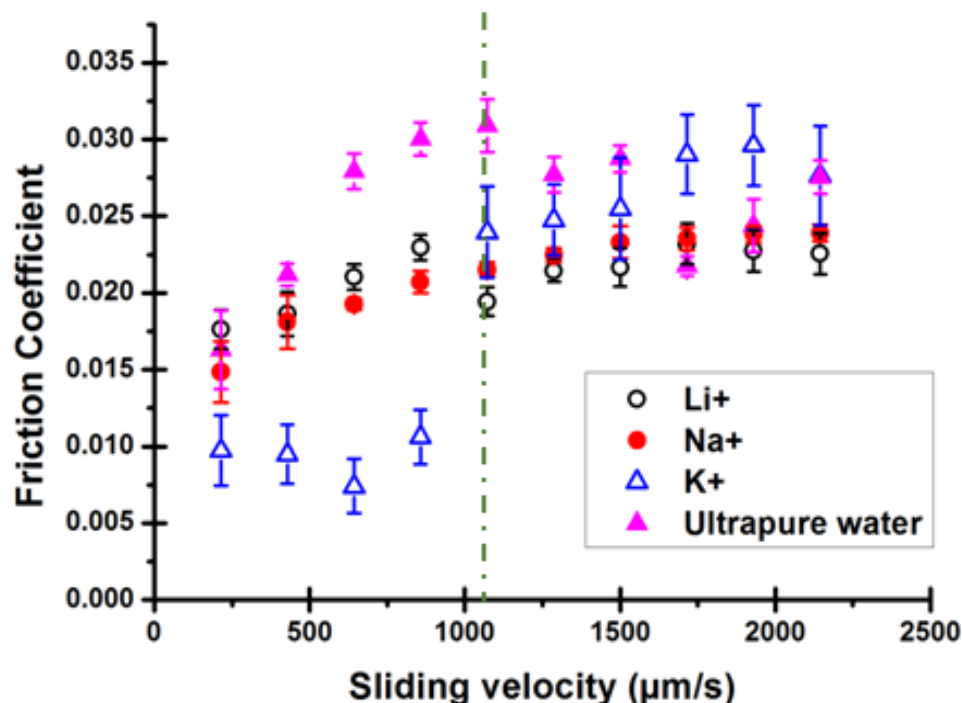


Figure 6.13 Friction coefficient as function of sliding velocity for bare glass measured in water or 10 mM Tris buffer containing 150 mM salts: LiCl, NaCl, or KCl. Measurements were done by CM-AFM with sliding velocity 200 – 2000 µm/s.

## 6.4 Characterization of thiol-functionalized gold substrates

Self-assembled monolayer (SAM) of oriented organic molecules is widely used in lubrication, electrochemistry, photochemical mechanism, electrical conduction, catalysis, and also biological membranes (Nuzzo & Allara 1983). SAMs were prepared through adsorption of alkanethiols solution (in ethanol) on gold substrate. The molecules are spontaneously organized on the substrate (Soriaga & Hubbard 1982). Gold layer is used because of its inertness toward oxidation or corrosion.

Initially, gold layer is hydrophilic. To enhance the hydrophilicity, mercapto-1-undecanol was used to functionalize the surface because it has alcohol end-group. Gold layer surfaces were functionalized with 1-undecanethiol ( $\text{CH}_3(\text{CH}_2)_{10}\text{SH}$ ) or mercapto-1-undecanol



(HS(CH<sub>2</sub>)<sub>9</sub>CH<sub>2</sub>OH). Because of the methyl end-group, 1-undecanethiol yields a hydrophobic monolayer on gold support. Thus, both can change the surface properties of gold layer to be hydrophobic or more hydrophilic. In order to characterize the surface treatment, we measured the water contact angle of the freshly functionalized surface (Zgura et al. 2010). Then, morphological study was done by AFM. CM-AFM was employed to observe the mechanical response (adhesion and friction force) of both surfaces as function of sliding velocity.

### 6.4.1 Contact angle of the surface

The contact angle measurement was illustrated on *Figure 6.14*. The surface functionalized with 1-undecanethiol has larger contact angle (100.1°) due to its hydrophobicity. In contrary, water can cover more surface area of the sample functionalized with mercapto-1-undecanol resulting in a small contact angle (20.2°). This value of contact angle was in the same range as one found in a previous report (Booth et al. 2009).

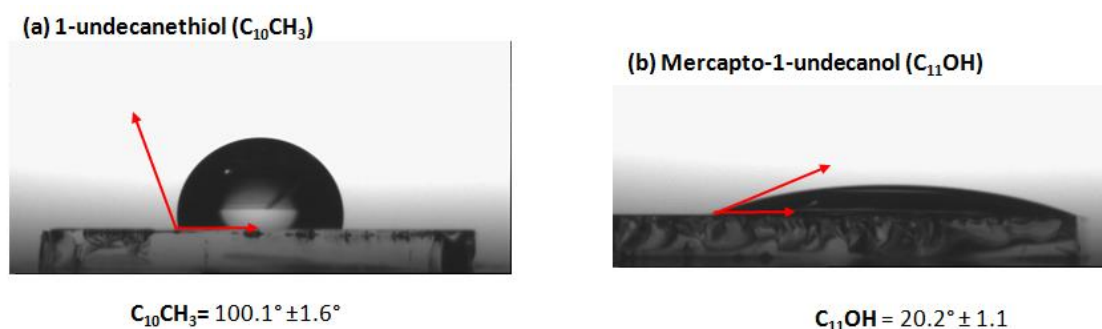


*Figure 6.14* Contact angle measurement on gold layer functionalized with (a) 1-undecanethiol (C<sub>10</sub>CH<sub>3</sub>) and (b) mercapto-1-undecanol(C<sub>11</sub>OH)

### 6.4.2 Morphology of the surface

AFM images were acquired before and after CM-AFM measurement. We do not spot any differences on the images (see *Figure 6.15*). The applied load is not high enough to generate plastic strain or wear.

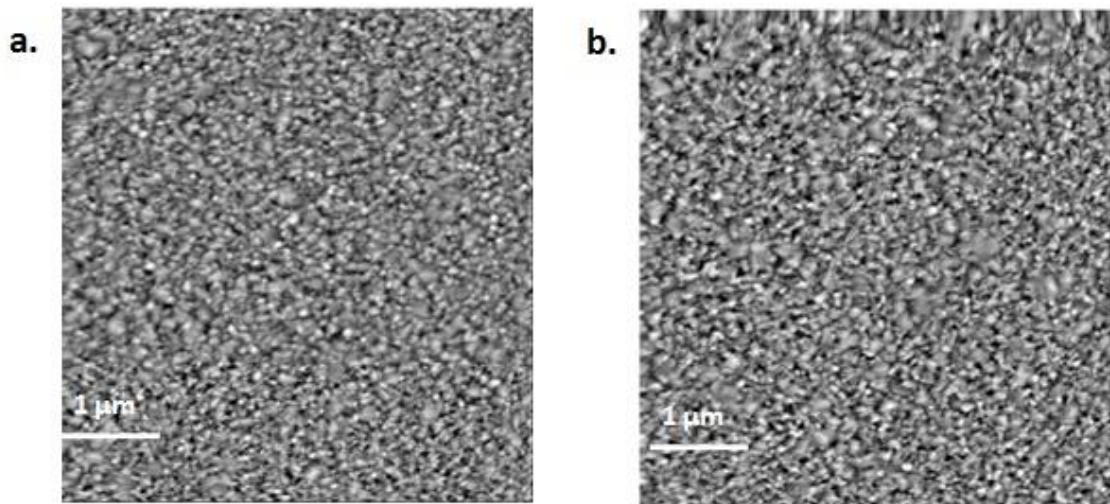


Figure 6.15 Gold-coated-glass surface functionalized with  $C_{10}CH_3$ , (a) before and (b) after circular mode AFM examination. Size =  $5 \mu m \times 5 \mu m$ , z-range = 10 nm

### 6.4.3 Mechanical Characterization of Functionalized-Gold Layer

For hydrophilic surface (functionalized with  $C_{11}OH$ ), adhesion force was absent in all range of sliding velocities (see Figure 6.16). Adhesion force was found only on hydrophobic surface (functionalized with  $C_{10}CH_3$ ) as shown on Figure 6.16. Adhesion force is the force needed to retract the tip from the surface thus it is negative. Furthermore, it is also found to be decreasing with sliding velocity (see Figure 6.17) even though it follows different trends compared to ones published by Noel et al (Noel et al. 2012). Noel et al did the measurement under air condition. Thus, it is clear that the medium of measurement affect the tip-surface interaction force.

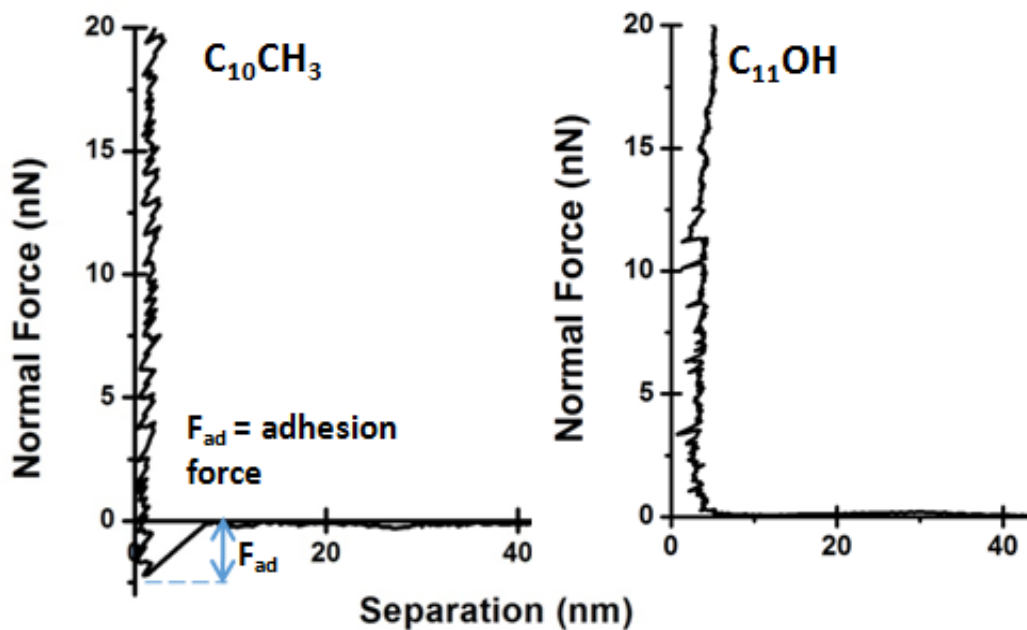


Figure 6.16 Normal force as function of separation distance of tip-surface measured by CM-AFM at sliding velocity of  $120 \mu\text{m/s}$  for hydrophobic ( $\text{C}_{10}\text{CH}_3$ ) and hydrophilic ( $\text{C}_{11}\text{OH}$ ) gold layer. Adhesion force is indicated as negative normal force

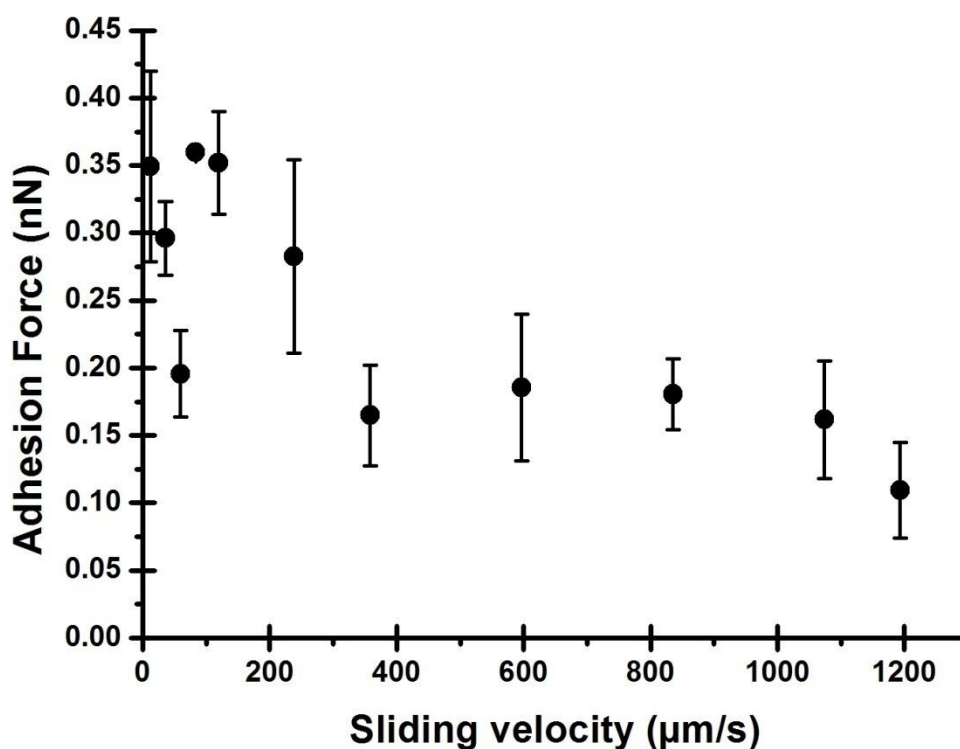


Figure 6.17 Adhesion force as function of sliding velocity for gold layer functionalized with  $\text{C}_{10}\text{CH}_3$ . The experiment was conducted in 10 mM Tris buffer pH 7.4 medium using CM-AFM; sliding velocity 10 – 1200  $\mu\text{m/s}$ )

Figure 6.18 shows the typical friction curve for hydrophobic gold layer found at various sliding velocities. Friction measurement was only done on hydrophobic surface. There is an abrupt jump in friction force when the tip contacts the sample surface then it increases linearly with the normal force. This result gives similar pattern with the Hertzian model indicating that thiol-functionalized gold surface behaves as near-elastic materials (Kiely & Houston 1999). The approaching and retracting curves are parallel to each other with small hysteresis. The initial friction force and friction coefficient of the surface are recorded for each sliding velocity. Friction coefficient is the ratio between friction and normal force.

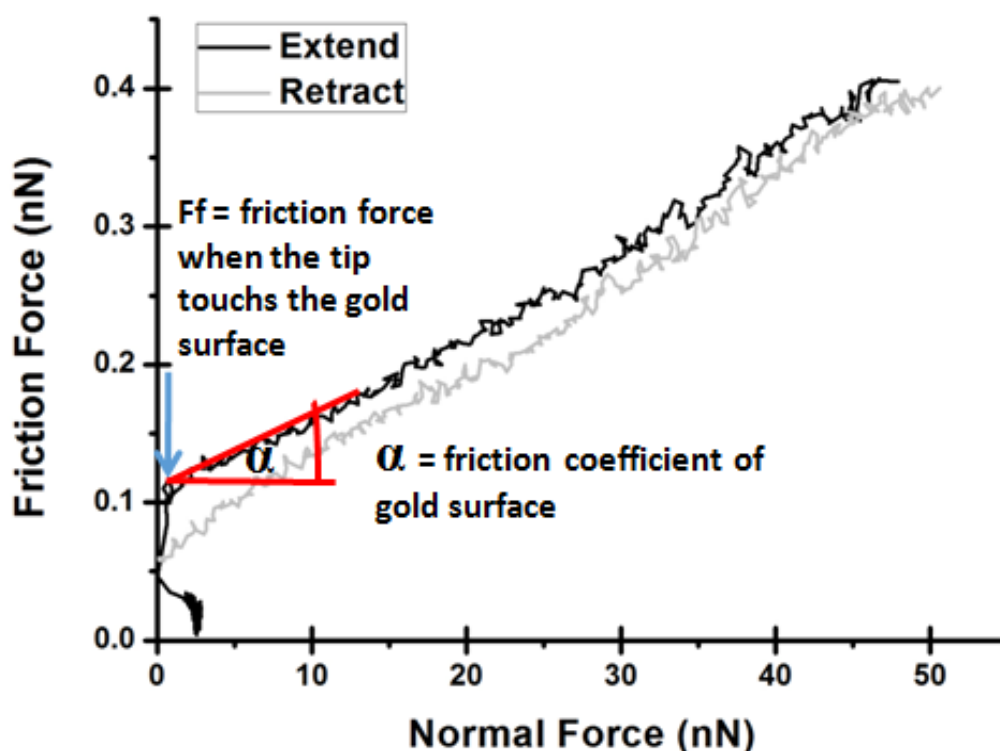


Figure 6.18 Friction force versus normal force of gold surface functionalized with  $C_{10}CH_3$  (hydrophobic surface) measured in 10 mM Tris buffer pH 7.4 (measured by CM-AFM; sliding velocity=120  $\mu\text{m/s}$ )

Contrary to the previous results on mica and glass surfaces, the friction force of hydrophobic substrate does not show increase with the sliding velocity (see Figure 6.19) and so does friction coefficient. The nature of the surface might alter the tip-substrate interaction forces compared to hydrophilic mica and glass surfaces. For all sliding velocities (12 – 1200  $\mu\text{m/s}$ ), the friction force and friction coefficient were ranging between 0.05-0.14 nN and 0.007-0.015 respectively. The friction coefficient found was five times lower than published value for

the same surface characterized in air (Booth et al. 2009). It is because we measured in liquid environment which eliminates the capillary forces. Measurement under air condition results water bridge between sample surface and AFM tip due to water vapor formed in the contact area. The asperities of the surface becomes the location for capillary condensation (Mazeran 2006).

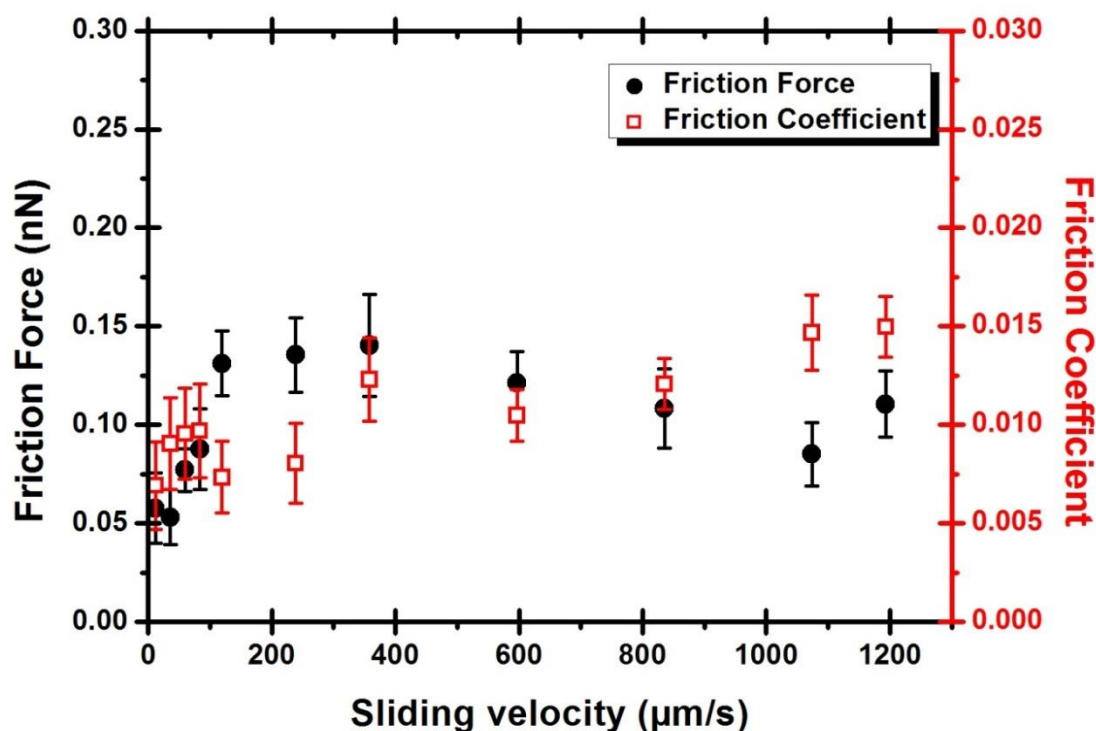


Figure 6.19 Friction force and friction coefficient of gold layer functionalized with  $C_{10}CH_3$  measured in medium of 10 mM Tris buffer pH 7.4 using CM-AFM (sliding velocity 10 – 1200  $\mu\text{m/s}$ )

## 6.5 Discussion

Circular mode AFM was used to characterize the nanomechanical properties of three surfaces: mica, glass, and functionalized gold layer. These surfaces are often used as solid substrates to deposit lipid membranes and immobilize biological samples. In general, comparison of different measurement environments (air or wet condition) was done. In addition, the effect of cations was also studied. There are many evidences that cations increase the mechanical resistance of supported lipid bilayers (Haverstick & Glaser 1987; Garcia-Manyes et al. 2005).

For all three surfaces, CM-AFM did not cause visible wear trace. The normal force

applied is low (<50 nN) and it is still under the critical point to avoid plastic deformation on the surface. Mica surface needs minimum 270 nN of load to produce wear trace (Xiao et al. 1996). For gold layer, this normal force will not damage the alkanethiol monolayers, because at higher force, the layers can be affected reversibly or irreversibly and the frictional forces become unstable (Lio et al. 1997).

In addition, the friction force of all surfaces gives similar pattern. In the beginning, there is sudden jump of friction force (also referred as jump-to-contact) due to the attractive forces during approach of the tip to the sample surface (Xiao et al. 1996). Then, the friction force increases linearly with applied normal force, following the law of Amonton  $F_f = \mu F_N$ . It allows us to calculate the friction coefficient of the surface (the slope of friction force curve). For functionalized surfaces, at larger range of applied force, the change in frictional behavior started to be seen at load of ~60 nN as it has faster increase of friction force (Xiao et al. 1996). Thus by working at lower load range, we can maintain the linearity of the friction curve.

Friction coefficient of mica measured in dry air that is found in this study (0.003) was 33 times smaller than ones reported by Srivastava and colleagues (0.1) (Srivastava et al. 2007). Besides, they found that at low velocity (0.1-1  $\mu\text{m/s}$ ) the friction increases linearly but at higher velocity, it settles at a constant value (steady state). It is completely different with what we have found. As we work at higher velocity range, we found that friction force increases linearly with sliding velocity.

In addition, the concentration of calcium ion increases the friction force of mica surface. Calcium ions replace potassium located at the surface of mica after cleavage. Calcium is considered to have strong water-binding affinity so it is less ready to lose its primary hydration shell to bind with negative lattice sites on mica. Calcium acts as bridge between negatively charged surfaces in adhesive contact resulting increase of adhesive forces (Alcantar et al. 2003). Besides,  $\text{Ca}^{2+}$  move much slower than  $\text{K}^+$  and  $\text{H}_3\text{O}^+$  (Xu & Salmeron 1998a). In liquid environment, the ions are hydrated by water molecules and mobile, they can be displaced by the tip and the mica lattice is resolved again. Meanwhile, in dry environment, humidity corresponds to the completion of a water layer on the surface (Xu et al. 1998). High mobility of  $\text{K}^+$  and uniform water film may lubricate the surface and decrease the friction force. The formation of water layer also happens in the presence of  $\text{Ca}^{2+}$ , however, its thickness is thinner than ones found in the presence  $\text{K}^+$ . Thus, the friction force of mica at high humidity in the presence of  $\text{Ca}^{2+}$  is higher than ones obtained in the presence of  $\text{H}_3\text{O}^+$  and  $\text{K}^+$  ( $\text{Ca}^{2+} > \text{H}_3\text{O}^+ > \text{K}^+$ )

(Xu & Salmeron 1998b). It is in agreement with our results regarding the effect of calcium's concentration on mica surface (see Figure 6.7) and the effects of alkali ions on glass surface (see Figure 6.11).

Furthermore, it is not only potassium ions that can alter the frictional properties of surface, but also other alkali ions (sodium and lithium ions). A previous study based on Monte Carlo simulation showed that the hydration shell of  $\text{Na}^+$  is constituted by three water molecules and is quite stable. However,  $\text{K}^+$  is unable to attract water molecules so the diameter of  $\text{K}^+$  is equal to its ionic diameter (Degrève et al. 1996). Thus, the potassium ion can decrease the friction force of glass significantly more than lithium and sodium even though potassium has the biggest ionic radius.

Moreover, measurement on hydrophobic surface presents adhesion force which is not found on hydrophilic surface (mica, glass, and gold layer functionalized by  $\text{C}_{11}\text{OH}$ ). The adhesion forces in air decreases at higher sliding velocity (Noel et al. 2012). On the curve of adhesion forces versus sliding velocity (see Figure 7.20), there are two regimes with different slopes of decrease. At low velocity, the slope is bigger while at higher velocity, the adhesion forces decrease slowly. Under air condition, the slow decrease of adhesion forces with time is related to surface adsorption (Christenson 1993). Thus, we can infer that in buffered medium containing high concentration of ion, it might be related to ion adsorption to the surface. After all, the general tribological properties of thiol-functionalized gold layer depend on its internal stabilities: cohesive interaction of van der Waals and the bond between adsorbate (alkanethiol) and substrate (gold layer) (Booth et al. 2009).

## 6.6 Conclusion

We have demonstrated the use of CM-AFM to characterize the frictional properties of mica, glass, and functionalized-gold-layer under different media (water, Tris buffer, etc). Our results show that friction and adhesion forces are dependent on the sliding velocity at nanoscale. It is important to highlight that we worked in liquid environment, at high sliding velocity, and considerably low load. These conditions can explain the discrepancies between our results and some references because they mainly worked in dry environment and at higher load range. One of the advantages of CM-AFM resides in the ability to study the viscous

properties using a direct approach. Furthermore, the composition of liquid medium is significantly affecting the surface friction and the viscous properties; for example the viscous friction coefficient decreases at higher ionic size of alkali ions.



*(this page is intentionally left blank)*

## **Direct measurement of viscous properties of lipid membranes by CM-AFM in the case of simple fluid SLBs**

For the first time, the measurement of normal and friction force on supported lipid bilayers can be done simultaneously because of the use of CM AFM. Moreover, observation at different sliding velocities allows us to acquire information about the velocity dependence properties of lipid membranes. It is because the friction force shows a linear relationship with sliding velocity. Thus, CM AFM becomes a technique that is able to measure viscous friction coefficient of biological samples. Easily prepared DiOleoylPhosphatidyl Choline SLBs was used as simple model of biomembranes in our experiments. Both circular mode parameters: amplitude and frequency affect the mechanical measurement.

# Chapter 7

## Direct measurement of viscous properties of fluid lipid membranes by CM AFM

### 7.1 Introduction

Relative variations of fluidity and mechanical response in lipid membranes are currently evaluated by numerous physical methods including dynamic light scattering (Ertel et al. 1993), surface force apparatus (Benz et al. 2004), Brewster angle microscopy (Kafi & Kwon 2008) and micropipette aspiration technique (Rawicz et al. 2000) among others. However, comparisons between different systems remain difficult because the effects of membranes' structure and fluidity are involved in the diffusion coefficients (or correlation times, or frictional coefficients) given by experiments (Hare et al. 1979). Besides, all the instruments mentioned above have common drawbacks; they are not adapted for mechanical characterization of supported lipid bilayers (SLBs) and they have limited resolution (Picas et al. 2012). These techniques require lipid molecules in the form of liposomes (giant unilamellar vesicles) which is less robust than SLBs.

Atomic Force Microscope (AFM) has opened new perspectives for investigations of phenomenological mechanisms at the nanoscale that are encountered in different fields such as material science, biology, tribology among others. Recently, Circular mode AFM (CM-AFM) is developed to measure physical properties that require high scanning velocities and/or continuous displacements with no rest periods (Nasrallah et al. 2011). This new AFM mode should represent a new accurate option for the nano mechanical characterization of different materials particularly for biological materials. Knowing this, the aim of this chapter is to demonstrate the ability of AFM circular mode to work in liquid medium for the quantification of the viscous properties of biomimetic membranes. Results can provide new insights about the relation between lipid membranes' nanomechanical properties and their possible use in biomedical applications.

## 7.2 Optimization of CM AFM parameters

As we have discussed in the previous chapter, there are two parameters that control the sliding velocity in CM AFM: amplitude and frequency of scanning. Both parameters change the sliding velocity in different way. Scanning amplitude regulates the sliding distance as it is linearly proportional with the circular diameter track. Frequency controls the time to complete one circular track. Bilayers of DOPC were prepared on glass solid support in these experiments.

In the case of punchthrough force, there are many reports stating that the force necessary to break the membrane is affected by tip-approach velocity (Butt & Franz 2002; Loi et al. 2002). Thus, we suspected that the punchthrough force would vary with sliding velocity. However, Figure 7.1 shows that the punchthrough force of DOPC SLBs does not have specific relation with sliding velocity which is regulated by changing the amplitude (and maintaining constant frequency of 175 Hz). Instead, it is considerably constant for all sliding velocities. For this reason, we considered the punchthrough force as one single population in order to compute the average value. Furthermore, this result indicates that the scanning amplitude range of 1-10 V (200 – 2000  $\mu\text{m/s}$  of sliding velocity) can be used for mechanical characterization of lipid membrane. It is the maximum amplitude range to maintain the linear response of the piezoelectric scanner (see section 5.3.3)

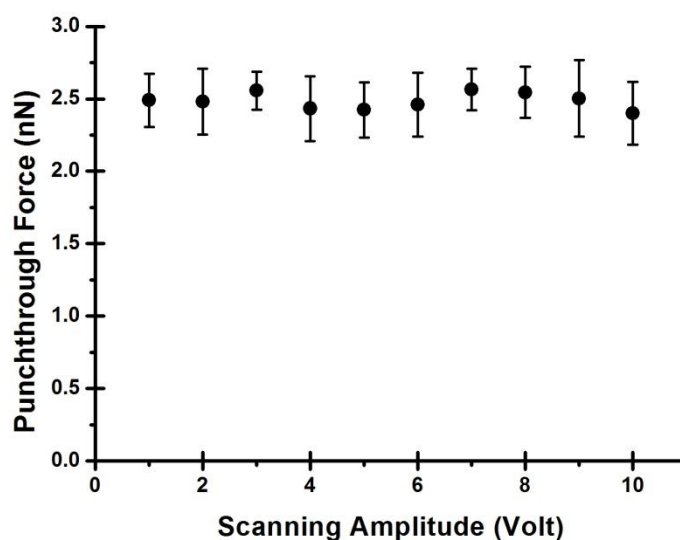


Figure 7.1 Punchthrough force of DOPC SLBs as function of sliding velocity. The inset image shows the variation of punchthrough force as function of scanning amplitude: 1-10 V which is equivalent with sliding velocity 200 – 2000  $\mu\text{m/s}$ . DOPC SLBs was prepared in 10 mM Tris buffer containing 150 mM NaCl and 3 mM  $\text{CaCl}_2$

## 7.3 Morphology of fluid lipid membranes

It has been proven that the mechanical response of confined lipid bilayers depends on a great variety of physical (e.g., temperature, lipid chain saturation, and ions concentration) and experimental (e.g., tip stiffness, radius and tip chemistry) parameters (Stetter & Hugel 2013; Garcia-Manyes et al. 2005; Garcia-Manyes & Sanz 2010). Therefore, during these experiments the same tip was used for a complete set of sliding velocities. In this study the set of sliding velocities varied from 215  $\mu\text{m/s}$  until 2150  $\mu\text{m/s}$ , calculated from the input of half-peak voltage and frequency. The AFM cantilevers used in this study were found to have a nominal spring constant of 0.1234 nN/nm and the LFM calibration constant was found to be 20.75 nN/V. As lipid bilayers in general are known to be particularly sensitive to variations of temperature, room environmental temperature was kept constant at  $\sim 21^\circ\text{C}$  during all the experiments. Before performing the circular mode, the AFM microlevers were cleaned by a series of chemical liquid treatment using water, ethanol, and dichloromethane. In order to have hydrophilic tip, UV ozone treatment was done during 15min just before AFM examination. Finally, previous experiments showed that TBS buffer does not have effects on the membrane fluidity nor tip adhesion.

Pure DOPC SLBs prepared by fusion vesicles method has flat surface (see *Figure 7.2*). The vertical section shows that the membranes' surface is smooth. In fact, the topography image cannot be strong proof of lipids deposited on glass surface due to absences of holes/defects on the surface. However, it is still providing an idea of surface's low roughness.

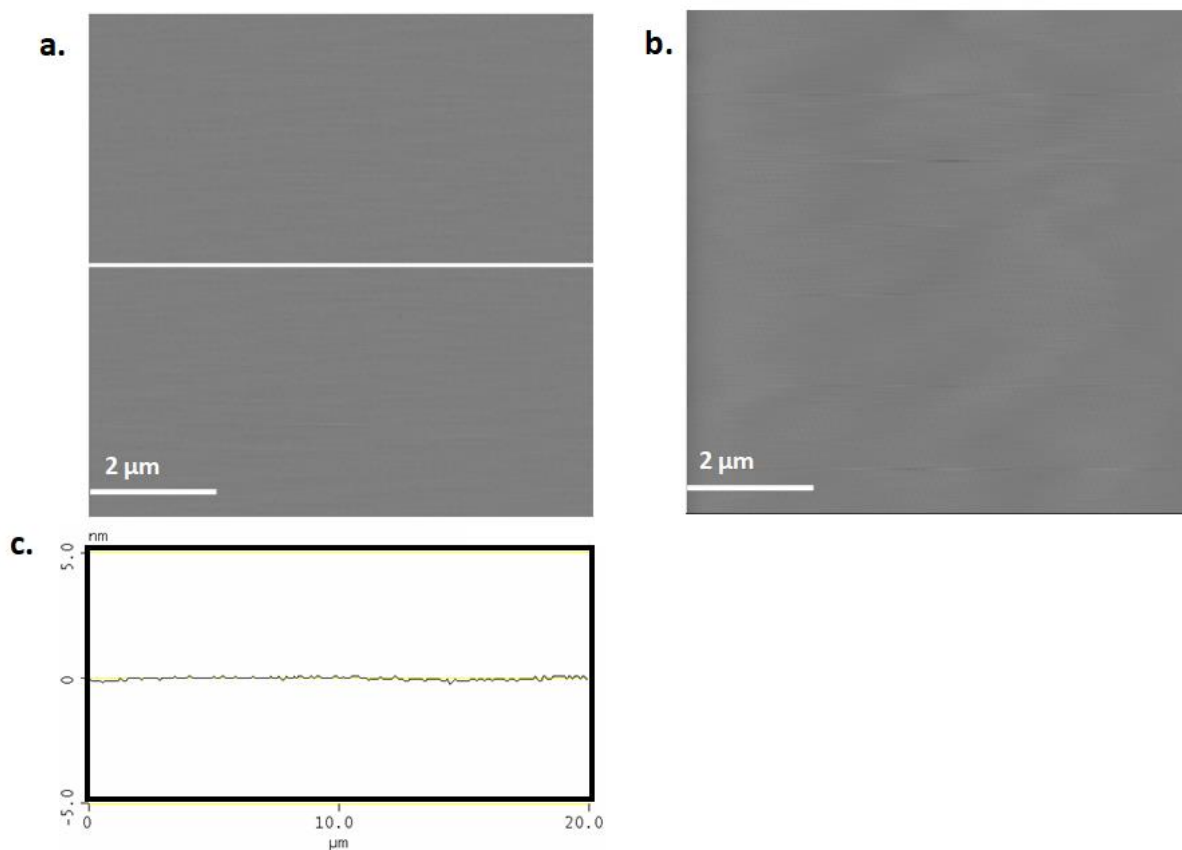


Figure 7.2 Topography image of DOPC (18:1) SLBs (a) before and (b) after mechanical measurement. (c) The cross section along the white line of the image before measurement. Size =  $20\mu\text{m} \times 20\mu\text{m}$ , z-range = 10nm

## 7.4 Mechanical resistance of fluid lipid bilayers

The force curve of deflection and friction were acquired simultaneously. We have evaluated the deflection curves in order to quantify two elements: the membrane thickness and the punch-through force or the maximum vertical force in which confined membrane can resist before being pierced by the AFM probe. Meanwhile, friction force and friction constant can be obtained from friction force curve.

Figure 7.3 shows the typical raw curve of deflection and friction for lipid bilayers. When the AFM probe pierces the membrane, a small jump can be detected in the force curve. Superimposed raw curves of deflection and friction signals show that the rupture of the lipid membrane is detected at the same time with the two curves. The normal force is increasing constantly since the tip contacts the membranes' surface. On the other hand, the friction curve forms a plateau during sliding on top of the membrane. The rupture of the membrane is

indicated by a small jump in deflection curve and an abrupt increase of the friction force. The oscillations noted on the deflection curve are due to high sliding velocity of CM AFM (more than 100  $\mu\text{m/s}$ ). In order to minimize these oscillations, very small tip-approaching velocity (15 nm/s) is used. Under these conditions, a continuous friction curve can be recorded every 30-100 seconds.

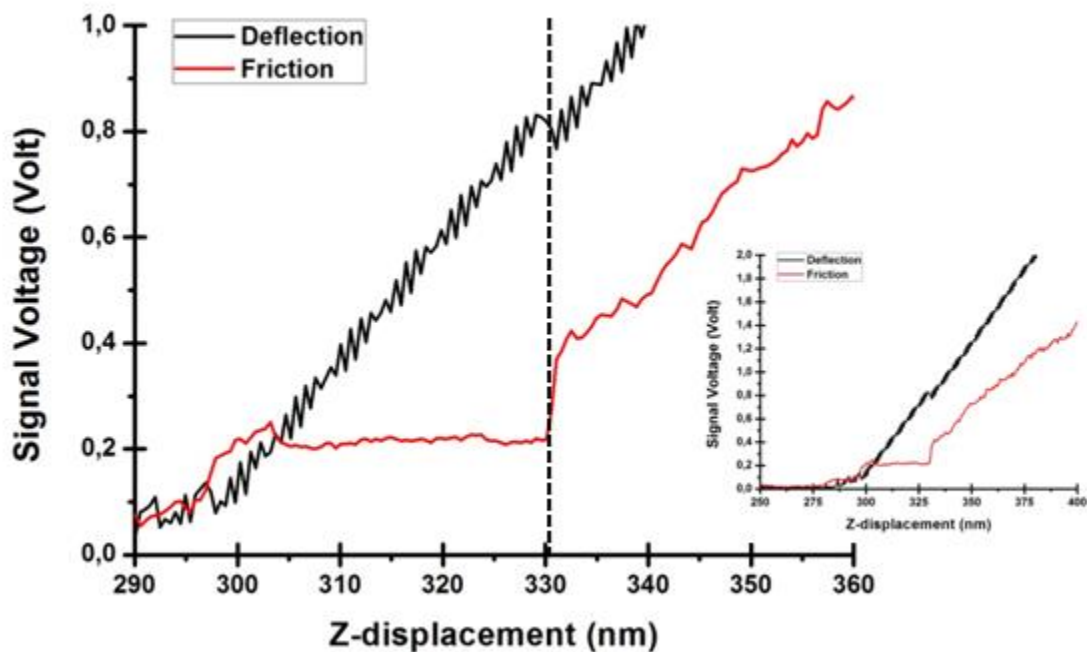


Figure 7.3 Comparison of raw curves of normal and lateral force. Perforation of the membrane by AFM tip is detected on both normal and lateral force curve (dashed vertical line)

The vertical distance from base line to the jump is recorded as punchthrough force while the horizontal distance is the membrane thickness. Therefore, the raw force curve voltage versus piezo displacement must be converted to force in nN versus vertical separation by multiplying with sensitivity and spring constant of cantilever. The converted curve looks like Figure 7.4. Then, the values of membranes' thickness and punchthrough force were recorded from each curve.

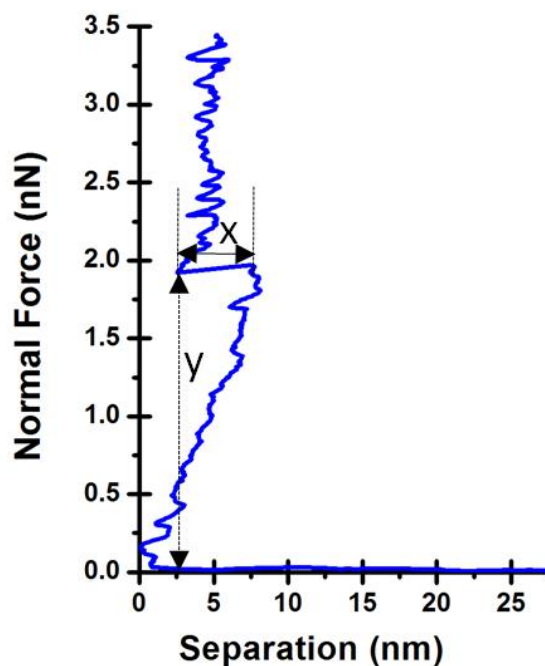


Figure 7.4 Example of AFM punch experiment yielding normal force versus separation obtained on DOPC bilayers; horizontal distance  $x$  refers to membranes' thickness while vertical distance  $y$  refers to punchthrough force.

One of the features of the AFM Circular mode is the tribological assessment. These tests allow the quantification of the tribological characteristics of (bio)organic layers to study their lateral organization. The friction force curves for DOPC bilayers generated from AFM circular mode showed similarity with the one measured by conventional AFM (compare Figure 3.12 with Figure 7.3). There are four regions spotted on the curve. The first region (a) is when the tip is far from the membrane's surface, so no interaction force is detected. Then, in the second region (b), the force starts to increase as it shows a slight jump to overcome repulsive electrostatic interaction force between tip and membrane (Oncins et al. 2005) before the tip contacts the membrane's surface. In this region, in CM AFM the tip slides on top of the membrane as the force is gradually increasing but it is still below the threshold force needed to punch the bilayer. Therefore there is a plateau in the friction curve corresponding to the AFM sliding on top of the membrane, probably among the polar heads of lipids. The third region (c) is when the tip finally breaks the membrane and touches the solid support. Small jump is observed in the normal force profile while there is drastic increase in friction force curve. At last, in the fourth region, the tip slides on the solid support as both forces keep increasing until it reached the maximum force applied.



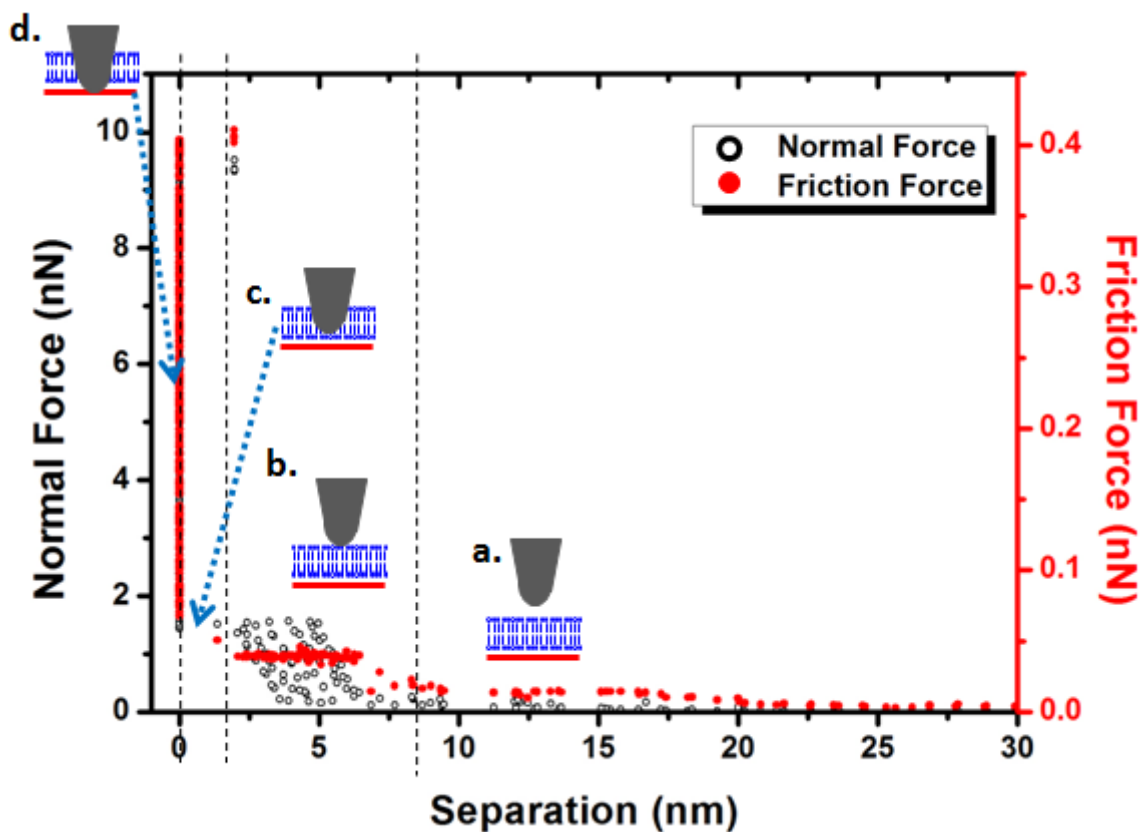


Figure 7.5 Curve of normal and friction forces as function of tip-membrane separation. The curve can be divided into four areas: (a) tip is relatively far from membrane, (b) tip contacts the membrane's surface, (c) tip punches the membrane, and (d) tip is in contact with the solid support

A total of 215 curves were processed. Results for both parameters are fitted by a Gaussian distribution representing the mean values and the corresponding standard deviation. In this case membrane thickness was found to be  $4.9 \pm 1.1$  nm (see Figure 7.6) and the punchthrough force is  $2.52 \pm 0.56$  nN (see Figure 7.7).

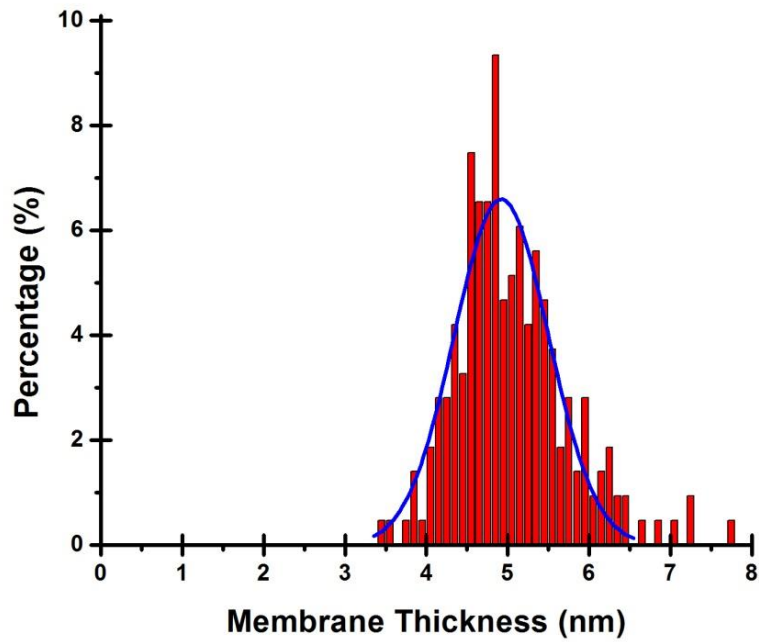


Figure 7.6 Histogram of DOPC thickness obtained by piercing the SLB with the AFM tip,  $n = 215$ . Measurements were done by CM-AFM with sliding velocity  $200 - 2000 \mu\text{m/s}$ . The solid line represents the gaussian fitting line. The average Gaussian thickness for DOPC is  $4.9 + 1.1 \text{ nm}$

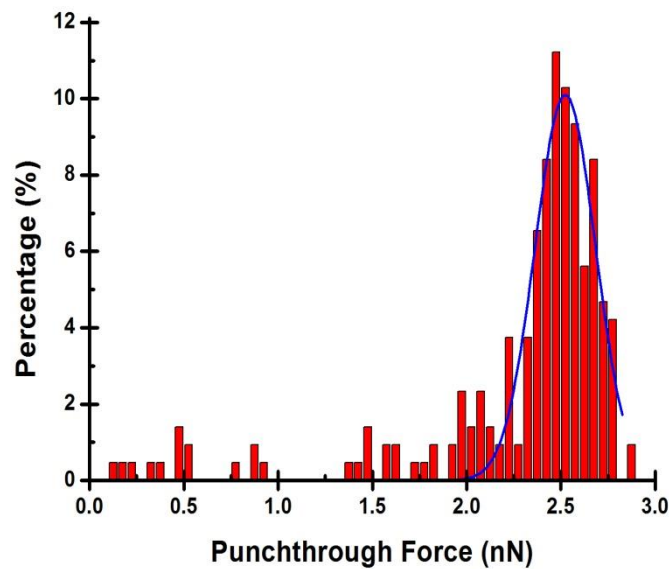


Figure 7.7 Histogram of DOPC punchthrough force obtained by piercing the SLB with the AFM tip,  $n = 215$ . Measurements were done by CM-AFM with sliding velocity  $200 - 2000 \mu\text{m/s}$ . The solid line represents the Gaussian fitting line. The average Gaussian punchthrough force for DOPC is  $2.52 + 0.56 \text{ nN}$

In certain curves, double jump was found this might be due to high ionic concentration in the medium and the presence lipid membranes attached on the AFM probe (Pera et al. 2004). However, the punchthrough force recorded is only the first jump because the height value (membranes' thickness) coincides with the correspond value (approximately 4nm) (Franz et al. 2002).

## 7.5 Friction measurement of fluid lipid membranes

The friction and normal force curves were combined to construct new curve of friction force versus normal force using a Matlab routine. From these curves, the initial friction force ( $F_0$ ) which is the friction between AFM tip and lipid head group was noted. Figure 7.8 shows the variation of friction force as a function of sliding velocity. The friction force is increased linearly with the increase of sliding velocity. It gives a proof that lipid membranes are viscous materials as their properties change with the velocity. The value of viscous friction coefficient was calculated from the slope of linear regression line. In this case for DOPC confined lipid bilayers, the viscous friction coefficient was found to be  $75.56 \pm 4.7 \text{ nN.s.m}^{-1}$  ( $R^2=0.98$ ).

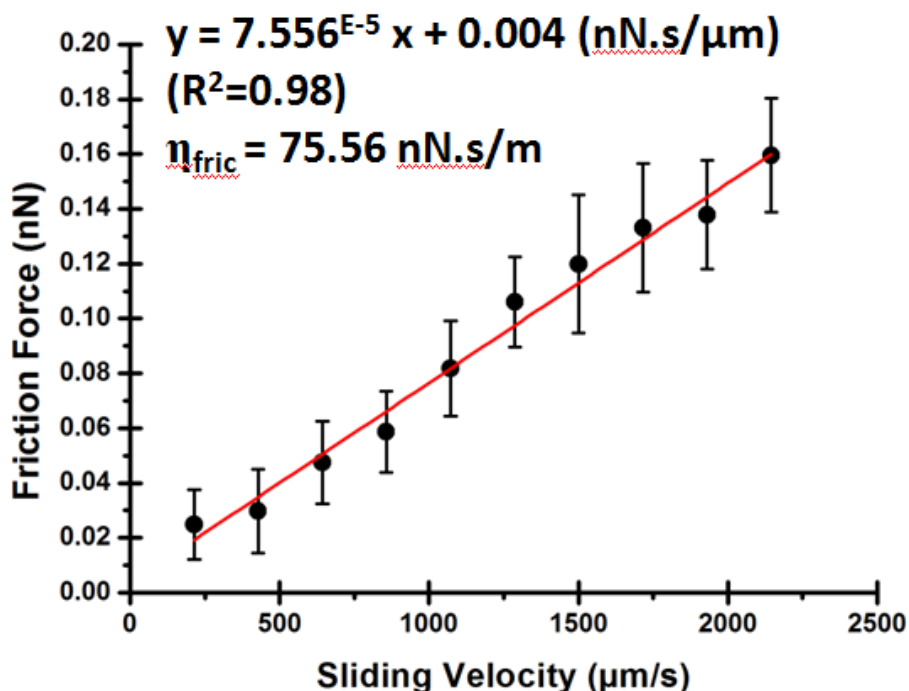


Figure 7.8 Curve of friction force of DOPC SLBs measured by CM-AFM as a function of the sliding velocity. The friction force recorded is the initial friction force when the tip begins to contact the surface

## 7.6 Discussion

We have quantified nanomechanical properties of confined supported lipid bilayers exposed by high and constant sliding velocities. The calibrated AFM circular mode was used to quantify the breakthrough force, thickness, friction force, and viscosity of organic lipid bilayers DioleoylPhosphatidyl Choline (DOPC) deposited on glass surface in buffered conditions.

The results obtained in this work for the membrane thickness (4.5nm) are within the classical values reported for pure DOPC membranes (Attwood et al. 2013; Pompeo et al. 2005; Chiantia et al. 2006; El Kirat et al. 2010). This fact confirms that the vesicle fusion method used to prepare the samples works as expected. In addition no artifacts of surface modification was found after assessments using circular mode due to characteristic of DOPC molecules which are very mobile by nature (Leroy et al. 2009). We assume that DOPC molecules diffuse to replace the molecules removed during tip sliding. DOPC molecules rearrange to fill the holes created by the tip (Oncins et al. 2005). Thus we can't find any defects or wear track of circular displacement.

In light of the results reported here and in agreement with the previous work of Garcia-Manyes (Garcia-Manyes & Sanz 2010), now it is clear that the breakthrough force at which a phospholipid bilayer breaks is a direct signature of the chemical composition and molecular organization of a particular bilayers in a precise buffered environment at a well-defined temperature. However, the punchthrough force measured at different sliding velocities used in this study was constant, contrary to what we found for the friction force. Thus, the calculation of average punchthrough force was done without considering different sliding velocities.

Another study that quantifies the breakthrough force on pure DOPC was reported by Chiantia et al. (Chiantia et al. 2006). This study reported 1.7 nN as the value required to break the DOPC SLBs membrane at 25°C. This value is lower than the value obtained in this study ( $2.52 \pm 0.56$  nN) due to different liquid environment, loading rate, and temperature of measurement. Morandat and El Kirat (Morandat & El Kirat 2011) obtained  $2.5 \pm 0.25$  nN for DOPC phase in the presence of DPPC domain. All reported values were acquired by conventional AFM. Therefore, the technique of circular displacement is as reliable as conventional AFM to measure breakthrough force and thickness of supported lipid bilayers.

Franz et al (2002) found that the punchthrough force linearly increase with the

logarithmic of approach speed of tip (Franz et al. 2002). The maximum tip-approaching velocity they used was 10  $\mu\text{m/s}$ . Even though we used very slow tip-approaching velocity of 15 nm/s, our tip also moves laterally at very high velocity (up to 2500  $\mu\text{m/s}$ ). Since the membranes' penetration can be considered as kinetic reaction, the increase of tip velocity increases the initial energy and decreases the activation barrier of the membrane, and then the reaction occurs faster. However, our results of punchthrough force only give small linear increase with sliding velocity (see Figure 7.1), thus it is considered as constant.

Figure 7.9 shows the comparison of friction curves of a DOPC SLB on glass substrate and a bare glass surface. The friction curve of glass surface appears as a single linear line as friction force is directly proportional to the normal force. It follows the friction theory of Amonton's law for friction on solid surface (Persson & Tosatti 1995). Due to the presence of DOPC SLBs deposited on glass substrate, there is a difference in friction force between bare glass surface and glass surface with DOPC SLBs deposited on it. The difference is noted as  $\Delta F_f$ . While the Figure 7.8 plots the friction before punch ( $F_{f0}$ ) between AFM tip and lipid polar head,  $\Delta F_f$  is considered to be the friction force of the whole lipid bilayers. The difference of friction force was plotted as function of sliding force as seen on Figure 7.10.  $\Delta F_f$  varies linearly as a function of the sliding velocity ( $R^2=0.92$ ). The regression line's slope is the friction viscous coefficient for the whole lipid bilayers and its value is three times higher than friction viscous coefficient at the lipid surface. Thus, we assume that the friction viscous coefficient is a function of membrane thickness.

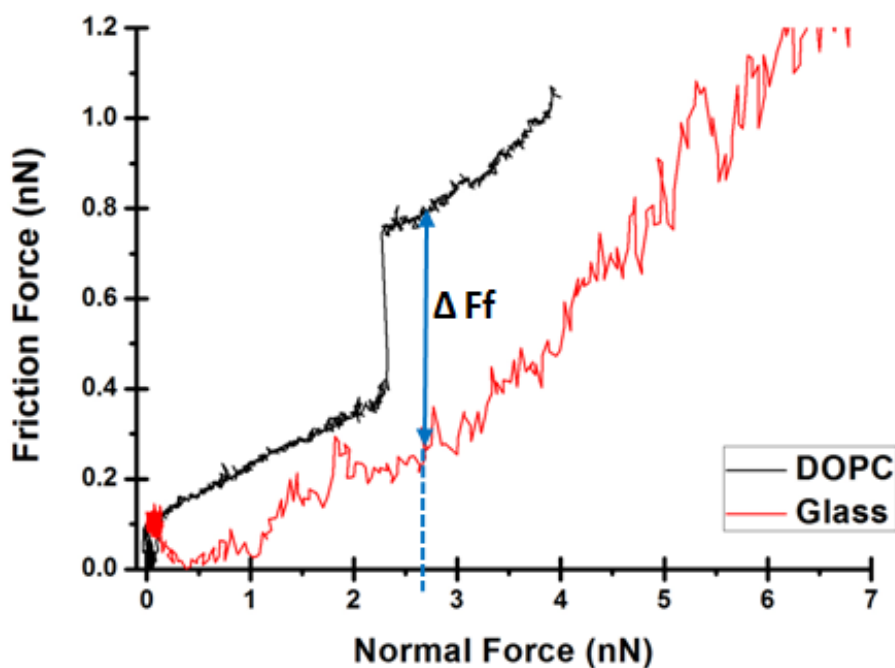


Figure 7.9 Comparison of friction curves of DOPC SLBs on glass substrate and bare glass surface measured in Tris Buffer pH 7.4 using CM-AFM at sliding velocity 200  $\mu\text{m/s}$ .

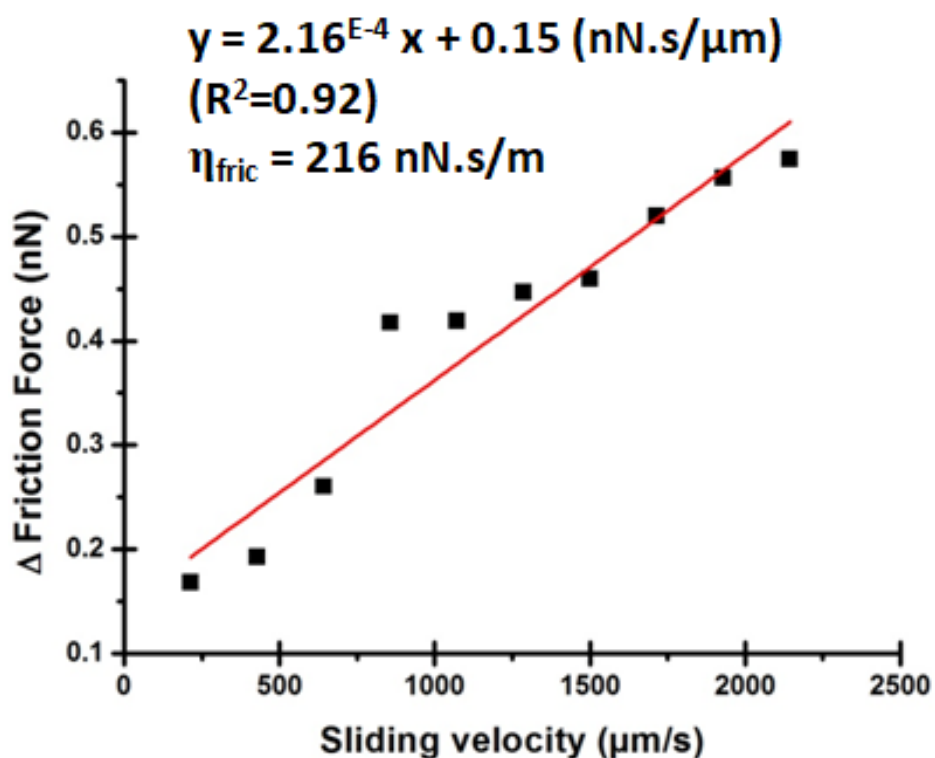


Figure 7.10 Difference of friction force of bare glass and glass as solid substrate for DOPC SLB versus sliding velocity ( $y=2.16E^{-4}x+0.15$ ;  $R^2=0.92$ ), measured using CM-AFM at sliding velocity 200 – 2000  $\mu\text{m/s}$

AFM circular mode highlights the time efficiency of examination compared to conventional AFM. We are able to acquire one full curve in relatively short time ( $\cong 30 - 100$  seconds) instead of  $\cong 4$  hours by conventional AFM. Additionally, on conventional AFM, a friction force curve was constructed by discrete points acquired from separated experiments hence there is variation in every points (showed by standard deviation) and it needs to be fitted.

Due to the nano and pico sensitiveness of this method, it is possible to determine the variation of initial friction with change of sliding velocity. This variation is then used to quantify the viscosity of confined membrane by calculating the slope of linear regression line of the variation. In this case, the results show a viscosity for pure SLBs DOPC equal to 75 nN.s/m. For comparison, the viscosity of plasma membranes of HT29 human colorectal adenocarcinoma cells is approximately 20 nN.s/m measured by photonic force microscopy consists of an optical trapping unit and an interferometric tracking unit (Jünger et al. 2015).

Table 7.1 shows comparison of our values with some published values. Surprisingly, the overall comparison showed that our value is higher than all references even though some used cholesterol in their lipid system. Cholesterol is known to increase the compactness of lipid bilayers thus higher mechanical resistance is recorded (Garcia-manyes et al. 2010). Petrov and Schwille derived Saffman and Delbruck (SD) hydrodynamic analysis (Petrov & Schwille 2008) and found viscosity of 1 nN.s/m for giant unilamellar vesicles (GUVs) mixture of 1:1 DOPC/DPPC + 30% cholesterol. The explanation of this was found in the difference of model membranes used in each study. All the references used vesicles (GUVs or LUVs) as their membrane model which has lower mechanical resistance due to the absence of solid support. While, the solid support has a strong influence on the behavior of lipid bilayers (Seeger et al. 2010). In reality, cell membranes are supported by mesh of proteins constituting the cytoskeleton (Picas et al. 2012; Nicolson 2014). The solid support (glass surface) substitutes the role of cytoskeleton in the model of lipid membranes.

Saffman and Delbruck (SD) were the first to present that lipid bilayers can be viewed as ultrathin fluid layers supplied with surface viscosity. The SD theory explained the time dependent model on flat fluid sheet with surface viscosity named as membranes, surrounded by a bulk fluid named as membrane liquid medium, (Camley et al. 2010). However, this analytic model only works on symmetric membrane with domains generated across both leaflets. Based on SD theory, the membrane viscosity can be calculated by using the relation  $\eta_m =$

$\eta \times d$  where  $\eta_m$ ,  $\eta$ , and  $d$  is the membrane viscosity ( $\text{N}\cdot\text{s}\cdot\text{m}^{-1}$ ), bilayers fluid viscosity ( $\text{N}\cdot\text{s}\cdot\text{m}^{-2}$ ), and membrane thickness (m) respectively. The nanometer size of lipid membranes' thickness renders the membrane viscosity very small (Honerkamp-Smith et al. 2013). Thus AFM might be the appropriate tools to address viscous behavior of lipid membranes.

It is thus necessary to use new mechanical models that allow the quantification of mechanical properties. By the moment, this could be particularly difficult due to the absence of imaginary component of the Fourier transform, which must have a physical sense. This component needs to be also represented from a mechanical point of view. Nevertheless, the results of our experiments are particularly interesting because they prove that the friction force was quasi-independent of the load but proportional to the sliding velocity suggesting that the friction force was mainly governed by viscous friction.



Table 7.1 Comparison of friction viscous coefficient

	<b>Lipid Composition</b>	<b>Measurement Technique</b>	<b><math>\eta(d)^1</math></b>	<b><math>\times</math> membrane thickness (4.5nm)<sup>2</sup></b>
<b>This work</b>	SLBs of DOPC	Circular mode AFM	N.A.	<b>75 nN.s/m (at 21°C)</b>
<b>Junger et al (Jünger et al. 2015)</b>	Adenocarcinoma cells	Photonic force microscopy		<b>20 nN.s/m</b>
<b>Cicuta et al. (Cicuta et al. 2007)</b>	GUVs of DOPC/DPPC + 30% Chol	Fluorescence microscopy and H NMR measurement	N.A.	<b>10 nN.s/m (at 21°C)<sup>3</sup></b>
<b>Petrov and Schwille (Petrov &amp; Schwille 2008)</b>	GUVs of DOPC/DPPC + 30% Chol	Analytic approximation	<b>N.A.</b>	<b>1nN.s/m (at 21°C)<sup>3</sup></b>
<b>Wu et al.(Wu et al. 2013)</b>	LUVs of DOPC	Fluorescence lifetime	<b><math>1.5 \times 10^{-10}</math> nN.s/m<sup>2</sup> (at 21°C)<sup>3</sup></b>	0.72 nN.s/m
<b>Honerkamp et al.(Honerkamp- Smith et al. 2013)</b>	GUVs of 85%DOPC+15%D PPC	Confocal microscopy	N.A.	<b>19nN.s/m</b>

<sup>1</sup> $\eta(d)$  : bilayer fluid viscosity

<sup>2</sup>membrane viscosity ( $\eta_m$ ). If in the reference, the author only gave bilayer fluid viscosity, we multiplied with membrane thickness acquired with our data sets. We assume that thickness of membrane is independent to method of preparation.

<sup>3</sup>approximated value because the author presented the result in curve of viscosity as a function of temperature

## 7.7 Conclusion

Finally, the circular mode AFM has been adapted for mechanical characterization of supported lipid bilayers and biological specimens in general. The parameters of CM AFM (frequency and amplitude) were optimized. Based on the results reported in this study, CM AFM was successfully employed in characterization of nanomechanical properties of lipid membranes. The results were comparable with those obtained by conventional AFM. CM AFM showed its strong advantages: the ability to perform continuous and constant sliding at high velocity. Moreover, this technique increases the time efficiency as it is able to measure normal and lateral force simultaneously. It is the first time that direct measurement of membrane viscosity was conducted on the nanometer scale.

The authors consider that circular mode could be employed for tribological investigations on big range of biological materials, not only confined supported lipid bilayers but also it could be extended to other biological materials e.g. collagen, cartilage, and more complex biomimetic membranes. All capabilities of this new method provide a very wide spectrum of options for tribological and nanomechanical applications.

*(this page is intentionally left blank)*

## Effect of environment onto nanomechanical properties of fluid lipid membranes

It is known that nano mechanical properties of lipid membranes are influenced by the ionic strength of the liquid medium. Higher ionic strength can increase the mechanical resistance of lipid membranes by modifying the lipid organization. It can also facilitate the adsorption of lipid vesicles onto solid substrate in vesicle fusion process. However, each type of cations can bring different effect to lipid organization. Thus, we have studied the effects of three monovalent alkali cations ( $\text{Li}^+$ ,  $\text{Na}^+$ , and  $\text{K}^+$ ) to SLB of DioleoylPhosphatidyl Choline. Potassium ions are found to improve both mechanical stability and tribological properties of DOPC membrane. While, lithium and sodium ions gave a similar effect.

## Chapter 8

# Effect of environment onto nanomechanical properties of fluid lipid membranes

### 8.1 Introduction

Mechanical stability of supported lipid bilayers can be quantified by the measurement of so-called punchthrough force or the force necessary to pierce the bilayers. Mechanical measurement by AFM has demonstrated that mechanical stability of supported lipid bilayers is affected by ionic strength of the liquid medium (Garcia-Manyes et al. 2005). Ionic strength increases the electrostatic interaction among phospholipid headgroups due to a charge screening effect, thus the hydrophobic tails have higher proximity and there is an increase of van der Waals interactions among lipids' headgroups (Oncins et al. 2005).

The group of monovalent cations (alkali group) can give dramatic effect to membranes' properties. Lithium ions perturb the liquid state in PhosphatidylSerine (PS), a negatively charged lipid membrane, and increase the critical temperature of Le (liquid expanded) to Lc (liquid condensed) transformation (Hauser & Shipley 1983; López Cascales & García de la Torre 1997). The increase of transformation temperature is due to the fact that  $\text{Li}^+$  has small ionic size and large hydration shell.

The presence of divalent cations in the medium such as:  $\text{Ca}^{2+}$  and  $\text{Mg}^{2+}$ , induces better and faster deposition of phosphocholine (PC) bilayers onto solid substrates and also increases the punchthrough force (Garcia-Manyes et al. 2005). Furthermore,  $\text{Na}^+$  and  $\text{Ca}^{2+}$  are found to have strong interaction with carbonyl oxygen group on PC lipid and they modify the molecular packing and lipid orientation (Vácha et al. 2009; Pandit et al. 2003; Bockmann et al. 2003).

To support this statement, molecular dynamic simulation was applied to illustrate the position of ions with respect to phospholipids molecules (Böckmann & Grubmüller 2004; Gurtovenko et al. 2005). In addition, ionic strength of the medium also affects the frictional properties of PC bilayers (Oncins et al. 2005) as measured with conventional AFM. They proposed a hypothesis in which at higher ionic strength, lipid molecules are less mobile to




allow re-assembly after penetration of the AFM tip in the bilayers.

While the effect of monovalent and divalent cations has been widely studied, the influence of different cations with the same valence on lipid membranes remains unclear. So, the aim of this study is to observe the effects of different cations in the alkali group presented in the medium Tris buffer on fluid lipid membranes of DOPC by using CM-AFM. Three different salts were added in the Tris buffer medium separately: LiCl, NaCl, and KCl; at the same concentration (150 mM). Punchthrough and friction forces were measured to quantify the mechanical properties of DOPC bilayers. Besides, measurement under different sliding velocities allows us to also study the viscous properties of the membrane. In the results below, the terms DOPC-Li, DOPC-Na, and DOPC-K refer to DOPC membranes characterized with different alkali salts.

## 8.2 Results

DOPC bilayers were prepared in 10 mM Tris buffer containing 3 mM  $\text{CaCl}_2$  and 150 mM XCl (XCl=alkali chloride salt). It was formed on clean glass. The vesicle fusion was held at 60°C for 60 minutes. Later, it was rinsed to remove the infused vesicles and the most part of the  $\text{Ca}^{2+}$ . Knowing the volume during fusion and the volume of rinsing, the final concentration of  $\text{Ca}^{2+}$  is 0.14 mM. The use of calcium ions is to facilitate the deposition and fusion of lipid vesicles on the substrate (Garcia-Manyes et al. 2005). We assume that calcium final concentration is too low to have a mechanical influence in measurements thus here we will only discuss the influence of alkali halide salts.

In liquid, the alkali halide salts are ionized into cations ( $\text{Li}^+$ ,  $\text{Na}^+$ , and  $\text{K}^+$ ) and chloride ions. The size of the three cations compared with their neutral atom radius is shown in Figure 8.1. The atomic numbers of Li, Na, and K are 3, 11, and 19 respectively. The ionic size of alkali cations is smaller than their atom size because they lose one electron in the outer layer and form +1 oxidation state. It is due to the fact that they have  $ns^1$  valence electron configuration. Thus the radius of their ionic state (crystal ionic radius) becomes 0.9; 1.16; and 1.52 Å for  $\text{Li}^+$ ,  $\text{Na}^+$ , and  $\text{K}^+$  respectively (Shannon 1976).

Li <sup>+</sup>		Li
90		134
Na <sup>+</sup>		Na
116		154
K <sup>+</sup>		K
152		196

*Figure 8.1 Comparison of crystal ion radius of cations used in these experiments (units in pm). These values are for 6-coordination number (reproduced from Shannon 1976)*

Figure 8.2 shows the histogram diagram of membranes' thickness. At a glimpse there is not significant change of membrane thickness with different alkali used. But in fact, there is small increase of thickness with the largest cations. The thickness is increased by 0.86 nm when we compare DOPC-Li and DOPC-K (the lowest and highest thickness, respectively). Pandit et.al showed that compared to pure PC membrane (in water), NaCl brought an increase of thickness by 0.22 nm (Pandit et al. 2003). The NaCl salts modify the lipid interaction by stabilizing the tail parts.

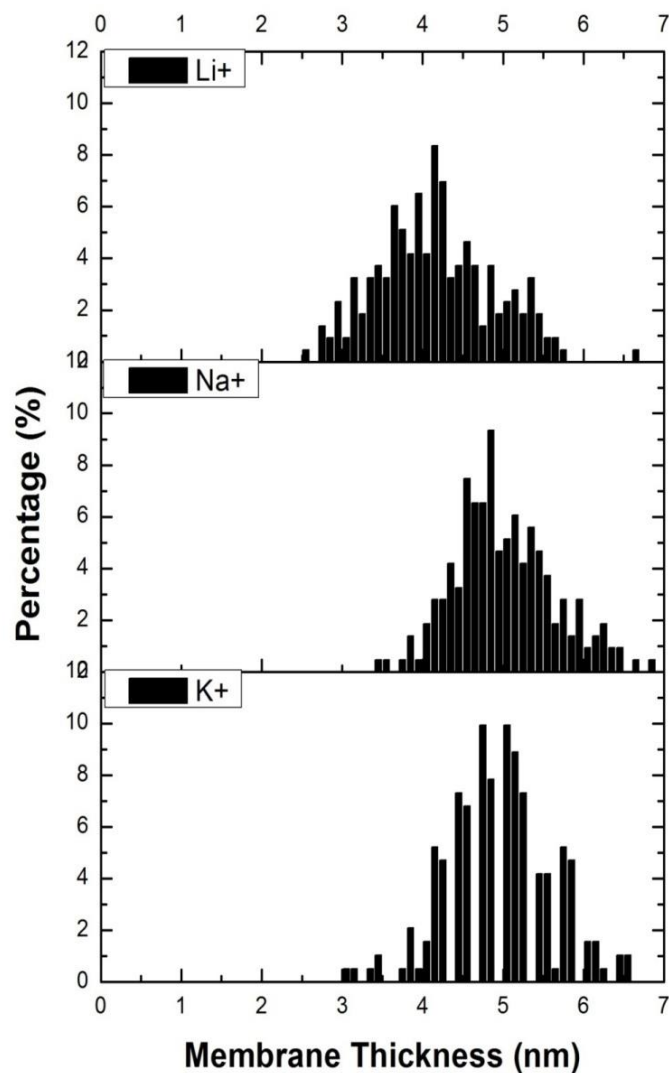


Figure 8.2 Histogram of membrane thickness measured with CM-AFM at sliding velocity 200 – 2000  $\mu\text{m/s}$  for each DOPC SLB prepared on different cations ( $\text{Li}^+$ ,  $\text{Na}^+$ , and  $\text{K}^+$ ) with concentration 150mM.

$\text{Li}^+$  :  $4.09 \pm 1.45$  nm;  $\text{Na}^+$  :  $4.9 \pm 1.1$  nm;  $\text{K}^+$  :  $4.95 \pm 1.31$  nm.

Many scientific articles report that alkali and alkaline ions affect the mechanical resistance of PC membranes (Haverstick & Glaser 1987; López Cascales & García de la Torre 1997; Bockmann et al. 2003; Gurtovenko et al. 2005; Garcia-Manyes et al. 2005; Cordoní et al. 2008; Gurtovenko & Vattulainen 2008; Vácha et al. 2009; Vácha et al. 2010). In general, cations can reduce the intermolecular distance in the bilayers promoted by polar headgroup screening enhancement (Garcia-Manyes et al. 2005). In addition, they can also modify the kinetics of the rupture process resulting to different activation energies. (Redondo-Morata et al. 2012). Our results also show the change in punchthrough force when different alkali ions



are involved (see Figure 8.3). There is a drastic increase of punchthrough force of DOPC-K (5.56 nN) compared to DOPC-Li and DOPC-Na. It might be related to the larger size of  $K^+$  ions.  $K^+$  offers an optimal size to fit the distance among PC headgroups (Redondo-Morata et al. 2012). However, the hydration layer of cations should be taken into consideration. Hydration shell of  $Na^+$  is constituted by three water molecules thus its diameter becomes approximately 5 Å. Meanwhile,  $K^+$  is unable to attract water molecules so the radius of hydrated  $K^+$  is equal with its ionic size (1.52 Å) (Degrève et al. 1996).

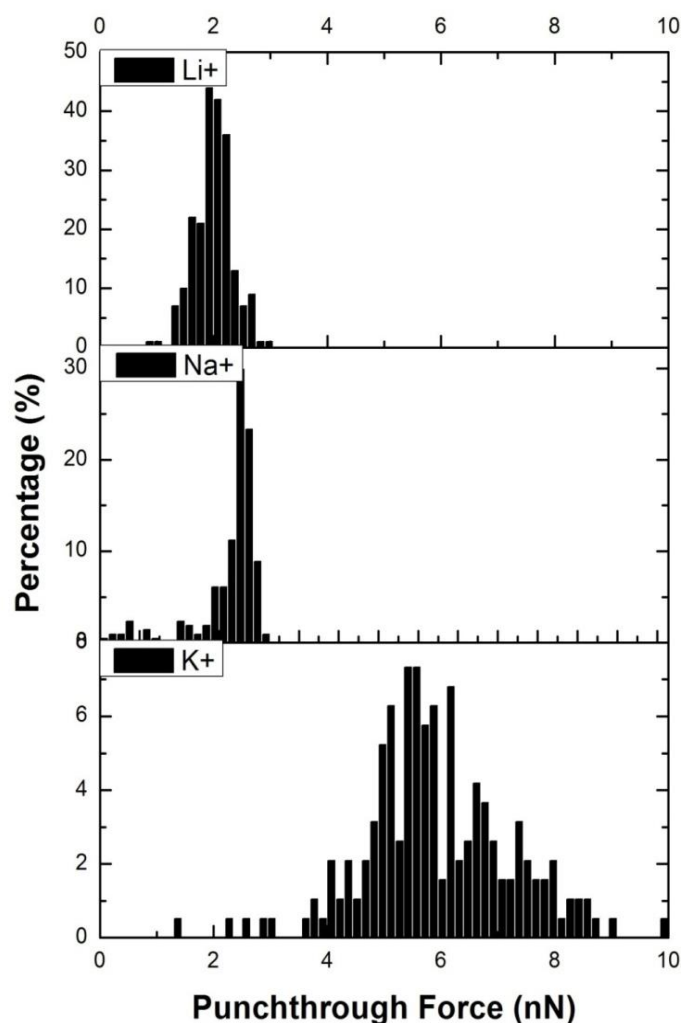


Figure 8.3 Histogram of membrane punchthrough force measured with CM-AFM at sliding velocity 200 – 2000  $\mu\text{m/s}$  for each DOPC SLB prepared on different cations ( $Li^+$ ,  $Na^+$ , and  $K^+$ ) with concentration 150mM.  $Li^+$  :  $2.01 \pm 0.56$  nN;  $Na^+$  :  $2.52 \pm 0.32$  nN;  $K^+$  :  $5.56 \pm 1.38$  nN

The typical raw force curve of DOPC bilayers measured in different media can be seen on Figure 8.4 and Figure 8.5 for normal and friction force respectively. The punchthrough force is defined as a force where the jump found in the normal force curve or when the tip pierced the membranes (the event was indicated by the dashed elips). In the friction force curve, the

dashed elips show the cloud of points generated when the AFM tip sliding through the membranes.

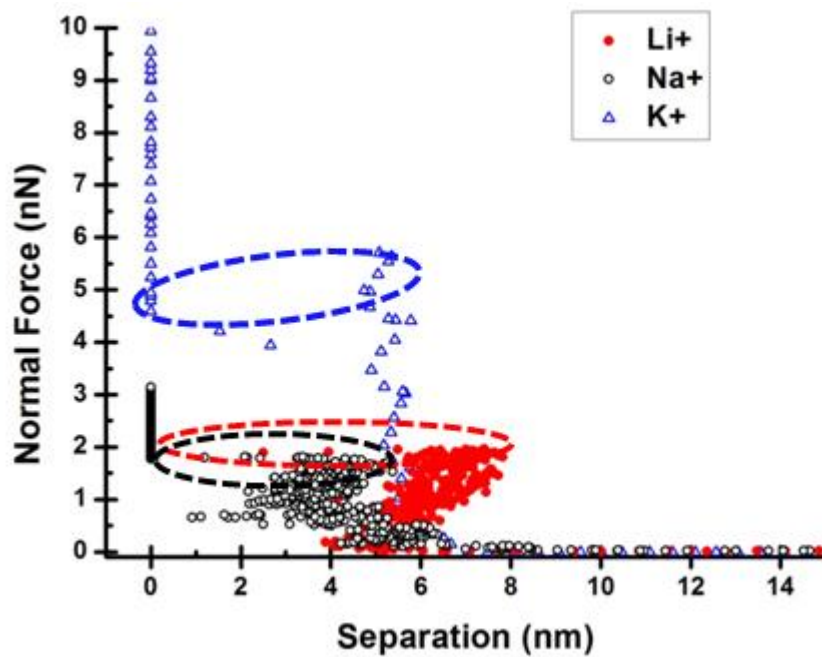


Figure 8.4 Normal forces versus separation curve of DOPC SLBs incubated with different cations. Measurement was done at sliding velocity of  $214\mu\text{m/s}$ . The dashed ellipse shows the event of membranes' perforation. The jump in curves indicates the rupture of the membranes

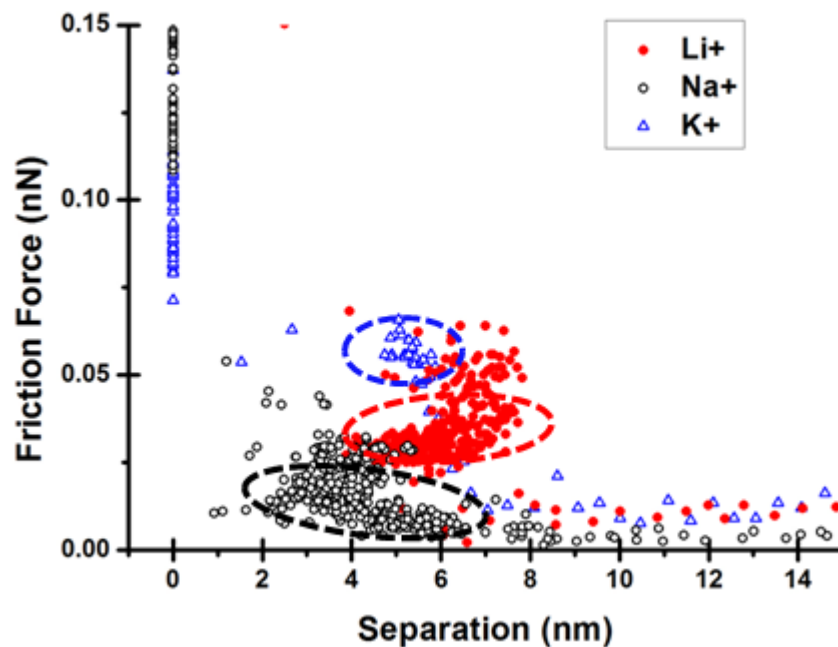


Figure 8.5 Friction force versus separation curve of DOPC SLBs incubated with different cations. Measurement was done at sliding velocity of  $214\mu\text{m/s}$ . The dashed ellipse shows the cloud of points that indicates the tip sliding on the membrane surface. The membrane rupture is detected by the jump

Here, it is clear that DOPC-K has the higher punchthrough force among the three. Meanwhile, between DOPC-Li and DOPC-Na, the difference is relatively small. Furthermore, friction force of each membrane has a plateau that is formed when the tip slides on top of the membrane. The cloud of point in friction curve of DOPC-K is located higher, indicating that DOPC-K also gives the highest friction force.

The great advantage of CM AFM is to permit the measurement of friction force at high sliding velocity. We have measured the friction force of each DOPC membrane at different sliding velocities and the result is shown in Figure 8.6. In all cases, friction is linearly proportional to the sliding velocity. The difference found is the slope of regression line that we define as the viscous friction coefficient (nN.m/s). There is approximately three-folds-increase of viscous friction coefficient in the presence of K<sup>+</sup> compared to other cations. The friction values of DOPC-Li and DOPC-Na are not far from each other at all sliding velocities. Besides, DOPC-K shows higher offset compared to the others (0.111 nN of friction force). While, DOPC-Li and DOPC-Na have 0.011 nN and 0.003 nN of offset respectively.

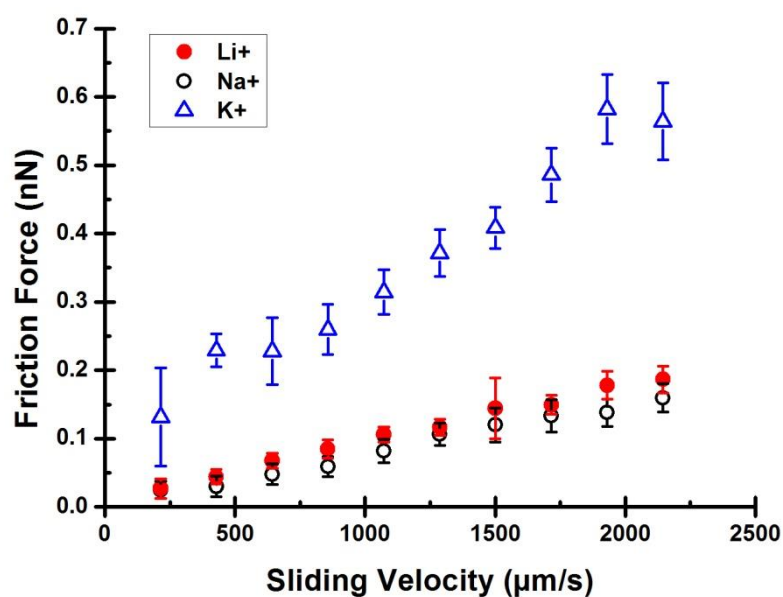


Figure 8.6 Friction force, measured by CM-AFM, as function of sliding velocity for DOPC SLBs incubated with three different cations. The viscous friction coefficients for DOPC prepared in the presence of LiCl, NaCl, and KCl are  $83.31 \pm 7.93$  nN.m/s ( $R^2=0.98$ );  $72.85 \pm 8.87$  nN.m/s ( $R^2=0.99$ ); and  $209.88 \pm 21.61$  nN.m/s ( $R^2=0.94$ ) respectively (measured as slope regression line of each data set)

## 8.3 Discussion

Considering the differences in size for each cations, both friction and punchthrough force give similar response: they are higher for larger ionic diameter. The relation between ionic size of cations, friction and punchthrough forces can be seen on Figure 8.7. The values of friction and punchthrough forces for DOPC found in the presence of  $\text{Li}^+$  and  $\text{Na}^+$  can be considered as similar. It indicates both  $\text{Li}^+$  and  $\text{Na}^+$  interact similarly with the lipid membranes. Meanwhile,  $\text{K}^+$  offers significant changes to membranes properties.

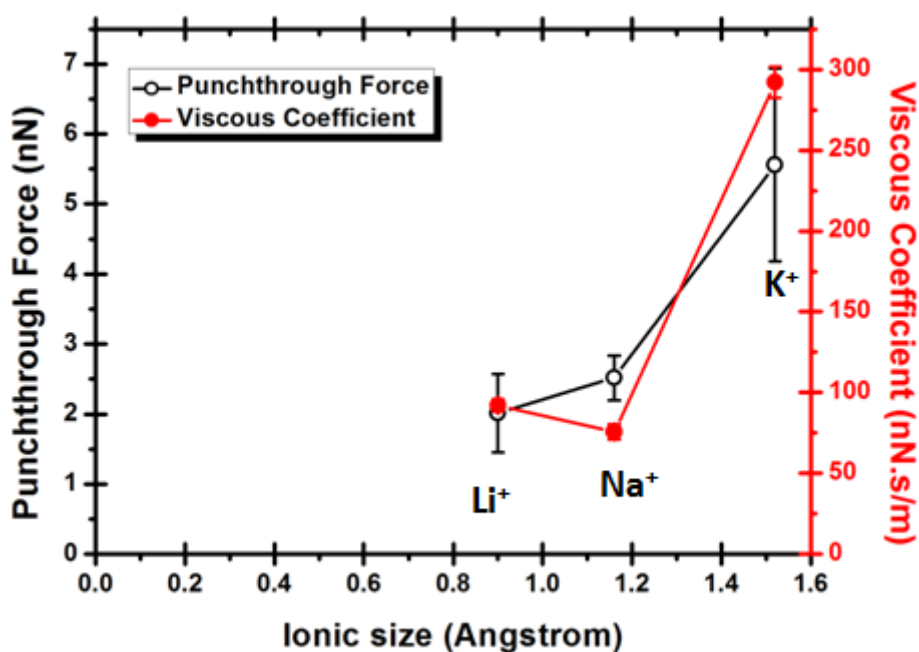


Figure 8.7 Punchthrough force and friction viscous coefficient of DOPC SLBs as function of ionic size ( $\text{Li}^+ = 0.9\text{\AA}$ ;  $\text{Na}^+ = 1.16\text{\AA}$ ; and  $\text{K}^+ = 1.52\text{\AA}$ ) measured by CM-AFM (sliding velocity 200 – 2000  $\mu\text{m/s}$ ).

However, Redondo-Morata et al, from their experimental results stated that  $\text{Li}^+$  does not have specific adsorption to the headgroup of PC membranes: for both fluid and gel-like phase; unlike the other cations (Redondo-Morata et al. 2012). But it should be highlighted that the interaction of  $\text{Li}^+$  can be different for each lipid membrane. For example, a small amount of  $\text{Li}^+$  has big dehydration effect on PhosphatidylSerine (PS) lipid membrane.  $\text{Li}^+$  increases the order of lipid tails resulting in a decrease of surface area per lipid (López Cascales & García de la Torre 1997). From our experimental results,  $\text{Li}^+$  might influence the lipid order at the same way as  $\text{Na}^+$  as DOPC gives the similar response under normal and lateral loading at different sliding velocities.

However, it should be noted that the real diameter of cations (including hydration layer) is bigger than the initial ionic size because the cations attract water molecules and form a hydration layer. In water, the hydration size of  $\text{Li}^+$ ,  $\text{Na}^+$ , and  $\text{K}^+$  are 5.3 Å; 4.7 Å; and 3.9 Å respectively (Kielland 1937) for six water molecules. It is in the condition that the cations have 6 coordination number (Shannon 1976) and they are able to attract the maximum number of water molecules. The complete properties of alkali cations are listed in Table 8.1. In order to be able to penetrate into the membrane, the ions must lose some water molecules.  $\text{Na}^+$  can lose up to three water molecules to bind with DPPC membranes (Pandit et al. 2003), thus its real diameter falls between ionic diameter and its hydration diameter (Redondo-Morata et al. 2012). In the same atomic group, the free energy of dehydration is decreasing, as a result  $\text{K}^+$  can easily lose its water molecule to bind carbonyl lipid group (Berg et al. 2002). So, its real diameter is equal to its ionic diameter (López Cascales & García de la Torre 1997). So finally,  $\text{K}^+$  has the smallest real hydration diameter.

*Table 8.1 Properties of alkali cations*

<b>Ion</b>	<b>Crystal ionic radius (Å)</b> (Shannon 1976)	<b>Dehydration free energy</b> (kJ/mol) (Berg et al. 2002)	<b>Hydration radius (Å)</b> (Kielland 1937)
<b><math>\text{Li}^+</math></b>	0.9	410	5.3
<b><math>\text{Na}^+</math></b>	1.16	301	4.7
<b><math>\text{K}^+</math></b>	1.52	230	3.9

There are still many debates about how cations influence the structure of lipid membranes. Surprisingly, the comparison between the result from molecular dynamics and direct experimental measurement, gives contrary explanation. As molecular dynamics support the weak interaction of  $\text{K}^+$  to lipid carbonyl group, direct mechanical measurement by AFM showed more significant effect of  $\text{K}^+$  (Redondo-Morata et al. 2012). Computation was used to locate monovalent ions in their interaction with lipid membranes. In the case of NaCl,  $\text{Na}^+$  cations accumulate near phosphate region, meanwhile  $\text{Cl}^-$  accumulates at the membrane surface. In the case of KCl,  $\text{K}^+$  is still able to penetrate the headgroup region even though it forms weaker interactions compared to  $\text{Na}^+$  (Vácha et al. 2009). It is in agreement with the precedent numerical analysis (Leontidis & Aroti 2009; Gurtovenko & Vattulainen 2008; Cordoní et al. 2008). Based on the results from molecular dynamics, compared to potassium,

sodium have stronger binding with carbonyl groups of lipids while, potassium does not bind to the bilayers (Cordomí et al. 2008). Moreover,  $K^+$  has smaller surface charge and less ordered hydration shell (weak attraction to water and lipid carbonyl group) (Gurtovenko & Vattulainen 2008).

In contrary with numerical analysis method, the direct mechanical measurement gives the inverse results. It might be due to miss-prediction of ionic size because it is a sensitive issue in molecular dynamics. Gurtovenko et al used Charmm force-field in which it was exaggerating the size of potassium ions (Gurtovenko & Vattulainen 2008).

The interaction of  $Cl^-$  with lipid molecules is also affected by the cations interacting with the membrane. There is more chloride ions accumulated on the membrane surface in the presence of  $Na^+$ . The use of KCl decreases the amount of  $Cl^-$  on the surface due to the inability of  $K^+$  to penetrate deeply into the membrane. Thus, both  $K^+$  and  $Cl^-$  are stacked on the surface (Gurtovenko & Vattulainen 2008).

Mechanical measurements reflect of lipid lateral organization. Due to its optimum ionic size that can better fit the distance between lipid head group,  $K^+$  improves the mechanical resistance of normal and lateral load of lipid membranes, compared with  $Li^+$  and  $Na^+$ . It is indicating that  $K^+$  is able to increase the order of lipid molecules. Indeed, the lipid molecules should be less mobile for DOPC-K as the viscous friction coefficient is higher. In addition, the offset found of DOPC-K indicates that it behaves differently compared to DOPC-Li and DOPC-Na. The low hydration state of potassium ions may favor the penetration of  $K^+$  which may allow the binding to carbonyl groups of lipids.

## 8.4 Conclusion

We have demonstrated the different effects provoked by different monovalent cations. The intermolecular interaction between anion, cation, and lipid molecules is mainly determined by the real size of the ion. Among the alkali cations we have tested, potassium ions improve the mechanical resistance of lipid membranes better than  $Li^+$  and  $Na^+$  because of its small size in water.  $K^+$  penetrates the lipid membranes after discarding its water molecules while  $Na^+$  stays hydrated with 3-5 water molecules. Ionic size is proportional with charge density, and it is used to calculate the cavity size of the solute (Leontidis & Aroti 2009). However, the real ionic size is still a matter of debate as it depends on the number of oxygen

water attracted to the ion, the free energy of dehydration, and also the intrinsic properties of the ions. It is also difficult to directly measure the ionic size. Furthermore, the interaction between lipid membrane and selective cations can explain the mechanisms of ion channels in muscle and nerve cells. The cations are transported through specific channels that act as filters: they selectively allow certain cations to pass through.

## Effect of lipid composition on nanomechanical properties of bicomponents membranes

Cell membranes are constructed by heterogeneous mixture of lipid and sterols. Each component is believed to have specific influence to the lateral organization of lipid membranes. Here, we study the mechanical properties of binary lipid mixtures consisting of fluid-like and gel-like lipids. CM AFM was used to measure the membranes' resistance to normal and lateral force under various sliding velocities and to observe the changes in morphology with the aim to demonstrate the effect of gel-like lipid DPPC to the system of fluid-like lipid DOPC. We found that the influence of DPPC was different at low, moderate, and high concentrations as it is related to the phase transition diagram of DOPC/DPPC mixtures.



## Chapter 9

# Effect of lipid composition on nanomechanical properties of bicomponents membranes

### 9.1 Introduction

Cell membranes consist of a mixture of lipid and sterols that control the flow properties of the membranes: surface shear viscosity and intermonolayer friction coefficient (den Otter & Shkulipa 2007). Surface shear viscosity quantifies the membrane's resistance against shear deformation while intermonolayer friction coefficient is defined as the ratio between the force per unit area and the sliding velocity. Because of its heterogeneous components, membranes present Liquid-ordered (Lo) microdomains, also called lipid rafts which are enriched in sphingolipids and cholesterol. Lo phase is surrounded by a liquid-disordered phase having a different lipid chain packing (Morandat & Kirat 2010).

In the presence of two or more lipids, lipid bilayers exhibit phase segregation. Both lipids should have different melting point (Morandat et al. 2013). Lo and gel domains which are more ordered than Ld domains, have better mechanical stability as they produce higher punchthrough force (Chiantia et al. 2006). The size of Lo and gel phases varies with composition of lipid systems in the bilayers (Nag & Keough 1993) and cooling rate during bilayers' preparation (Blanchette et al. 2006). Cholesterol is known to affect the morphology and the domain size (Rinia et al. 2001). Phase segregation can be found not only on mixture of fluid-gel lipids but also on fluid-fluid lipids; for example the mixture of DiPalmitoyl PhosphatidylEthanolamine (DPPE) and 1,2 Dielaidoyl-sn-glycero-3-phosphatidylcholine (DEPC) (Fallis 1995).

Phosphatidylcholine lipid is the most abundant in eukaryotic cells. We took DOPC/DPPC binary mixtures as an example because they are very common in lipid system biophysical studies. The melting point of DOPC is  $-17^{\circ}\text{C}$  thus it has fluid-like behavior at room temperature (Picas et al. 2012). Meanwhile DPPC has  $T_m$  of  $41^{\circ}\text{C}$  giving gel-like behavior at room temperature. Two lipids with different phase states at room temperature can affect the overall membranes functionality (Attwood et al. 2013).

We have demonstrated in the previous chapter that the mechanical properties of the lipid membrane reflect membrane's molecular organization (Garcia-Manyes & Sanz 2010). Thus, in this study, our aim is to observe the influence of lipid mixture composition of DOPC/DPPC to the overall membranes' structure/properties by measuring its mechanical stability, including its friction properties. The viscous properties of membranes with various compositions will also be discussed as CM AFM allows friction measurement at wide range of sliding velocities.

## 9.2 Results

SLBs of DOPC/DPPC in various compositions were prepared in 10 mM Tris buffer containing 150 mM NaCl on glass surface. SLBs were imaged before (see Figure 9.1) and after mechanical circular mode measurement. We did not find circular traces on lipid surface after CM AFM measurement thus we did not show the images. The pure DOPC image shows a homogenous flat surface of assembled-lipid molecules. Until 25% of DPPC, both lipids are miscible as no phase separation can be seen in images. When as many as 30% DPPC was added, phase separation appears. The brighter areas correspond to gel-like domains which is rich with DPPC molecules. Meanwhile, the darker areas correspond to fluid-like domains, dominated by DOPC molecules. The step height different between both domains is  $1.1 \pm 0.2$  nm which is in accordance with previously published articles (Morandat & Kirat 2006). As the concentration of DPPC is increasing, the gel domain is getting larger. In the 100% DPPC topography image, there are some holes (darker area) due to incomplete fusion process.

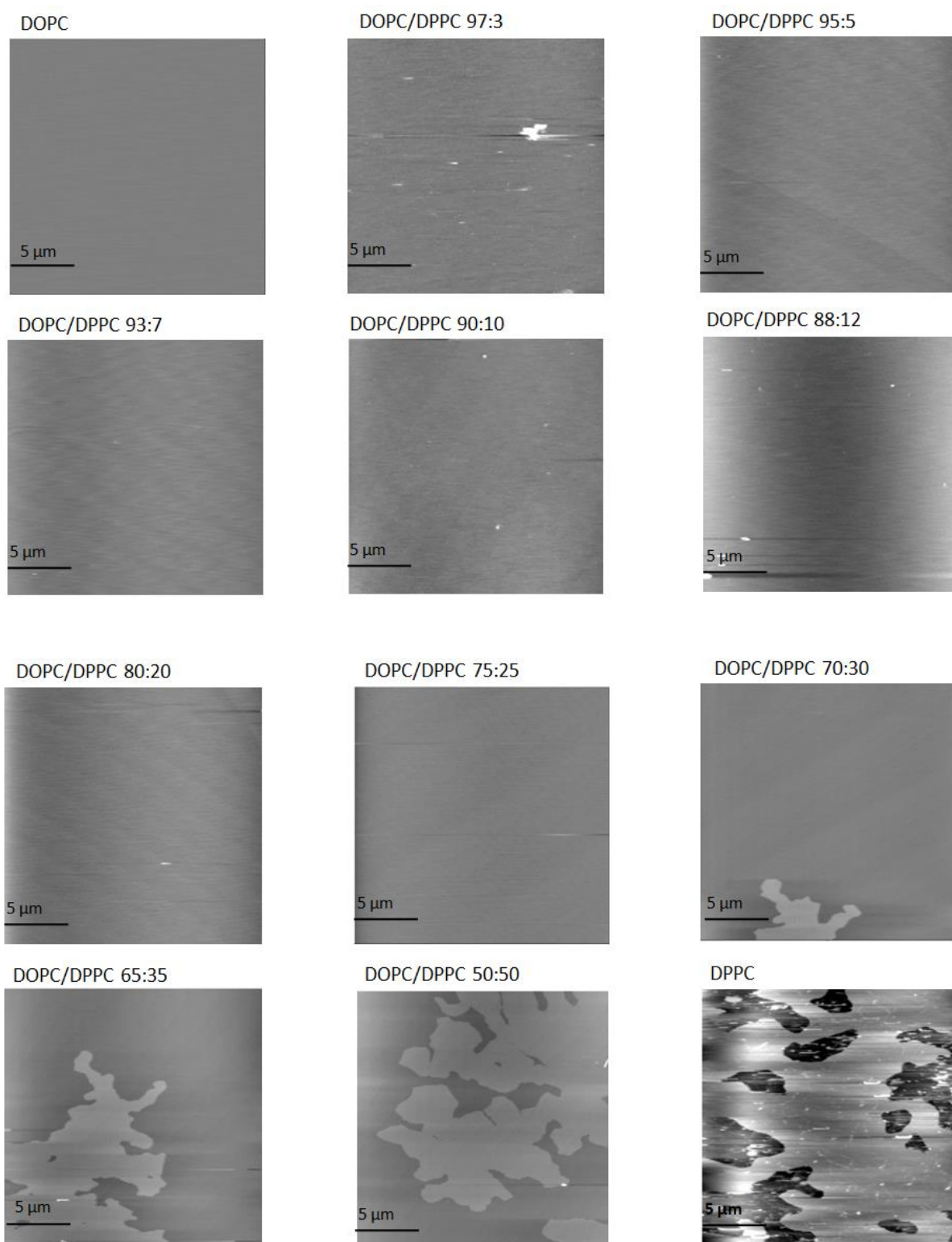


Figure 9.1 Image of DOPC/DPPC SLBs with different composition. Size = 20 $\mu$ m x 20 $\mu$ m, z-range = 10nm

The compilation of histogram corresponding to membranes' punchthrough force is displayed on Figure 9.2. Meanwhile, Figure 9.3 gives us more details about the Gaussian curve fitting. The average Gaussian value is the peak of the fitting curve. With the increased amount of DPPC, the mechanical resistance of lipid mixture to punches is improved. However, when the amount of DPPC reaches 12%, the lipid mixture starts to behave differently as we have a decreasing value.

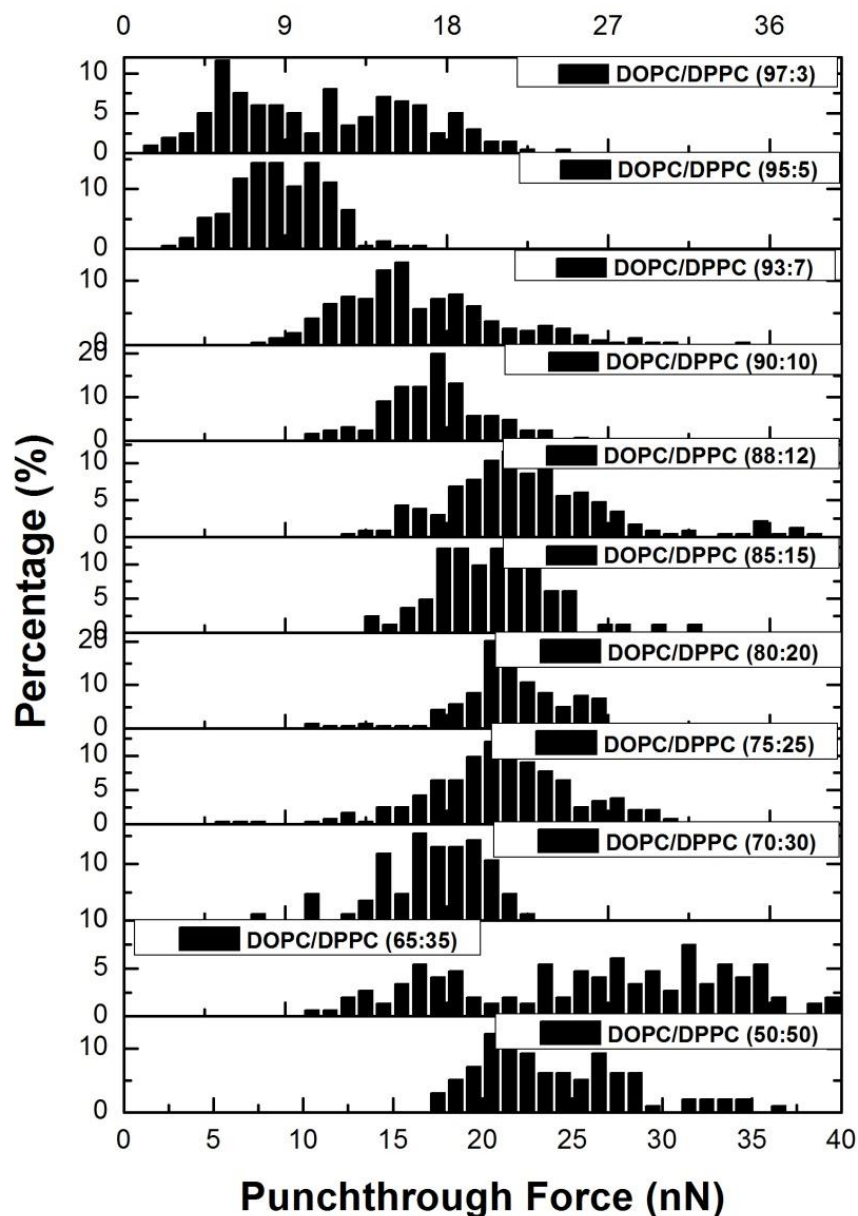


Figure 9.2 Histogram of punchthrough forces of DOPC/DPPC SLBs measured by CM-AFM (sliding velocity: 200 – 2000  $\mu\text{m/s}$  all combined) with various ratios prepared in 10 mM Tris containing 150 mM NaCl and 3mM  $\text{CaCl}_2$

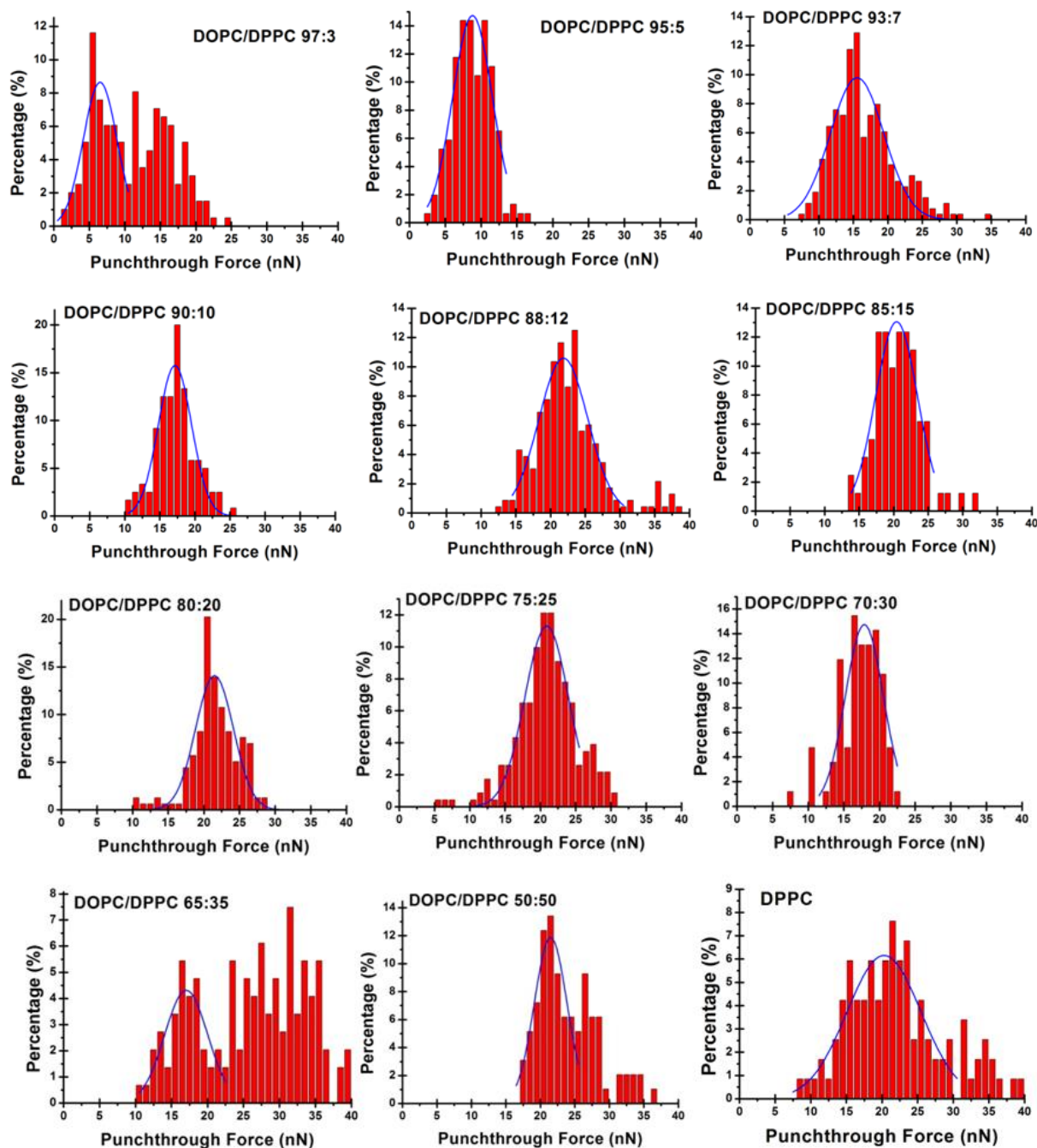


Figure 9.3 Histogram of membranes' punchthrough forces for DOPC/DPPC SLBs measured by CM-AFM (sliding velocity: 200 – 2000  $\mu\text{m/s}$  all combined) with various ratios prepared in 10 mM Tris containing 150 mM NaCl and 3mM  $\text{CaCl}_2$ . The blue solid line represents the average Gaussian fit.

Friction measurement under different sliding velocities gives access to direct examination of membranes' viscous properties. In all cases, the friction force increases linearly with the increase of sliding velocity (see Figure 9.4). The viscous friction coefficient is measured as the slope of regression line for each lipid binary mixture.

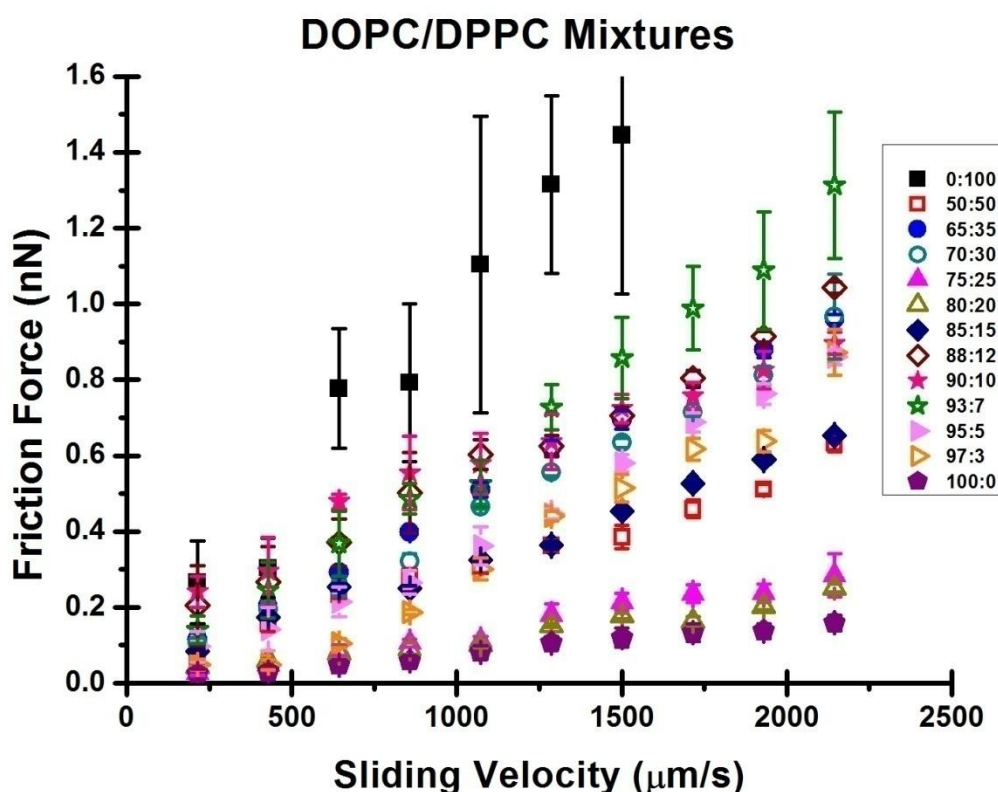


Figure 9.4 Friction force of lipid bilayers measured by CM-AFM as a function of the sliding velocity for DOPC/DPPC SLBs prepared with various lipid ratios. All lipid membranes were prepared in 10 mM Tris containing 150 mM NaCl and 3mM CaCl<sub>2</sub>.

The punchthrough force and friction viscous coefficient obtained from the regression line of data in Figure 9.4 are resumed in **Error! Reference source not found.** Figure 9.5 gives the complete comparison of punchthrough forces and viscous friction coefficients as function of DPPC's composition. Considering the standard deviation of each measurement, the friction force at the membranes' surface is linearly dependent to the sliding velocity for all mixtures composition. Thus, we assume that the linearity of friction force to sliding velocity is independent to the chemical composition of lipid membranes. Interestingly, The curves' slope is not linearly dependent with the concentration of DPPC, and based on our results, we can divide the curve area into three sections. From 0 to 12%, both the punchthrough force and the viscous coefficient are increasing linearly. Between DPPC concentrations of 12-30%, the punchthrough force is relatively constant. On the contrary, the viscous coefficient is decreasing from 488nN.s/m to 114nN.s/m but later it was recovered to its initial value of 423nN.s/m at

DPPC concentrations of 30%. Later on, there is drastic increase of friction viscous coefficient when the DOPC molecules are absent (pure DPPC SLBs).

*Table 9.1 Summary of mechanical characterization of DOPC/DPPC binary mixture by CM AFM*

<b>DOPC (%)</b>	<b>DPPC (%)</b>	<b>Punchthrough Force (nN)</b>	<b>Viscous friction coefficient (nN.s/m)</b>	<b>Intercept (friction at v=0m/s) (nN)</b>	<b>R<sup>2</sup></b>
<b>0</b>	100	20.3 ± 10.4	1040.0 ± 40.2	-0.074	0.98
<b>50</b>	50	21.5 ± 4.7	334.3 ± 12.5	0.065	0.97
<b>65</b>	35	17.1 ± 6.0	458.1 ± 3.7	0.012	0.99
<b>70</b>	30	18.0 ± 5.8	425.3 ± 3.1	0.016	0.99
<b>75</b>	25	20.9 ± 6.2	125.2 ± 5.0	-0.002	0.97
<b>80</b>	20	21.5 ± 5.3	114.5 ± 2.0	0.017	0.97
<b>85</b>	15	22.1 ± 6.1	306.6 ± 1.8	0.028	0.99
<b>88</b>	12	21.9 ± 7.1	488.5 ± 1.8	0.055	0.98
<b>90</b>	10	17.2 ± 4.8	465.9 ± 8.9	0.257	0.97
<b>93</b>	7	15.5 ± 7.8	561.3 ± 22.1	0.012	0.97
<b>95</b>	5	8.8 ± 5.6	381.1 ± 5.2	-0.084	0.98
<b>97</b>	3	6.5 ± 4.7	276.6 ± 4.8	-0.127	0.92
<b>100</b>	0	2.5 ± 0.3	75.56 ± 4.7	0.004	0.98

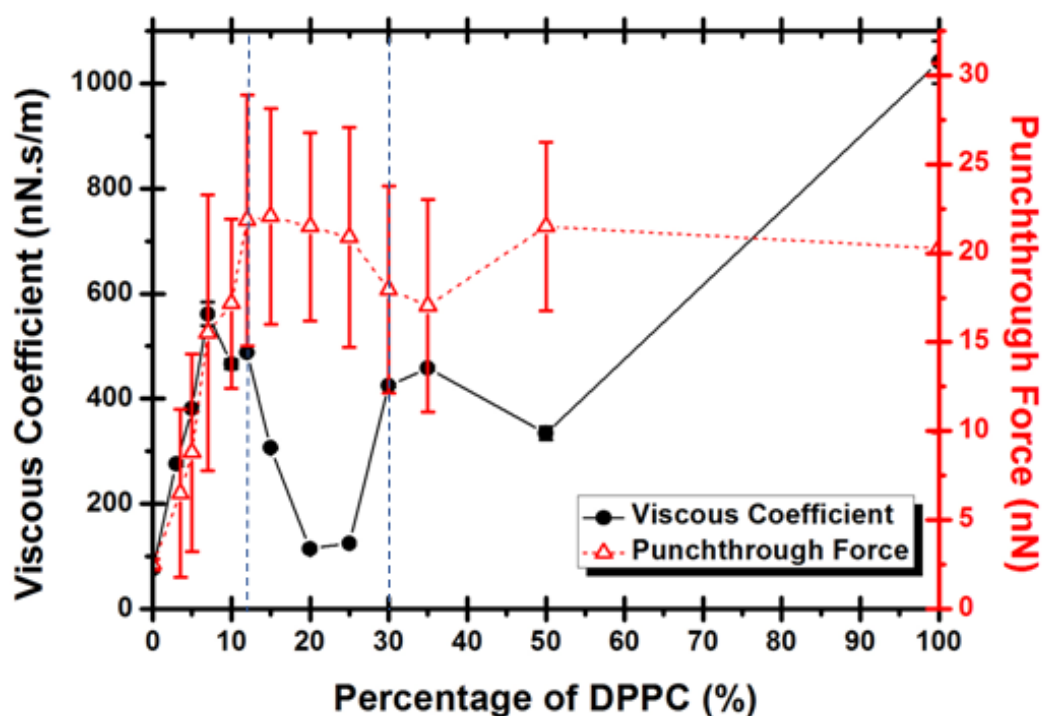


Figure 9.5 Friction viscous coefficient and punchthrough force of DOPC/DPPC SLBs as a function of DPPC %mol in the membrane, measured by CM-AFM (sliding velocity 200 – 2000  $\mu\text{m/s}$ )

### 9.3 Discussion

It is worth noting that at low concentration of DPPC, it was well-mixed with DOPC molecules, so no domains were seen in AFM images. Over the threshold value of 35% at room temperature ( $T=22^\circ\text{C}$ ) (Elliott et al. 2005), DPPC is then able to segregate in gel domains as the fluid phase is saturated with DPPC molecules, (Bernchou et al. 2009).

The evolution of punchthrough force and friction viscous coefficient as a function of DPPC composition in DOPC/DPPC mixtures (Figure 9.5) shows that it can be divided into three regimes: 0-12% DPPC; 12-30% DPPC and 30-100% DPPC. The phase diagram of DOPC/DPPC can be seen on Figure 9.6.



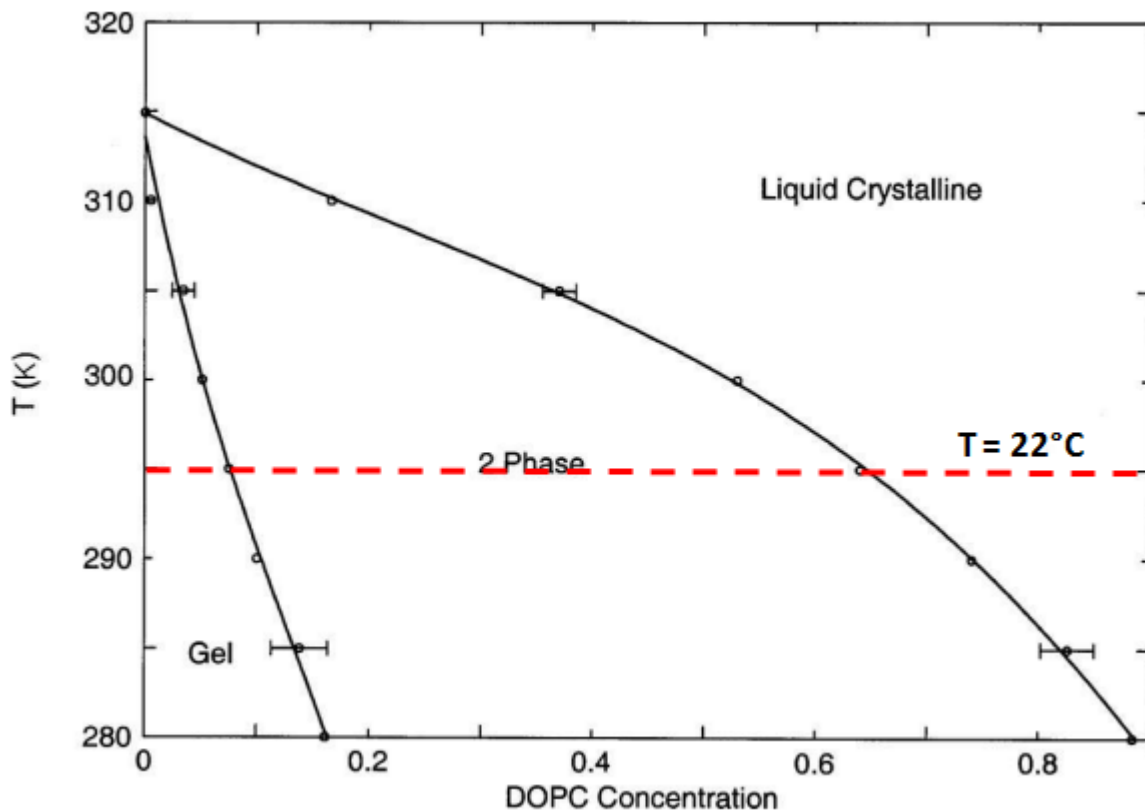


Figure 9.6 Phase diagram of DOPC/DPPC lipid mixture as a function of the volume fraction of DOPC obtained by calculation based on self-consistent field theory. The red dashed line indicates our measurement temperature ( $T=22^{\circ}\text{C}$ ). (reproduced from Elliott et al. 2005)

#### **DPPC percentage of 0-12%**

At low concentration of DPPC, both the DOPC, and the DPPC molecules are miscible resulting in a homogeneous surface of the bilayers as seen in AFM images. As seen on Figure 9.6, single gel phase is presented at DPPC concentration lower than  $\sim 35\%$  (at  $T=22^{\circ}\text{C}$ ). DPPC molecules are all spread in the fluid phase composed of DOPC molecules mainly and this may result in the reinforcement of membrane's mechanical properties. Indeed, this is what we observed: the addition of DPPC in small quantities allows linear increase of lipid's punchthrough force (Figure 9.5).

#### **DPPC percentage of 12-30%**

In this range of concentrations, the coexistence of  $L_o$  and  $L_d$  phases should be present if we consider the dramatic decrease of the viscous coefficient decreasing to values close to the one for DOPC alone. In this range, we can consider that DPPC molecules begin to segregate into small domains, so that the main phase probed with the AFM sliding tip is the fluid DOPC.

However, it is worth noting that no domains of gel DPPC can be found at percentages below 30%. So another explanation could be that the DPPC begin to be in a less favorable interaction with DOPC which may weaken the membrane. The formation of nanodomains unseen in AFM images is also a possible explanation: as proposed earlier, the gel phase can exist as nanosize domains but they are difficult to spot on AFM image because of a lack of phase height difference the fluid phase (Blanchette et al. 2006). For example, Lo nanodomains can be found in DPPC/Dilauroyl-PC/cholesterol bilayers mixture at very low concentration of cholesterol (0.16-0.25 mol fraction) by using fluorescence resonance energy transfer (FRET) analysis (Feigenson & Buboltz 2001). Observation on LUV of DOPC/DPPC showed that at 25% DPPC, < 4 Å radius of gel-like domains were formed in liposomes meanwhile at 50% DPPC, the domain radius was increased to 14 Å (Keishi & Hiroshi 2013).

Within this range of DPPC percentages, the punchthrough force is relatively constant while the viscous friction coefficient shows a decrease. It seems that the normal force indentation cannot detect the presence of nanodomains and treated the membrane as homogeneous lipid mixture which has reach its saturated point thus the mechanical resistance has reach its maximum point. We assume that the strengthening effect by DPPC molecules is maximized at concentration of 12%. By contrast, the lateral sliding of the AFM probe can detect the phase separation thereby resulting in a decrease in viscosity coefficient of the membrane. It might be due to high sliding velocity (>200 μm/s) so that the AFM tip is able to detect the high mobility of lipid molecules. Meanwhile, the tip-approaching velocity is as low as 15nm/s.

#### ***DPPC percentage of 30-100%***

At this concentration, the phase separation becomes visible as the DPPC-rich domains appeared in microscale size. The size of the this domain is increasing with the increase of DPPC concentration (Keishi & Hiroshi 2013). It is in agreement with the phase diagram (see Figure 9.6) in which the coexistence of Lo and Ld phases started to appear at percentages above 25% of DPPC in DOPC (Uppamoochikkal et al. 2010). However, the critical concentration of DPPC can differ depending on the system and the method of observation. For example, Suga and Umakoshi found that the phase separation is starting at 50% of DPPC in LUVs systems, observed by TEMPO quenching method (Keishi & Hiroshi 2013).

In addition, the Gaussian mean punchthrough force value remains relatively constant while the viscous friction coefficient soars back to the initial value range before decreasing. At

100% of DPPC, the viscous friction coefficient is at the maximum value. However, the histogram of membranes' thickness and punchthrough forces (see Figure 9.2 and Figure 9.3) show important variations sometimes. It can be the drawback of co-existing domains. Moreover, the amount of gel domain probed may change from one sample measurement to another, resulting variation of values. For friction measurement, in the presence of gel and fluid domains, the friction value recorded is the mean value for all features (gel and fluid) because it is difficult to distinguish the friction of gel and fluid domains. Nevertheless, the friction mean maintains its linear behavior against sliding velocity.

## 9.4 Conclusion

We have demonstrated the effect of increasing the gel phase in a fluid membrane by addition of DPPC in DOPC SLBs. The morphology and mechanical properties of DOPC/DPPC SLBs changed with the concentration of DPPC. At critical concentration (30 % DPPC), the phase separation occurred while below 30% DPPC, the mixture seems to be miscible under our conditions (deposited on a glass support). Measurement of friction in various sliding velocity allows us to study the viscous properties of lipid mixtures by deducting the friction viscous coefficient. This measurement can only be done with CM-AFM that can generate high and continuous sliding velocity (up to 2000 $\mu\text{m/s}$ ). The friction viscous coefficient reveals an intermediate behavior, the formation of nanodomains, that are not detected by conventional AFM. In short, CM-AFM is able to investigate the unseen transition in bicomponents lipid membranes that are able to segregate different phases.

## Effect of chain length on nanomechanical properties of pure SLBs

Phospholipids are amphiphilic molecules that have hydrophilic and hydrophobic groups. The hydrophobic part consists of two carbon chains for which the length and saturation can be varied from one lipid to another. Here, we will discuss the effect of carbon number in tail chain to the mechanical and frictional properties of lipid membranes. Dilauriloyl phosphatidylcholine (DLPC), dimyristoyl phosphatidylcholine (DMPC), and dipalmitoyl phosphatidyl choline (DPPC) with 12, 14, and 16 carbons respectively were prepared and measured by CM-AFM separately. We found that lipid with longer carbon chain has better mechanical resistance and higher friction viscous coefficient.

# Chapter 10

## Effect of chain length to nanomechanical properties of pure SLBs

### 10.1 Introduction

A single phospholipid molecule consists of a hydrophilic head group and a hydrophobic carbon chain tail. Lipid molecules can be positively or negatively charged or they can be zwitterionic (*i.e.* bearing a headgroup with the same amount of both positive and negative charges). The charge of lipids depends on their headgroup. There are various headgroups such as: phosphatidylcholine (PC) and phosphatidylethanolamine (PE) which are zwitterionic or phosphatidylglycerol (PG) and phosphatidylserine (PS) which are negatively charged. Meanwhile, the hydrophobic part is made of a carbon chain more or less long. The saturation of lipids correspond to the amount of double bonds (=unsaturations) found in the carbon tail. For example, DOPC has two acyl chains, each with 18 carbons and one double bond per tail. As a result DOPC is noted (18:0), the first number corresponding to the number of carbons per chain and the second number corresponding to the number of unsaturations. The presence of double bonds can modify the lipid membranes' properties significantly. For example, for the lipid DiStearoyl PhosphatidylCholine (DSPC) with 18 carbons per chain but with no unsaturations (18:0), the punchthrough force is 20 times higher (Garcia-manyes et al. 2010) than for DOPC (18:1) that has one unsaturation per chain (Chiantia et al. 2006).

Thus the mechanical properties of lipid membranes are strongly affected by their chemical composition such as: hydrophobic tail length, hydrophilic headgroup, and level of chain saturation (Garcia-manyes et al. 2010). Garcia et al found that the punchthrough force of PC membrane increases with increase of tail chain length.

The aim of this study is to quantify the friction force of lipids with different tail chain length. By using CM-AFM, we have an access to observe the viscous properties of SLBs under various sliding velocities.

## 10.2 Results

CM-AFM is used to measure the friction of pure (*i.e.* single component) lipid membranes DMPC, DLPC, and DPPC in 10 mM Tris buffer with 150 mM NaCl. The final concentration of lipid is 1 mM deposited on glass surface and heated at 60°C for 1 hour. CM-AFM was done with a silicon nitride tip, spring constant = 0.4489 N/m and lateral force calibration constant = 32.76 nN/V. We used a frequency of 175 Hz and amplitude range from 1 to 10 V.

The membranes thickness was measured as the vertical distance obtained for jump through during penetration by AFM tip. The average value of thickness is referred to Gauss average value calculated from the data histograms shown in Figure 10.1. Unfortunately, the histogram of DLPC shows wide variations (high standard deviation). Its thickness' histogram shows two data populations: first population is referred to the real thickness with an average value of  $3.78 \pm 1.17$  nm. Given its fluid-like characteristic, DLPC molecules can attach to the AFM probe as monolayers or bilayers so the thickness measured with the peak on the right side of the histogram is 1.5-2 times higher than real thickness; including the thickness of lipid on the AFM probe.

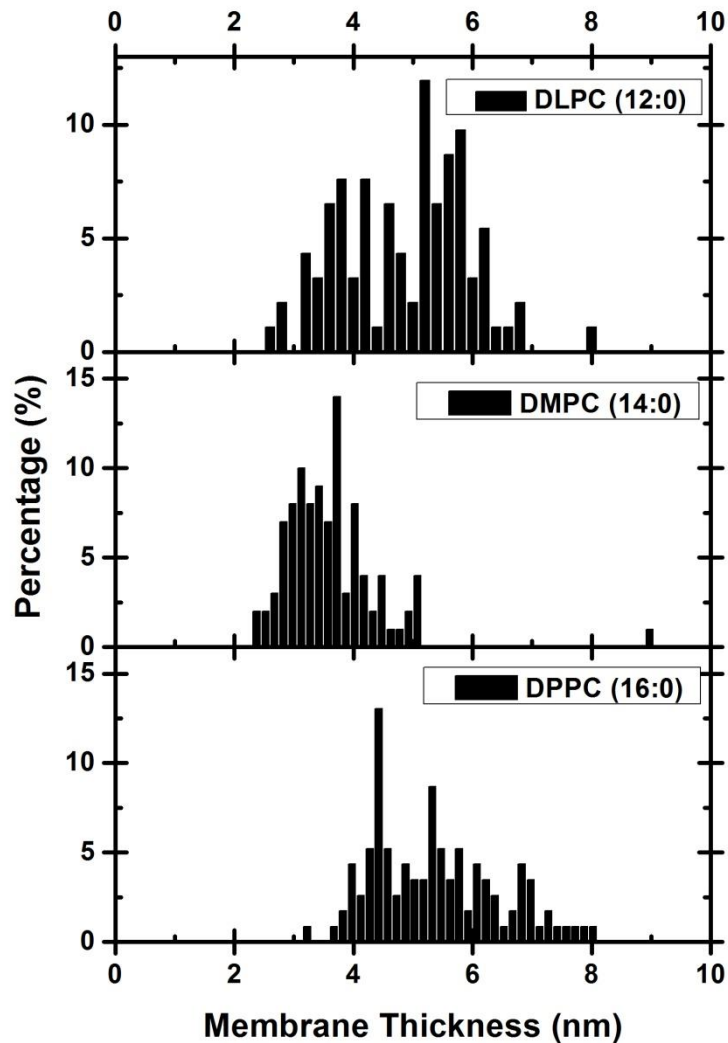


Figure 10.1 Histogram of membranes' thickness of SLBs of DLPC, DMPC, and DPPC incubated in 10 mM Tris containing 150 mM NaCl at pH 7.4 and were measured with punchthrough experiments by CM-AFM (sliding velocity: 200 – 2000  $\mu\text{m/s}$  all combined)

Figure 10. 2 compares the histogram of membranes' punchthrough forces or the force necessary to pierce the membrane with detail of Gaussian average line shown in Figure 10.3. These results are in agreement with the report published by Garcia-Manyes et al showing that the punchthrough force is increasing with the number of carbon in tail chains (Garcia-manyes et al. 2010).

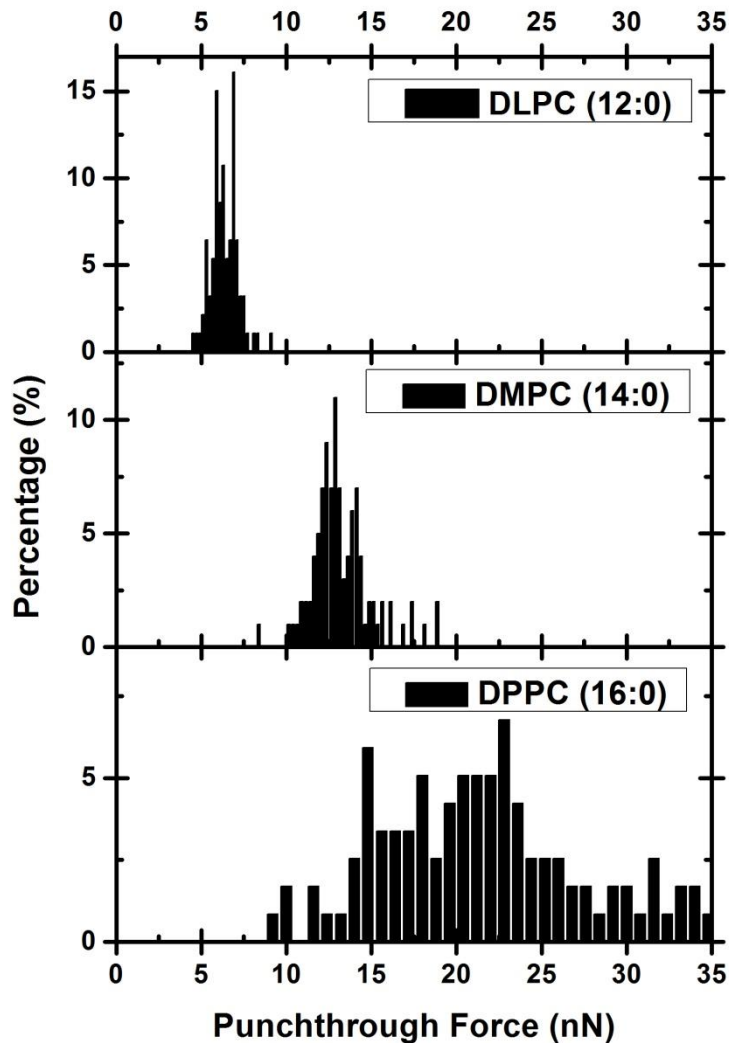


Figure 10. 2 Comparison of histogram of membranes' punchthrough force measured by CM-AFM (sliding velocity: 200 – 2000  $\mu\text{m/s}$  all combined) for SLBs of DLPC, DMPC, and DPPC prepared on 10 mM TBS containing 150 mM NaCl and 3 mM  $\text{CaCl}_2$  pH 7.4

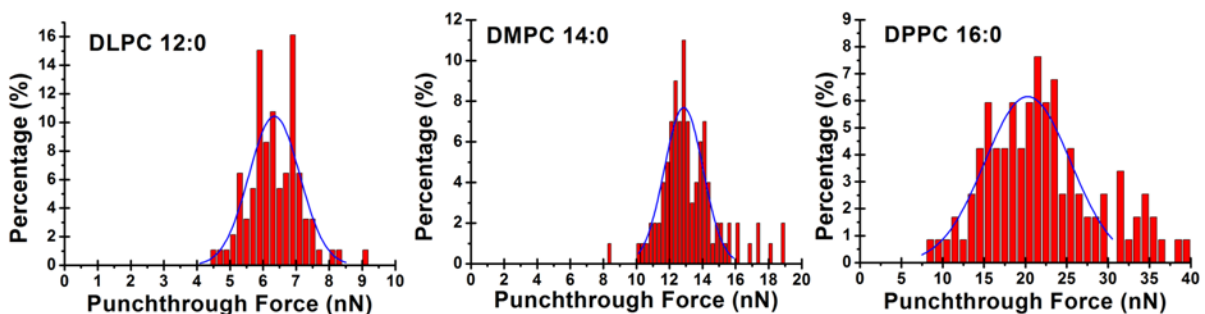


Figure 10.3 Histogram of membranes' punchthrough force for SLBs of DLPC, DMPC, and DPPC prepared on 10 mM TBS containing 150 mM NaCl and 3 mM  $\text{CaCl}_2$ . The solid line represents the average Gaussian line. DLPC :  $6.34 \pm 1.5$  nN; DMPC :  $12.86 \pm 2.34$  nN; DPPC :  $20.27 \pm 10.39$  nN



The measurement of friction at different sliding velocities was done to determine the viscous properties of the single component membranes. For all lipid membranes, friction force increases linearly with the increase of sliding velocity (see Figure 10.4). The slope of regression line is referred to as the viscous friction coefficient in nN.s/m.

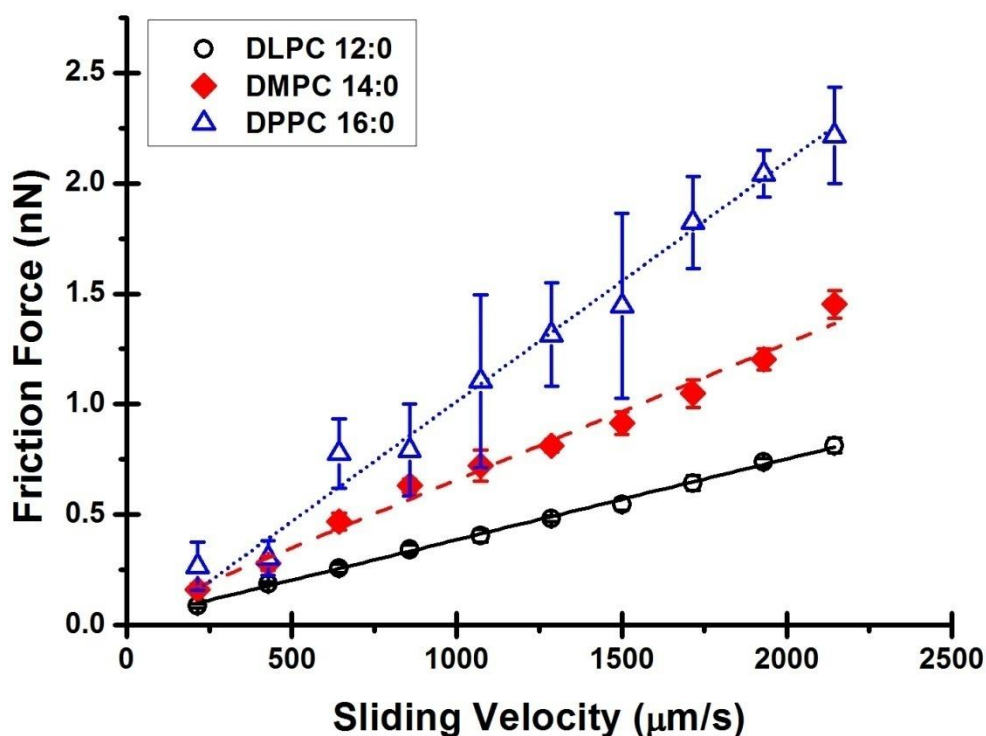


Figure 10.4 Friction force measured by CM-AFM as a function of the sliding velocity for three PC SLBs with different chain lengths. The viscous friction coefficient of DLPC is  $383.15 \pm 4.9$  nN.s/m ( $R^2=0.99$ ); of DMPC is  $649.17 \pm 11.28$  nN.s/m ( $R^2=0.99$ ); and of DPPC is  $1040 \pm 40.2$  nN.s/m ( $R^2=0.99$ ).

Figure 10.5 gives the evolution of the punchthrough force and the viscous friction coefficient as a function of the number of carbons the hydrophobic tail of PC lipids. Both entities are increasing linearly with the length of tail chains. Punchthrough force is increasing by 3.3 nN per carbon number ( $R^2 = 0.99$ ). This value is the same as the one published by Garcia-Manyes et al. ((Garcia-manyes et al. 2010)). Meanwhile, the viscous friction coefficient is increasing 141.1 nN.s/m per carbon number ( $R^2 = 0.98$ ).

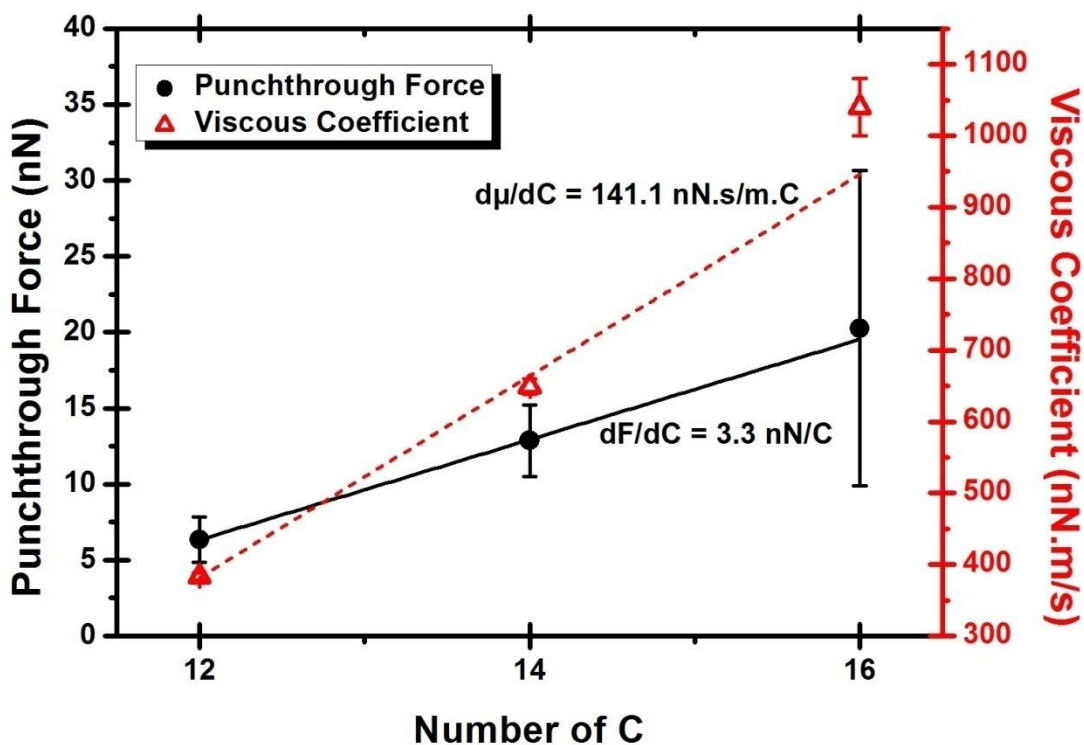


Figure 10.5 Punchthrough force and friction viscous coefficient of PC lipid with different chain lengths.

### 10.3 Discussion

The three lipid characterized has different gel-to-liquid transition temperatures ( $T_m$ ). DPPC with the longer hydrocarbon chain has higher  $T_m$ . Mechanical measurement by CM-AFM was always done at 21°C. Thus, in this condition, DLPC is in fluid state, DMPC is in critical transition state, while DPPC is in gel state. The difference of physical states can results in different mechanical properties. Thus, the measurement of punchthrough forces and friction by CM-AFM can be used as an indication of lipids' physical condition.

Our experimental results showed that there is an increase of 3.3 nN and 141.1 nN.s/m of punchthrough force and friction viscous coefficient respectively per additional two  $\text{CH}_2$  group per hydrocarbon chain. This increase indicates better packing between longer lipid tail chains (Garcia-manyes et al. 2010). Longer tails interact better than shorter tails. From this result, we can expect even higher punchthrough force value for lipids whose longer tail chain. However, if we look back our results for DOPC SLBs 18:1, we obtained punchthrough force of  $2.52 \pm 0.56$  nN. It is due to the effect of unsaturation that causes a bend in the hydrocarbon

chain (Berg et al. 2002). This bend decrease the compactness of lipid chain and so the  $T_m$  is lowered. DOPC molecules have one cis double bond in their tail chain. Thus, even though DOPC has more carbon than DPPC, it has lower  $T_m$  and lower punchthrough force.

Furthermore, each additional  $-\text{CH}_2-$  group generates approximately  $-2.1\text{kJ/mol}$  to the free energy of two hydrocarbon chains interaction as suggested by Berg et al (Berg et al. 2002). Thus, there might also be correlation between entropic contribution and the change of lipid's structure due to addition of two carbons.

Previously, measurement of membranes' viscosity was done mostly on micron size vesicles (GUV). Viscosity of membranes can be deduced from friction of latex particles which are attached on the surface of vesicles (Dimova et al. 2000) by using the theory derived by Danov (Danov et al. 1995). They assumed that there is not any slip between particle surface and lipids. In this latex bead-lipid vesicle systems, the size of the bead must be much smaller than lipid vesicle so that the membrane surface is considered to be flat. Dimova et al has showed that the viscosity of DMPC at above its melting point is varied exponentially with line fit equation of  $\eta_m = 25 \cdot 10^{-6} |T - 23.4|^{-1.4} sp$  (Dimova et al. 2000), where  $T$  is the temperature in celcius. The defined the membranes' viscosity in surface poise ( $sp$ ) unit that indicate the dependency of viscosity to membranes' thickness.

$$\eta_m = \eta \times d \quad (10.1)$$

$$1 sp = 10^{-3} Pa m s = 10^{-3} N \cdot s/m \quad (10.2)$$

where  $\eta_m$ ,  $\eta$ , and  $d$  is the membrane viscosity ( $\text{N}\cdot\text{s}\cdot\text{m}^{-1}$ ), bilayers fluid viscosity ( $\text{N}\cdot\text{s}\cdot\text{m}^{-2}$ ), and membrane thickness (m) respectively (Camley et al. 2010; Shkulipa et al. 2005).

Compared to the Saffman technique (Saffman & Delbrück 1975) which is based on the diffusion of a molecular probe, the microscopic technique involving bead-lipids systems gives higher value, at the range of  $10^{-6} sp$ . While membranes' viscosity calculated through equation of Saffman is in the range of  $10^{-7} sp$ . For example, by using the data acquired from Smith et al (Smith et al. 1979), Waugh (Waugh 1982) obtained viscosity of DMPC to be  $4 \times 10^{-7} sp$ . Meanwhile, by inputting the data from the work of Cherry et al (Cherry et al. 1977), viscosity of DMPC is  $1.5 \times 10^{-6} sp$ .

By converting our results into *surface.poise* ( $sp$ ) unit through simple conversion below,

$$\begin{aligned}\eta_m^{DLPC} &= (383 \pm 0.05) \text{ nN s/m} = (3.83 \pm 0.05) 10^{-7} \text{ N s/m} \\ &= (3.83 \pm 0.05) 10^{-4} \text{ sp}\end{aligned}$$

we obtained SLBs' viscosity is  $(3.83 \pm 0.05) \times 10^{-4} \text{ sp}$  ;  $(6.5 \pm 0.11) \times 10^{-4} \text{ sp}$  ; and  $(1.04 \pm 0.04) \times 10^{-3} \text{ sp}$  for DLPC, DMPC and DPPC SLBs respectively. The result of DMPC is two degrees higher than the values reported probably because we used supported lipid bilayers so we cannot exclude the influence of the solid substrates on the mechanical properties of membranes.

Different ranges of viscosity values are also found for DLPC and DPPC. Wu et al used fluorescence lifetime imaging to determine the viscosity of 200 nm sized LUVs and by multiplying with approximate membranes' thickness value (4.5 nm), they obtained  $7.37 \times 10^{-7} \text{ sp}$  ;  $9.63 \times 10^{-7} \text{ sp}$  ; and  $1.46 \times 10^{-6} \text{ sp}$  for DLPC, DMPC and DPPC SLBs respectively (Wu et al. 2013). The multiplication with membranes' thickness is because their reported value is the bulk viscosity.

## 10.4 Conclusion

There are already many reports regarding the variation of mechanical properties of lipids with different headgroups. Meanwhile, the influence of tail group remains unclear. We have tested a group of PC lipids with various lengths of tail chains. All the PC tested were considered to be viscous materials because the membranes' friction varied linearly with sliding velocity. The friction is defined as a time-dependent response. There is linear relationship between punchthrough force, friction viscous coefficient and length of tail chains of lipid molecules. Again, CM-AFM allowed us to characterize the nanomechanical differences between lipid membranes with good precision and in short time.

*(this page is intentionally left blank)*

# Conclusions and Perspectives

---

# Conclusion and Perspectives

## A. Conclusion

We have presented our three years of work in the previous chapters. The invention of CM-AFM has brought a new insight in the characterization of biological samples. Compared to the conventional AFM, CM-AFM has many advantages:

1. Constant, continuous, and high sliding velocity
2. Practical, accurate and simultaneous measurement of both the normal and the friction forces thanks to the use of a harmonic signal
3. Continuous measurement of forces in realtime.

The results obtained for the measurements on lipid membranes demonstrate these advantages.

In the beginning, several adjustments were done to adapt the technique to the samples' condition. The special characteristic of biological samples is the requirement of aqueous medium. Calibrations were done to observe the linearity of piezoelectric scanner in regards to its circular displacement. Thus, we have defined the limits of CM-AFM:

- Frequency: 50 – 400 Hz
- Amplitude: 0.1 – 10 Volts

By varying these two control parameters, it is possible to generate sliding velocities within the range of 10 to 6000  $\mu\text{m/s}$ . In comparison, the conventional AFM is typically limited to 100 $\mu\text{m/s}$ .

In addition, lateral force calibration was also done for the tip as it is required in friction measurement. It yields the lateral calibration factor that is used to convert the friction force to nanoNewtons. To facilitate our experiment, a simpler protocol called scratch method was developed based on the wedge method.

Several solid substrates were characterized in liquid environment by CM-AFM before testing the lipid membranes. These results demonstrate the different characteristics between micro and nanoscale regimes of friction. For every solid surfaces tested, the friction force is linearly dependent on the sliding velocity. In addition, surfaces' friction is also affected by the liquid composition.

From the previous experiments, we are aware of the linear relation of the friction force with the sliding velocity but also that friction is sensitive to environmental changes. Measurements on fluid DOPC lipid membranes indicate that results obtained with CM-AFM are comparable to conventional AFM for punchthrough force and friction measurements. Besides, on our knowledge, CM-AFM is the first direct approach to measure membrane's viscous friction as we deduce the friction viscous coefficient directly from friction measurement with various sliding velocities. As expected, both punchthrough force and viscous friction coefficient of DOPC are significantly affected by the presence of different cations. The introduction of alkali cations alters the interaction between lipid molecules. Here, we only tested alkali cations, and among them, potassium gives the strongest effect to membranes' stability. We assume that there is relationship between the cations' size and the mechanical properties of lipid membranes.

As in nature, the cell membrane is composed by multiple types of lipid and sterols; we also studied the effect of membranes lipid composition to their nanomechanical properties. In order to have a drastic change, two lipids with very different properties were mixed in various concentrations. We worked with a binary lipid mixture consisting of fluid and gel lipids (DOPC and DPPC, respectively). Under our experimental conditions, up to 25% of DPPC, DOPC/DPPC mixture membranes yield homogenous fluid phase while from 30% of DPPC, phase segregation was spotted. By measuring the friction of these membrane mixtures at various sliding velocities, it is possible to deduce the friction viscous coefficient. The value of friction viscous coefficient reveals an intermediate behavior in membranes: while no segregation of domains can be seen on images, the friction behavior reveals the presence of (sub) nanodomains.

Finally, at the term of this project, few drawbacks of CM-AFM should be fixed. Indeed, CM-AFM does not have the capability to make an offset yet. Furthermore, the AFM probes could be sliding in both fluid and gels phases thus resulting in ambiguous results.

Besides studying the external factor of lipid systems, we also studied the internal factor that can modify the nanomechanical properties of lipid membranes. The acyl chains of phospholipids greatly influence the dynamics of the resulting membranes (viscosity, fluidity, membrane diffusion coefficient). For the phosphatidylcholine lipid, we have tested DLPC, DMPC, and DPPC having 12, 14, and 16 carbons on their tail chains, respectively. Our results reveal that there is a linear relationship between carbon chain length and the mechanical



properties of lipid membranes. For each additional two carbons, there is an increase of 3.3 nN and 141.1 nN.s/m for punchthrough force and friction viscous coefficient respectively.

## **B. Future Perspectives**

Until recently, conventional AFM has successfully explored membranes' mechanics and structure on the nanometer scale. But, given the fact that lipid molecules have high mobility, conventional AFM failed to detect the viscous properties of lipid membranes. The available techniques to study the viscous properties of biological membranes work on microscale by using free-standing lipids (liposomes) (Cicutta et al. 2007; Wu et al. 2013; Honerkamp-Smith et al. 2013). However, CM-AFM can solve the issue of conventional AFM especially regarding the non-constant and low sliding velocity in friction measurement. The new CM-AFM demonstrated its powerfulness in probing the existence of capillary forces on dry solid surfaces due to the presence of water meniscus (Mazeran 2006; Noel et al. 2012). With our experimental results, we can confirm that CM-AFM can also be used to characterize the biological samples under aqueous environment. Thus, it gives new possibilities to measure the nanomechanical properties of others biological samples under native conditions. Large group of biomaterials are interesting to be studied: such as protein layers (*e.g.* collagen), cartilage especially in joints, living cells and more complex biomimetic membranes. In general, CM-AFM can be considered as very useful to characterize surfaces with dynamic properties that are rapidly changing. CM-AFM could also be very useful to probe the friction by dissecting samples layer-by-layer in thickness with sub-nanometer resolution.

## A. AFM Components

The main component of atomic force microscopy is shown at the Figure 1. From top to bottom, it consists of AFM head, scanner, and AFM base.

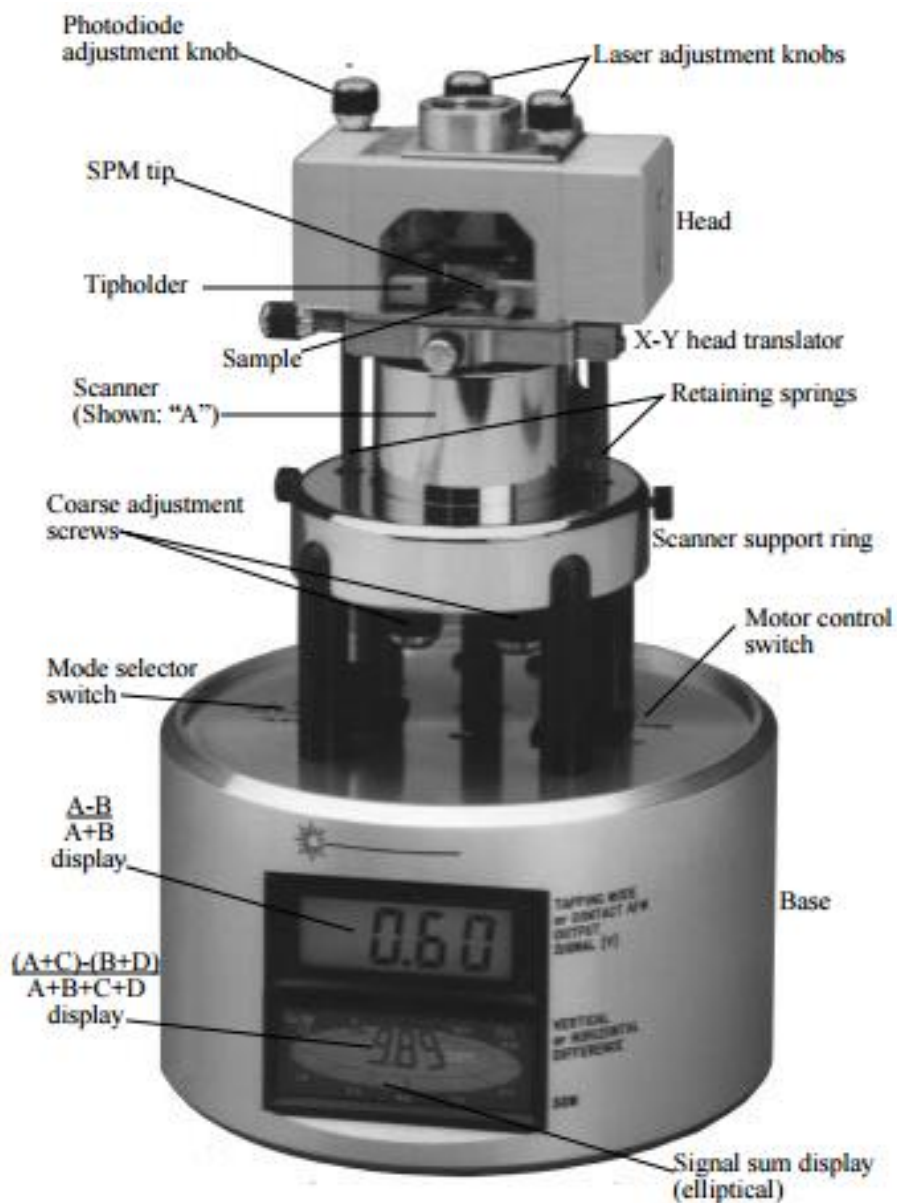
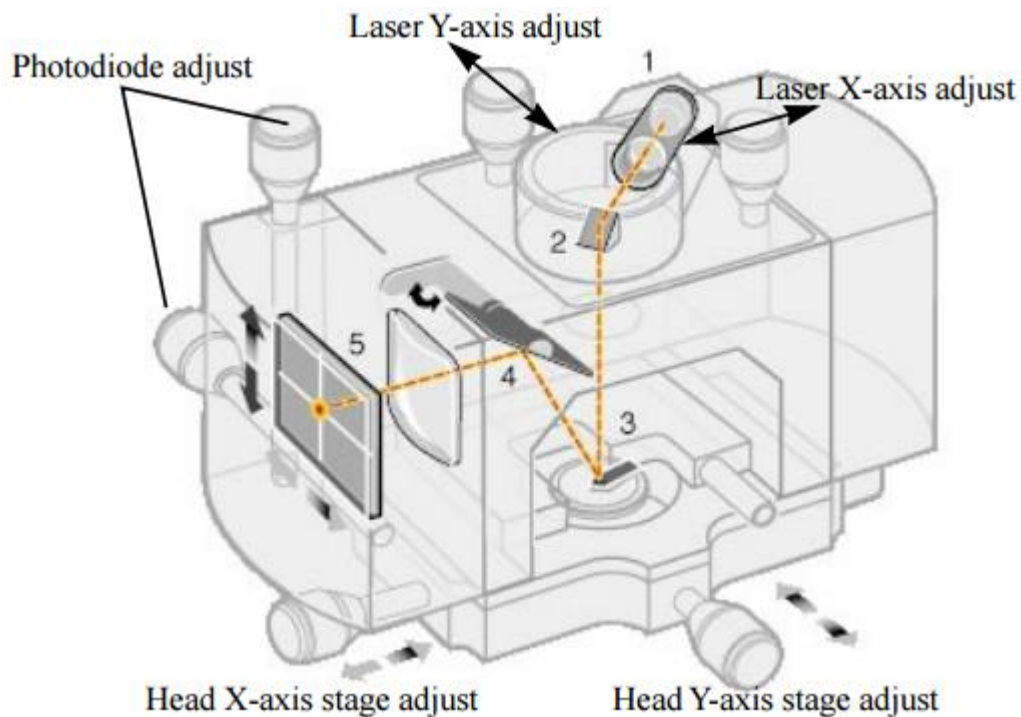


Figure 1 MultiMode atomic force microscopy (reproduced from Anon 1998)

## ***A.1 Optical Head***

Figure 2 shows the AFM head which is occupied by various adjustment knobs and also tip holder. It includes the laser source, mirror, tilt mirror, tip holder, and photodiode detector. The mirror system assures the reflected laser can be detected by photodiode. Position of laser and photodiode detector can be adjusted by turning the knobs on the head AFM while observing the shape of laser beam.



*Figure 2 Head of atomic force microscopy and its component: (1) laser, (2) mirror, (3) tip holder, (4) tilt mirror, and (5) photodiode detector (reproduced from Anon 1998).*

## ***A.2 Tip Cantilever***

Cantilever probe could be made from different materials to have various rigidities. It could also differ in operation mode. In contact mode AFM, most probes are made from silicon nitride which has good flexibility and easy to use. This kind of tips can be easily captured by the sample's surface tension in which the tip is trapped in vapor layer on the sample surface. This surface force exerts force which is enough to deform softer sample. Thus, silicon nitride is more suitable for soft sample. In the market, there are existed with many different sizes and coatings in order to adjust the characteristic of sample. For measurement in liquid, there are

triangular and rectangular cantilever exist. Figure 3 shows one example of triangular cantilever with pyramide tip at the edge.

For tapping mode operation, crystal silicon probe which is stiffer than silicon nitride probe is more favorable. It is more brittle, thus more careful treatment is necessary while setting up the tip and the sample.

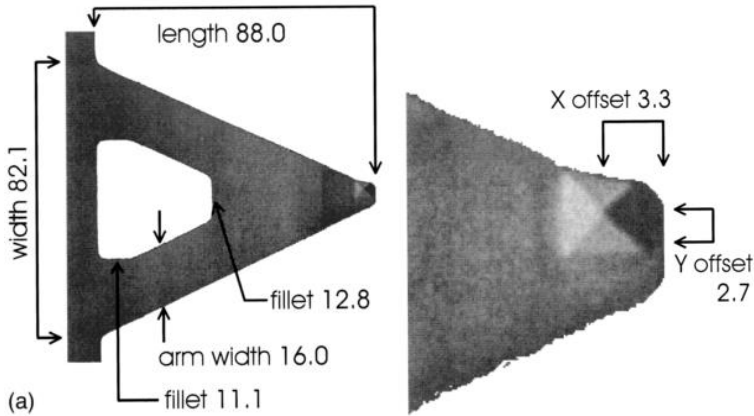


Figure 3 Example of AFM cantilever (not used in our experiment) (reproduced from Ogletree et al. 1996)

The cantilever probe is mounted in the tip holder which is varied on medium of measurement. Figure 4 shows the example of tip holder for measurement in air and liquid. For measurement in liquid, it is equipped with liquid bath to store some amount of liquid and liquid channel to allow liquid transfer (only if necessary).



(a)



(b)

Figure 4 Example of tip holder, (a) for measurement in air (reproduced from Anon 1998) and (b) for measurement in liquid

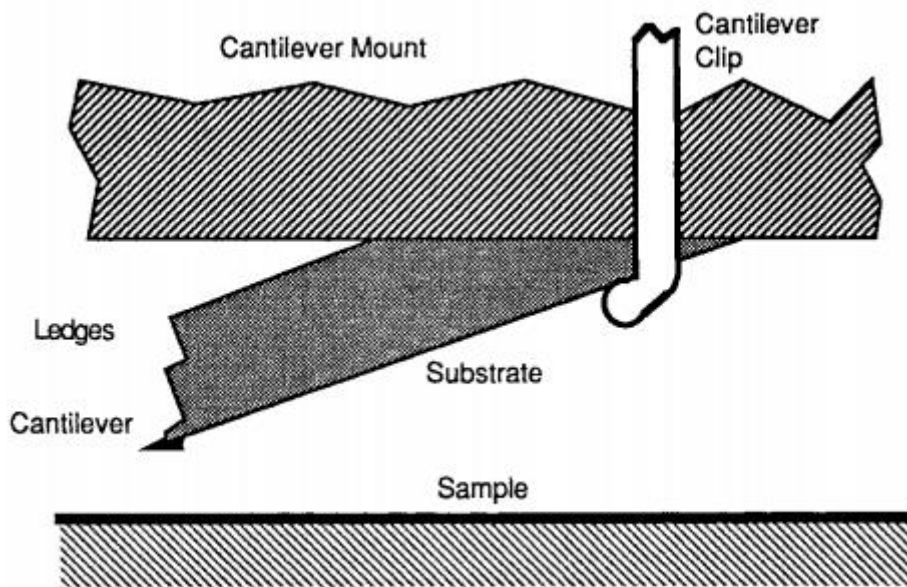


Figure 5 Position of cantilever probe mounted on the tip holder (not to scale) (reproduced from Bhushan 1995)

AFM image is the result of physical interaction between the tip and sample surface. Consequently, there are series of artifact that can appear due to change of tip's geometry (Ricci

& Braga 2004). Depending on the vertical and horizontal dimension of the features scanned, the curvature size and the angle of the tip are important in producing the artifact. The artifacts can be avoided by choosing the tip which is appropriate with the predicted size of the imaged feature. Several main artifacts that are often found in AFM image are:

➤ **Features appeared larger than reality**

Imaging of a very small object such as nanoparticles, nanotubes, globular protein, or DNA strands are easily subjected to image broadening. In this case, sharper tip is more preferred than conical tip because it can minimize the artifact. However, ultrasharp tips (tip radii  $\sim 1-2$  nm) cannot be used for measurement in liquid medium due to its relatively high force constant Figure 6 illustrates the imaging of protruded feature by sharp and dull tip. In spite of misinformation about lateral size, the height of the sample is measured correctly (Ricci & Braga 2004)

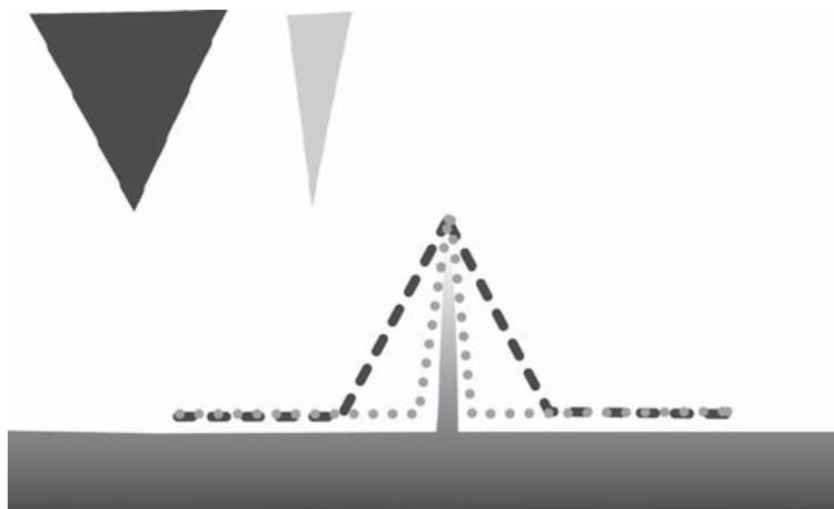


*Figure 6 Traces followed by a dull (dark line) and sharp probe (light line) as they go over a protruding feature. In this case, the side of the tip causes a broadening of objects in the image. (reproduced from Ricci & Braga 2004)*

➤ **Repetition of abnormal pattern**

Sometime, the tip can have more than one protrusion as seen in Figure 7 as a result of defect during production. In this case, when very small features such as nanoparticles are imaged, a so-called “double image” will appear along the fast scanning direction because both

protrusions are touching the sample. Furthermore, the shape of the features will be elongated or will become triangular, depends on the geometry of the tip apex.

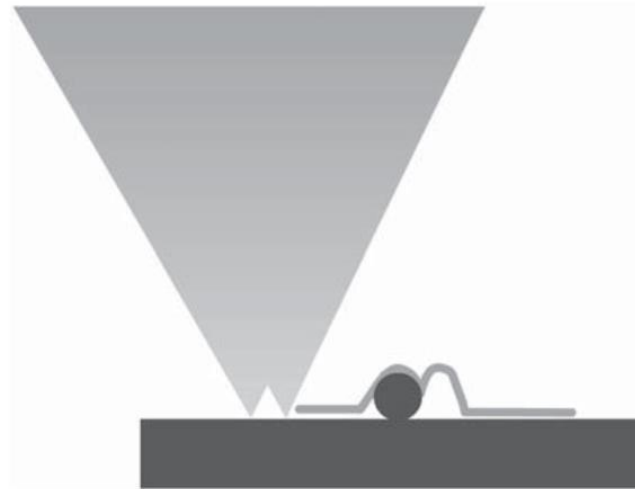


*Figure 7 A double tip will cause shadow or double image along the scanning direction (reproduced from Ricci & Braga 2004)*

➤ **Holes appeared smaller and shallower than reality**

In reality, there is not any flat surface. In nano scale, the surface has certain roughness with peak and valley feature. When the tip images the hole on the surface, the dimension will be smaller than the reality. It is because the tip may not reach the bottom of the hole as seen in Figure 8. However, the opening of the hole is still measurable.

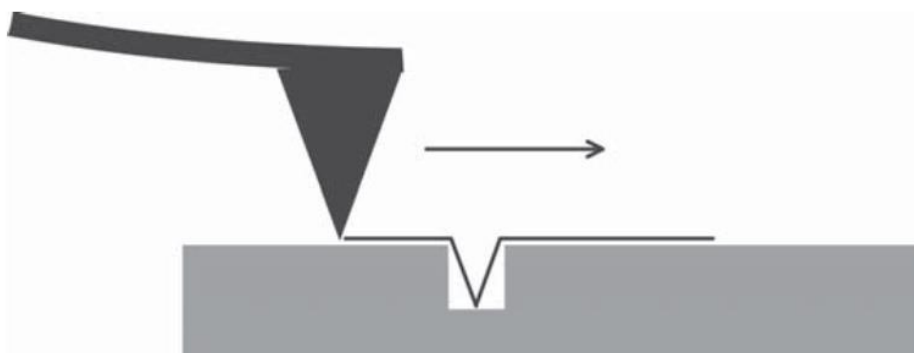


*Figure 8 Imaging of small hole on the sample (reproduced from Ricci & Braga 2004)*

### ➤ **Damaged or contaminated tip**

There are several common reason for the tip to get damaged such as scanning a rough surface, using a high scan speed, high tip-approaching velocity, normal wear and tear over several scans (Sinha 2009) . The features still can be imaged even though it may give the wrong information about the shape and the dimension. A damaged tip can produce asymmetric profile when imaging a regular test pattern as seen in Figure 9. Beside, the AFM image may have many triangular features, pairs of features with similar shape and ghost objects (nonexistent features) (Ukraitsev et al. 2012). In the case of contamination, the AFM image can be blurred. The debris is sometime attached onto the tip and is dragged along during imaging. Consequently, it results diagonal track that may be misinterpreted as a surface feature.

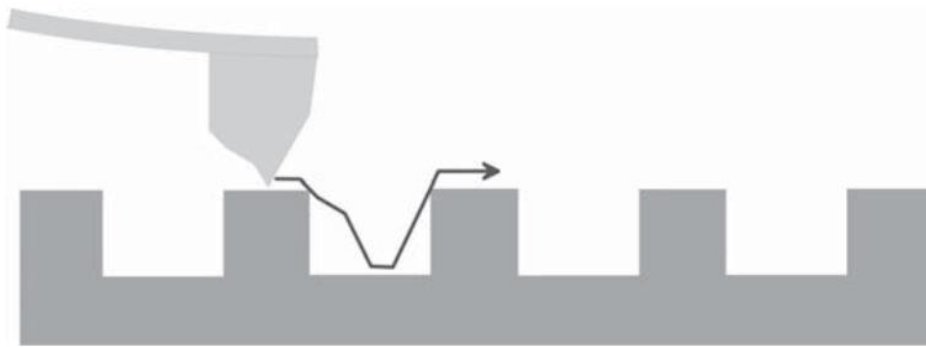


*Figure 9 A badly damaged tip creates artifact while scanning a regular test pattern (reproduced from Ricci & Braag 2004)*

To avoid damaging the tip, it is recommended to do slow tip approach. In ideal condition, the tip should have proper ratio of tip apex and dimension of the sample feature. If the features are larger than tip apex, the image will get blurred. In contrast, if the features are smaller than tip apex, there will be multiple peculiar shapes found on the image. But, if the surface is unknown, large tip-surface distance is preferred. The result of first scan can be used to determine the suitable tip-surface distance.



### A.3 Piezoelectric Scanner

Scanner plays an important role in tip-sample interaction as it decides the distance between tip and sample surface. It is made from piezoelectric material that can deform as response to change of voltage. There are many types of scanner available in the market. It varies with maximum scan size and maximum vertical range. Longer scanners yield larger scan size while shorter scanners give smaller images size. Smaller scanners tend to be more noise-free at acoustic frequencies due to their compact size and rigidity. In other side, for larger scanner, it needs extra noise dampening precautions to have small scan size with high resolution. Thus, the choice of scanner is depending on type of sample and information desired. In our AFM set up, we used scanner model J-vertical (see Figure 10 (a)) with maximum scan size of  $125\ \mu\text{m} \times 125\ \mu\text{m}$  and vertical range of  $5\ \mu\text{m}$ . As it is widely known that AFM required flat sample, the maximum roughness of sample is limited by its maximum vertical range. Figure 10 (b) illustrates the orientation of electrode in the scanner. Voltage applied to conductive areas of the tube creates movement along the X-Y-Z axes. When acquiring an image, the horizontal axis (X) is referred to as the fast axis and the vertical axis (Y) is known as slow axis (see Figure 10).

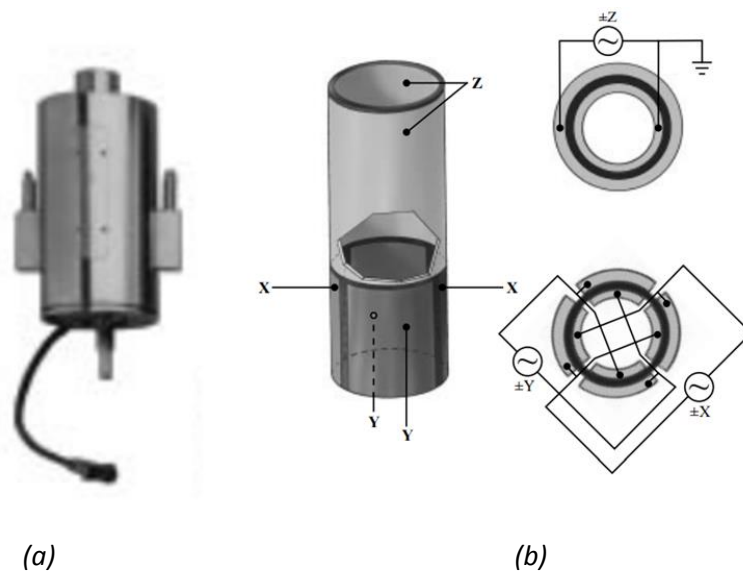
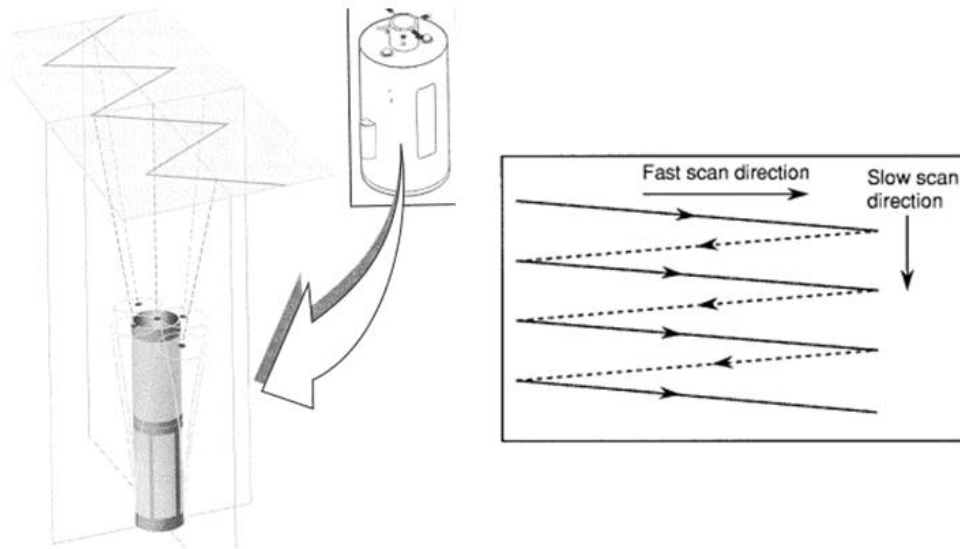


Figure 10 (a) Scanner vertical J used in our AFM instrument, and (b) Typical scanner piezo tube and XYZ electrical configurations (reproduced from Anon 1998)



*Figure 11 Schematic of triangular pattern trajectory of the AFM tip as the sample is scanned in two dimensions (reproduced from Anon 1998)*

There are certain common artifacts that are caused by piezoelectric scanner. It should be noted that the properties of scanner are changed with time and use. With high frequency of usage, piezoelectric material will become more sensitive to drive the signal. In contrast, when the scanner is left idle, it will be depolarized and will be less sensitive (Ricci & Braga 2004). Thus, periodic calibration of piezoelectric scanner is necessary. Below, several common artifacts related to piezoelectric scanner are listed.

➤ **Effect of nonlinear scanner**

In ideal condition, the scanner extends linearly with the driving signal. However, in reality, the plot of scanner extension as function of driving signal will not be straight but curvy as seen as Figure 12. The accepted nonlinearity ranges from 2-25%.

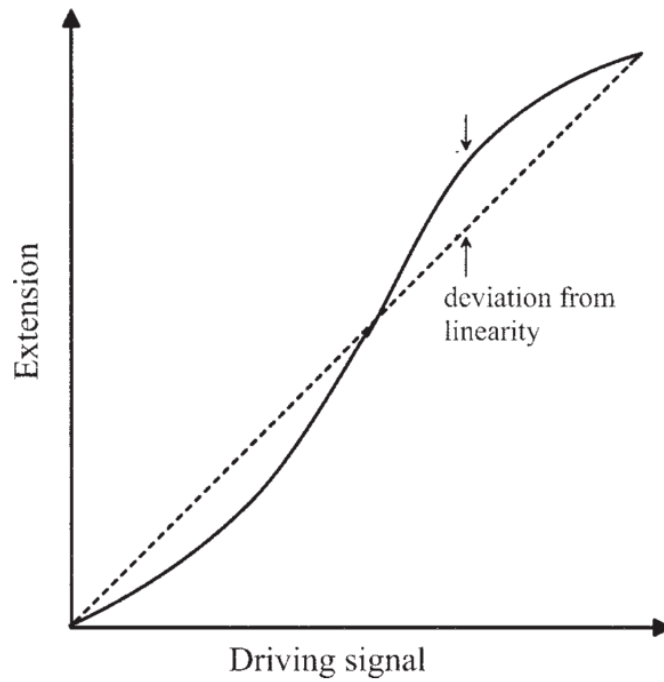


Figure 12 Curve of the scanner extension versus driving signal. Straight line shows the real relationship between scanner extension and driving signal (reproduced from Ricci & Braga 2004)

Usually, piezoelectric scanner can be calibrated by imaging calibration grid which consists of periodic squares. Nonlinearity of scanner causes distortion on AFM calibration grid image. The square becomes smaller on side (see Figure 13). In this case, the scanner needs to be linearized. Furthermore, the scanner has to be calibrated by giving the correct x and y values measured from the line profiles. It is possible that a linear scanner is not calibrated.

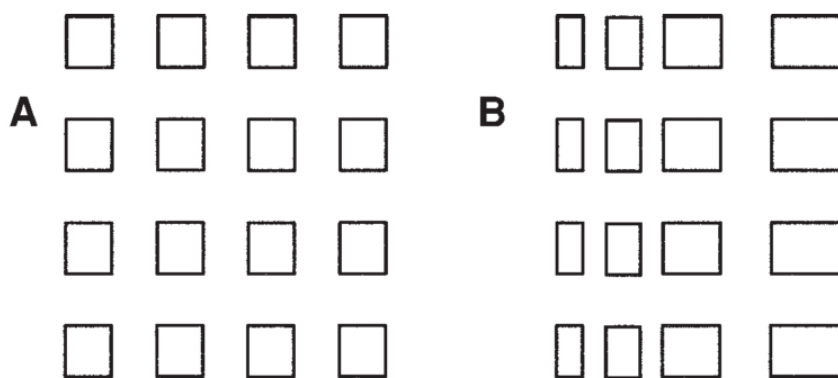


Figure 13 (A) Normal calibrated grid and (B) distortion of a test pattern due to scanner nonlinearity (reproduced from Ricci & Braga 2004)

➤ **Effect of hysteresis**

Another issue with piezoelectric scanner is hysteresis behavior. When it scans a feature with different scanning direction, the driving signal does not correspond the same position. It can be observed by comparing the sample profile measured during tracing left-to-right with profile of retrace right-to-left. If there is a hysteresis, there will be a lateral shift between two profiles as seen on Figure 14. It should be noticed that there is also vertical hysteresis due to contraction and extension of the scanner.

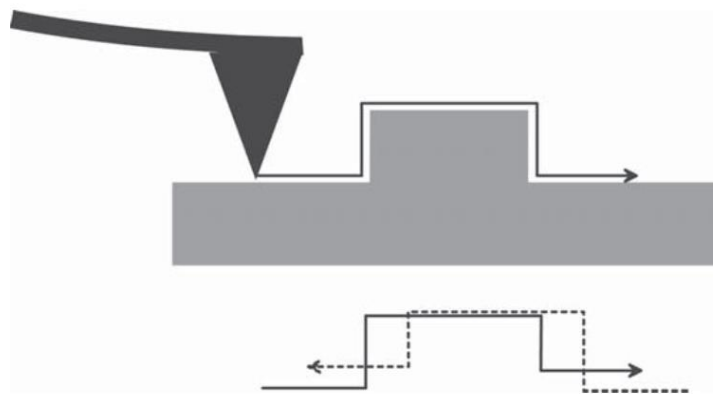


Figure 14 Effect of scanner hysteresis on a scan. Straight line represents the trace scan and the dotted line represents the retrace scan (reproduced from Ricci & Braga 2004)

➤ **Effects of creep**

Moreover, due to variation of driving voltage, piezoelectric scanner can have creep effect. The mechanism of piezoelectric scanner does not allow fast voltage adaptation. The dimensional change occurs at two steps: the first step is happened very fast while the second step takes much longer time (Ricci & Braga 2004). Consequently, different scan rate will have different magnification. Moreover, abrupt zoom in or zoom up a feature will shift the center point of the image. The creep effect is more obvious on sample whose parallel lines as the results will be a bending lines (see Figure 15).

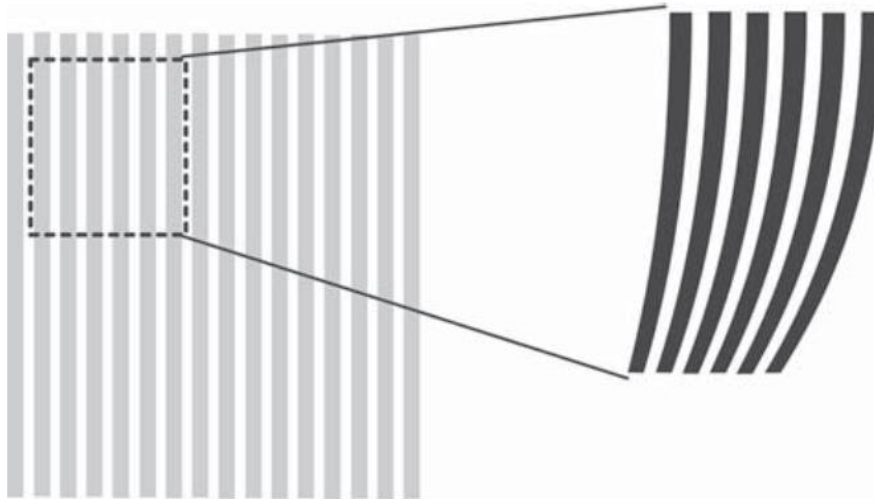


Figure 15 Creep effect on sample whose parallel lines. The bending lines is a result of zooming up in a larger image (reproduced from Ricci & Braga 2004)

➤ **Effect of cross coupling**

On moveable scanner AFM, the position of the tip is fixed during imaging. The scanner has one free end where the sample is attached, while another end is attached to the microscope body. Because of that, the displacement of scanner will follow an arc pattern (see Figure 16) and not a plane. As consequent, the image will show a bow which is evident at low magnification.

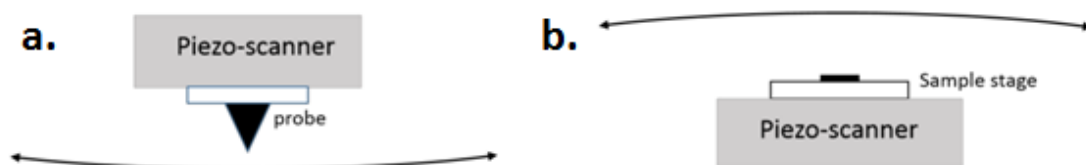


Figure 16 Typical curved trajectories of piezoelectric scanner attached to (A) probe or (B) sample stage (reproduced from Sinha 2009)

Most of AFM programs are provided to subtract this artifact by subtract the appropriate curve from each line during acquisition. This process is called line leveling technique (Sinha 2009). For relatively flat sample with few prominent features, the use of line

levelly technique can cause shadow-like streaks across the particles. This kind of artifact can be avoided by applying line-leveling selectively or by excluding region with the particles.

#### ***A.4 Photodiode Detector***

There are four elements in the photodiode detector to provide different information depending on the operating mode. The four elements are combined to form the total (SUM) signal. Measurement of deflection of the cantilever is done by calculating the total of the amplified differential signal between the top two elements (Equation 2.1). This differential signal is used directly in the contact AFM. For the tapping mode operation, it is fed into RMS converter or phase module. In other hand, the amplified differential signal between SUM of the two elements on the left and right gives a measure of the torsion of the cantilever and is used to measure friction in the Lateral Force Microscopy (Equation 2.2).

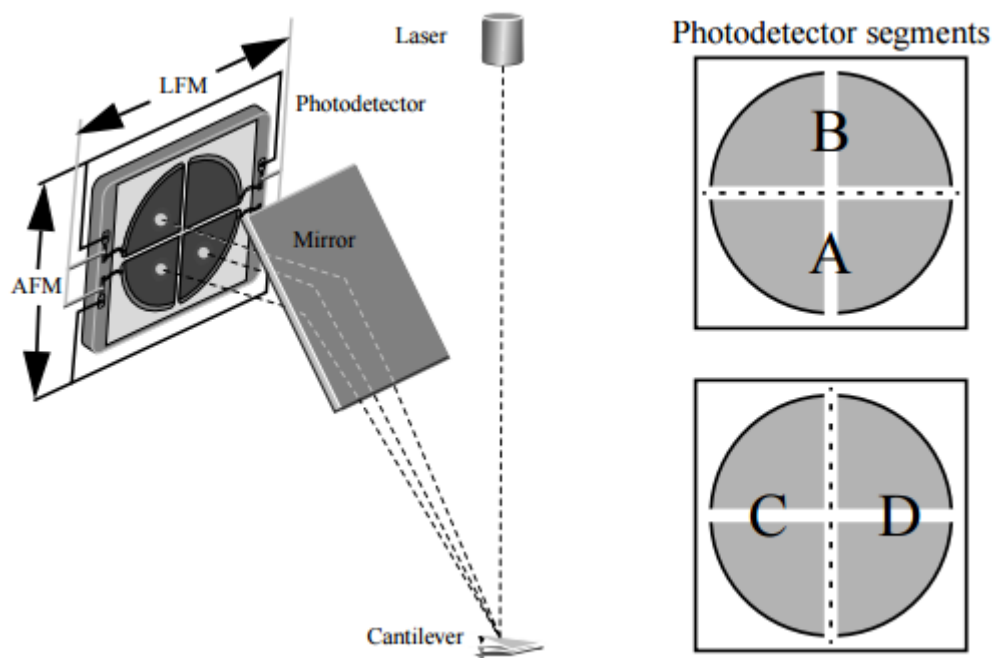


*Figure 17 Quad photodetector arrangement (reproduced from Anon 1997)*

$$\text{Normal deflection} = \frac{B - A}{B + A} \quad (1)$$

$$\text{Torsional deflection} = \frac{C - D}{C + D} \quad (2)$$

## ***A.5 Loop Feedback***

In order to produce high quality three-dimensional image, AFM has electronic feedback loop to control tip-sample interaction precisely. It keeps the tip and sample surface have enough distance to detect interaction force or being at the same Setpoint by adjusting various gains in the feedback circuit. The tip will not be able to detect interaction force if it is too far from setpoint while it will crash the sample surface if it passes the setpoint. Here, we will discuss three more important parameters (proportional, integral, and look ahead gains). Proportional and integral gains control the response time of the feedback loop.

### **➤ Proportional Gain**

This parameter is to control velocity of scanner to alter the force. It is called proportional gain because it sets the velocity of scanner proportionally to change of setpoint (tip-sample interaction). For example, with setpoint set on  $a$ , the tip is at the position of  $a-1$  (too close to sample surface). In order to return at the original setpoint, tip will move at velocity  $v$  at proportional gain value **1**. If the operators put proportional gain value of **2**, tip will move at velocity  $2v$  when it is at the position of  $a-2$ . So, there is multiplication by two. It works in linear model and is based on short time error. The tip will move faster in higher proportional gain value but it will not detect small change of setpoint increasing risk of the tip crash the surface. Therefore, high proportional gain value is not recommended for surface whose many height variation.

### **➤ Integral Gain**

Integral gain is used to maintain constant interaction force based on accumulation of error at longer time range (long time error). With only proportional gain, tip has constants

error around the setpoint resulting cumulative error after some interval of time. Continuing the example given in proportional gain explanation part, the actual position of tip and its setpoint value is noted for some period of time to record the error at each time interval. If the average error value puts the tip below or over the setpoint, the scanner will move accordingly (upward or downward) to return to the original setpoint. The effect of integral gain feedback is to reduce total error by addressing error over a longer period of time. It can minimize the fluctuating effect of proportional gain feedback while narrowing the error closer to the setpoint value. However, integral gain is very sensitive, thus it must be used carefully to avoid overshoot the setpoint which is tent to happen at high integral gain.

### ➤ **Look Ahead Gain**

This parameter gives a prediction function of the sample morphology. It is to ensure optimal tracking over the sample surface. The effect of look ahead gain is to keep the tip within close range of setpoint so the proportional and integral can perform better. For the sample surface which has repetitive (ordered) topography or is relatively flat, we can maximize the look ahead gain value. Otherwise, if the sample is relatively rough or wavy, this gain needs to be minimized as the topography is less predictive.

## **B. Basic Principle**

As shown in Figure 18, a standard atomic force microscopy (AFM) composed by three main components: mechanics AFM head, high voltage electronics, and computer software. In the mechanical part, there are tip's deflection system and the sample movement system. Cantilever with tip, laser source, piezoelectric scanner, photodiode detector, and sample stage are included in this section. Mechanical response of sample recorded by photodiode detector as signal of normal and lateral force as well ( $F_N$  and  $F_L$ ) as well as the total intensity of light ( $\Sigma$ ) are transferred to the electric part. This section amplifies voltages from digital signal processor (DSP) to move the piezoelectric scanner (XYZ voltages). It also collects and transfer signal of  $F_N$ ,  $F_L$  and  $\Sigma$  to DSP. Overall this system is called feedback loop because it regulates the movement of scanner (XYZ voltages) as respond of tip-sample interaction ( $F_N$ ,  $F_L$  and  $\Sigma$ ). The last, there is computer, DSP, and software to control the AFM setup. Control parameter adjustment was



done in this part (Baro & Reifenberger 2012).

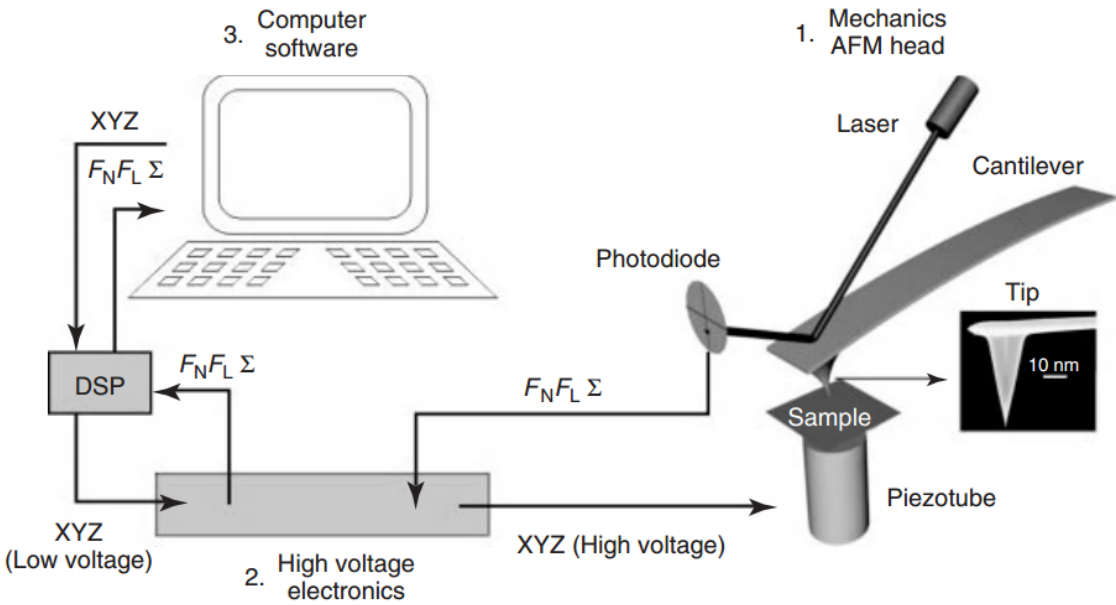


Figure 18 Components of a standard atomic force microscope. (1) The AFM head and the piezoelectric stage. (2) The high voltage electronics. (3) The computer, Digital Signal Processor (DSP), and software that controls the AFM setup (reproduced from Baro & Reifenberger 2012)

# References

---

- Akbarzadeh, A. et al., 2013. Liposome: classification, preparation, and applications. *Nanoscale Research Letters*, 8(1), p.102.
- Albert, B. et al., 2002. *Molecular Biology of The Cell*, 4<sup>th</sup> eds.: Garland Science.
- Alcantar, N., Israelachvili, J. & Boles, J., 2003. Forces and ionic transport between mica surfaces: Implications for pressure solution. *Geochimica et Cosmochimica Acta*, 67(7), pp.1289–1304.
- Alessandrini, A. & Facci, P., 2012. Nanoscale mechanical properties of lipid bilayers and their relevance in biomembrane organization and function. *Micron*, 43(12), pp.1212–23.
- Allen, M. S., Sumali, H. and Penegor, P. C. (2009). Effect of tip mass on atomic force microscope calibration by thermal method abstract, *IMAC*, pp. 1–9.
- Alsten, J. Van & Granick, S., 1990. Shear rheology in a confined geometry: polysiloxane melts. *Macromolecules*, 23(22), pp.4856–4862.
- Andersson, S., Söderberg, A. & Björklund, S., 2007. Friction models for sliding dry, boundary and mixed lubricated contacts. *Tribology International*, 40(4), pp.580-587.
- Anderson, E. V et al., 2011. Shape-Independent Lateral Force Calibration. *ACS Applied Materials and Interfaces*, 3, pp.3256–3260.
- Ando, T., 2014. High-speed AFM imaging. *Current Opinion in Structural Biology*, 28(1), pp.63-68
- Ando, T., Uchihashi, T. & Kodera, N., 2013. High-speed AFM and applications to biomolecular systems, *Annual Review of Biophysics*, 42(3), pp.393-414.
- Anon, 1998. Multimode™ SPM Instruction Manual: Version 4.31. *Veeco Instruments*, pp. 2-35
- Attwood, S.J., Choi, Y. & Leonenko, Z., 2013. Preparation of dopc and dppc supported planar lipid bilayers for atomic force microscopy and atomic force spectroscopy. *International Journal Of Molecular Sciences*, 14(2), pp.3514–39.
- Bagatolli, L.A., 2006. To see or not to see: Lateral organization of biological membranes and fluorescence microscopy. *Biochimica et Biophysica Acta - Biomembranes*, 1758(10), pp.1541–1556.
- Baro, A.M. & Reifenberger, R.G., 2012. *Atomic Force Microscopy in Liquid - Biological*

*Applications*, Weinheim: Wiley VCH.

- Bausch, A.R. et al., 1998. Local measurements of viscoelastic parameters of adherent cell surfaces by magnetic bead microrheometry. *Biophysical Journal*, 75(4), pp.2038–2049.
- Beauvais, E., Morandat, S. & El Kirat, K., 2013. *The Size and Shape of Gel Phase Domains in Supported Lipid Membranes Can be Tuned by Changing The Temperature of Vesicle Fusion*. Université de Technologie de Compiègne.
- Benz, M. et al., 2004. Correlation of afm and sfa measurements concerning the stability of supported lipid bilayers. *Biophysical Journal*, 86(2), pp.870–879.
- Bennewitz, R., 2005. Friction force microscopy. *Materials Today*, 8(5), pp.42–48.
- Berg, J., Tymoczko, J. & Stryer, L., 2002. *Biochemistry*, New York: W.H. Freeman and Company.
- Bernchou, U., Ipsen, J.H. & Simonsen, A.C., 2009. Growth of solid domains in model membranes: quantitative image analysis reveals a strong correlation between domain shape and spatial position. *Journal of Physical Chemistry B*, 113(20), pp.7170–7177.
- Blanchette, C.D. et al., 2006. Galactosylceramide domain microstructure: impact of cholesterol and nucleation/growth conditions. *Biophysical Journal*, 90(12), pp.4466–4478.
- Bockmann, R.A. et al., 2003. Effect of Sodium Chloride on a Lipid Bilayer. *Biophysical Journal*, 85(9), pp.1647–1655.
- Böckmann, R.A. & Grubmüller, H., 2004. Multistep binding of divalent cations to phospholipid bilayers: A molecular dynamics study. *Angewandte Chemie - International Edition*, 43(8), pp.1021–1024.
- Bogdanovic, G., Meurk, A. & Rutland, M.W., 2000. Tip friction - Torsional spring constant determination. *Colloids and Surfaces B: Biointerfaces*, 19(4), pp.397–405.
- Bhushan, B., 1995. *Handbook of Micro/ Nanotribology*. 2nd ed. B. Bhushan, ed., Boca Raton: CRC Press.
- Bhushan, B., 2008. Nanotribology, nanomechanics and materials characterization. *Nanotribology, Nanomechanics, and Materials Characterization*. pp. 789–856.
- Bhushan, B. ed., 2011a. *Nanotribology and Nanomechanics I: Measurement Techniques and Nanomechanics* Third Edit., Heidelberg: Springer.
- Bhushan, B. ed., 2011b. *Nanotribology and Nanomechanics II; Nanotribology, Biomimetics, and Industrial Applications* Third Edit., Columbus Ohio: Springer.
- Bhushan, B., 2007. Nanotribology and nanomechanics of MEMS/NEMS and

- BioMEMS/BioNEMS materials and devices. *Microelectronic Engineering*, 84(3), pp.387–412.
- Binnig, G., Quate, C. & Gerber, C., 1986. Atomic Force Microscope. *Physical Review Letters*, 56(9), pp.930–933.
- Bisson, E.E., 1968. Friction, wear and the influence of surfaces. *Symposium on Surface Integreties*, pp.1–12.
- Bloo, M.L., Haitjema, H. & Pril, W.O., 1999. Deformation and wear of pyramidal, silicon-nitride AFM tips scanning micrometre-size features in contact mode. *Measurement: Journal of the International Measurement Confederation*, 25(3), pp.203–211.
- Booth, B.D. et al., 2009. Tribology of monolayer films: Comparison between n-alkanethiols on gold and n-alkyl trichlorosilanes on silicon. *Langmuir*, 25(17), pp.9995–10001.
- Bowden, F.P. & Hughes, T.P., 1939. The Mechanism of Sliding on Ice and Snow. *Proceedings of the Royal Society A: Mathematical, Physical and Engineering Sciences*, 172(949), pp.280–298.
- Braun, O.M., 2005. Nanotribology : mechanisms of friction on the atomic scale.
- Braun, O.M. & Naumovets, A.G., 2006. Nanotribology: Microscopic mechanisms of friction. *Surface Science Reports*, 60(6–7), pp.79–158.
- Braun, O.M. & Röder, J., 2002. Transition from stick-slip to smooth sliding: an earthquakelike model. *Physical review letters*, 88(9), p.96102.
- Burnham, N. A. et al.(2003) Comparison of calibration methods for atomic-force microscopy cantilevers, *Nanotechnology*, 14(1), pp. 1–6.
- Butt, H.-J. & Franz, V., 2002. Rupture of molecular thin films observed in atomic force microscopy. I. *Physical Review. E*, 66(3), p.31601.
- Camley, B.A. et al., 2010. Lipid bilayer domain fluctuations as a probe of membrane viscosity. *Biophysical Journal*, 99(6), pp.L44–L46.
- Cain, R.G., Biggs, S. & Page, N.W., 2000. Force Calibration in Lateral Force Microscopy. *Journal of Colloid and ilterface Science*, 227(1), pp.55–65.
- Camley, B.A. et al., 2010. Lipid bilayer domain fluctuations as a probe of membrane viscosity. *Biophysical Journal*, 99(6), pp.L44–L46.
- Cannara, R.J., Eglin, M. & Carpick, R.W., 2006. Lateral force calibration in atomic force microscopy: A new lateral force calibration method and general guidelines for optimization. *Review of Scientific Instruments*, 77(5), p.53701.

- Cao, M., Deng, L. & Xu, H., 2015. Study of PNA-DNA hybridization by AFM-based single-molecule force spectroscopy. *Colloids and Surfaces A: Physicochemical and Engineering Aspects*, 470, pp.46–51.
- Carpick, R.W., Agrait, N., et al., 1996. Measurement of interfacial shear (friction) with an ultrahigh vacuum atomic force microscope. *Journal of Vacuum Science & Technology B: Microelectronics and Nanometer Structures*, 14(2), p.1289.
- Carpick, R.W., Ogletree, D.F. & Salmeron, M., 1997. Lateral stiffness: A new nanomechanical measurement for the determination of shear strengths with friction force microscopy. *Applied Physics Letters*, 70(12), pp.1548–1550.
- Carpick, R.W., Ogletree, D.F. & Salmeron, M., 1996. Variation of the Interfacial Shear Strength and Adhesion of a Nanometer-Sized Contact. *Langmuir*, 7463(15), pp.3334–3340.
- Carpick, R.W. & Salmeron, M., 1997. Scratching the Surface: Fundamental Investigations of Tribology with Atomic Force Microscopy. *Chemical Reviews*, 97(4), pp.1163–1194.
- Chernyakova, Y.M. & Goldade, V.A., 2016. Biophysical and biotribological aspects of joints functioning and medicamental correction. *Biotribology*, 6, pp.29–35.
- Cherry, R.J., Muller, U. & Schneider, C., 1977. Rotational Diffusion of Bacteriorhodopsin in Lipid Membranes. *Federal of Europe Biochemistry Society*, 80(2), pp.465–469.
- Chiantia, S. et al., 2006. Combined AFM and two-focus SFCS study of raft-exhibiting model membranes. *ChemPhysChem*, 7(11), pp.2409–2418.
- Christenson, H.K., 1993. Adhesion and surface energy of mica in air and water. *The Journal of Physical Chemistry*, 97(46), pp.12034–12041.
- Chung, K.H., Lee, Y.H. & Kim, D.E., 2005. Characteristics of fracture during the approach process and wear mechanism of a silicon AFM tip. *Ultramicroscopy*, 102(2), pp.161–171.
- Cicuti, P., Keller, S.L. & Veatch, S.L., 2007. Diffusion of liquid domains in lipid bilayer membranes. *Journal of Physical Chemistry B*, 111(13), pp.3328–3331.
- Cleveland, J. P. et al. (1993) 'A nondestructive method for determining the spring constant of cantilevers for scanning force microscopy', *Review of Scientific Instruments*, 64(2), pp. 403–405.
- Coles, J.M., Chang, D.P. & Zauscher, S., 2010. Molecular mechanisms of aqueous boundary lubrication by mucinous glycoproteins. *Current Opinion in Colloid and Interface Science*, 15(6), pp.406–416.
- Cordomí, A., Edholm, O. & Perez, J.J., 2008. Effect of ions on a dipalmitoyl

- phosphatidylcholine bilayer. A molecular dynamics simulation study. *Journal of Physical Chemistry B*, 112(5), pp.1397–1408.
- Danov, K. et al., 1995. Influence of the Surface Viscosity on the Hydrodynamic Resistance and Surface Diffusivity of a Large Brownian Particle. *Journal of Colloid and Interface Science*, 175, pp.36–45.
- Dazzi, A. et al., 2015. Resonance enhanced AFM-IR: A new powerful way to characterize blooming on polymers used in medical devices. *International Journal of Pharmaceutics*, 484(1–2), pp.109–114.
- Degrève, L., Vechi, S.M. & Junior, C.Q., 1996. The hydration of the Na<sup>+</sup> and K<sup>+</sup>. *Biochimica et biophysica acta*, 1274(1996), pp.149–156.
- Dekkiche, F. et al., 2010. Stability and tribological performances of fluid phospholipid bilayers: effect of buffer and ions. *Colloids and surfaces. B, Biointerfaces*, 80(2), pp.232–9.
- Den Otter, W.K. & Shkulipa, S. a, 2007. Intermonolayer friction and surface shear viscosity of lipid bilayer membranes. *Biophysical journal*, 93(2), pp.423–433.
- Derjaguin, B.V., Muller, V.M. & Toporov, Y.P., 1975. Effect of contact deformations on the adhesion of particles. *Journal of Colloid and Interface Science*, 53(2), pp.314–326.
- Derler, S. & Gerhardt, L.C., 2012. Tribology of skin: Review and analysis of experimental results for the friction coefficient of human skin. *Tribology Letters*, 45(1), pp.1–27.
- Dhinojwala, A. & Granick, S., 1997. Relaxation time of confined aqueous films under shear. *Journal of the American Chemical Society*, 119(1), pp.241–242.
- Dimova, R., Pouligny, B. & Dietrich, C., 2000. Pretransitional Effects in Dimyristoylphosphatidylcholine Vesicle Membranes: Optical Dynamometry Study. *Biophysical Journal*, 79(1), pp.340–356.
- Discher, D.E., 2005. Tissue Cells Feel and Respond to the Stiffness of Their Substrate. *Science*, 310(5751), pp.1139–1143.
- El Kirat, K. et al., 2005. Sample preparation procedures for biological atomic force microscopy. *Journal of Microscopy*, 218(1), pp.199–207.
- El Kirat, K. et al., 2005. Fusogenic tilted peptides induce nanoscale holes in supported phosphatidylcholine bilayers. , 68(13), pp.3116–3121.
- El Kirat, K., Morandat, S. & Dufrêne, Y.F., 2010. Nanoscale analysis of supported lipid bilayers using atomic force microscopy. *Biochimica et biophysica acta*, 1798(4), pp.750–65.

- Elings, V. B. and Gurley, J. A. 1991. Method of driving a piezoelectric scanner linearly with time. United States of America.
- Elliott, R. et al., 2005. Phase separation of saturated and mono-unsaturated lipids as determined from a microscopic model. *Journal of Chemical Physics*, 122(4), pp.1–11
- Enachescu, M. et al., 1999. Observation of proportionality between friction and contact area at the nanometer scale. *Tribology Letters*, 7, pp.73–78.
- Ertel, A. et al., 1993. Mechanical properties of vesicles. I. Coordinated analyses of osmotic swelling and lysis. *Biophysical Journal*, 64(2), pp.435–442.
- Fallis, A., 1995. *Structure and Dynamics of Membranes From Cells to Vesicles*, Elsevier: Amsterdam
- Falvo, M.R. & Superfine, R., 2000. Mechanics and Friction at The Nanometer Scale. *Journal of Nanoparticle Research*, 2, pp.237–248.
- Fang, T.-H., Chang, W.-J. & Tsai, S.-L., 2005. Nanomechanical characterization of polymer using atomic force microscopy and nanoindentation. *Microelectronics Journal*, 36(1), pp.55–59.
- Fang, T.H. & Chang, W.J., 2004. Nanoindentation characteristics on polycarbonate polymer film. *Microelectronics Journal*, 35(7), pp.595–599.
- Feigenson, G.W. & Buboltz, J.T., 2001. Ternary Phase Diagram of Dipalmitoyl-PC/Dilauroyl-PC/Cholesterol: Nanoscopic Domain Formation Driven by Cholesterol. *Biophysical Journal*, 80(6), pp.2775–2788.
- Feiler, A., Attard, P. & Larson, I., 2000. Calibration of the torsional spring constant and the lateral photodiode response of frictional force microscopes. *Review of Scientific Instruments*, 71(7), pp.2746–2750.
- Felice, B. et al., 2014. Drug delivery vehicles on a nano-engineering perspective. *Materials Science and Engineering: C*, 41, pp.178–195.
- Francis, L.W. et al., 2010. Optimized sample preparation for high-resolution AFM characterization of fixed human cells. *Journal of Microscopy*, 240(2), pp.111–121.
- Franz, V. et al., 2002. Tip penetration through lipid bilayers in atomic force microscopy. *Colloids and Surfaces B: Biointerfaces*, 23(2–3), pp.191–200.
- Fu, W. & Zhang, W., 2017. Hybrid AFM for Nanoscale Physicochemical Characterization: Recent Development and Emerging Applications. *Advance Science News*, p.1603525.
- Gao, H., Dong, Y. & Martini, A., 2014. Atomistic study of lateral contact stiffness in friction

- force microscopy. *Tribology International*, 74, pp.57–61.
- Garcia-Manyes, S., Oncins, G. & Sanz, F., 2005a. Effect of ion-binding and chemical phospholipid structure on the nanomechanics of lipid bilayers studied by force spectroscopy. *Biophysical journal*, 89(3), pp.1812–26.
- Garcia-Manyes, S., Oncins, G. & Sanz, F., 2005b. Effect of temperature on the nanomechanics of lipid bilayers studied by force spectroscopy. *Biophysical journal*, 89(6), pp.4261–74.
- Garcia-manyes, S., Redondo-morata, L. & Oncins, G., 2010. Nanomechanics of Lipid Bilayers : Heads or Tails ?. *Journal of The American Chemical Society*, (14), pp.12874–12886.
- Garcia-Manyes, S. & Sanz, F., 2010. Nanomechanics of lipid bilayers by force spectroscopy with AFM: a perspective. *Biochimica et Biophysica Acta*, 1798(4), pp.741–9.
- Gauthier, M. et al., 2002. Interplay between Nonlinearity, Scan Speed, Damping, and Electronics in Frequency Modulation Atomic-Force Microscopy. *Physical Review Letter*, 89(14), p.146104.
- Gebeshuber, I. et al, 2005. Diatom bionanotribology - biological surfaces in relative motion: their design, friction, adhesion, lubrication and wear. *Journal of Nanoscience and Nanotechnology*, 5(1), pp.1–9.
- Gee, M.L. et al., 1990. Liquid to solidlike transitions of molecularly thin films under shear. *The Journal of Chemical Physics*, 93(3), pp.1895–1906.
- Geffen, V. Van, 2009. *A study of friction models and friction Compensation*. Technische Universiteit Eindhoven, pp.1–24.
- Giessibl, F.J. et al., 2004. Stability considerations and implementation of cantilevers allowing dynamic force microscopy with optimal resolution: the qPlus sensor. *Nanotechnology*, 15(2), pp.S79–S86.
- Gnecco, E. & Meyer, E., 2014. *Elements of Friction Theory and Nanotribology Combining*, Cambridge University Press: Cambridge
- Granick, S., 1991. Motions and relaxations of confined liquids. *Science*, 253, pp.1374–1379.
- Grant, L.M. & Tiberg, F., 2002. Normal and lateral forces between lipid covered solids in solution, *Biophysical Journal*, 82, pp.1373-1385.
- Green, C. P. et al. (2004) Normal and torsional spring constants of atomic force microscope cantilevers, *Review of Scientific Instruments*, 75(6), pp. 1988–1996.
- Guegan, J. et al., 2016. The relationship between friction and film thickness in ehd point contacts in the presence of longitudinal roughness. *Tribology Letters*, 64(3), pp.1–15.



- Gurtovenko, A. a et al., 2005. Effect of monovalent salt on cationic lipid membranes as revealed by molecular dynamics simulations. *Journal of Physical Chemistry B*, 109(44), pp.21126–21134.
- Gurtovenko, A.A. & Vattulainen, I., 2008. Effect of NaCl and KCl on phosphatidylcholine and phosphatidylethanolamine lipid membranes: insight from atomic-scale simulations for understanding salt-induced effects in the plasma membrane. *Journal of Physical Chemistry B*, 112(7), pp.1953–1962.
- Ha, J.-L. et al., 2005. Effects of frictional models on the dynamic response of the impact drive mechanism. *Journal of Vibration and Acoustics*, 128(1), pp.88–96.
- Hare, F., Amiel, J. & Lussan, C., 1979. Is an average viscosity tenable in lipid bilayers and membranes? A comparison of semi-empirical equivalent viscosities given by unbound probes: a nitroxide and a fluorophore. *Biochimica et Biophysica Acta (BBA) - Biomembranes*, 555(3), pp.388–408.
- Hauser, H. & Shipley, G.G., 1983. Interactions of monovalent cations with phosphatidylserine bilayer membranes. *Biochemistry*, 22(9), pp.2171–8.
- Haverstick, D.M. & Glaser, M., 1987. Visualization of Ca<sup>2+</sup>-induced phospholipid domains. *Proceedings of the National Academy of Sciences of the United States of America*, 84(13), pp.4475–9.
- Haverstick, D.M. & Glaser, M., 1988. Visualization of domain formation in the inner and outer leaflets of a phospholipid bilayer. *Journal of Cell Biology*, 106(6), pp.1885–1892.
- Hertz, H.R., Jones, D. & Schott, G., 1896. *Miscellaneous papers*
- Hirano-Iwata, A. et al., 2010. Free-standing lipid bilayers in silicon chips-membrane stabilization based on microfabricated apertures with a nanometer-scale smoothness. *Langmuir*, 26(3), pp.1949–1952.
- Hirano-Iwata, A., Niwano, M. & Sugawara, M., 2008. The design of molecular sensing interfaces with lipid-bilayer assemblies. *TrAC - Trends in Analytical Chemistry*, 27(6), pp.512–520.
- Hirano, A. et al., 2003. A single-channel sensor based on gramicidin controlled by molecular recognition at bilayer lipid membranes containing receptor. *Biosensors and Bioelectronics*, 18(8), pp.973–983.
- Homola, A.M. et al., 1990. Fundamental experimental studies in tribology: the transition from “interfacial” friction of undamaged molecularly smooth surfaces to normal friction

- with wear. *Wear*, 136, pp.65–83.
- Honerkamp-Smith, A.R. et al., 2013. Membrane viscosity determined from shear-driven flow in giant vesicles. *Physical Review Letters*, 111(3), pp.1–5.
- Hu, H.W. & Granick, S., 1992. Viscoelastic dynamics of confined polymer melts. *Science* 258(5086), pp.1339–42.
- Hutter, J. L. and Bechhoefer, J. 1993. Calibration of Atomic-Force Microscope Tip. *Review of Scientific Instruments*, 64(11), pp.1868-1873
- Ichinose, I., 2010. *Nanostructured Thin Films and Surface* C. S. S. R. Kumar, Weinheim: Wiley.
- Israelachvili, J.N., Mitchell, D.J. & Ninham, B.W., 1977. Theory of self-assembly of lipid bilayers and vesicles. *BBA - Biomembranes*, 470(2), pp.185–201.
- Israelachvili, J.N., 2013. *Intermolecular and Surface Forces*. 3<sup>rd</sup> eds., San Diego: Elsevier.
- Jena, B.P. & Horber, J.K.H., 2002. *Atomic Force Microscopy in Cell Biology*, San Diego: Elsevier Science.
- Johnson, K.L., Kendall, K. & Roberts, A.D., 1971. Surface energy and the contact of elastic solids. *Proceedings of the Royal Society A: Mathematical, Physical and Engineering Sciences*, 324(1558), pp.301–313.
- Johnson, S.M. & Buttress, N., 1973. The osmotic insensitivity of sonicated liposomes and the density of phospholipid-cholesterol mixtures. *BBA - Biomembranes*, 307(1), pp.20–26.
- Johnson, K.L., 1985. Contact Mechanics. *Journal of the American Chemical Society*, 37(22), pp.1–17.
- Jünger, F. et al., 2015. Measuring Local Viscosities near Plasma Membranes of Living Cells with Photonic Force Microscopy. *Biophysical Journal*, 109(5), pp.869–882.
- Kafi, A.K.M. & Kwon, Y.S., 2008. Brewster angle microscopic study of mixed lipid-protein monolayer at the air-water interface and its application in biosensing. *Talanta*, 76(5), pp.1029–1034.
- Keishi, S. & Hiroshi, U., 2013. Detection of Nanosized Sized Ordered Domains in DOPC / DPPC and DOPC / Ch Binary Large Unilamellar Vesicles Using a TEMPO Quenching Method. *Langmuir*, 29, pp.4830–4838.
- Kielland, J., 1937. Individual Activity Coefficients of Ions in Aqueous Solutions. *Journal of the American Chemical Society*, 59(9), pp.1675–1678.
- Kiely, J.D. & Houston, J.E., 1999. Contact hysteresis and friction of alkanethiol self-assembled monolayers on gold. *Langmuir*, 15(13), pp.4513–4519.

- Kim, D.E. & Suh, N.P., 1991. On microscopic mechanisms of friction and wear. *Wear*, 149(1–2), pp.199–208.
- Klein, J. & Kumacheva, E., 1995. Confinement-induced phase transitions in simple liquids. *Science*, 269(5225), pp.816–819.
- Kodera, N. et al., 2010. Video imaging of walking myosin V by high-speed atomic force microscopy. *Nature*, 468(7320), pp.72–6.
- Komanduri, R., Chandrasekaran, N. & Raff, L.M., 2000. MD simulation of indentation and scratching of single crystal aluminum. *Wear*, 240(1–2), pp.113–143.
- Kontturi, A.-K. et al., 1997. Study of ion transfer across phospholipid monolayers adsorbed at micropipette ITIES. *Journal of Electroanalytical Chemistry*, 424(1–2), pp.69–74.
- Koutsos, V. et al., 1998. Isolated polymer chains via mixed self-assembled monolayers: morphology and friction studied by scanning force microscopy. *Macromolecules*, 31(1), pp.116–123.
- Kumacheva, E., 1998. Interfacial friction measurement in surface force apparatus. *Progress in Surface Science*, 58(2), pp.75–120.
- Laouini, A. et al., 2012. Preparation, Characterization and Applications of Liposomes: State of the Art. *Journal of Colloid Science and Biotechnology*, 1(2), pp.147–168.
- Larsen, T. et al., 2002. Comparison of wear characteristics of etched-silicon and carbon nanotube atomic-force microscopy probes. *Applied Physics Letters*, 80(11), pp.1996–1998.
- Leiro, J.A., Torhola, M. & Laajalehto, K., 2017. The AFM method in studies of muscovite mica and galena surfaces. *Journal of Physics and Chemistry of Solids*, 100, pp.40–44.
- Leonenko, Z. V et al., 2004. Investigation of temperature-induced phase transitions in DOPC and DPPC phospholipid bilayers using temperature-controlled scanning force microscopy. *Biophysical journal*, 86(6), pp.3783–93.
- Leontidis, E. & Aroti, A., 2009. Liquid expanded monolayers of lipids as model systems to understand the anionic hofmeister series : 2 . Ion partitioning is mostly a matter of size. *Journal of Physical Chemistry B*, 113, pp.1460–1467.
- Leroy, S. et al., 2009. Probing biolubrication with a nanoscale flow. *Soft Matter*, 5(24), pp.4997–5002.
- Lio, A., Charych, D.H. & Salmeron, M., 1997. Comparative atomic force microscopy study of the chain length dependence of frictional properties of alkanethiols on gold and

- alkylsilanes on mica. *Journal of Physical Chemistry B*, 101(19), pp.3800–3805.
- Liu, E., Blanpain, B. & Celis, J.P., 1996. Calibration procedures for frictional measurements with a lateral force microscope. *Wear*, 192(1–2), pp.141–150.
- Liu, Y. et al., 2011. A new AFM nanotribology method using a T-shape cantilever with an off-axis tip for friction coefficient measurement with minimized Abbé error. *Tribology Letters*, 41(1), pp.313–318.
- Loi, S. et al., 2002. Rupture of molecular thin films observed in atomic force microscopy. II. Experiment. *Phys. Rev. E*, 66(3), p.31602.
- López Cascales, J.J. & García de la Torre, J., 1997. Effect of lithium and sodium ions on a charged membrane of dipalmitoylphosphatidylserine: a study by molecular dynamics simulation. *Biochimica et biophysica acta*, 1330(2), pp.145–56.
- Lotfi, M., Nejib, M. and Naceur, M. (2013). Cell Adhesion to Biomaterials: Concept of Biocompatibility, *Advances in Biomaterials Science and Biomedical Applications*, pp. 207–242.
- Lyubchenko, Y.L. et al., 1992. Atomic force microscopy imaging of double stranded DNA and RNA. *Journal of Biomolecular Structure and Dynamics*, 10(3), pp.589–606.
- Lyubchenko, Y.L., 2012. Preparation of DNA and nucleoprotein for AFM imaging. *Micron*, 42(2), pp.196–206.
- Maestrelli, F. et al., 2006. Effect of preparation technique on the properties of liposomes encapsulating ketoprofen-cyclodextrin complexes aimed for transdermal delivery. *International Journal of Pharmaceutics*, 312(1–2), pp.53–60.
- Maru, M.M. & Tanaka, D.K., 2007. Consideration of stribeck diagram parameters in the investigation on wear and friction behavior in lubricated sliding. *Journal of the Brazilian Society of Mechanical Sciences and Engineering*, 29(1), pp.55–62.
- Maugis, D., 1992. Adhesion of spheres: The JKR-DMT transition using a dugdale model. *Journal of Colloid And Interface Science*, 150(1), pp.243–269.
- Mayer, L.D. et al., 1985. Solute distributions and trapping efficiencies observed in freeze-thawed multilamellar vesicles. *BBA - Biomembranes*, 817(1), pp.193–196.
- Mazeran, P.-E., 2006. Effect of sliding velocity on capillary condensation and friction force in a nanoscopic contact. *Materials Science and Engineering: C*, 26(5–7), pp.751–755.
- McClements, D. J. (1999) *Food Emulsion : Principles, Practice, and Techniques*. Boca Raton: CRC Press.

- Merkel, R., Sackmann, E. & Evans, E., 1989. Molecular friction and epitactic coupling between monolayers in supported bilayers. *Journal de Physique*, 50(12), pp.1535–1555.
- Miller, C., 1986. *Ion Channel Reconstitution* C. Miller, ed., New York: Springer Science+Business Media, LLC.
- Minami, H. et al., 1991. Ion channel sensors for glutamic acid. *Analytical Chemistry*, 63(23), pp.2787–2795.
- Moon, J.J. et al., 2011. Interbilayer-crosslinked multilamellar vesicles as synthetic vaccines for potent humoral and cellular immune responses. *Nature Materials*, 10(3), pp.243–251.
- Mora-Huertas, C.E., Fessi, H. & Elaissari, a, 2010. Polymer-based nanocapsules for drug delivery. *International Journal of Pharmaceutics*, 385(1–2), pp.113–42.
- Morandat, S. & Kirat, K. El, 2006. Membrane resistance to triton x-100 explored by real-time Atomic Force Microscopy. *Langmuir*, (15), pp.5786–5791.
- Morandat, S. et al., 2013. Atomic force microscopy of model lipid membranes. *Analytical and Bioanalytical Chemistry*, 405(5), pp.1445–61.
- Morandat, S. & Kirat, K., 2010. Exploring the properties and interactions of supported lipid bilayers on the nanoscale by Atomic Force Microscopy. *Microscopy: Science, Tecnology, Applications and Education*.pp.1925-1939
- Morandat, S. & El Kirat, K., 2011. Cytochrome c provokes the weakening of zwitterionic membranes as measured by force spectroscopy. *Colloids and surfaces. B, Biointerfaces*, 82(1), pp.111–117.
- Morris, D.J., Myers, S.B. & Cook, R.F., 2004. Sharp probes of varying acuity: Instrumented indentation and fracture behavior. *Journal of Materials Research*.pp.165–175.
- Mui, B.L. et al., 1993. Osmotic properties of large unilamellar vesicles prepared by extrusion. *Biophysical Journal*, 64(2), pp.443–453.
- Nag, K. & Keough, K.M., 1993. Epifluorescence microscopic studies of monolayers containing mixtures of dioleoyl- and dipalmitoylphosphatidylcholines. *Biophysical Journal*, 65(3), pp.1019–1026.
- Nasrallah, H., Mazeran, P.-E. & Noël, O., 2011. Circular mode: a new scanning probe microscopy method for investigating surface properties at constant and continuous scanning velocities. *The Review of Scientific Instruments*, 82(11), p.113703.
- Nicolson, G.L., 2014. The Fluid - Mosaic Model of Membrane Structure: Still relevant to understanding the structure, function and dynamics of biological membranes after

- more than 40 years. *Biochimica et Biophysica Acta - Biomembranes*, 1838(6), pp.1451–1466.
- Noel, O., Mazeran, P.-E. & Nasrallah, H., 2012. Sliding velocity dependence of adhesion in a nanometer-sized contact. *Physical Review Letters*, 108(1), p.15503.
- Nuzzo, R.G. & Allara, D.L., 1983. Adsorption of bifunctional organic disulfides on gold surfaces. *Journal of American Chemical Society*, 105(13), pp.4481–4483.
- Ogletree, D.F., Carpick, R.W. & Salmeron, M., 1996. Calibration of frictional forces in atomic force microscopy. *American Institut of Physics*, 67(9), pp.3298–3306.
- Ogura, T. et al., 2011. Nanoindentation measurement of interfacial reaction layers in 6000 series aluminum alloys and steel dissimilar metal joints with alloying elements. *Journal of Japan Institute of Light Metals*, 61(6), pp.250–254.
- Oguchi, T. et al., 2010. AFM surface morphology and friction force studies of microscale domain structures of binary phospholipids. *Colloids and surfaces. B, Biointerfaces*, 79(1), pp.205–9.
- Okumura, Y. et al., 2007. Electroformation of giant vesicles on a non-electroconductive substrate. *Journal of the American Chemical Society*, 129(6), pp.1490–1491.
- Olson, F. et al., 1979. Preparation of liposomes of defined size distribution by extrusion through polycarbonate membranes. *BBA - Biomembranes*, 557(1), pp.9–23.
- Olsson, H. et al., 1998. Friction Models and Friction Compensation. *European Journal of Control*, 4(3), pp.176–195.
- Oncins, G., Garcia-manyes, S. & Sanz, F., 2005. Study of frictional properties of a phospholipid bilayer in a liquid environment with lateral force microscopy as a function of NaCl concentration. *Langmuir*, 21(16), pp.7373–7379.
- Opitz, A. et al., 2005. Nanofriction mechanisms derived from the dependence of friction on load and sliding velocity from air to UHV on hydrophilic silicon. *Tribology Letters*, 20(3–4), pp.229–234.
- Pandit, S.A., Bostick, D. & Berkowitz, M.L., 2003. Molecular dynamics simulation of a dipalmitoylphosphatidylcholine bilayer with NaCl. *Biophysical Journal*, 84(6), pp.3743–3750.
- Parasassi, T. et al., 1991. Quantitation of lipid phases in phospholipid vesicles by the generalized polarization of Laurdan fluorescence. *Biophysical Journal*, 60(1), pp.179–189.

- Parlinska-Wojtan, M. et al., 2008. Microstructural comparison of material damage in GaAs caused by Berkovich and wedge nanoindentation and nanoscratching. *Scripta Materialia*, 59(3), pp.364–367.
- Peetla, C., Stine, a & Labhasetwar, V., 2009. Biophysical interactions with model lipid membranes: applications in drug discovery and drug delivery. *Molecular pharmaceuticals*, 6(5), pp.1264–1276.
- Pelletier, C.G.N., 2008. *Mechanical Characterization of Glassy Polymers using Instrumented Indentation*. Eindhoven University of Technology.
- Pera, I. et al., 2004. Using the atomic force microscope to study the interaction between two solid supported lipid bilayers and the influence of synapsin I. *Biophysical journal*, 87(4), pp.2446–55.
- Persson, B.N.J. & Tosatti, E., 1995. *Physics of Sliding Friction*, Springer.
- Persson, B.N.J., 2000. *Sliding Friction: Physical Principles and Applications*. 2<sup>nd</sup> eds, Berlin: Springer-Verlag.
- Petrov, E.P. & Schwille, P., 2008. Translational diffusion in lipid membranes beyond the Saffman-Delbruck approximation. *Biophysical journal*, 94(5), pp.L41–L43.
- Pettersson, T. et al., 2007. Comparison of different methods to calibrate torsional spring constant and photodetector for atomic force microscopy friction measurements in air and liquid. *Review of Scientific Instruments*, 78(9).
- Picas, L., Milhiet, P.-E. & Hernández-Borrell, J., 2012. Atomic force microscopy: a versatile tool to probe the physical and chemical properties of supported membranes at the nanoscale. *Chemistry and physics of lipids*, 165(8), pp.845–60.
- Picas, L., Rico, F. & Scheuring, S., 2012. Direct measurement of the mechanical properties of lipid phases in supported bilayers. *Biophysical Journal*, 102(1), pp.L01–L03.
- Pidgeon, C., Hunt, A.H. & Dittrich, K., 1986. Formation of Multilayered Vesicles from Water/Organic-Solvent (W/O) Emulsions: Theory and Practice. *Pharmaceutical Research: An Official Journal of the American Association of Pharmaceutical Scientists*, 3(1), pp.23–34.
- Polozov, I. V et al., 2001. Osmotically induced membrane tension modulates membrane permeabilization by class L amphipathic helical peptides: nucleation model of defect formation. *Biophysical journal*, 81(2), pp.949–959.
- Pompeo, G. et al., 2005. AFM characterization of solid-supported lipid multilayers prepared

- by spin-coating. *Biochimica et Biophysica Acta - Biomembranes*, 1712(1), pp.29–36.
- Pouvreau, C., 2007. *Indentation Fracture of Gallium Arsenide*. Ecole Polytechnique Federale de Lausanne.
- Qian, L., Xiao, X. & Wen, S., 2000. Tip in situ chemical modification and its effects on tribological measurements. *Langmuir*, 16(2), pp.662–670.
- Quintanilla, M.A. & Goddard, D.T., 2008. A calibration method for lateral forces for use with colloidal probe force microscopy cantilevers. *The Review of scientific instruments*, 79(2 Pt 1), p.23701.
- Rathinam, M., Thillaigovindan, R. & Paramasivam, P., 2009. Nanoindentation of aluminum (100) at various temperatures. *Journal of Mechanical Science and Technology*, 23(10), pp.2652–2657.
- Raviv, U., Laurat, P. & Klein, J., 2002. Time dependence of forces between mica surfaces in water and its relation to the release of surface ions. *Journal of Chemical Physics*, 116(12), pp.5167–5172.
- Rawicz, W. et al., 2000. Effect of chain length and unsaturation on elasticity of lipid bilayers. *Biophysical journal*, 79(1), pp.328–339.
- Redondo-Morata, L., Oncins, G. & Sanz, F., 2012. Force spectroscopy reveals the effect of different ions in the nanomechanical behavior of phospholipid model membranes: The case of potassium cation. *Biophysical Journal*, 102(1), pp.66–74.
- Reitsma, M.G., 2007. Lateral force microscope calibration using a modified atomic force microscope cantilever. *Review of Scientific Instruments*, 78(10), pp.81–84.
- Reitsma, M.G., Gates, R.S. & Cook, R.F., 2008. Lateral force cantilever for precise atomic force microscope friction measurements. *Proceeding of the XIth International Congress and Exposition*, 1(i).
- Ricci, D. & Braga, P.C., 2004. Recognizing and avoiding artifacts in AFM imaging. *Methods in Molecular Biology*. 242, pp.25–37.
- Rinia, H.A. et al., 2001. Imaging domains in model membranes with atomic force microscopy. *FEBS Letters*, 504(3), pp.194–199.
- Ruan, J.-A. & Bhushan, B., 1993. Atomic-scale friction measurements using friction force microscopy: Part I - General principles and new measurement techniques. *The American Society of Mechanical Engineers*.
- Sackmann, E., 1996. Membranes : Supported and Scientific Practical Applications. *Science*,



- Sader, J. E., Chon, J. W. M. and Mulvaney, P. (1999). Calibration of rectangular atomic force microscope cantilevers. *Review of Scientific Instruments*, 70(10), pp. 3967–3969.
- Saffman, P. & Delbrück, M., 1975. Brownian motion in biological membranes. *Proceedings of the National Academy of Sciences*, 72(8), pp.3111–3113.
- Saffman, P.G., 1976. Brownian motion in thin sheets of viscous fluid. *Journal of Fluid Mechanics*, 73, p.593.
- Sarikaya, M., 1999. Biomimetics: Materials fabrication through biology. *Proceedings of the National Academy of Sciences*, 96(25), pp.14183–14185.
- Scherge, M. & Gorb, S.S., 2001. *Biological Micro- and Nano-tribology; Nature's Solutions*, New York: Springer.
- Seeger, H.M. et al., 2009. Effect of physical parameters on the main phase transition of supported lipid bilayers. *Biophysical journal*, 97(4), pp.1067–76.
- Seeger, H.M. et al., 2010. Supported lipid bilayers on mica and silicon oxide : Comparison of the main phase transition behavior. *Journal of Physical Chemistry B*, pp.8926–8933.
- Shannon, R.D., 1976. Revised effective ionic radii and systematic studies of interatomic distances in halides and chalcogenides. *Acta Crystallographica Section A*, 32(5), pp.751–767.
- Shimshick, E.J. & McConnell, H.M., 1973. Lateral phase separation in phospholipid membranes. *Biochemistry*, 12(12), pp.2351–2360.
- Shitamichi, Y., Ichikawa, M. & Kimura, Y., 2009. Mechanical properties of a giant liposome studied using optical tweezers. *Chemical Physics Letters*, 479(4–6), pp.274–278.
- Shkulipa, S.A., den Otter, W.K. & Briels, W.J., 2005. Surface viscosity, diffusion, and intermonolayer friction: simulating sheared amphiphilic bilayers. *Biophysical journal*, 89(2), pp.823–829.
- Simons, K. & Ikonen, E., 1997. Functional rafts in cell membranes. *Nature*, 387(6633), pp.569–72.
- Simons, K. & Sampaio, J.L., 2011. Membrane Organization and Lipid Rafts. *Cold Spring Harbour Perspectives in Biology*, pp.1–18.
- Singer, S.J., Nicolson, G.L. & others, 1972. The fluid mosaic model of the structure of cell membranes. *Science*, 175(23), pp.720–731.
- Sinha, K.K., 2009. Artifacts in AFM.

- Sivebaek, I.M., Samoilov, V.N. & Persson, B.N.J., 2010. Velocity dependence of friction of confined hydrocarbons. *Langmuir*, 26(11), pp.8721–8728.
- Smith, L.M. et al., 1979. Antibodies bound to lipid haptens in model membranes diffuse as rapidly as the lipids themselves. *Proceeding of National Academy of Sciences of the USA*, 76(9), pp.4177–4179.
- Soriaga, M.P. & Hubbard, A.T., 1982. Determination of the Orientation of Aromatic Molecules Adsorbed on Platinum Electrodes. The Effect of Solute Concentration. *Journal of American Society*, 104, pp.3937–3945.
- Sotres, J. & Arnebrant, T., 2013. Experimental investigations of biological lubrication at the nanoscale: The cases of synovial joints and the oral cavity. *Lubricants*, 1(4), pp.102–131.
- Srivastava, A., Astrom, K.J. & Turner, K.L., 2007. Experimental characterization of micro-friction on a mica surface using the lateral motion and force measurement capability of an instrumented indenter. *Tribology Letters*, 27(3), pp.315–322.
- Stark, R.W., Schitter, G. & Stemmer, A., 2004. Velocity dependent friction laws in contact mode atomic force microscopy. *Ultramicroscopy*, 100(3–4), pp.309–317.
- Stetter, F.W.S. & Hugel, T., 2013. The nanomechanical properties of lipid membranes are significantly influenced by the presence of ethanol. *Biophysical Journal*, 104(5), pp.1049–1055.
- Sumomogi, T. et al., 2005. Nanoscale mechanical properties of ultrahigh-purity aluminum. *Materials Transactions*, 46(9).
- Souza, T.G.F., Ciminelli, V.S.T. & Mohallem, N.D.S., 2015. An assessment of errors in sample preparation and data processing for nanoparticle size analyses by AFM. *Materials Characterization*, 109, pp.198–205.
- Spyratou, E. et al., 2009. Line optical tweezers: A tool to induce transformations in stained liposomes and to estimate shear modulus. *Colloids and Surfaces A: Physicochemical and Engineering Aspects*, 349(1–3), pp.35–42.
- Starostina, N. & West, P., 2006. Part II : Sample Preparation for AFM Particle Characterization. *Probe Microscopy*, pp.1–9.
- Szlufarska, I., Chandross, M. & Carpick, R.W., 2008. Recent advances in single-asperity nanotribology. *Journal of Physics D: Applied Physics*, 41(12), p.123001.
- Tabor, D., 1992. *Fundamentals of friction: Macroscopic and microscopic processes* I. L. Singer & H. M. Pollock, eds., Kluwer Academic Publishers.

- Takeyasu, K. ed., 2014. *Protein-Ligands Interaction*, Boca Raton: Humana Press-Springer.
- Tao, Z. & Bhushan, B., 2006. Surface modification of AFM silicon probes for adhesion and wear reduction. *Tribology Letters*, 21(1), pp.1–16.
- Uchihashi, T. et al., 2016. Functional extension of high-speed AFM for wider biological applications. *Ultramicroscopy*, 160, pp.182–196.
- Ukraitsev, E. et al., 2012. Artifacts in Atomic Force Microscopy of Biological Samples. *Atomic Force Microscopy Investigations into Biology - From Cell to Protein*. Pp.29-54. Rijeka: Intech
- Uppamoochikkal, P., Tristram-Nagle, S. & Nagle, J.F., 2010. Orientation of tie-lines in the phase diagram of DOPC/DPPC/cholesterol model biomembranes. *Langmuir*, 26(22), pp.17363–17368.
- Uto, M. et al., 1990. Biosensor development reconstituted in a lipid with a glutamate bilayer receptor. *Analytical Sciences*, 6(April), pp.221–225.
- Vácha, R. et al., 2009. Effects of alkali cations and halide anions on the DOPC lipid membrane. *Journal of Physical Chemistry A*, 113(26), pp.7235–7243.
- Vácha, R. et al., 2010. Mechanism of interaction of monovalent ions with phosphatidylcholine lipid membranes. *Journal of Physical Chemistry B*, 114(29), pp.9504–9509.
- Van Bambeke, F. et al., 1993. Alterations in membrane permeability induced by aminoglycoside antibiotics: studies on liposomes and cultured cells. *European Journal of Pharmacology: Molecular Pharmacology*, 247(2), pp.155–168.
- Varenberg, M., Etsion, I. & Halperin, G., 2003. An improved wedge calibration method for lateral force in atomic force microscopy. *Review of Scientific Instruments*, 74(7), pp.3362–3367.
- Vaziri, A. & Mofrad, M.R.K., 2007. Mechanics and deformation of the nucleus in micropipette aspiration experiment. *Journal of Biomechanics*, 40(9), pp.2053–2062.
- Veijgen, N.K., 2013. *Skin friction: A novel approach to measuring In Vivo Human Skin*, Universiteit Twente
- Vié, V. et al., 1998. Distribution of ganglioside G M1 between two-component, two-phase phosphatidylcholine monolayers. *Langmuir*, 14(16), pp.4574–4583.
- Virgala, I. & Kelemen, M., 2013. Experimental friction identification of a DC Motor. *International Journal of Mechanics and Applications*, 3(1), pp.26–30.

- Wang, F. & Zhao, X., 2007. Effect of contact stiffness on wedge calibration of lateral force in atomic force microscopy. *Review of Scientific Instruments*, 78(4).
- Waugh, R.E., 1982. Surface viscosity measurements from large bilayer vesicle tether formation. II. Experiments. *Biophysical journal*, 38(1), pp.29–37.
- Wasmer, K. *et al.* (2008). Dicing of gallium-arsenide high performance laser diodes for industrial applications. Part I. Scratching operation, *Journal of Materials Processing Technology*, 198(1–3), pp. 114–121.
- Westwood, M. *et al.*, 2012. Combined QCMD and AFM studies of lysozyme and poly-L-lysine-poly- galacturonic acid multilayers. *Carbohydrate Polymers*, 89(4), pp.1222–1231.
- Worthman, L.-A.D. *et al.*, 1997. Cholesterol in condensed and fluid phosphatidylcholine monolayers studied by epifluorescence microscopy. *Biophysical journal*, 72(6), pp.2569–2580.
- Wu, Y. *et al.*, 2013. Molecular rheometry: direct determination of viscosity in Lo and Ld lipid phases via fluorescence lifetime imaging. *Physical Chemistry Chemical Physics*, 15(36), p.14986.
- Xiao, X. *et al.*, 1996. Chain length dependence of the frictional properties of alkylsilane molecules self-assembled on mica studied by Atomic Force Microscopy. *Langmuir*, 12(2), pp.235–237.
- Xie, H. *et al.*, 2008. Calibration of lateral force measurements in atomic force microscopy with a piezoresistive force sensor. *The Review of scientific instruments*, 79(3), p.33708.
- Xu, L. *et al.*, 1998. Wetting and capillary phenomena of water on mica. *Journal of Physical Chemistry B*, 102(97), pp.540–548.
- Xu, L. & Salmeron, M., 1998a. An XPS and Scanning Polarization Force Microscopy of the exchange and mobility of surface ions on mica. *Langmuir*, 7463(98), pp.5841–5844.
- Xu, L. & Salmeron, M., 1998b. Effects of surface ions on the friction and adhesion properties of mica. *Langmuir*, 14(8), pp.2187–2190.
- Zgura, I. *et al.*, 2010. Nanostructured gold layers . III . Functionalization of gold. , 12(8), pp.1729–1738.

*(this page is intentionally left blank)*

# List of Figures

---

Figure 1.1 Scheme of sliding motion between rectangular block over a flat surface. $F$ is the normal force while $f$ is the pulling force. The left image showing the magnification of solid-solid interface (reproduced from Persson & Tosatti 1995) .....	21
Figure 1.2 (a) Basic setup for friction experiments using silicon model system and (b) ideal tangential force curve (reproduced from Scherge & Gorb 2001) .....	24
Figure 1.3 Stribeck curve (reproduced from Coles et al.2010) .....	26
Figure 1.4 Relation between friction force and sliding velocity based on Stribeck model (reproduced from Ha et al. 2005) .....	27
Figure 1.5 Scheme of Hertz model of contact (reproduced from Scherge & Gorb 2001) .....	30
Figure 1.6 (a) Basic setup for adhesion and indentation experiments and (b) force-indentation curve to measure adhesion force and indentation (reproduced from Scherge & Gorb 2001).....	31
Figure 1.7 Scheme of Johnson-Kendall-Roberts model of contact (reproduced from Scherge & Gorb 2001) .....	33
Figure 1.8 Relationship between applied load and contact area for various model of contact (reproduced from Carpick & Salmeron 1997) .....	36
Figure 1.9 The Tomlinson Model (reproduced from Braun & Nauvometts 2006).....	37
Figure 1.10 The Frenkel-Kontorova Model (reproduced from Braun & Nauvometts 2006).....	38
Figure 1.11 Schematic of capillary water bridges formed in the contact area of hydrophilic surfaces. The asperities act as nucleating site for capillary condensation. (reproduced from Mazeran 2006) .....	39
Figure 1.12 Cross section of AFM image before and after wear experiment (reproduced from Bloo et al. 1999) .....	41
Figure 2.1 Design of commercial AFM/FFM (reproduced from Bushan 1995).....	45
Figure 2.2 Development of AFM techniques in biology domaine (reproduced from Takeyasu 2014) 46	
Figure 2.3 Illustration contact mode AFM.....	47
Figure 2.4 Illustration of tapping mode AFM .....	48
Figure 2.5 Reflection of laser beam through air-liquid interface; (left) without liquid cell, (middle) with liquid cell, and (right) with liquid cell whose input and output inlet for liquid exchange (reproduced from Baro & Reifenberger 2012) .....	49
Figure 2.6 Illustration of tip-sample surface interaction force (reproduced from Anon 1998) .....	50
Figure 2.7 Schematic of a typical force curve obtained on AFM measurement on supported lipid bilayers (reproduced from Morandat & Kirat 2010) .....	51

<i>Figure 2.8 Example of force curve (reproduced from Garcia-Manyes &amp; Sanz 2010).....</i>	<i>52</i>
<i>Figure 2.9 Indentation of lipid bilayer by AFM tip (reproduced from Morandat et al. 2013) .....</i>	<i>52</i>
<i>Figure 2.10 Illustration of the tip oscillation (reproduced from Bhushan 2011b) .....</i>	<i>55</i>
<i>Figure 2.11 Illustration of surface apparatus (reproduced from Israelachvili 2013).....</i>	<i>58</i>
<i>Figure 2.12 Contact area between two curved surfaces in SFA (reproduced from Persson 2000)...</i>	<i>59</i>
<i>Figure 3.13 Phospholipid molecule (A) schematically, (B) by semi-developed formula, (C) as a space-filling model, and (D) as a symbolic cartoon (reproduced from Albert et al. 2002).....</i>	<i>67</i>
<i>Figure 3.14 Model membrane systems (abbreviation are available in table 4.1) (reproduced from Williams &amp; Daviter 2013).....</i>	<i>69</i>
<i>Figure 3.15 Confocal fluorescence images of GUV of DPPC/DLPC 1:1; with Dil-C20:0 and Bodipy-PC dyes at mole fraction ~0.001. Excitation was at 488 nm. The upper right image is the fluorescence emission through a 585 nm LP filter (exclusively from Dil-C20:0). The upper left image is the emission through a 522/35 nm BP filter (exclusively from Bodipy-PC). The bottom image is the merger colorized image. The bar represents 5 μm. (reproduced from Feigenson and Buboltz. 2001).....</i>	<i>72</i>
<i>Figure 3.16 Example of apparatus of BLM. BLM is formed across an aperture of silicon (Si<sub>3</sub>N<sub>4</sub>) chip that has been silanized with 2% (v/v) 3-cyanopropyltrimethylchlorosilane (CPDS) (reproduced from Hirano-Iwata et al. 2010) .....</i>	<i>74</i>
<i>Figure 3.17 Example of ion channel-based lipid-bilayer sensors: (a) GluR receptor in channel and (b) gramicidin (reproduced from Hirano-Iwata et al. 2008).....</i>	<i>75</i>
<i>Figure 3.18 Cartoon of the structure of a supported lipid bilayer (reproduced from Alessandrini &amp; Facci 2012) .....</i>	<i>76</i>
<i>Figure 3.19 Preparation methods for the formation of SLBs (reproduced from El Kirat et al. 2010).....</i>	<i>77</i>
<i>Figure 3.20 Punchthrough force curve of a DiMyristoyl PhosphatidylCholine (DMPC) SLB measured with conventional AFM at (a) 20.1 °C, (b) 29.5 °C, (c) 40.9 °C, and (d) 52.4 °C in 10mM Hepes/NaOH containing 150mM NaCl and 20 mM MgCl<sub>2</sub> pH 7.4(reproduced from Garcia-Manyes et al. 2005b) .....</i>	<i>80</i>
<i>Figure 3.21 Effect of cations on the punchthrough force of SLBs. Force measurement was done by conventional AFM at 25°C in 20mM Hepes/XOH containing 150mM XCl (X is the monovalent ion present in the buffer) pH 7.4 (reproduced from Redondo-Morata et al. 2012) .....</i>	<i>82</i>
<i>Figure 3.22 The effect of (A) tail chain length and (B) lipid saturation level to mechanical resistance of lipid bilayers. All SLBs were prepared in 10mM Hepes/NaOH pH 7.4 containing 150mM NaCl and 20mM MgCl<sub>2</sub>. Force measurement was done on DiMyristoyl PhosphatidylCholine 14:0; DiPalmitoyl PhosphatidylCholine 16:0; Distearoyl PhosphatidylCholine 18:0 and DiArachidoyl PhosphatidylCholine (20:0) to study the effect of tail chain length. While, measurement was</i>	

done on DSPC 18:0; 18:1; 18:0:1; 18:2; and 18:3 to determine the of lipid saturation level. 83

Figure 3.11 Schemes, topography images, and line sections of mixtures of lipids 1-palmitoyl-2-oleoyl-sn-glycero-3-phosphoethanolamine (POPE) and 1-palmitoyl-2-oleoyl-sn-glycero-3-phospho-(1'-rac-glycerol) (POPG). POPE/POPG SLBs was prepared on mica at temperature (a) below and (b) above melting point. (c) POPE/POPG SLBs was prepared on silicon oxide. Regardless the fusion temperature, SLBs prepare on silicon oxide give coupled transition. AFM imaging was done in 10mM potassium dihydrogen citrate, 150mM KCl at pH 7. ( $T_{inc}$  = fusion temperature,  $T_m$  = melting temperature) (reproduced from Seeger et al. 2010) ..... 85

Figure 3.12 Vertical force versus lateral force curves obtained for DiMyristoyl PhosphatidylCholine (DMPC) SLBs characterized by conventional AFM in Tris buffer pH 7 containing NaCl with concentration (a) 0 M, (b) 0.01 M, (c) 0.05 M, and (d) 0.1 M (reproduced from Oncins et al. 2005)..... 86

Figure 3.13 Mechanical interaction between tip and lipid bilayer during friction measurement (a) in pure water and (b) in the presence of sodium chloride (reproduced from Oncins et al. 2005) ..... 87

Figure 3.14 (a) Friction forces on mixture of DSPC/DLPC monolayer(50:50) %mol, measured on along the scan line shown in (b) AFM topographic image. DSPC/DLPC monolayer was transferred onto a cleaved mica surface by horizontal lifting method. (reproduced from Oguchi et al.2010) ..... 87

Figure 3.15 Torsion displacements of pure monolayers of DSPC and DLPC as function of temperature. Each monolayer was prepared by horizontal lifting method in which the hydrophobic chains of the lipids face the outer surface of the substrate. (reproduced from Oguchi et al.2010). 88

Figure 4.1 Chemical structure of lipids used in this study: DiLauryloyl PhosphatidylCholine (DLPC) 12:0, DiMyristoyl PhosphatidylCholine (DMPC) 14:0, DiPalmitoyl PhosphatidylCholine (DPPC) 16:0, and DiOleoyl PhosphatidylCholine (DOPC) 18 :1 (reproduced from www.avantilipids.com) ..... 93

Figure 4.2 (a) Image of scratched surface taken by optical microscope (the scale bar refers to 0.2 mm) and (b) illustration of side view of scratch making on flat glass making (arrow shows the scanning direction)..... 95

Figure 4.3 Force balance of a droplet at a solid-gas interface (reproduced from Lotfi, Nejib, and Naceur, 2013)..... 98

Figure 4.4 Scheme of circular mode AFM..... 100

Figure 4.5 Schematic of circular mode AFM for characterization of lipid bilayers..... 102

Figure 4.6 Illustration of mechanical systems between AFM tip, lipid membranes, and solid substrate during friction measurement ..... 104



Figure 4.7 Components of circular mode AFM in our laboratory .....	104
Figure 4.8 Scheme of cable connection between components of AFM in our laboratory .....	105
Figure 4.9 High voltage outputs panel on signal access module (SAM).....	106
Figure 5.6 Model of contact of AFM tip on tilted surface (a) during ascending and (b) during descending the slope.....	115
Figure 5.7 Image of (a) topography (z-range = 100 nm) and friction image: (b) trace and (c) retrace (z-range = 0.5 Volt) of gold layer surface. Size 1 $\mu\text{m}$ x 1 $\mu\text{m}$ . (d) Line profile analysis along the white straight line .....	119
Figure 5.8 Image of (a) topography (z-range = 100 nm) and friction image: (b) trace and (c) retrace (z-range = 0.5 Volt) of diamond layer surface. Size 1 $\mu\text{m}$ x 1 $\mu\text{m}$ .(d) Line profile analysis along the white straight line .....	120
Figure 5.9 Image of (a) topography (z-range = 100 nm) and friction image: (a) trace and (c) retrace (z-range = 0.1 Volt) of aluminum surface (on the triangular scratch). Size 1 $\mu\text{m}$ x 1 $\mu\text{m}$ . (d) Line profile analysis along the white straight line .....	122
Figure 5.10 Image of (a) topography (z-range = 250 nm) and friction image: (a) trace and (c) retrace (z-range = 0.5 Volt) of polycarbonate surface (on the triangular scratch). Size 5 $\mu\text{m}$ x 5 $\mu\text{m}$ .(d) Line profile analysis along the white straight line.....	123
Figure 5.11 Image of (a) topography (z-range = 60 nm) and friction image: (a) trace and (c) retrace (z-range = 0.1 Volt) of cover slip glass surface (on the triangular scratch). Size 2 $\mu\text{m}$ x 2 $\mu\text{m}$ . (d) Line profile analysis along the white straight line.....	125
Figure 5.12 Cover slip glass image of (a) surface slope, (b) total friction (T+R) and (c) difference of friction (T-R). Size 3 $\mu\text{m}$ x 3 $\mu\text{m}$ . (d-f) Histogram of the surface slope, total friction (T+R) and difference of friction (T-R) respectively .....	126
Figure 5.13 Image of (a) topography (z-range = 100 nm) and friction image: (a) trace and (c) retrace (z-range = 0.1 Volt) of fused silica surface (on the triangular scratch). Size 3 $\mu\text{m}$ x 3 $\mu\text{m}$ . (d) Line profile analysis along the white straight line.....	127
Figure 5.14 Fused silica image of (a) surface slope, (b) total friction (T+R) and (c) difference of friction (T-R). Size 3 $\mu\text{m}$ x 3 $\mu\text{m}$ . (d-f) Histogram of the surface slope, total friction (T+R) and difference of friction (T-R) respectively. ....	128
Figure 5.15 Determination of lateral calibration coefficient from LFM signal measured in air atmosphere.....	129
Figure 5.16 Determination of lateral calibration coefficient from LFM signal measured in MillQ water medium .....	130
Figure 5.17 Comparison of lateral calibration force for the same cantilever measured in different medium: air and water .....	131

Figure 5.18 Scanning as function of voltage amplitude: 0 - 0.5 Volt.....	133
Figure 5.19 Scanning as function of frequencies: 1 – 100 Hz.....	135
Figure 5.20 Scanning as function of frequencies: 100 – 2000 Hz.....	135
Figure 5.21 Scanning as function of frequency: 1000 - 10000 Hz.....	136
Figure 5.22 (a) Friction image of GaAs surface after circular AFM with sliding velocity of 786 $\mu\text{m/s}$ for 2.5 minutes (z-scale = 10nm). (b) Section curve along the red line to visualize the width and the thickness of wear due to sliding of AFM tip.....	137
Figure 5.18 Circular trace diameter as function of frequencies at constant amplitude of 3Volt, quasistatic values are given at 0 Hz frequency. The linear regression line is made on limited frequency ranging from 50 to 400 Hz. ....	138
Figure 5.19 Circular trace diameter measured by CM-AFM at various amplitudes plotted as function of frequencies.....	140
Figure 5.20 Circular trace diameter measured by CM-AFM at various frequencies plotted as function of amplitudes .....	140
Figure 5.21 Friction image of mica surface after circular AFM: amplitude = 0.1 - 10 Volt; frequency = 300 Hz (size 5x5 $\mu\text{m}$ , z-scale = 0,1 Volt) .....	142
Figure 6.1 Topography image of mica surface after experiment by CM-AFM in air at sliding velocity 1000 $\mu\text{m/s}$ . Size 5 $\mu\text{m}$ x 5 $\mu\text{m}$ ; z-range = 10 nm. The tip used has a spring constant of (a) 0.2 N/m and (b) 0.05 N/m.....	145
Figure 6.2 Example of curve of friction force versus normal force measured on mica (in water medium; sliding velocity = 215 $\mu\text{m/s}$ ). The important values recorded are the initial friction force $F_f$ , indicated by the arrow, and friction coefficient $\alpha$ (slope). ....	146
Figure 6.3 Friction force versus sliding velocity of mica surface examined by CM-AFM in air (sliding velocity = 20 –2200 $\mu\text{m/s}$ ), in ultrapure water, and in Tris-NaCl buffer (sliding velocity = 20 – 2000 $\mu\text{m/s}$ ).....	147
Figure 6.4 Friction coefficient versus sliding velocity of mica surface examined by CM-AFM in air (sliding velocity = 20 –2200 $\mu\text{m/s}$ ), in ultrapure water, and in Tris-NaCl buffer (sliding velocity = 20 –2000 $\mu\text{m/s}$ ).....	148
Figure 6.5 Friction force versus sliding velocity of mica surface examined by CM-AFM in air (sliding velocity = 20 –2200 $\mu\text{m/s}$ ), in ultrapure water, and in Tris-NaCl buffer (sliding velocity = 20 – 2000 $\mu\text{m/s}$ ).....	149
Figure 6.6 Friction coefficient versus sliding velocity of mica surface examined by CM-AFM in air (sliding velocity = 20 –2200 $\mu\text{m/s}$ ), in ultrapure water, and in Tris-NaCl buffer (sliding velocity = 20 –2000 $\mu\text{m/s}$ ).....	150
Figure 6.7 Friction force versus sliding velocity of mica surface examined by CM-AFM (sliding velocity =	

20 –2200  $\mu\text{m/s}$ ) in different liquid composition measured at  $f = 175 \text{ Hz}$  and  $A = 0.1 -10 \text{ V}$ . The viscous friction coefficient ( $\eta$ ) for mica in Tris is  $54.94 \pm 3.47 \text{ nN.s/m}$  ( $R^2=0.99$ ); in Tris+3mM  $\text{Ca}^{2+}$  is  $60.45 \pm 5.48 \text{ nN.s/m}$  ( $R^2=0.95$ ); and in Tris+150mM  $\text{Ca}^{2+}$  is  $188.45 \pm 13.57 \text{ nN.s/m}$  ( $R^2=0.98$ )..... 151

Figure 6.8 Friction coefficient versus sliding velocity of mica surface examined by CM-AFM in different ionic compositions measured by CM-AFM; sliding velocity 20 –2200  $\mu\text{m/s}$ )..... 151

Figure 6.9 Bare glass surface (a) before and (b) after circular mode AFM examination (amplitude = 10 V; frequency= 175 Hz). Size = 5  $\mu\text{m}$  x 5  $\mu\text{m}$ , z-range = 10 nm ..... 152

Figure 6.10 Example of curve of friction force versus normal force measured on glass (Measured by CM-AFM in water medium; sliding velocity = 215 $\mu\text{m/s}$ ). The important values recorded are the initial friction force  $F_f$  indicated by the arrow and friction coefficient  $\alpha$  (slope) ..... 153

Figure 6.11 Friction force as function of sliding velocity for bare glass measured in 10 mM Tris buffer containing 150 mM salts. The viscous friction of glass friction measured in water, buffer containing lithium, sodium, or potassium is  $383.6 \pm 22.17 \text{ nN.m/s}$  ( $R^2=0.95$ );  $161.11 \pm 2.62 \text{ nN.m/s}$  ( $R^2=0.98$ );  $91.04 \pm 2.93 \text{ nN.m/s}$  ( $R^2=0.98$ ); and  $10.44 \pm 1.42 \text{ nN.m/s}$  ( $R^2=0.85$ ) respectively. Measurements were done by CM-AFM with sliding velocity 200 –2000  $\mu\text{m/s}$ . ..... 154

Figure 6.12 Viscous friction coefficient of bare glass surface in the presence of different cations as function of their crystalline ionic size respectively (Shannon 1976). ( $\text{Li}^+ = 0.90 \text{ \AA}$ ;  $\text{Na}^+ = 1.16 \text{ \AA}$ ; and  $\text{K}^+ = 1.52 \text{ \AA}$ ). The zero point of ionic size refers to the measurement in ultra pure water. Measurements were done by CM-AFM with sliding velocity 200 –2000  $\mu\text{m/s}$ ..... 154

Figure 6.13 Friction coefficient as function of sliding velocity for bare glass measured in water or 10 mM Tris buffer containing 150 mM salts: LiCl, NaCl, or KCl. Measurements were done by CM-AFM with sliding velocity 200 –2000  $\mu\text{m/s}$ ..... 155

Figure 6.14 Contact angle measurement on gold layer functionalized with (a) 1-undecanethiol ( $\text{C}_{10}\text{CH}_3$ ) and (b) mercapto-1-undecanol ( $\text{C}_{11}\text{OH}$ ) ..... 156

Figure 6.15 Gold-coated-glass surface functionalized with  $\text{C}_{10}\text{CH}_3$ , (a) before and (b) after circular mode AFM examination. Size = 5  $\mu\text{m}$  x 5  $\mu\text{m}$ , z-range = 10 nm ..... 157

Figure 6.16 Normal force as function of separation distance of tip-surface measured by CM-AFM at sliding velocity of 120  $\mu\text{m/s}$  for hydrophobic ( $\text{C}_{10}\text{CH}_3$ ) and hydrophilic ( $\text{C}_{11}\text{OH}$ ) gold layer. Adhesion force is indicated as negative normal force ..... 158

Figure 6.17 Adhesion force as function of sliding velocity for gold layer functionalized with  $\text{C}_{10}\text{CH}_3$ . The experiment was conducted in 10 mM Tris buffer pH 7.4 medium using CM-AFM; sliding velocity 10 –1200  $\mu\text{m/s}$ ) ..... 158

Figure 6.18 Friction force versus normal force of gold surface functionalized with  $\text{C}_{10}\text{CH}_3$  (hydrophobic

<i>surface) measured in 10 mM Tris buffer pH 7.4 (measured by CM-AFM; sliding velocity=120 <math>\mu\text{m/s}</math>).....</i>	159
<i>Figure 6.19 Friction force and friction coefficient of gold layer functionalized with C10CH3 measured in medium of 10 mM Tris buffer pH 7.4 using CM-AFM (sliding velocity 10 –1200 <math>\mu\text{m/s}</math>) ..</i>	160
<i>Figure 7.1 Punchthrough force of DOPC SLBs as function of sliding velocity. The inset image shows the variation of punchthrough force as function of scanning amplitude: 1-10 V which is equivalent with sliding velocity 200 –2000 <math>\mu\text{m/s}</math>. DOPC SLBs was prepared in 10 mM Tris buffer containing 150 mM NaCl and 3 mM CaCl2 .....</i>	167
<i>Figure 7.2 Topography image of DOPC SLBs (a) before and (b) after mechanical measurement. (c) The cross section along the white line of the image before measurement. Size = 20<math>\mu\text{m}</math> x 20<math>\mu\text{m}</math>, z-range = 10nm.....</i>	169
<i>Figure 7.3 Comparison of raw curves of normal and lateral force. Perforation of the membrane by AFM tip is detected on both normal and lateral force curve (dashed vertical line).....</i>	170
<i>Figure 7.4 Example of AFM punch experiment yielding normal force versus separation obtained on DOPC bilayers; horizontal distance x refers to membranes' thickness while vertical distance y refers to punchthrough force. ....</i>	171
<i>Figure 7.5 Curve of normal and friction forces as function of tip-membrane separation. The curve can be divided into four areas: (a) tip is relatively far from membrane, (b) tip contacts the membrane's surface, (c) tip punches the membrane, and (d) tip is in contact with the solid support.....</i>	172
<i>Figure 7.6 Histogram of DOPC thickness obtained by piercing the SLB with the AFM tip, n = 215. Measurements were done by CM-AFM with sliding velocity 200 –2000 <math>\mu\text{m/s}</math>. The solid line represents the gaussian fitting line. The average Gaussian thickness for DOPC is 4.9 + 1.1nm .....</i>	173
<i>Figure 7.7 Histogram of DOPC punchthrough force obtained by piercing the SLB with the AFM tip, n = 215. Measurements were done by CM-AFM with sliding velocity 200 –2000 <math>\mu\text{m/s}</math>. The solid line represents the Gaussian fitting line. The average Gaussian punchthrough force for DOPC is 2.52+ 0.56 nN .....</i>	173
<i>Figure 7.8 Curve of friction force of DOPC SLBs measured by CM-AFM as a function of the sliding velocity. The friction force recorded is the initial friction force when the tip begins to contact the surface .....</i>	174
<i>Figure 7.9 Comparison of friction curves of DOPC SLBs on glass substrate and bare glass surface measured in Tris Buffer pH 7.4 using CM-AFM at sliding velocity 200 <math>\mu\text{m/s}</math>.....</i>	177
<i>Figure 7.40 Difference of friction force of bare glass and glass as solid substrate for DOPC SLB versus sliding velocity(<math>y=2.16E-4x+0.15</math>; <math>R^2=0.92</math>), measured using CM-AFM at sliding velocity 200</i>	

–2000 $\mu\text{m/s}$ .....	177
Figure 8.1 Comparison of crystal ion radius of cations used in these experiments (units in pm). These values are for 6-coordination number (reproduced from Shannon 1976).....	186
Figure 8.2 Histogram of membrane thickness measured with CM-AFM at sliding velocity 200 – 2000 $\mu\text{m/s}$ for each DOPC SLB prepared on different cations ( $\text{Li}^+$ , $\text{Na}^+$ , and $\text{K}^+$ ) with concentration 150mM. $\text{Li}^+$ : $4.09 \pm 1.45$ nm; $\text{Na}^+$ : $4.9 \pm 1.1$ nm; $\text{K}^+$ : $4.95 \pm 1.31$ nm.....	187
Figure 8.3 Histogram of membrane punchthrough force measured with CM-AFM at sliding velocity 200 – 2000 $\mu\text{m/s}$ for each DOPC SLB prepared on different cations ( $\text{Li}^+$ , $\text{Na}^+$ , and $\text{K}^+$ ) with concentration 150mM. $\text{Li}^+$ : $2.01 \pm 0.56$ nN; $\text{Na}^+$ : $2.52 \pm 0.32$ nN; $\text{K}^+$ : $5.56 \pm 1.38$ nN....	188
Figure 8.4 Normal forces versus separation curve of DOPC SLBs incubated with different cations. Measurement was done at sliding velocity of $214 \mu\text{m/s}$ . The dashed ellipse shows the event of membranes' perforation. The jump in curves indicates the rupture of the membranes..	189
Figure 8.5 Friction force versus separation curve of DOPC SLBs incubated with different cations. Measurement was done at sliding velocity of $214 \mu\text{m/s}$ . The dashed ellipse shows the cloud of points that indicates the tip sliding on the membrane surface. The membrane rupture is detected by the jump .....	189
Figure 8.6 Friction force, measured by CM-AFM, as function of sliding velocity for DOPC SLBs incubated with three different cations. The viscous friction coefficients for DOPC prepared in the presence of LiCl, NaCl, and KCl are $83.31 \pm 7.93$ nN.m/s ( $R^2=0.98$ ); $72.85 \pm 8.87$ nN.m/s ( $R^2=0.99$ ); and $209.88 \pm 21.61$ nN.m/s ( $R^2=0.94$ ) respectively.....	190
Figure 8.7 Punchthrough force and friction viscous coefficient of DOPC SLBs as function of ionic size ( $\text{Li}^+ = 0.9 \text{ \AA}$ ; $\text{Na}^+ = 1.16 \text{ \AA}$ ; and $\text{K}^+ = 1.52 \text{ \AA}$ ) measured by CM-AFM (sliding velocity 200 – 2000 $\mu\text{m/s}$ ).....	191
Figure 9.1 Image of DOPC/DPPC SLBs with different composition. Size = $20 \mu\text{m} \times 20 \mu\text{m}$ , z-range = $10 \text{ nm}^2$ .....	198
Figure 9.2 Histogram of punchthrough forces of DOPC/DPPC SLBs measured by CM-AFM (sliding velocity: 200 –2000 $\mu\text{m/s}$ all combined) with various ratios prepared in 10 mM Tris containing 150 mM NaCl and 3mM $\text{CaCl}_2$ .....	199
Figure 9.3 Histogram of membranes' punchthrough forces for DOPC/DPPC SLBs measured by CM-AFM (sliding velocity: 200 –2000 $\mu\text{m/s}$ all combined) with various ratios prepared in 10 mM Tris containing 150 mM NaCl and 3mM $\text{CaCl}_2$ . The blue solid line represents the average Gaussian fit .....	200
Figure 9.4 Friction force of lipid bilayers measured by CM-AFM as a function of the sliding velocity for DOPC/DPPC SLBs prepared with various lipid ratios. All lipid membranes were prepared in	

10 mM Tris containing 150 mM NaCl and 3mM CaCl <sub>2</sub> .....	201
Figure 9.5 Friction viscous coefficient and punchthrough force of DOPC/DPPC SLBs as a function of DPPC % mol in the membrane, measured by CM-AFM (sliding velocity 200 –2000 μm/s) .....	203
Figure 9.6 Phase diagram of DOPC/DPPC lipid mixture as a function of the volume fraction of DOPC obtained by calculation based on self-consistent field theory. The red dashed line indicates our measurement temperature (T=22°C). (reproduced from Elliott et al. 2005).....	204
Figure 10.1 Histogram of membranes' thickness of SLBs of DLPC, DMPC, and DPPC incubated in 10 mM Tris containing 150 mM NaCl at pH 7.4 and were measured with punchthrough experiments by CM-AFM (sliding velocity: 200 – 2000 μm/s all combined) .....	210
Figure 10. 2 Comparison of histogram of membranes' punchthrough force measured by CM-AFM (sliding velocity: 200 – 2000 μm/s all combined) for SLBs of DLPC, DMPC, and DPPC prepared on 10 mM TBS containing 150 mM NaCl and 3 mM CaCl <sub>2</sub> pH 7.4 .....	211
Figure 10.3 Histogram of membranes' punchthrough force for SLBs of DLPC, DMPC, and DPPC prepared on 10 mM TBS containing 150 mM NaCl and 3 mM CaCl <sub>2</sub> . The solid line represents the average Gaussian line. DLPC : $6.34 \pm 1.5$ nN; DMPC : $12.86 \pm 2.34$ nN; DPPC : $20.27 \pm 10.39$ nN.....	211
Figure 10.4 Friction force measured by CM-AFM as a function of the sliding velocity for three PC SLBs with different chain lengths. The viscous friction coefficient of DLPC is $383.15 \pm 4.9$ nN.s/m ( $R^2=0.99$ ); of DMPC is $649.17 \pm 11.28$ nN.s/m ( $R^2=0.99$ ); and of DPPC is $1040 \pm 40.2$ nN.s/m ( $R^2=0.99$ ). .....	212
Figure 10.5 Punchthrough force and friction viscous coefficient of PC lipid with different chain lengths. ....	213
Figure 1 MultiMode atomic force microscopy (reproduced from Anon 1998).....	221
Figure 2 Head of atomic force microscopy and its component: (1) laser, (2) mirror, (3) tip holder, (4) tilt mirror, and (5) photodiode detector (reproduced from Anon 1998).....	222
Figure 3 Example of AFM cantilever (not used in our experiment) (reproduced from Ogletree et al. 1996).....	223
Figure 4 Example of tip holder, (a) for measurement in air (reproduced from Anon 1998) and (b) for measurement in liquid .....	224
Figure 5 Position of cantilever probe mounted on the tip holder (not to scale) (reproduced from Bhushan 1995).....	224
Figure 6 Traces followed by a dull (dark line) and sharp probe (light line) as they go over a protruding feature. In this case, the side of the tip causes a broadening of objects in the image. (reproduced from Ricci & Braga 2004).....	225

<i>Figure 7 A double tip will cause shadow or double image along the scanning direction (reproduced from Ricci &amp; Braga 2004)</i> .....	226
<i>Figure 8 Imaging of small hole on the sample (reproduced from Ricci &amp; Braga 2004)</i> .....	226
<i>Figure 9 A badly damaged tip creates artifact while scanning a regular test pattern (reproduced from Ricci &amp; Braag 2004)</i> .....	227
<i>Figure 10 (a) Scanner vertical J used in our AFM instrument, and (b) Typical scanner piezo tube and XYZ electrical configurations (reproduced from Anon 1998)</i> .....	228
<i>Figure 11 Schematic of triangular pattern trajectory of the AFM tip as the sample is scanned in two dimensions (reproduced from Anon 1998)</i> .....	229
<i>Figure 12 Curve of the scanner extension versus driving signal. Straight line shows the real relationship between scanner extension and driving signal (reproduced from Ricci &amp; Braga 2004)</i> .	230
<i>Figure 13 (A) Normal calibrated grid and (B) distortion of a test pattern due to scanner nonlinearity (reproduced from Ricci &amp; Braga 2004)</i> .....	230
<i>Figure 14 Effect of scanner hysteresis on a scan. Straight line represents the trace scan and the dotted line represents the retrace scan (reproduced from Ricci &amp; Braga 2004)</i> .....	231
<i>Figure 15 Creep effect on sample whose parallel lines. The bending lines is a result of zooming up in a larger image (reproduced from Ricci &amp; Braga 2004)</i> .....	232
<i>Figure 16 Typical curved trajectories of piezoelectric scanner attached to (A) probe or (B) sample stage (reproduced from Sinha 2009)</i> .....	232
<i>Figure 17 Quad photodetector arrangement (reproduced from Anon 1997)</i> .....	233
<i>Figure 18 Components of a standard atomic force microscope. (1) The AFM head and the piezoelectric stage. (12) The high voltage electronics. (3) The computer, Digital Signal Processor (DSP), and software that controls the AFM setup (reproduced from Baro &amp; Reifenberger 2012)</i> ..	236

# List of Tables

---

<i>Table 1.1 Macrofriction versus Microfriction (reproduced from Scherge &amp; Gorb 2001).....</i>	<i>19</i>
<i>Table 2.2 Comparison between SFA and FFM (reproduced from Bhushan 2011b) .....</i>	<i>54</i>
<i>Table 3.1 An overview of model membrane systems (reproduced from Takeyasu. 2014) .....</i>	<i>68</i>
<i>Table 4.1 Properties of lipid used in this study .....</i>	<i>110</i>
<i>Table 5.1 Comparison of lateral force calibration constant measured in different medium for several AFM tips whose different stiffness.....</i>	<i>131</i>
<i>Table 5.2 Constant of circular track diameter per amplitude voltage .....</i>	<i>139</i>
<i>Table 5.3 Regression line fitting of the curve in the Figure 5.20.....</i>	<i>141</i>
<i>Table 7.1 Comparison of friction viscous coefficient.....</i>	<i>180</i>
<i>Table 8.1 Properties of alkali cations.....</i>	<i>192</i>
<i>Table 9.1 Summary of mechanical characterization of DOPC/DPPC binary mixture by CM AFM..</i>	<i>202</i>



*(this page is intentionally left blank)*

# Communications

---

## Scientific Articles in preparation

- R. N. Baiti, S. Jaramillo-Isaza, K. El Kirat , O.Noël , and P-E. Mazeran. ***Quantification of nanomechanical properties of supported lipid bilayers using the AFM circular mode.***
- R. N. Baiti, S. Jaramillo-Isaza, K. El Kirat , O.Noël , and P-E. Mazeran. ***Study the effect of environment onto nanomechanical properties of fluid lipid using the AFM circular mode.***
- P-E. Mazeran, R. N. Baiti, S. Jaramillo-Isaza, K. El Kirat , and O.Noël , and. ***Calibration of lateral force in atomic force microscopy using a scratched sample.***

## Oral Presentations

- S. Jaramillo-Isaza, R. N. Baiti , K. El Kirat , O.Noël , and P-E. Mazeran. ***Assessment of nanomechanical properties of biomimetic membranes using AFM Circular Mode.*** 2016. Nanoinbio Conference. Guadeloupe, France
- S. Jaramillo-Isaza, R. N. Baiti , K. El Kirat , O.Noël , and P-E. Mazeran ***Quantitative measurement of the viscosity of biomimetic membranes using the AFM Circular Mode.*** 2016. AFM Biomed Conference. Porto, Portugal
- R. N. Baiti, S. Jaramillo-Isaza, K. El Kirat , O.Noël , and P-E. Mazeran. ***Nano-mechanical characterization of biomimetic membranes using the Circular Mode AFM.*** 2016. European Society of Biomechanics Congress. Lyon, France.

## Poster

- R. N. Baiti, S. Jaramillo-Isaza, K. El Kirat , O.Noël , and P-E. Mazeran. ***Nanotribological measurement using AFM circular mode .*** 2016. Nanoinbio Conference. Guadeloupe, France

*(this page is intentionally left blank)*